Ag-Ge Bi-lobed Nanoparticles: Synthesis, Structure, and Plasmonic Properties

By

Karen Carr Bustillo

A dissertation submitted in partial satisfaction of the

requirements for the degree of

Doctor of Philosophy

in

Engineering – Materials Science and Engineering

in the

Graduate Division

of the

University of California, Berkeley

Committee in charge:

Professor Eugene E. Haller, Chair
Professor Daryl C. Chrzan
Professor Jeffrey A. Reimer

Spring 2013

Ag-Ge Bi-lobed Nanoparticles: Synthesis, Structure, and Plasmonic Properties

Copyright 2013

by

Karen Carr Bustillo

Abstract

Ag-Ge Bi-lobed Nanoparticles: Synthesis, Structure, and Plasmonic Properties

by

Karen Carr Bustillo

Doctor of Philosophy in Engineering - Materials Science and Engineering

University of California, Berkeley

Professor Eugene E. Haller, Chair

A novel metal-semiconductor bi-lobed nanoparticle is introduced as a hybrid plasmonic nanostructure. This nanostructure, comprised of a lobe of Ag and a lobe of Ge, forms in a matrix due to phase segregation of the constituents and is thermodynamically stable at room temperature. The interface structure is imaged with high-resolution electron microscopy and found to be an incoherent interface with the {111} planes of the Ag and Ge components parallel to each other explaining the low Ag-Ge interfacial energy. The hemispherical shape of the silver fraction and the shared Ag-Ge interface produce a unique surface plasmon resonance in the visible to near infra-red range. This localized surface plasmon resonance is measured as an ensemble average using optical spectrophotometry and the resonance near 1.5 eV is assigned to the plasmon mode located at the Ag-Ge interface in agreement with numerical simulations. It is proposed that the metal surface plasmon couples to the semiconductor at the shared interface and that the magnitude of this coupling can be probed with a surface-enhanced Raman experiment. Single particle electron energy-loss spectra and energy-filtered transmission electron images elucidate the electronic transitions in the semiconductor and metal as well as localized surface plasmon modes and bulk plasmon modes for both semiconductor and metal. Pulsed laser melting of the bi-lobed structure, followed by quenching to a mixed non-equilibrium Ag-Ge phase, results in significant reduction of the measured localized surface plasmon, which demonstrates the application of an optical switch.

Dedication

I dedicate this thesis to the loving memory of my father, Edward F. Carr. My father was a professor of physics at the University of Maine, Orono, where he mentored graduate students and pursued his research in the field of liquid crystals. He believed that the pursuit of truth through science required the highest objectivity and ethical standards. He believed that, through international meetings and collaboration, science could bridge countries and cultures, and that scientists had the responsibility to be a voice in the moral dilemmas that challenge our human condition. He believed, deep in his heart, that women are equally as capable as men of being scientists and engineers. The memory of my father has sustained and inspired me – he would have loved to have seen this day.

Table of Contents

Acknowledgments

First and foremost I would like to thank my advisor Professor Eugene E. Haller, for giving me the opportunity to complete the doctoral degree I started so many years ago. Professor Haller co-advised me during my studies of hydrogenated defects in silicon, and, when I expressed an interest in returning to complete the degree, he welcomed and supported me. His contagious curiosity, high ethical standards, and concern for his students make his group a thriving place to do research. Additionally, Professor Haller gathers a group of wonderful people around him, and we all benefit from one another's contributions.

I was fortunate to start my graduate studies under the guidance of Professor Jeffrey Reimer in the Chemical Engineering Department. From him, I learned a love of spectroscopy. His humility and commitment to teaching are an inspiration. He served on my qualifying exam committee, as well as my dissertation committee. I will always be grateful for his continued support.

Professor Dubon has had the knack of checking-in with me just when I needed a piece of advice. He served as the Chair of my qualifying exam committee and has been enthusiastic about my progress. I want to thank Professor Andy Minor and Professor Luke Lee who served on my qualifying exam committee, and Professor Daryl Chrzan who was a member of my dissertation committee and a participant in the Ge nanoparticle group.

I am grateful to the Department of Materials Science and Engineering for providing me with an outstanding education. I have been fortunate to have been taught classic subjects by the best professors: Electron Microscopy by Professor Ronald Gronsky, Thermodynamics by Professor John Morris, Semiconductors by Professor Eugene Haller, Spectroscopy by Professor Jeffrey Reimer, Quantum Mechanics by Professor John Clarke, Fracture Mechanics by Professor Rob Ritchie, and Crystallography by Professor Daryl Chrzan. These are the best teachers in their fields, and I am grateful for their service to public education. The hours in these classes have been some of the happiest of my life.

I thank my colleagues on the second floor of Building 2 at LBNL. To all the members in the Haller and Dubon groups, and in the Ge nanoparticle group, especially Marie Mayer, Erin Ford, Holland Smith, and James Mastendrea – I am grateful for their comaraderie. I appreciate the help from two theorists, Cosima Boswell-Koller and Carolyn Sawyer, who always answered my questions. Holland Smith is responsible for all of the Mathematica coding in my thesis. Jeff Beeman helped me with equipment, taught me best practices in the lab, and was always available to bounce around ideas. Joel Ager allowed me to help manage the Photoluminescence Lab, where I very much enjoyed training other users and helping to facilitate good research. Thank

goodness Lothar Reichertz was always available to help in the Photoluminescence Lab! Julian Guzman introduced me to sample preparation. Kin Man Yu did most of the RBS spectrometry in this thesis, and Wladek Walukiewicz helped me to understand the electronic nature of the Ag-Ge interface. David Hom handled many issues so that I did not have to, and provided support to all graduate students. I learned Raman spectroscopy from Ruben Lieten and am grateful for his continued collaboration. Bill Hanson has been a wonderful source of information, helpful hints, and the occasional random piece of material (for example, Er foil!).

I was fortunate to work with a talented group of scientists at the National Center for Electron Microscopy and to have access to state-of-the-art electron microscopes and sample preparation equipment. Chengyu Song spent hours teaching me the finer points of the Tecnai microscope, and was always patient and calm. Peter Ercius shared his enthusiasm for microscopy and explained many concepts. I am tremendously indebted to Marissa Mancuso who taught me everything I know about sample preparation, rescuing many samples along the way; her careful, deliberate technique is an art.

I am grateful for the collaboration with Vivian Ferry who ran all the numerical simulations in this dissertation and also coached me in the details of plasmonics.

I want to thank Drue McCarthy for her constant encouragement and support with this project. Drue proofread this entire manuscript, and was always eager to listen to the details of my research.

My sister, Liz, wrote in her Ph.D. thesis some years ago, "My sister…led the way so many times…" Liz, I may have started first, but this time it was your turn to lead, and you have been a role model for balancing a family and a career as a scientist!

I am deeply grateful for the rich lives of both my mother and father. My mother, an extraordinary elementary school teacher for her entire career, is still always learning, always pushing to do the next big project, engaged with life and with others. My father loved his career as a scientist and shared that love with his family.

Finally, I thank my family, Jim, Maria, and Luke, who supported me from start to finish. I am grateful for their patience and understanding.

Chapter 1 Introduction

We live in a time of unprecedented information accessibility and portability realized by the ever-shrinking size of the electronics that do the work. When describing technology, everyone understands the concept that less is more; smaller devices lead to faster speeds and more memory. The number of mobile phone users has increased from 16% of the world's population in 2002, mostly in the developed world, to over 86% percent of the world's population by the end of 2012, and smart phone ownership is increasing at a rate of 42% per year.[1] Never before has a single technology so quickly changed the daily lives of people in all countries, in all cultures, and most significantly, across all economic means. Indeed, the ability to send images or messages instantly, to anyone, was an effective tool for changing political systems in the Middle East in 2011, fondly referred to as the Arab spring. No other platform has so leveled the playing field. More than any other feature, it is "size" that has facilitated the technology. The concept of "less is more" has been shown to be true in physics as well.

When Moore's law was introduced in 1965,[2] the typical channel length for a CMOS transistor was 10 microns. Materials were described in terms of "microstructure" and "micro-labs" were built to conduct materials research necessary for the next generation of technology. Now, channel lengths are manufactured that are only tens of nanometers, almost three orders of magnitude less, and "nanostructures" and "nanoscience" are the relevant descriptors of materials science. Our appetite for more with less – more information in less time, with less packaging, using less power, and for less money – fuels the search for materials that can be controlled on the nanoscale.

Nanoscale control often means engineering the materials as composites of carefully designed building blocks. Patterning from the "top down" using photo- or e-beam-lithography has been the conventional process used to define nanostructures. But the diffraction of light in optical lithography and the throughput of e-beam methods limit future application of these techniques. Indeed, synthesizing materials with nanoscale structure has motivated revolutionary processing pathways, such as mimicking protein folding[3] or using DNA to facilitate self-assembly.[4] Colloidal chemistry has perfected the synthesis of nanoparticles with narrow size distributions; these particles can be ordered subsequently in an inorganic matrix.[5]

The synthesis used in this work relies on a simple concept. In a state of thermodynamic equilibrium, the Ag-Ge system is a strongly segregating alloy, and, in the appropriate solid matrix, an equilibrium particle with a given structure will form. Regardless of the process used to synthesize the Ag-Ge combination in the first place – whether it is defined by lithography, ion-implanted into a matrix, synthesized using wet chemistry, or, as in this work, sputtered in thin films – the particle configuration is fixed when at equilibrium, regardless of the history of the material. The ability to return to an original state reproducibly, despite material history, suggests the application of memory storage or "switch."

When the scale of the building block shrinks, the properties of the material sometimes change. For example, as the diameter of a nanoparticle decreases, quantum confinement of the charge carriers can alter the electronic band structure of the particle.[6] As the volume to surface ratio decreases, the role of the surface becomes more important; this concept is demonstrated by melting point depression in nanoparticles.[7] Mie scattering from a particle, on the order of, but less than the wavelength of incident radiation, is a perfect example of the interaction of size with surface. It is, in fact, boundary conditions of the curved particle or the flat surface that give rise to surface plasmons from gold or silver nanostructures that are responsible for the new field of plasmonics.[8]

Noble metal nanoparticles possess unique optical properties in the visible and near infra-red region of the electromagnetic spectrum. Although the physics for understanding their interactions with light was developed in the previous century,[9] the development of nanoscale characterization tools and improvements in computational power to simulate plasmonic interactions has breathed life into this rich area of science. Indeed, scientists from many disciplines study plasmonics, and applications address diverse problems. Single molecule detection for medical diagnostics and environmental hazards is made possible with devices that sense the plasmon resonance shift due to a local change in the refractive index.[10, 11] Clinical trials that utilize core-shell gold nanospheres to damage or ablate cancer cells by specific attachment and local heating are underway.[12-14] Using gold or silver nanostructures to couple light into optical devices holds promise for optical communications.[15] Researchers in the fields of solar energy[16-18] and catalysis[19-21] have even examined plasmonic nanostructures as avenues for efficiency improvements in their respective technologies.

1.1 Motivation

Although many applications utilize a single gold or silver nanoparticle, hybrid-nanostructures that contain a second component made of a metal, dielectric, or semiconductor are being designed.[22-24] As described in a recent review,[22] these two-component nanostructures can be divided into two groups: those whose second component passively alters the optical properties of the metal and those whose second component serves an additional active function. An example of a passive component is the use of gold-covered silica cores for use in the

aforementioned photothermal therapy.[12]   The silica core serves to tailor the absorption band of the particle to the near-infra-red therapeutic window of the human body. The gold shell absorbs the infra-red radiation and locally heats.   An example of an active component is a gold nanoparticle with a magnetic core that provides enhanced contrast for imaging applications.[25] The ferromagnetic core responds to magnetic field gradients and modulates the infra-red signal, thereby enhancing infra-red contrast in the images.

This project introduces a plasmonic particle made of one volume fraction noble metal and one volume fraction semiconductor – a bi-lobed hybrid nanoparticle as shown in Figure 1-1. The model system chosen is the Ag-Ge system, although the Au-Ge, Ag-Si, and Au-Si systems are equally accessible, and properties of Au-Ge particles will be presented as well. The unique shape of the hemispherical Ag component combined with the refractive index of the Ge at the shared interface is expected to produce an interesting surface plasmon resonance lineshape – an example of a passive hybrid structure. Additionally, it is expected that a localized surface plasmon mode from the Ag fraction will be supported at the Ag-Ge interface resulting in transduction of a surface-enhanced Raman response from the Ge component. This active function of the Ge component will serve as a "reporter" for the presence of the plasmon excitation. Future plasmonic devices may likely involve integration of both a semiconductor and a plasmonic material.
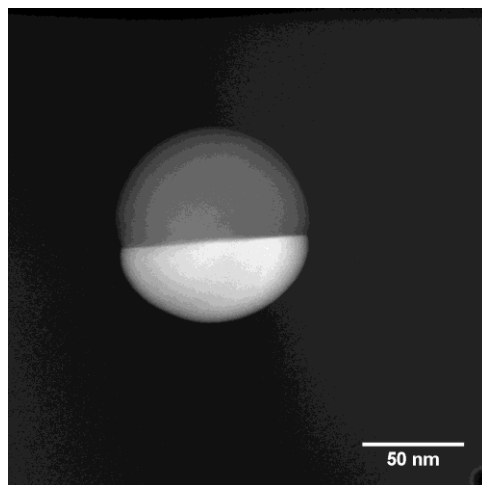
Figure 1-1.   High-angle annular dark-field scanning TEM image of a Ag-Ge bi-lobed nanoparticle embedded in SiO_2. The bright area is Ag and the darker area is Ge.

Surface-enhanced Raman spectroscopy (SERS) has been suggested as a tool for in-vivo imaging of specific cells.[26]   Qian et al. described an experiment whereby gold nanoparticles coated with a Raman-sensitive dye molecule selectively attached to the cell membranes of cancer cells in a mouse. By exciting the localized surface plasmon mode in the gold nanoparticle, the surface-enhanced Raman signal from the adsorbed dye molecules was detected as a function of position.   One could imagine a Au-Ge bi-lobed particle replacing the Au-dye molecule

3

combination in a similar experiment, with the Raman signal from the phonon mode in Ge being detected instead of the dye molecule. The Ge "reporter" is an ubiquitous part of the particle, stable and non-reactive.

A second application of the active function of this bi-lobed particle is as an optical switch. Pulsed laser melting has been shown to create a homogeneous mixture of the metal and semiconductor constituents[27, 28] due to the high cooling rates in the silica matrix.[29] Re-solidification into the bi-lobed configuration is possible with low-temperature rapid thermal annealing. The melting-recrystallization cycle has been repeated demonstrating a robust phase transition cycle.[28] It will be reported in Chapter 4 that after laser melting an amorphous alloy of Ag-Ge does not possess a localized surface plasmon resonance, and therefore would not couple to an adjacent optical component. The author envisions an optical switch that would be turned "off" (amorphized) with a high-energy laser pulse and turned "on" (re-crystallized in bi-lobed configuration) with a low-energy laser pulse. In the "off" position, the plasmonic particle would not be able to couple to an adjacent optical waveguide; in the "on" position, the particle would couple to the waveguide. The results of structural and optical characterization of pulsed-laser melting of Ag-Ge particles are included in Chapter 5.

A third application of an active function of this bi-lobed particle can be found in the study of surface plasmon physics. The Ag-Ge bi-lobed structure has been proposed to facilitate study of the dynamics of localized surface plasmon modes.[30] The decay of the plasmon excitation due to both radiative and non-radiative events occurs on a time scale of femtoseconds.[8, 31] Pump-probe experiments using an attosecond probe pulse in the extreme UV will modulate the absorption edge of Ge near 32 eV. Samples suitable for these experiments have been supplied to a collaborator[30] in the Department of Chemistry at UC Berkeley. This collaboration is described in Chapter 6.

One application of the passive nature of this particle involves its potential for forming a cup-shaped SERS substrate. It is possible that the Ag-Ge interface is curved in shape rather than being atomically flat. Whether the surface is curving into the silver, making the silver cup-shaped, or into the Ge, making the silver component more sphere-like, is determined by the relative values of the interface energies between the Ag-SiO$_2$ and Ge-SiO$_2$. Cup-shaped Ag components would result in a rim of high electric field, after removing the Ge component by etching, making an interesting SERS substrate.[32] Previous cup-shaped configurations have been realized with larger structures (>200nm) but not for the more technologically relevant 10-100 nm structures. The possibility of creating a cup-shaped SERS particle will be investigated using tomography in the transmission electron microscope. This project is in collaboration with a group in the Department of Materials Science at UCLA.[33] The microscopy is performed on the state-of-the-art Transmission Electron Aberration-corrected Microscope (TEAM) at LBNL, Berkeley.

The embedded Ag-Ge nanoparticles in this dissertation have drawn interest in the microscopy community as a model for evaluating simulation techniques and fundamental materials questions. A group in the Department of Materials Science at UCLA[34] is using material and TEM samples fabricated by the author to evaluate a new tomography reconstruction technique. This inverse Fourier Transform technique has been used successfully to reconstruct crystalline and polycrystalline particles; it is now desired to attempt this process with a particle consisting of two elements.

Indeed, a bi-lobed metal-semiconductor nanoparticle, isolated and supported in a matrix, serves as an "experimental test tube" for the study of the metal-semiconductor interactions. The system can be used to study surface plasmon dynamics, behavior of a localized surface plasmon on an absorbing substrate, surface-enhanced Raman scattering in a solid, and electromagnetic modes coupling into a semiconductor. The sample size is well-suited for both ensemble-averaged experiments and single particle measurements.

1.2 Review of literature for plasmonic metal-semiconductor systems

Research regarding plasmonic coupling to semiconductors is limited.[20, 35-37] Reports in the literature concerning plasmonic interactions between a metal and semiconductor fall into four categories. There are studies of the broadening and red-shifting of the localized surface plasmon resonance by embedding plasmonic nanoparticles into amorphous silicon[38-40] or forming Ag nanoparticles on the exterior surfaces of Ge nanowires.[41] There are investigations of the interactions of Au nanoparticles with the II-VI semiconductor CdSe with respect to emission enhancement or quenching.[35, 42] There are studies using noble metal structures to redirect light or enhance absorption for photovoltaic applications, done mostly with a dielectric layer between the semiconductor and the metal.[43] Finally, SERS studies of a Ge thin film on an Au substrate[44] and Ag island film on a Si substrate[45] have both demonstrated that a surface-enhanced signal is possible from a semiconductor. This work intends to further investigate direct coupling of the localized surface plasmon of a noble metal to a semiconductor with a shared interface.

1.3 The model system: Ag-Ge bi-lobed particles

The model system chosen is that of an Ag-Ge bi-lobed particle. This bi-lobed particle, as shown in Figure 1-1, is synthesized from a supersaturation of Ag and Ge in a SiO_2 matrix. Ag and Ge are strongly segregating elements; the eutectic phase diagram for this binary system shows nearly pure Ge and Ag segregation at room temperature. The constituents can be co-sputtered as thin films in an RF sputtering system with reasonable control over composition and film thickness. This fabrication technique, similar to those available in semiconductor manufacturing facilities, has high throughput. Subsequent annealing in an argon environment at

840˚C for one hour provides the temperature and time for diffusion of the Ge and Ag to precipitate from the matrix.

1.4 Structure of bi-lobed particles

The structure of the particles is imaged with transmission electron microscopy (TEM), using an FEI F20 Ultra-Twin Tecnai microscope at 200kV at the National Center for Electron Microscopy at LBNL, Berkeley, CA. The silver and germanium lobes are evident using high-angle annular dark-field (HAADF) microscopy also called Z-contrast, in the scanning transmission mode (STEM). In STEM mode the electron beam is focused to a probe size on the order of a nanometer and scanned over the sample surface. A annular-shaped detector collects electrons scattered through high angles (>5 degrees) and assigns a signal intensity to each pixel. These high-angle scattering events arise from interactions of the electron with the nucleus of the sample with a scattering cross section proportional to a value approaching Z^2.[46] In a Z-contrast image shown in Figure 1-1, the brightest area is Ag with Z=47. The darkest area is from the $Si_xGe_{1-x}O_2$ matrix (background) with an average Z of ~13. With Z-contrast imaging, it is possible to evaluate particle sizes, and approximate volume fraction of the components.

Further investigation of the interface structure of the particle is possible with high-resolution transmission electron microscopy. In this mode, contrast is derived from the phase interference between different diffraction conditions. Evidence of crystallinity is demonstrated by lattice fringes in the phase contrast image. A Fourier transformation on either side of the interface results in identification of the {111} planes of the Ag hemisphere being parallel to the {111} planes of the Ge hemisphere. High-resolution STEM images at different orientations of the particle have identified that the interface may align preferentially along a <110> direction in the Ag and Ge crystals. Investigations into possible strain in the Ag or Ge crystal are ongoing. Indeed, because of the small dimensions, it is probable that the nanoparticles will be able to sustain larger than normal lattice strain, which may result in interesting material properties.

Electron energy-loss spectroscopy (EELS) in the electron microscope confirms the identification of Ag and Ge in the nanoparticles by scanning through the high-loss region covering the characteristic core electron loss. The M-5 edge of the Ag atom at 367 eV and the L-2, L-3 edges of the Ge atom near 1200 eV are both evident in the EELS spectrum.

Samples for electron microscopy are prepared as cross-sections of the film layers and are thinned with mechanical dimpling and ion milling or by wedge polishing followed by ion milling. Additional TEM samples are fabricated by depositing the embedded nanoparticles directly on purchased TEM grids made from thin silicon nitride and silicon dioxide membranes.

It should be mentioned that with particle sizes approaching 100 nm in diameter, imaging using scanning electron microscopy (SEM) is also possible. Correlation to atomic force microscopy (AFM) has been utilized in the past as a more efficient way to measure particle

size.[47] Sample preparation for both of these characterization techniques requires releasing the particles from the SiO_2 matrix by etching with hydrofluoric acid and then sonicating the particles in methanol, resulting in a fine dispersion of the particles on the silicon substrate surface. Alternatively, the solvent containing the excess particles can be dropped on the desired substrate for examination. Results using SEM and AFM techniques are presented in Chapter 4.

1.5 Characterization of optical properties

1.5.1 UV-Vis-NIR spectrophotometry of ensemble

Standard characterization of the optical properties of plasmonic nanostructures includes a far-field optical absorption measurement of the ensemble, either as suspended particles in solution or dispersed in a thin film on a transparent substrate. Figure 1-2 shows an optical extinction spectrum for Ag nanoparticles in SiO_2. When the frequency of the incident light is equal to the natural frequency of the localized surface plasmon, resonance occurs. A UV-Vis-near IR spectrophotometer scans the wavelength of interest (x axis) and the transmission of the light is measured and converted to an extinction (y axis). Extinction is the term used to describe the light that is not transmitted; it is the sum of the absorbed and scattered radiation. The energy of the resonance and the lineshape are characteristics of a particular plasmonic nanostructure; they are a function of the dielectric properties of the metal and matrix, and the shape, size, and density of the particles. It is expected that the hemispherical shape of the silver component and the high refractive index of the Ge will shift and broaden the surface plasmon resonance compared with the spectrum from spherical Ag particles in SiO_2. The resonance lineshape will determine the excitation laser wavelength for subsequent SERS experiments.
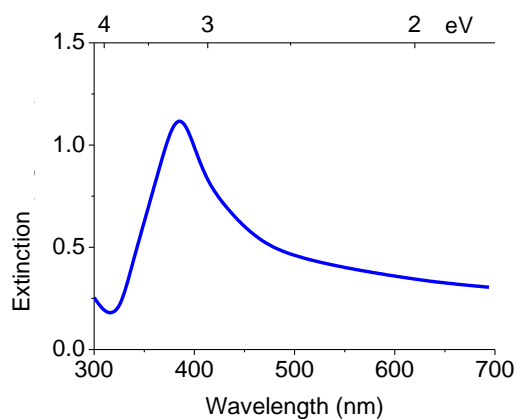
Figure 1-2. Extinction spectrum of Ag nanoparticles embedded in SiO_2.

1.5.2 Single particle EELS

Low-loss EELS in the TEM is ideally suited to map the localized surface plasmon intensity at different locations in the nanoparticle.[48] Recently, mapping of surface plasmon modes of both Au[49] and Ag[50] nanorods and Ag spheres[51] has been achieved using EELS in the low-loss region. Interaction with an electron beam allows probing of "dark" modes not accessible with light spectroscopy because the fast electron has momentum in the propagation direction, allowing it to couple to longitudinal modes such as volume plasmons.[49, 51] Dark-field scattering from single particles was correlated to single particle EELS mappings and simulated electric field maps.[50] In the case of the Ag-Ge bi-lobed particles, the energy range of interest is in the 1 to 8 eV range, the very low-loss region. Such low-energy measurements require a monochromator to reduce the width of the dominant zero-loss peak in the EELS spectrum. The energy resolution specification in the FEI Tecnai microscope with the monochromator as measured by the FWHM of the zero-loss peak is < 0.2eV.

1.5.3 Single particle energy-filtered TEM (EFTEM)

Single particle energy-filtered TEM images formed by transmitted electrons that have lost a given amount of energy are complementary to the EELS spectra. The transmitted electrons are dispersed using a magnet. A narrow slit, 0.5 – 1.0 eV wide, is positioned in front of the detector at the location analogous to the back focal plane. In this way an image of the sample is formed only by electrons with a specified energy loss. These images are analogous to images formed by selecting diffracted beams with the objective aperture and provide an intuitive feel of the interactions in the sample. Energy resolution is limited by the size of the slit and the stability of the incident beam to remain focused at a given spot, in this case +/- 1 eV.

1.5.4 Numerical calculations

Mie's seminal paper published in 1908 provided the analytical solution in 68 pages to Maxwell's equations for a sphere in a homogeneous matrix. For many applications, the assumptions hold well to first order, but they fall short when shapes other than spheres are involved. Indeed, the shape of the nanostructure is one of the most interesting and influential variables in plasmonics.[52] Colloidal synthesis techniques, e-beam writers, and even DNA templates are being used to fabricate particles with interesting shapes. Computers now have sufficient power to simulate the shapes' measured extinction cross sections and model the consequential electric fields. Two of the most commonly used numerical methods are finite-difference time-domain (FDTD) and discrete dipole approximation (DDA).[53, 54] The input parameters for both of these methods are the complex dielectric constants as a function of wavelength for the metal and the matrix, and the size and shape of the plasmonic structure. Maxwell's equations are solved for the electric and magnetic fields both inside and outside the structure, and the absorption and scattering (the sum of which is the extinction) cross sections can be calculated. Numerical calculations of the Ag-Ge bi-lobed particles have been performed

by a collaborator[55] from the Department of Chemistry at UC Berkeley. The numerically generated extinction spectra from a distribution of particles are correlated to the optical extinction measurements of the ensemble. Single particle electric field simulations together with calculated extinction cross sections correlate to the low-loss EELS mappings.[50, 51, 56]

1.5.5 Characterization of localized surface plasmon coupling to semiconductors

It is desirable to confirm and quantify the degree to which the Ge component is coupled to the localized surface plasmon mode in the Ag. The hypothesis is that, upon irradiation with a wavelength within the localized surface plasmon resonance band, a surface plasmon mode will be sustained at the Ag-Ge interface. It is proposed that the enhanced electric field extends into the Ge with sufficient strength to cause an enhanced Raman signal from the Ge at the interface.

Bulk Ge produces a Raman signal near 300 cm^{-1} due to scattering by optical phonon modes. Ge nanocrystals embedded in SiO_2 also produce a measurable Raman signal.[57] Micro-Raman measurements of single particles as well as ensemble measurements are suggested. It is expected that Raman spectra using different laser excitation energies near the measured localized surface plasmon resonance could confirm the active contribution from the silver plasmon.

1.6 Outline

Following this introduction, Chapter 2 includes a description of the optical properties of hybrid metal-semiconductor nanoparticles, emphasizing the localized surface plasmon. Chapter 3 includes a description of the synthesis of the bi-lobed nanoparticles including discussion of the solubility and diffusion of constituents. Characterization of the structure and composition will be described in Chapter 4 including particle sizes, interface structure, and removal of the nanoparticles from the matrix. Chapter 5 presents a description of the ensemble and single particle optical measurements, and numerical simulations of the optical properties. Chapter 6 will conclude this report with a summary of findings and a discussion of potential future work.

1.7 Conclusion

A novel hybrid plasmonic nanostructure consisting of one volume fraction silver and one volume fraction germanium is synthesized and characterized. This bi-lobed particle shows a unique optical absorption lineshape due to the hemispherical shape of the Ag component and the relatively large refractive index of the germanium at the Ag-Ge interface. Numerical calculations of the electric field in the near-field are correlated to low-loss EELS and EFTEM mappings, and simulations of the extinction lineshape are correlated to optical extinction measurements of the ensemble to complete a full description of the plasmonic character of the bi-lobed particle.

Further characterization of the plasmonic properties would be possible using single particle dark-field scattering and/or cathodoluminescence. It is further hypothesized that a localized surface plasmon mode exists at the metal-semiconductor interface which could be evident in the surface-enhanced Raman signal from the germanium. Observation of the SERS signal would confirm the metal-semiconductor structure as a promising active hybrid plasmonic structure.

Chapter 2 Background for Optical Properties of Nanoparticles

2.1 Introduction

This chapter will provide background regarding the optical properties of hybrid nanoparticles comprised of one hemisphere of a noble metal, Ag, and one hemisphere of a semiconductor, Ge. Interest will be limited to electromagnetic radiation in the near-IR to near-UV. For this study's purposes, this range corresponds to energies of 0.5 to 10 eV, wavelengths of 2500 to 125 nm and frequencies of $1x10^{14}$ to $2.5x10^{15}$ Hz. The optical response in this frequency range originates primarily from two distinct physical processes: 1. Mie resonances caused by the interaction of light with an object possessing at least one dimension of 10-100 nm, and 2. Electronic transitions, predominantly interband transitions from valence band to conduction band in the semiconductor and from the 4d orbital to the 5s orbital in the metal. First, this chapter will provide an overview of plasmonics as it relates to this work. Second, the dielectric response as a function of energy will be presented for both Ag and Ge. Third, the variables affecting the localized surface plasmon resonance (LSPR) will be presented, followed by an explanation of the enhanced electric field at the surface. Finally, the electronic structure of the Ag-Ge interface will be discussed.

2.2 Plasmonics

2.2.1 Plasmons

A plasmon is defined as a collective oscillation of the free carriers. In a metal, such as silver, these free carriers are the conduction electrons responsible for the atom's high thermal and electrical conductivity. In a semiconductor, such as germanium, the free carriers can be carrier electrons obtained by substitutional doping, or bound valence electrons participating in covalent bonds. If the semiconductor has been heavily doped with acceptors, holes can create a plasmon. Both carrier electrons (or holes) and valence electrons can produce independent plasmons in a semiconductor. In a dielectric, such as silicon dioxide, the bound valence electrons are responsible for the plasmons. Analogous to photons as the quantized packet of

electromagnetic radiation, plasmons are the quantized packet of a charge density fluctuation. Plasmons are excited in solids by photons or charged particles such as fast electrons. Plasmons can be divided into two different types: bulk (or volume) plasmons and surface plasmons. Surface plasmons can be divided into two categories determined by the geometry of the structure: surface plasmon polaritons are along planar interfaces, and localized surface plasmons are at the curved surfaces of bounded objects like nanoparticles.

Figure 2-1 shows a schematic of the free electrons oscillating about the positively charged atom cores in response to an excitation for three different geometries: bulk material, a thin film, and a nanometer-sized sphere. Each geometrical configuration results in a different subset of plasmons. The bulk material contains a volume plasmon (Figure 2-1(a)) that is a longitudinal wave established by a charge density fluctuation of the conduction or valence electrons. The thin film (Figure 2-1(b)) facilitates a propagating surface plasmon at the interface of the thin metal film and vacuum or matrix sometimes called a surface plasmon polariton. The word polariton is added to indicate the coupling of the plasmon with a photon. The nanometer-sized particle (Figure 2-1(c)) facilitates a localized surface plasmon, which is a standing wave, also at the interface of the particle and vacuum or matrix. It is important to realize that the bulk plasmon is an intrinsic property of the material; all three geometries can manifest bulk plasmons. By contrast, the surface plasmons, both propagating at the planar interface and non-propagating at the curved interface, arise from the interface with a different material, be it vacuum, liquid, or solid. As explained below in the discussion of the Mie theory, the surface plasmons arise out of imposing boundary conditions on the collective oscillations. The term "plasmonics" when used to describe a field of scientific study is concerned with the surface plasmons: surface plasmon polaritons or localized surface plasmons.

a) Bulk or Volume Plasmon
- longitudinal
- propagating

b) Surface Plasmon Polariton
- transverse
- propagating

c) Localized Surface Plasmon
- transverse
- non-propagating
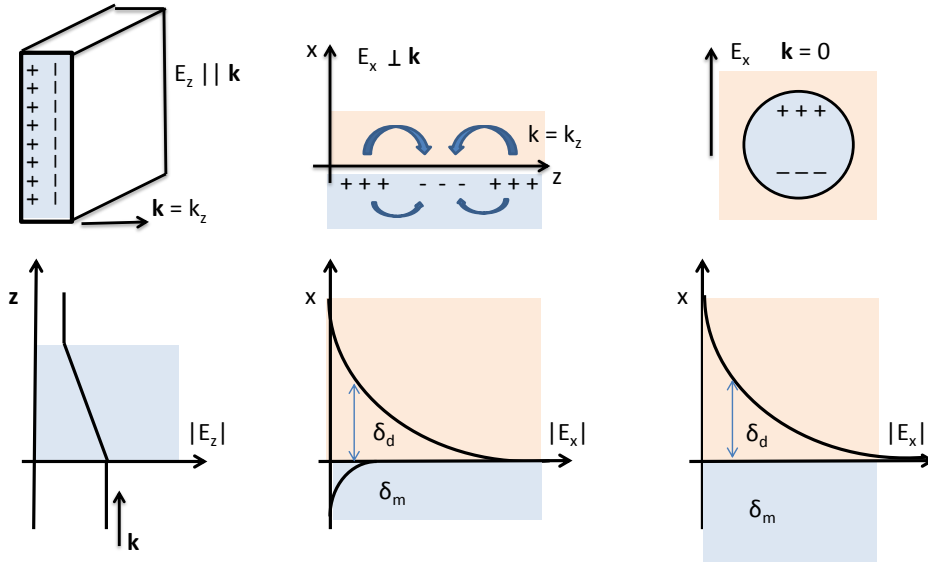
Figure 2-1. Schematic of three types of plasmons and their geometries. Top row: (a) volume plasmon in the bulk of the metal, semiconductor or insulator; (b) surface plasmon polariton propagating at the planar interface of the metal and the dielectric; (c) localized surface plasmon, a standing wave mode at the interface of the metal and the dielectric. Bottom row shows the corresponding magnitude of the electric field as a function of distance from the interfaces: (a) The decrease in electric field magnitude through the metal is due primarily to interband transitions which cause some absorption; (b) and (c) The magnitude of the electric field decays to 1/e inside the metal according to the skin depth, $\delta_m(\omega)$, and into the dielectric with the characteristic length, $\delta_d(\omega)$, on the order of the optical wavelength.

2.2.2 Bulk plasmons

Bulk or volume plasmons were first discovered by Ritchie[58] when he observed discrete energy-loss peaks at low energies (<50 eV) in the spectrum of electrons transmitted through thin films of metals. He explained the low-loss absorptions as arising from a collective oscillation of charge density that he named a plasmon. The charge density can arise from the conduction electrons in a metal, from free carriers in a doped semiconductor, or from bound valence electrons in a semiconductor or an insulator. The lowest-order mode of bulk plasmons occurs at or near the plasma frequency, ω_p, which will be discussed in section 2.3.3. Fast electrons are able to excite longitudinal volume plasmon oscillations and these volume plasmon modes are observed in the transmission electron microscope. Because electromagnetic radiation has transverse electric field vectors, it is not able to couple to the longitudinal volume plasmons and optical spectroscopy cannot be used to observe these "dark modes." Bulk plasmons in Ag, Ge, and SiO_2 and their relationship to experimental EELS data for the Ag-Ge particles will be discussed in Chapter 5.

2.2.3 Surface plasmon polariton

A surface plasmon polariton occurs at a planar interface of a metal and a dielectric medium. These surface plasmons are allowed to propagate along the interface with the electric field decaying evanescently into the metal with a decay length of δ_m, and also into the dielectric with a decay length of δ_d. These decay lengths are further described in section 2.3.6. The interest of these modes is largely in the field of optical communications where it is hoped that nanometer-sized structures will be able to confine optical signals of wavelengths much larger than the size of the structures.[59] In this way plasmonics is able to go beyond the diffraction limit. Currently, the most common application is a sensor that detects changes in the local refractive index at the surface of a plasmonic film. For the most part this project is not concerned with propagating surface plasmon polaritons.

2.2.4 Localized surface plasmon

A localized surface plasmon occurs at the interface between a metal or semiconductor and a dielectric in response to incident electromagnetic radiation. It is localized, meaning that the wave does not propagate; it is essentially a standing wave. One can imagine the free electrons oscillating about their ionic cores. When the incident light has a frequency equal to the natural frequency of the oscillation, a resonance is observed as a strong absorption by the plasmon as shown in Figure 2-2.
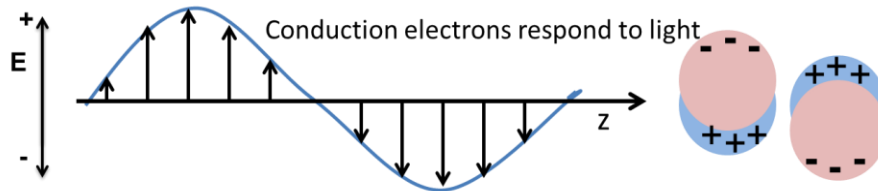
Figure 2-2. Schematic of a localized surface plasmon on the surface of a spherical nanoparticle. The oscillating electric field of the incident radiation induces an oscillation of the conduction electrons at their natural frequency, resulting in a phenomenon called localized surface plasmon resonance.

The localized surface plasmon resonance (LSPR) is responsible for the gold color of stained glass containing silver particles. Incident photons with wavelengths in the blue region of the visible spectrum are absorbed by the LSPR and light with wavelengths in the yellow region of the electromagnetic spectrum are transmitted. These are, in fact, the colors visible in the thin films of this project when deposited on a visibly transparent substrate as shown in Figure 2-3. The silver nanoparticles make the film yellow, and gold nanoparticles make the film a rosy pink.
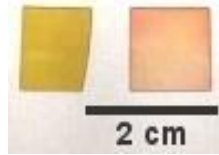
Figure 2-3. Photograph of SiO$_2$ thin film containing Ag nanoparticles (left) and Au nanoparticles (right) deposited on fused silica substrates.

These standing-wave modes were first mathematically derived by Gustav Mie as he tried to explain the different colors observed in colloidal solutions of gold particles with different turbidity. His famous paper published in 1908, *Contributions on the Optics of Turbid Media, Particularly Colloidal Metal Solutions,*[9] derives expressions for the absorption and scattering cross sections of an incident plane wave on a sphere. The problem is shown schematically in Figure 2-4 and is often referred to as Mie scattering. There are two aspects to highlight. The first aspect is that the geometry of the structure is less than, but on the order of, the wavelength of light being used. This study is concerned with nanoparticles on the order of 10 to 100 nm and incident light with wavelengths from 200 nm to 2 μm. The second important aspect is that the dielectric properties of the sphere and the matrix are described by complex quantities; they can have real and imaginary components. Solving Maxwell's equations for the electric field inside and outside of the sphere results in normal modes on the surface – these are the localized surface plasmon modes. These modes are present because of the geometry of the particles in a matrix. The matrix can be vacuum, liquid, or solid. For silver and gold nanoparticles these modes interact with light in the visible region of the spectrum.
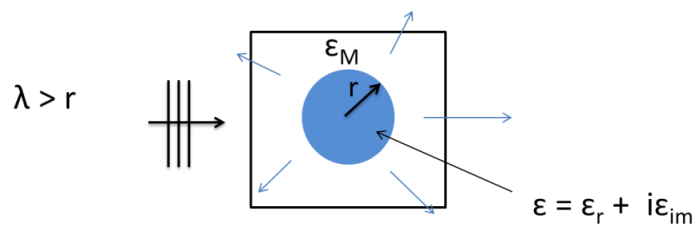
Figure 2-4. Mie scattering. A sphere with a complex dielectric constant, ε, is embedded in a matrix with dielectric constant, ε$_M$. A plane wave is incident from the left. The light is both absorbed by the particle and scattered in all directions.

It is to be noted that nanometer-sized structures are being treated classically with electrodynamics. In fact, the classical electrodynamics treatment is sufficient to describe the metal particle because the energy separation between levels in a metal is much smaller than the energy, kT, at room temperature.[60] It is only for structures less than 1-2 nm in size that quantum size-effects become sufficient to discretize the energy levels in silver or gold nanoparticles.[60]

15

Similarly for the semiconductor, Ge, Maxwell's equations for the interaction of light with the particle must be solved. The Bohr radius of the Ge atom[61] is 17.7 nm due to the low effective mass of the electron in this semiconductor. For dimensions smaller than this radius, energy separations can be on the order of kT at room temperature, and therefore the particle can behave like a potential well where the energy levels are discrete. It becomes necessary to utilize quantum mechanics for a rigorous analysis of the optoelectronic response for particle sizes significantly below the Bohr radius. However, for the purposes of this research, because the particles are in the range of 10 to 100 nm, this study proceeded to first order with a classical description. This approach has recently been shown to be appropriate for Ge nanoparticles embedded in SiO_2.[62]

Two of the findings of the Mie treatment are the absorption cross section, C_{abs} and the scattering cross section, C_{sca}[8, 63] for the interaction of light with the particle. For a spherical particle much smaller than the wavelength of incident light, only the dipolar terms in the expansion are dominant (this assumption is good for spherical Ag nanoparticles on the order of 20 nm in diameter); the cross sections are given by

$$C_{sca} = \frac{8\pi}{3} k^4 r^6 \left| \frac{\varepsilon - \varepsilon_M}{\varepsilon + 2\varepsilon_M} \right|^2 \qquad\qquad 2.1$$

$$C_{abs} = 4\pi k r^3 \, Im\left[\frac{\varepsilon - \varepsilon_M}{\varepsilon + 2\varepsilon_M} \right] \qquad\qquad 2.2$$

where k is the wavevector, r is the particle radius, and ε and ε_M are the particle and matrix complex dielectric functions respectively. It is apparent immediately that the scattering cross section scales with r^6 whereas the absorption cross section scales with r^3. Indeed absorption processes are more important for smaller particles, for example, for particles with diameters less than 20 nm. Scattering becomes dominant as particles become larger, for example, for particles with diameters greater than 20 nm. A second qualitative note is that the absorptive processes are derived from the imaginary part of the dielectric function. The imaginary components are understood as being dissipative or absorbing.

In the laboratory one can measure the localized surface plasmon resonance as the extinction of the light in a spectrophotometer; it is light that is not transmitted. When working with semiconductors it is common to understand this lack of transmission as absorption due to electronic transitions. In the case of plasmonic particles, the word extinction (or absorbance) is used to mean the sum of the absorption plus scattering. Absorption in this context refers to any dissipative process. The incident light excites either a localized surface plasmon resonance or an electronic transition in the particle. After excitation, the light is either re-emitted as scattered light or truly absorbed and lost due to phonon relaxation when either the plasmon excitation decays or the carriers thermalize. The angular dependence of the scattered light depends on the

polarization and shape of the nanostructure; light may be scattered in all directions or preferentially in specific directions.[63] The measurement accounts for the intensity of scattered light that is not directed toward the spectrophotometer detector, as well as the intensity of incident light lost to thermal relaxation. This quantity is the extinction of the sample.

The summation of the scattering and absorption cross sections result in an extinction cross section for the dipole mode, C_{ext}, which can be considered as the strength of the plasmonic response to light.[8, 63]

$$C_{ext} = 9\frac{\omega}{c}\varepsilon_M^{3/2} V \frac{\varepsilon_{im}}{[\varepsilon_r + 2\varepsilon_M]^2 + \varepsilon_{im}^2} \qquad 2.3$$

where V is the particle volume and ω is the frequency of incident light. The real part of the dielectric function of the particle is labeled ε_r and the imaginary part is labeled ε_{im}. The most important aspect in the above equation is that the extinction is a maximum when the sum of $(\varepsilon_r + 2\varepsilon_M)$ is a minimum. For particles embedded in glass or SiO_2 as in this work, the dielectric function of SiO_2 in the wavelength range 150 nm to 3500 nm is non-absorbing and so has a purely real value that has a positive sign.[64] Consequently, the smallest value of the parenthesis is achieved when the real part of the dielectric function of the metal nanoparticle is negative and equal in magnitude to twice the dielectric function of the matrix. The scattering and absorption are resonantly enhanced at this incident wavelength and this is often called the Frölich condition.[60] Additionally, one can conclude from the equation above that the plasmonic response is strongest with a smaller value for the imaginary component, ε_{im}, of the particle; it is the imaginary part that keeps it bounded – without the imaginary component the cross section would be infinite. It is crucial that both Ag and Au have negative values for ε_r in the visible spectrum, and this is the fundamental reason for their use as plasmonic particles in the visible region of the spectrum. Ag has a smaller value for ε_{im} at the Frölich condition than Au, which is why silver has a stronger plasmonic response.

2.3 Dielectric response of Ag and Ge

2.3.1 The optical constants: refractive index and dielectric constant

The optical properties of a bulk material, a material's response to incident electromagnetic radiation, can be described by two pairs of related optical constants: the complex refractive index and the complex dielectric constant. While their values are often stated at zero frequency, in reality they are optical functions of the frequency. The complex refractive index, n = n + ik, is the more familiar of the pair. The real part of the refractive index, n, is the phase velocity of light through a medium. The imaginary part of the refractive index, k, also called the extinction coefficient, represents energy attenuated in the material corresponding to damping of the oscillator (not to be confused with the wavevector, k, which is specified in

italics). The real, ε_r, and imaginary, ε_{im}, components of the dielectric constant are related to the refractive index through the following equations:[8]

$$\varepsilon_r = n^2 - k^2 \qquad\qquad 2.4$$

$$\varepsilon_{im} = 2\,n\,k \qquad\qquad 2.5$$

$$n^2 = \frac{\varepsilon_r}{2} + \frac{1}{2}\sqrt{\varepsilon_r^2 + \varepsilon_{im}^2} \qquad\qquad 2.6$$

$$k = \frac{\varepsilon_2}{2\,n} \qquad\qquad 2.7$$

The optical constants of the noble metals and semiconductors are listed as tables and graphs in the well-known references of Palik,[64] Philipp and Ehrenreich,[65, 66] and Johnson and Christy.[67]

2.3.2 Description of dielectric response

The complex dielectric constant, $\varepsilon = \varepsilon_r + i\varepsilon_{im}$, is a fundamental material property that indicates how a material responds to incident electromagnetic radiation. It is a measure of the material's ability to screen the alternating electric field of the incident radiation. Because light radiates at many wavelengths, the dielectric constant is a function of wavelength or frequency, $\varepsilon(\omega)$. The atomic processes responsible for screening vary at different frequencies from motion of space charges at the lowest frequency to oscillations of the electron cloud at the highest frequency. In this study's energy range from 0.5 to 10 eV, the dominant screening arises from motion of bound valence electrons and free conduction electrons.[68] In general, the dielectric function is also a function of the wavevector, k, which is indicated as an italic k (not to be confused with the extinction coefficient, k). However, one of the simplifying assumptions of this treatment is that the particle is small compared with the wavelength of light. In this regime, the electric field can be considered the same for all positions in the particle and one can, for the most part, ignore the k dependence. The most significant exception to the k=0 assumption is that, as the particle becomes larger such that retardation effects become significant, the width of the plasmonic lineshape broadens and higher-order modes become more important.[60]

The dielectric functions from bulk material are used to describe nanostructures. As mentioned previously, because the particles are generally larger than those susceptible to quantum size effects, using the bulk dielectric functions is reasonable and has been shown repeatedly to provide good agreement between experiment and simulation.[62] For plasmonic nanoparticles < 10 nm in diameter, where the particles are smaller than the mean free path for the oscillating electrons, a corrective term is typically employed to account for chemical interface damping.

Electromagnetic radiation has both an electric and magnetic field vector. The analogous constant for the response of a material to the magnetic fields of the incident radiation is the magnetic permeability, μ. For the noble metals and group IV semiconductors in the visible frequency range, the permeability is assumed to be 1.[60] This is a very reasonable assumption.

2.3.3 The plasma frequency

In the case of noble metals, and silver in particular, in the visible frequency range, the screening process is based on the ability of the large number of conduction electrons (10^{22}/cm^3) to oscillate in opposition to the incident field. For frequencies below 9.7×10^{14} Hz, corresponding to light of energies less than 4 eV and wavelengths longer than 310 nm, in bulk silver, the conduction electrons oscillate to counteract the incident field resulting in reflection of the incident light.   The frequency below which the light is reflected is known as the plasma frequency, ω_p. This phenomenon is evident when silver appears reflective and shiny; it is non-transparent in the visible. This measured plasma frequency at 4 eV is the sum of the screening due to the 5s conduction electrons and the interband transition between an initial 4d state and a final 5s state. The Drude model is used to address the behavior of the conduction electrons.

The Drude model for a metal assumes a "sea" of unbound conduction electrons where the plasma frequency is given by the simple relation

$$\omega_{p0} = \sqrt{\frac{n \, q^2}{m \, \varepsilon_0}}$$

$$2.8$$

where n is the number of free electrons or conduction electrons, q is the charge of the electron, m is the mass of the electron and ε_0 , is the permittivity of free space equal to 8.854×10^{-12} F/m. Given that q, m and ε_o are all constants, the plasma frequency scales as the $\sqrt{n}$.   Using a simple approach, the one unpaired 5s electron in the silver atom is assumed to be the source of the band of conduction electrons. Ag has a density of 5.9×10^{22} atoms/cm^3; that concentration becomes the conduction electron density, n. The energy at the plasma frequency, E_{p0}, is calculated to be 9 eV and is given by

$$E_{p0} = \frac{h \, \omega_{p0}}{2 \, \pi}.$$

$$2.9$$

Table 2-1 gives calculated and measured plasma frequencies for the metals, semiconductors, and dielectrics of interest. The difference between calculations using this simple Drude model and experimentally measured values is due to interband transitions. The use of more complex optical models can include effects of interband transitions, and they compare to experimental measurements more favorably.

Table 2-1. Plasma frequency.

Material	n (electrons/cm^3)	m_e (kg)	Energy at ω_p (calculated)	Energy at ω_p (measured)
Ag	5.86x10^{22}	9.1x10^{-31}	9 eV	4 eV[60]
Au	5.900x10^{22}	9.1x10^{-31}	9 eV	2.3 eV[69]
Ge p-type, free carrier holes	5x10^{18} (holes/cm^3)	Effective mass of hole = .29m_e	8.3x10^{-5} .154eV = 8046 nm	NA
Ge valence electron	17.6x10^{22} = 4x atomic density of Ge	9.1x10^{-31}	15.6 eV	16.3[70, 71]
Si valence electron	20x10^{22}	9.1x10^{-31}	16.6 eV	16.9-17.4[70]
SiO$_2$	4 x 6.6x10^{22}= 26.4x10^{22}	9.1x10^{-31}	19.1 with correction get 21.1	22.4[71]

In the case of a semiconductor, there are two plasma frequencies: a free carrier plasma frequency and a valence electron plasma frequency. The free carrier plasma frequency is caused by the screening of free carriers, and n, in this case, refers to the free carrier density. The sputtering process used to fabricate the embedded Ge particles can introduce contaminants and the p-type carrier concentration is estimated to be 10^{14} to 10^{18} cm^{-3} corresponding to a plasma frequency in the IR. The second plasma frequency of interest in this work is due to the oscillation of the valence electrons participating in the covalent bonding. Ge has four unpaired valence electrons per atom and a density of 4.4x10^{22} atoms/cm^3, which results in a calculated plasma frequency of 15.6 eV. The measured ω_p is between 15.9-16.3 eV.[70, 71]

A dielectric material can also have a plasma frequency where the screening is again facilitated by oscillation of the valence electrons. SiO$_2$ is tetrahedrally bound with four valence electrons. Using the density of SiO$_2$, a plasma frequency of 19.1 eV is calculated. The measured ω_p is 22.4 eV.[71]

The plasma frequency of the conduction electrons in a metal or the valence electrons in a semiconductor or dielectric is related to the frequency of the lowest-order bulk or volume plasmon.

2.3.4 Experimental values of the dielectric response, $\varepsilon(\lambda)$

Experimentally, the dielectric constant can be determined by measuring the optical response using ellipsometry or reflectance spectroscopy, and relating the real and imaginary components through the use of the Kramers-Kronig relations.[60] Alternatively, electron energy-loss spectroscopy (EELS) of thin films can be used to measure the energy-loss function which is

directly related to the imaginary part of the dielectric function, and the real component is found using Kramers-Kronig relations.[64]

The energy-loss function is defined[72] as

$$Im\left(-\frac{1}{\varepsilon}\right) = \frac{\varepsilon_{im}}{\varepsilon_r^2 + \varepsilon_{im}^2} \qquad 2.10$$

Figure 2-5(a) shows the relationship between reflectivity and the energy-loss function. At the plasma frequency, the reflectivity increases and the energy-loss function forms a peak. The width of the peak is inversely proportional to the relaxation time.[72] In the EELS experiments described in Chapter 5, the bulk plasmon peak corresponding to Im(-1/ε) will be used to chemically map the presence of Ge and SiO_2. Fortunately the energy-loss function for germanium is very strong making it a sensitive detector of the presence of Ge, as shown in Figure 2-5(b).
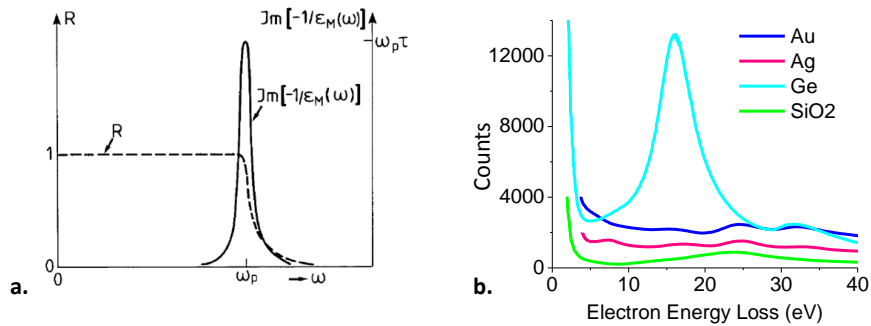
Figure 2-5. (a) Schematic behavior of the loss function and the optical reflectance as obtained from the Drude model. Figure is from Sturm.[73] (b) Comparison of energy-loss functions for Ge, Ag, Au, and SiO_2.[74]

The dielectric function of silver is plotted in Figure 2-6. In the region below 4 eV, the real part is negative; a negative real part of the dielectric constant is required to satisfy the Frölich condition for a localized surface plasmon resonance. The LSPR of silver nanoparticles 20-40 nm in diameter occurs in the region near 3 eV. The actual position will be a strong function of the matrix, but for air, water, or glass it is close to 3 eV. In this region, the magnitude of the imaginary component is close to zero, which is why the silver plasmonic response is so strong.

The function in Equation 2.10 is a maximum when $\varepsilon_r \rightarrow 0$. It follows that the maximum of the energy-loss function, corresponding to the lowest-order volume plasmon mode, coincides at the energy where $\varepsilon_r(\lambda)$ crosses the x-axis. The zero-crossing of the real part in Figure 2-6 lies at 4 eV, corresponding to the plasma frequency or volume plasmon energy. As shown in Figure

2-5(b), the volume plasmon in Ag does not have a strong energy-loss function. It so happens that the interband transition of a bound 4d electron to the one unfilled 5s state occurs at 3.9 eV, and this electronic transition is observed as the peak in the imaginary component of the dielectric function.
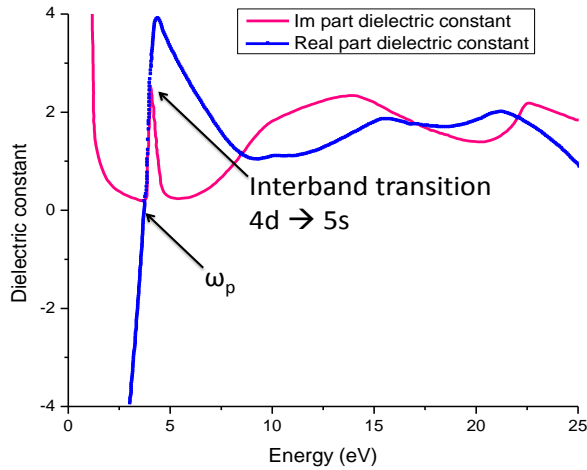
Figure 2-6. The real (ε_r) and imaginary (ε_{im}) parts of the dielectric function of bulk Ag calculated using a Kramers-Kronig analysis from reflectivity curves. Graph is from Ehrenreich and Philipp.[66]

The dielectric function of Ge is plotted in Figure 2-7. The data chosen for this graph is a composite of data from Aspnes and Potter in the Palik reference. As previously stated, because the nanoparticles are large enough that they do not exhibit quantum size-effects, the dielectric constants measured for bulk Ge are considered to be more accurate than data from Ge nanoparticles. In general, using ellipsometry to measure the optical properties of nanoparticles is highly dependent on the accuracy of the effective mean model used to model the layered system; this is the reason why ellipsometric measurements of nanoparticles are not used.

22
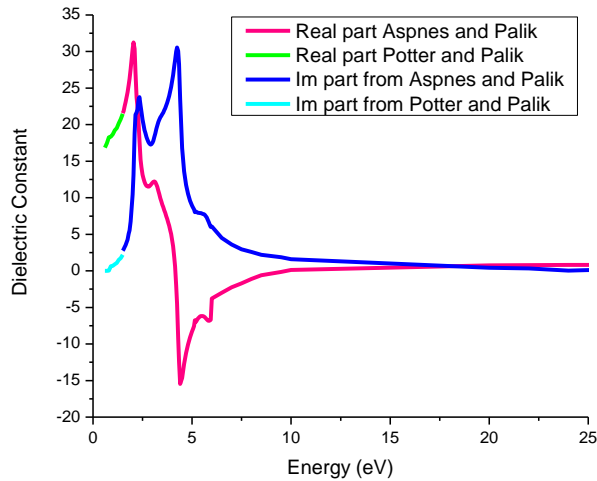
Figure 2-7. Real (green and red line) and imaginary (blue and cyan line) parts of the dielectric function of bulk Ge. Data from Aspnes and Potter from Palik.[64]

As can be seen from Figure 2-7, the real part of the dielectric constant crosses the x-axis at 15-16 eV, the value for the bulk plasmon of Ge.

Using a refractive index for air (n~1) to glass (n~1.5) in Equation 2.3 realizes two potential Frölich conditions near 4 eV and 6 eV. Only the one near 6 eV has an imaginary component that is small enough to realize a significant LSPR. Hanrath[75] and Uhrenfeldt[62] also predicted an LSPR for the Ge nanowires and nanoparticles respectively.

2.3.5 Interband transitions

The electronic structure for Ag is $4d^{10}5s^1$. For the case of Ag, the free electron model must be modified by the interband transitions from the 4d electron of the Ag shell to the 5s electron. These interband transitions begin at ~3.9 eV;[60] they occur near the χ and L points of the Brillouin zone. If these interband transitions are accounted for, the plasma frequency of Ag is reduced from the 9 eV value calculated using the Drude model to 4 eV, which is also measured using EELS.

An examination of the dielectric function of Ge reveals a number of sharp features in the imaginary part corresponding to absorptive electronic transitions. The fundamental absorption edge, E_o, is a weak indirect transition at 0.66 eV in Ge. The dominance of the direct optical transitions in the semiconductor are noted at $E_0 = 0.9$ eV at the Γ point, $E_1 = 2.2\text{-}2.4$, $E_0^{`} = 3.2\text{-}3.4$ and $E_2 = 4.3$ eV.[62, 76] The subscripts 0, 1 and 2 are assigned to transitions at the zone center, along the [111] directions, and along the [100] directions, respectively.[76]

23

A thorough study of the optical properties of small (2.5 to 6 nm diameter) Ge nanoparticles embedded in SiO_2 was recently published.[62] One finding from the study was that absorption by nanoparticles in the energy range from 0.5 to 6 eV was dominated by interactions at the particle/matrix interface caused by Mie scattering. Although the particle size was significantly less than the Bohr radius[61] of 17.7 nm, quantum confinement effects were immeasurable compare to Mie scattering effects. It was found that the absorption cross section per atom was less in the nanocrystals than in bulk material. The absorption spectrum showed a reduced absorption due to the interband transitions and an increased absorption due to the localized surface plasmon resonance observed at 6-7 eV. The observed LSPR for Ge was predicted in section 2.3.4.

2.3.6 Skin depth

Below the plasma frequency, although the light is reflected, the electric field is allowed to penetrate into the metal to a distance called the skin depth. The penetration of light into a metal decreases exponentially from the surface and attenuation of the electric field to an amount 1/e is defined as the skin depth, δ_m.

$$\delta_m = \frac{\lambda}{2\pi k} \qquad\qquad 2.11$$

The absorption (or extinction) coefficient, k, is just the imaginary component of the refractive index and can be derived from the complex dielectric function. This description is valid as long as the mean free path of the electrons is less than the skin depth. The mean free path of Ag at room temperature is 52-57 nm and the skin depth at relevant energies is listed in Table 2-2. One can see that this criterion is satisfied for 4 eV and almost satisfied for 2 and 3 eV.

Table 2-2. Skin depth and mean free path of metals at room temperature.

Material	Ag	Au
Mean free path at 273˚K	52^{60} nm to 57 nm	42 nm
δ_m (2 eV, 620 nm)	24 nm	31 nm
δ_m (3 eV, 413 nm)	29 nm	37 nm
δ_m (4 eV, 310 nm)	82 nm	27nm

The optical extinction coefficient or absorption coefficient, α, can be defined as

$$I = I_0 e^{-\alpha x} \qquad\qquad 2.12$$

This low-frequency limit is valid when λ is large compared to the mean free path of the electrons in the metal, *l*. Table 2-3 shows the decay length defined when $I/I_0 = 0.5$ for various semiconductors and energies of interest.

Table 2-3. Decay length of radiation into semiconductor.

Wavelength (nm)	Energy (eV)	Ge α (cm^{-1})	thickness in Ge at $I/I_0 = 0.5$	Si α (cm^{-1})	thickness in Si at $I/I_0 = 0.5$
415	3.00	532921	13 nm	219139	32 nm
506	2.45	406928	17 nm	55256	125 nm
604	2.05	182954	38 nm	19912	348 nm
800	1.55	35386	196 nm	4094	1693 nm
855	1.45	28296	245 nm	2458	2820 nm

2.4 Localized surface plasmon resonance (LSPR)

2.4.1 Resonance shift and linewidth dependence on variables

The frequency of the surface plasmon resonance is a sensitive function of the dielectric properties of particle and matrix, and the size, shape and density of particles. This is the basis for many technological applications – the shift in resonance frequency is monitored as a function of local environment outside of the particle which affects the dielectric constant. For example some biosensors detect molecules adsorbed to the surface of a silver film thereby changing the dielectric properties of the film. The home pregnancy test measures a shift in the LSPR (color change on the test) when the presence of a pregnancy hormone causes agglomeration of Au nanoparticles resulting in effective change in particle size.

Some simple simulations using a source code from a not-for-profit website called Nanohub.org can illustrate the origins of shape and position of the LSPR. Nanohub was created by the NSF-funded Network for Computational Nanotechnology. The plasmonic resonator package is called Nanosphere Optics Lab Field Simulator, and is available free of charge.[77] It uses Mie theory to calculate absorption, scattering, and extinction cross sections for spherical particles, where analytic solutions exist. It models the localized surface plasmon resonance lineshape and electric field intensities in and near the particle by solving Maxwell's equations for a given set of input parameters. The inputs are the material of the particle (Ag, Au or Si), the particle size, and the real part of the refractive index of the matrix. The following four plots were simulated using the Nanosphere Optics Lab Field Simulator.

The dependence of LSPR on particle diameter is shown in Figure 2-8. This example uses a silver nanoparticle with a variable diameter in a silicon dioxide matrix with a refractive index, n = 1.46. The y axis is the extinction efficiency, the extinction cross section divided by the physical cross section of the nanoparticle. One first notes that the maximum plasmonic effect is achieved with a particle that is 40 nm in diameter; this size particle also has one of the narrowest lineshapes. As particle sizes increase to 100 nm, the lineshape broadens and shifts to longer wavelengths due to phase-retardation effects. At these sizes, the assumption of k=0 no longer holds; in this size regime, the electric field of the incident radiation is not a constant everywhere in the particle. Additionally, one notes the presence of an additional peak that is blue-shifted and exhibits a narrow lineshape. This arises from a higher-order mode, most likely the quadrupolar mode.[16] Figure 2-9 shows electromagnetic modes from the original paper by Gustav Mie[9] showing the first- and second-order solutions to Maxwell's equations for a spherical particle interacting with an incident electromagnetic plane wave. As the particle diameter becomes longer than the mean free path of an electron in silver (~52-57 nm at room temperature), the electron effectively cannot reach the other side and so it oscillates in shorter arcs causing the presence of the quadrupolar mode.
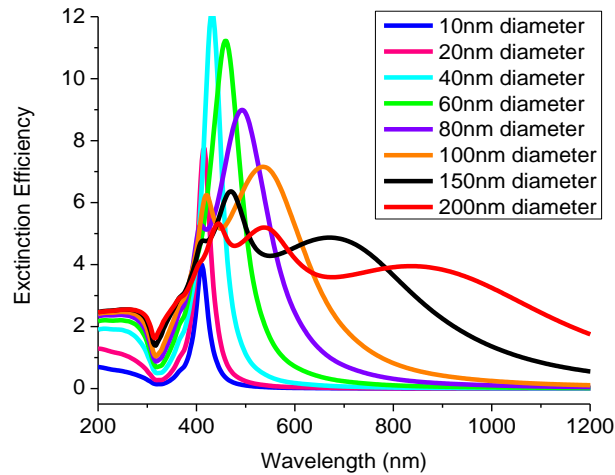
Figure 2-8. LSPR dependence on particle size. Extinction curves are simulated using a spherical Ag nanoparticle in an SiO_2 matrix with a refractive index, n = 1.46.
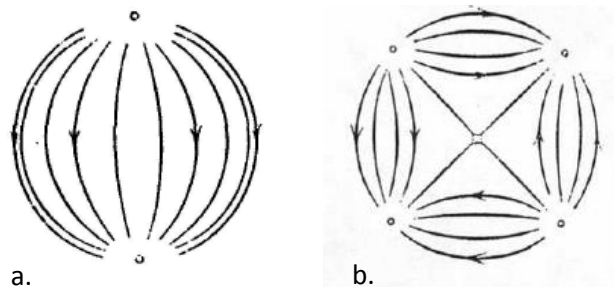
Figure 2-9. Electromagnetic modes: (a) Dipolar mode; (b) Quadrupolar mode. Drawings are from the original paper by Gustov Mie[9] showing the first and second order solutions to Maxwell's equations for a spherical particle interacting with an incident electromagnetic plane wave.

Figure 2-10 shows the LSPR dependence on the refractive index of the matrix. This simulation utilizes a 40 nm diameter Ag particle in a matrix with various refractive indices. The effect of the value of the real part of the refractive index is to shift the peak to longer wavelengths. At longer wavelengths the peaks also broaden and the higher-order mode peaks appear. The magnitude of the plasmonic response increases slightly from n=1.5 to n=3.5 showing the effect of increasing the difference between the refractive index of the particle and the matrix. The simulation does not allow for modeling the effects of a significant magnitude of the imaginary part of the refractive index, k, corresponding to absorbing terms. The larger the k value, the more damped the plasmonic response will become.
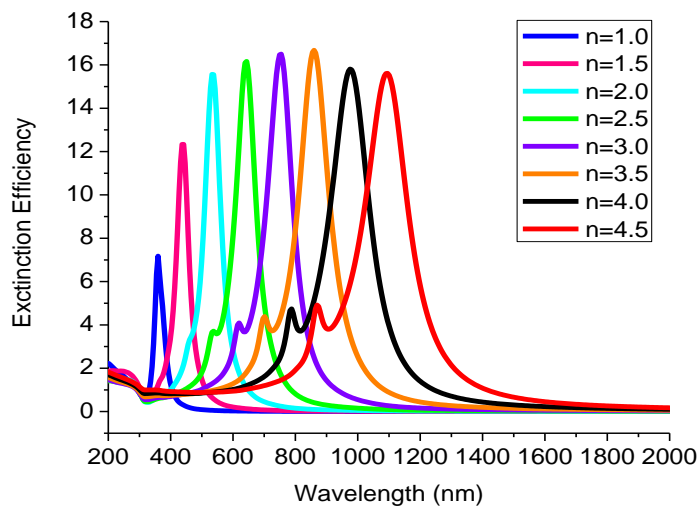
Figure 2-10. LSPR dependence refractive index of the matrix. Extinction curves are simulated using a 40 nm diameter spherical Ag nanoparticle in a matrix with various refractive indices.

Figure 2-11 shows the LSPR dependence on the particle material using a particle 40 nm in diameter in a matrix with a refractive index or 1.46. Ag has the strongest plasmonic response with an LSPR of ~3 eV in glass. The response of Au is approximately 3x less due to the larger imaginary part of the dielectric constant at the resonance frequency of ~2.4 eV. Silicon has no plasmonic response in the visible range although an LSPR can be found near 5 eV due to the bound valence electrons and in the IR if the material is heavily doped.
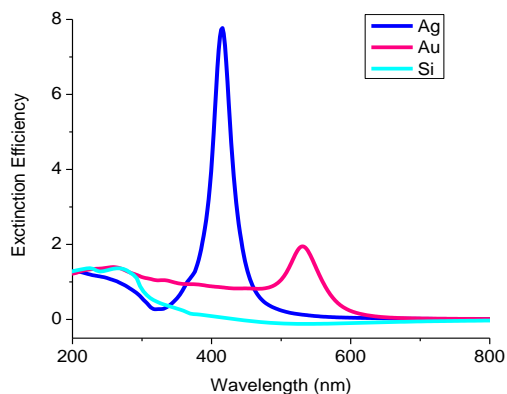
Figure 2-11. LSPR dependence on the particle material Ag, Au or Si. Extinction curves are simulated using a 40 nm particle in SiO_2 with n=1.46.

A final simulation examines the LSPR of a range of sizes of Ag nanoparticles in a refractive index of 4.5. The refractive index of Ge is a complex quantity with a largely varying magnitude in our energy range of interest as shown in Figure 2-12(b). In the visible range, n varies from 4 to almost 6. The value 4.5 was chosen because it is in the 1.2-1.5 eV range where one would expect to see the resonance as shown in Figure 2-13. The values for the refractive index of Ag are included below for comparison.
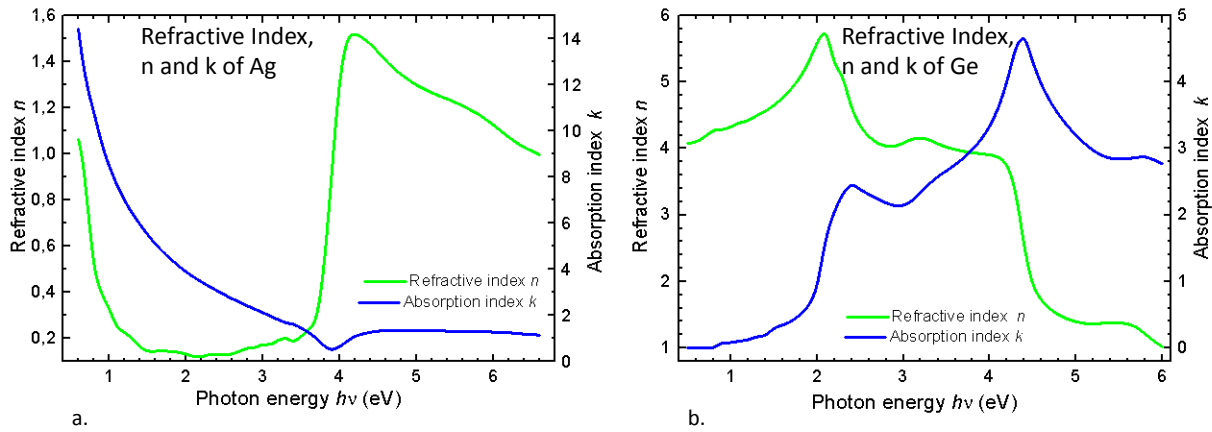
Figure 2-12. Refractive indices of Ag and Ge from www.ioffe.ru/SVA/NSM/Semicond/index.html.[78]
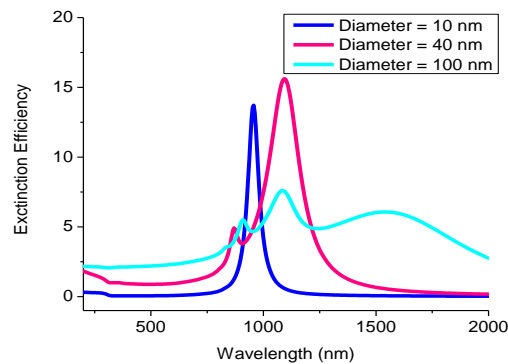
Figure 2-13. LSP resonance of an Ag particle in a matrix where n = 4.5. Extinction curves are simulated for an Ag particle in a matrix with n = 4.5 for particles of various sizes found in this work.

The remaining parameter that has not been discussed is that of the shape. The solutions to Maxwell's equations have been analytically solved for a sphere first by Mie and subsequently by others for the shape of an ellipse.[63] Numerical methods exist to estimate the response of other shapes and these will be used in Chapter 5 to simulate the bi-lobed structure. Most non-trivial shapes are characterized by experimental measurements such as the seminal work done by Mock et al.[52] showing the wavelength increase from 400 to 700 nm in going from spherical- to pentagonal- to triangular-shaped Ag nanoparticles.

2.4.2 Simple models of Ag-Ge system

In this project the hybrid nanoparticle has one strong plasmonic component, the Ag half, and one semiconductor component, the Ge half. The Ge half behaves as a dielectric, as an absorbing material, and possibly as a weak plasmonic material. The dielectric properties of the

29

strong plasmonic hemisphere are fixed by the choice of Ag. The size range will be controlled by the synthesis parameters although the ensemble will represent a distribution of sizes. The density of particles will be assumed to be separated sufficiently such that coupling between particles does not affect the LSPR. The shape of the plasmonic component is a hemisphere, which cannot be modeled analytically. The dielectric properties of the matrix will be determined by the refractive index of the SiO_2 matrix. It will be shown that in many samples, a significant amount of Ge remains in the glass, which will increase the refractive index above the standard 1.46.

The Ag-Ge interface can be thought of as a matrix interface as shown in Figure 2-14. In a "back-of-the-envelope" calculation, one can model a Ag sphere in both a SiO_2 matrix and in a Ge matrix. The author predicts that a primary localized surface plasmon mode will be supported at the Ag-SiO_2 interface corresponding to the mode with energy ~3 eV modeled in Figure 2-8, and, further, that a second localized surface plasmon mode will be supported at the Ag-Ge interface, with energy of 1.2 to 1.5 eV as modeled in Figure 2-13.
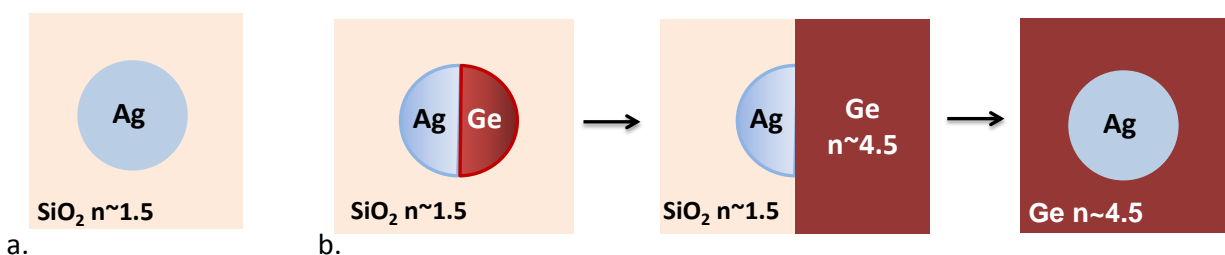
Figure 2-14. A simple model to predict the LSPR of an Ag-Ge bi-lobed particle. (a) Ag in an SiO_2 matrix; (b) The effect of Ge at the Ag interface can be modeled as though Ge is a matrix with refractive index, n ~ 4.5.

2.4.3 Ensemble measurement of LSPR

In the laboratory one can measure the localized surface plasmon resonance as an extinction of the light in a spectrophotometer. To make a thorough measurement of the extinction requires an integrating sphere to collect all of the scattered light.[63] However, a good approximation can be made by measuring the transmittance while accounting for the reflection as shown in Figure 2-15(a). The lamp intensity is I_0, the reflected fraction is R, and the transmitted fraction measured by the detector is T. The definition of the absorbance, A, otherwise called the extinction, is given by the ratio of the incoming photon intensity, I_{in} to the out-going photon intensity, I_{out},

$$I_{in}/I_{out} = 10^{-A} \qquad\qquad 2.13$$

$$I_{in} = I_0 - R \qquad\qquad 2.14$$

$$I_{out} = T \qquad\qquad 2.15$$

$$Log(T/(I_0 - R)) = -A \qquad\qquad 2.16$$

$$A = -Log(T/(1 - R)) \qquad\qquad 2.17$$

In the above description the reflected light is assumed to be largely from the reflection at each interface where the refractive index changes, i.e., from the surface, and each subsequent layer. Additionally, the nanoparticles themselves will reflect light, or, more specifically, a certain fraction of the light will be backscattered. Experimentally, the reflectance is measured using a reflectance module on the spectrophotometer. The transmittance measured by the detector is an upper bound as it includes light not interacting with the material, as well as light that is scattered in the forward direction. Nonetheless, this experimental measurement of the absorbance of the LSPR is quite accurate.
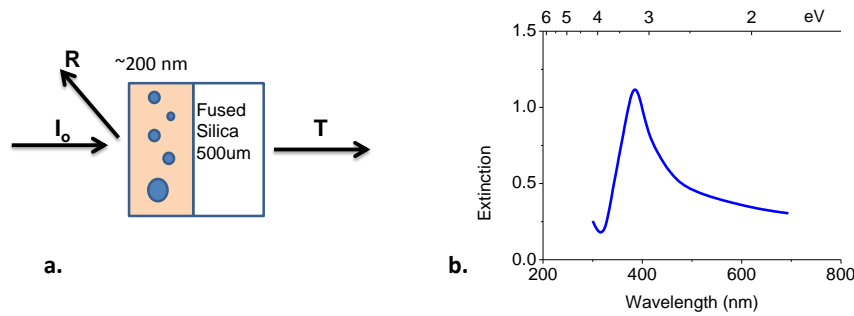
Figure 2-15. (a) Schematic of ensemble measurement of LSPR using a UV-Vis spectrophotometer; (b) Resulting spectrum showing extinction of LSPR for a thin film of silicon dioxide containing Ag nanoparticles.

The plot on the right in Figure 2-15(b) shows the extinction or absorbance as a function of wavelength or energy for a film containing silver nanoparticles in silicon dioxide. The resonance peak is at about 400 nm or 3.1 eV. To minimize $\varepsilon_r + 2\varepsilon_M$, in equation 2.3, a refractive index of 1.5 for SiO_2 is used, resulting in a ε_r value of -4.5 at resonance. The plot of the dielectric function of Ag in Figure 2-6 provides a value for the energy at resonance of 2.95 eV or 420 nm, close to what is measured for an ensemble of particles deposited in this work. Notice that this simple calculation did not involve the size or shape of the particles. The condition $\varepsilon_r + 2\varepsilon_M$ in Equation 2.3 is for spherical particles only and considers only the dipole mode of the expansion. This assumption is applicable for particles on the order of 20 nm in diameter. The mean free path of an electron in silver at room temperature is 52-57 nm. Nanoparticles that are

much smaller than 20 nm begin to experience increased surface scattering which red-shifts the LSPR and broadens the lineshape.[60]   As the restoring force decreases in larger particles, the resonance red shifts and higher-order modes appear. [60]   For example, the oscillation might be within one quadrant of the particle resulting in the quadrupolar mode. Another way of stating this limitation is to say that the dipole mode is the only mode retained so long as the electric field can be considered in the quasi-static regime – it has the oscillatory time dependence but the magnitude does not vary over the size of the particle.   This limitation assumes that the wavelength of incident light is on the order of, but greater than the dimension of the particle.

2.4.4 Summary

This section has described the various parameters affecting the position and the width of the localized surface plasmon resonance for noble metal nanoparticles in general. It presented a simple model as a starting point for probing the LSPR of the Ag-Ge bi-lobed particle.   An effective summary of the size effects of plasmonic particles is shown in the schematic in Figure 2-16 which is taken directly from Kreibig and Vollmer.[60]   It provides a basic understanding of the plasmonic response of metal nanoparticles.
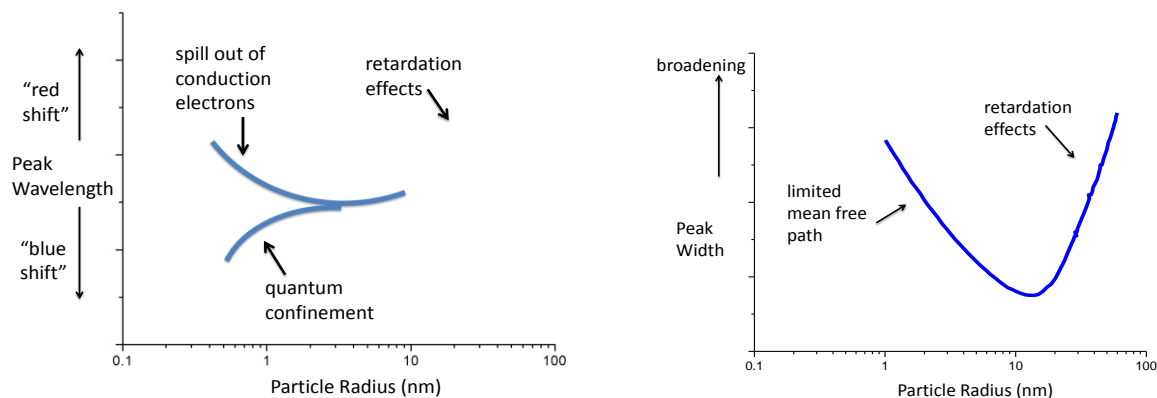
Figure 2-16. Schematic dependence of dipole mode of LSPR in position and width for a metal particle as a function of particle size. Incident light is in the visible range. From Kriebig and Volmer.[60]

2.5 Enhanced spectroscopies

2.5.1 Enhanced local electric field

One consequence of a localized surface plasmon is the potential for enhanced electric fields near the surface of the particle. The curved surface of a nanostructure produces a restoring force on the electrons at resonance conditions which can lead to field amplification at the surface as well as inside the particle.[8]   As shown in the schematic in Figure 2-1(c), the electric field intensity in the near-field decays exponentially from the interface between the metal and the

dielectric and into the matrix. The intensity of the field varies over the surface of the particle and is dependent on the polarization of the incident light. The magnitude of the field intensity (the electric field squared) can easily be one to several orders of magnitude larger than the incident field.   This concentration of field is responsible for the enhanced signal in many of the spectroscopies used in applications.

Using the same Optical Field Simulator[77] from nanohub.org, one can simulate the electric field intensity for a 30 nm diameter Ag particle in a medium with a refractive index of 1.5. Figure 2-17 shows the enhanced electric field at the surface of the particle for both x and y polarizations of incident light at the localized surface plasmon resonance of 427 nm. The black ring defines the Ag particle boundaries. The color scale indicates that the magnitude of the electric field intensity (E-field squared) can increase from negligible in the far-field to close to 300 at certain spots on the surface of the particle. As the incident light moves off-resonance, the electric field intensity decreases significantly. Although polarization effects can be measured for oriented nanostructures, the particles in this work are randomly oriented. Light used in the spectrophotometer is unpolarized. The electrons in the microscope will generate electric fields of all polarizations. The experiments with Raman scattering will utilize linearly polarized light but the particles are randomly oriented. The measurements in this work will be an average of all polarizations.
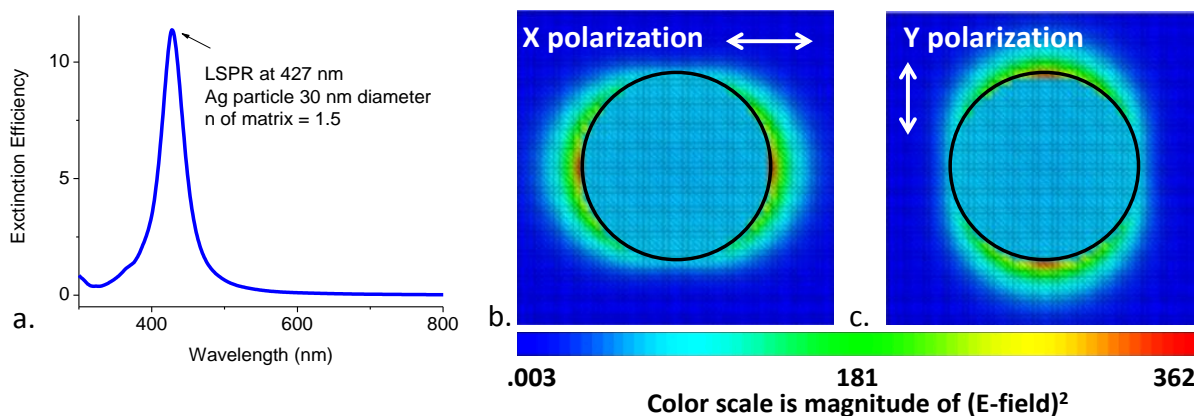
Figure 2-17. Simulation of electric field intensity for a 30 nm Ag particle embedded in a matrix with n=1.5. (a) Resonance at 427 nm. In the color images, the electric field intensity (units of $(statVolt/cm)^2$ for incident light of 427 nm with: (b) x-polarization; (c) y-polarization.

It is instructive to examine the absorption (or extinction) cross section for a particle in a plane wave (Figure 2-18). The enhanced electric field in the near-field caused by plasmonic resonance bends the energy flux lines.[63] The particle has effectively a larger absorption cross section than its diameter. Consequently the particle acts as a concentrator of the fields and is able to transduce the incident radiation to the high local fields which are responsible for the

enhanced spectroscopies.   Enhanced signal in phenomena such as Raman scattering,[79] fluorescence,[80] spontaneous emission,[35, 81] and infra-red absorption[82] have all been observed.
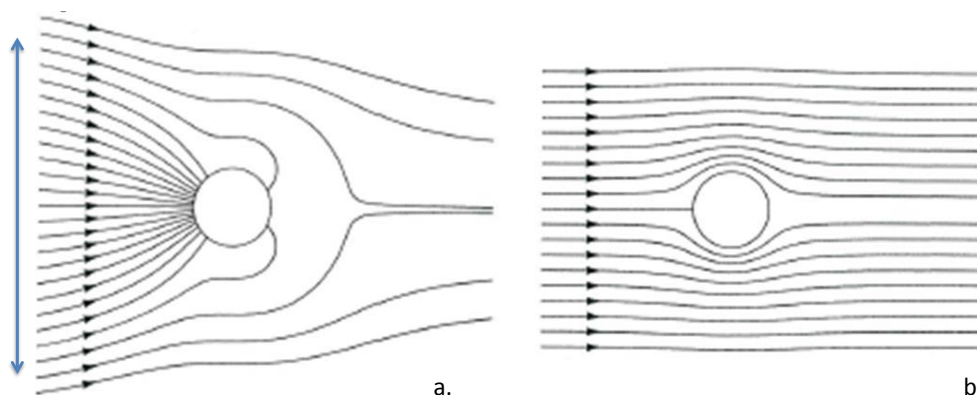
Figure 2-18. Field lines of the total Poynting vector (excluding those that scattered) around a small aluminum sphere illuminated by light of energy: (a) 8.8 eV (on resonance), and (b) 5 eV (off resonance). The blue arrow in a) indicates the effective radius of the sphere for absorption of light. From Bohren and Huffman.[63]

2.5.2 Description of enhanced Raman, fluorescence, transmission, and absorption

The presence of a resonantly enhanced electric field at the surface of noble metal nanostructures is the basis for many enhanced spectroscopies. The most familiar is surface-enhanced Raman spectroscopy or SERS. SERS was first observed in 1977 when investigators measured an anomalously high Raman signal from adsorbates on a roughened Ag electrode surface.[83, 84]   While the mechanism behind SERS remains controversial, the electromagnetic model posits that the effect arises from the enhanced electric field in the near-field of noble metal nanostructure or morphology of thin surfaces with dimensions in the 10-100 nm range.[79, 80] The technique usually measures the Raman signal of liquid adsorbates on these plasmonic surfaces.

Raman scattering occurs because incident light, most commonly single wavelength laser radiation, experiences a shift in wavelength when scattered by the rotational or vibrational modes of molecules. These are very small shifts, measured in inverse centimeters or wavenumbers, which amount to hundredths of eV in energy. The light can either be absorbed by the vibrational/rotational mode which is the more probable Stokes shift, or released by the mode, called the anti-Stokes shift.

In surface-enhanced Raman spectroscopy, the adsorbed molecule is close, within nanometers, to the plasmonic surface such that it feels the enhanced electric field. One can think of a three-step process: 1. The incoming light is effectively amplified by the strong local electric field. 2. The amplified radiation scatters from the mode of the molecule. 3. The scattered light is then amplified a second time as it leaves the particle surface and is detected by the detector. In this manner the effect of the enhanced local electric field is doubled. Because it is the intensity

of the light that is detected, the SERS effect is known to scale as the electric field to the fourth power,[85] and is the basis for the anomalously high signal. In practice, single molecules can be detected with signal enhancements commonly reported as high as reported as $10^4 – 10^8$.[79] In practice, the adsorbed molecules must find the "hot-spots" of each particle, for example the red locations in the image simulations of Figure 2-17, in order to be enhanced.

Surface-enhanced Raman spectroscopy of solids is also possible. In the case of Ge, the Raman scattering occurs because of phonon scattering from optical phonons. The first order Stokes Raman shift occurs at 299.8 cm^{-1} and the ε is fairly strong. Raman spectroscopy is routinely used to examine Ge nanoparticles with a sensitivity to concentrations as low as 4×10^{16} cm^{-2}; it is a realizable measurement.[57] Recent measurements of surface-enhanced Raman signals have been observed on a thin Ge film deposited on a SERS active gold substrate.[44] Previously SERS was used to study the strain of a 30 nm silicon layer deposited on a thick $Si_{1-x}Ge_x$ layer by depositing a SERS active Ag thin film on the strained layer.[45] The presence of the Ag sufficiently enhanced the Si Raman signal from the strained layer to discriminate the signal from the unstrained $Si_{1-x}Ge_x$ layer.

Based on the simulation shown in Figure 2-13, the LSPR at the shared interface is expected to facilitate a surface-enhanced Raman effect in the Ge when irradiating the bi-lobed nanoparticles with laser light in the 800-1000 nm range. This SERS effect is expected to be measurable. Probing the Raman signal as a function of incident laser light with wavelengths of 488 nm, 514 nm, 542 nm, 636 nm, and 780 nm is expected to help elucidate the presence of a surface-enhanced effect.

2.6 Electronic configuration of the Ag-Ge interface

A discussion of the electronic and plasmonic nature of this hybrid Ag-Ge nanoparticle would not be complete without discussing the behavior of electrons and holes at the interface. In fact, although such behavior is difficult to predict, this system can act like a "test tube" to experimentally probe the interactions at the interface. At one extreme, one could imagine a static space charge that would sustain a strong and measurable electric field at the interface. At the other extreme, one could imagine the electronic transitions of the Ge becoming so pervasive that the field is heavily damped reducing any field enhancement at the interface. In order to measure enhanced Raman scattering or enhanced absorption, the field must be supported at the interface. While the dielectric constant completely describes the electronic and plasmonic transitions in the material, it does not describe the charge separation at the interface. The effect of the charge separation is to have a dielectric function at the interface (and perhaps some distance into the semiconductor) that varies from the bulk function assumed to be valid for the remainder of the particle.

The bi-lobed nanoparticles are synthesized in a RF sputtering system used by a large number of users, who deposit a wide variety of materials. The materials include some of the most common deep and shallow defects in Ge. The following dopants are p-type in Ge: Ag (triple acceptor), Cu, Au, Pt, Mn, Ni, Co, Cr, Zn, and Al, of which Ag is the most significant. Donors in Ge include: Li, Sb, P, As, S, Se, and Te. Because of the preponderance of p-type dopants, it is assumed that the Ge nanoparticles are doped p-type (normal for Ge) with a concentration of 10^{14}-10^{18} atoms/cm^3. This number is a estimation based on experience,[86] however, the actual magnitude will not change the analysis outcome.

Germanium is also known to have a large number of dangling bonds at the interface, a problem for its widespread use as a semiconductor. These dangling bonds are known to pin the Fermi level to a level called the Fermi stabilization energy, E_{Fs}. The Fermi stabilization energy for most zinc-blende semiconductors has a well-accepted value of 4.9 eV below the vacuum level.[87] Silver has a work function of 4.3 - 4.5 eV below the vacuum level, which means that at the Ag-Ge interface, a few electrons will spill over from the metal into the semiconductor (Figure 2-19(a)). Because there are so many free electrons in the metal, an almost negligible space charge is created in the metal. In the semiconductor, electrons will compensate acceptors in the interface region. In a typical metal-semiconductor junction with silicon as the semi-conductor, this space charge region creates a Schottky barrier.

There are two cases. In Figure 2-19(a), no pinning is assumed at the Fermi level due to native defects. In this case electrons from the metal will drop down to the acceptors in the Ge and deplete that region of holes, the charge carriers. Having a larger depletion width means that the electric field will be less screened by the motion of the holes and more supported at the interface. In Figure 2-19(b) the Fermi level is assumed to be pinned at the interface due to native defects, largely dangling bonds. In this case there will be a very small depletion region meaning that the holes just outside the interface will be mobile and will be able to move to screen the electric field. Therefore, the effective localized surface plasmon mode will be less supported.
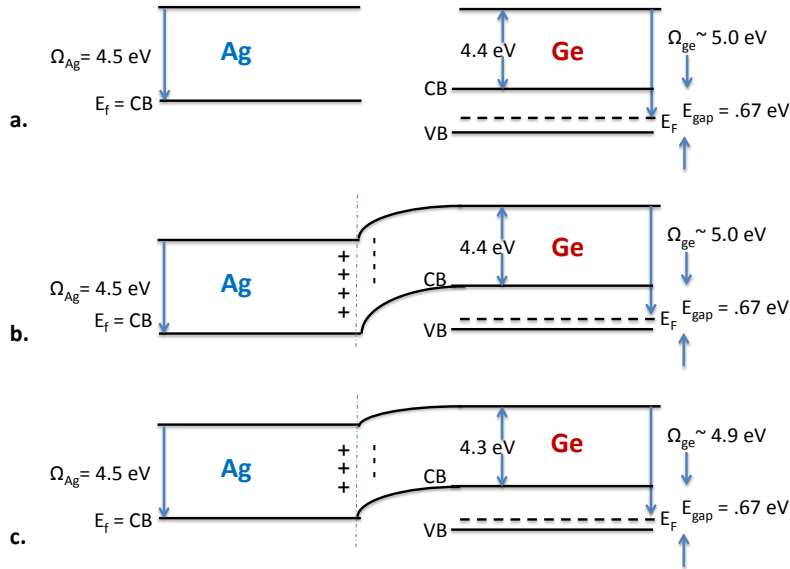
Figure 2-19. Electronic configuration of the Ag-Ge interface. (a) Work functions of bulk Ag and Ge prior to forming an interface; (b) Electrons from the Ag interface compensate Ge acceptors creating a depletion layer that is dependent on the work function difference between Ag and Ge; (c) Native defects at the Ge interface pin the Fermi level to the Fermi stabilization energy of 4.9 eV below vacuum, and consequently reduce the depletion layer.

2.7 Change of dielectric properties due to impurity scattering

According to the bulk phase diagram for the Ag-Ge system, the solubility of Ag in Ge is less than 0.1 atomic%. However, the solubility of Ge in Ag is on the order of 1 atomic% at room temperature. These estimates are for material reaching equilibrium; however, as the temperature is reduced, diffusion decreases, and consequently these values represent lower limits of observed solubility. It is possible that even higher concentrations of Ge are found near the interface of the bi-lobed particles. It is instructive to ask what effect these contaminants will have on the plasmonic response of the Ag. The predominant effect would be an increase in resistivity due to impurity scattering caused by the Ge contamination. This is expected to decrease the mean free path of electrons in the Ag from 52-57 nm at room temperature to a lesser value. As discussed in Section 2.3.2, a shorter mean free path will result in smaller nanoparticles experiencing higher order modes and broadening due to phase retardation.

2.8 Summary

The interaction of incident light in the visible region of the spectrum on a metal nanoparticle with dimensions of nanometers is dominated by the presence of a localized surface plasmon resonance. It is this interaction of light at the interface between the metal and the surrounding medium that facilitates enhanced absorption and scattering which is responsible for

not only the colors of stained glass, but also for powerful medical diagnostics and treatment modalities. This chapter has described the optical properties important for analysis of the Ag-Ge bi-lobed particles.

Chapter 3 Synthesis of Ag-Ge Nanoparticles

3.1 Introduction

Embedded metal-semiconductor bi-lobed nanoparticles are synthesized by co-sputtering Ag and Ge into a thin film of SiO_2 followed by thermal annealing. Because of the low solubility of Ag and Ge in the glass matrix, Ag and Ge precipitate out of the matrix and form nanoparticles. Bi-lobed nanoparticles form, as opposed to other configurations, such as isolated Ag and Ge particles or core/shell particles, because the Ag-Ge interface energy is low compared to the Ag/SiO_2 or Ge/SiO_2 interface energy. Consequently, the lowest free energy is a spherical particle, with approximately one volume fraction Ag and one volume fraction Ge, sharing an incoherent, but low-energy interface. The size of the particles can be controlled by altering the composition of the film and the film thickness. A range of sizes, from 5 nm to 100 nm in diameter, has been fabricated as shown in Figure 3-1.
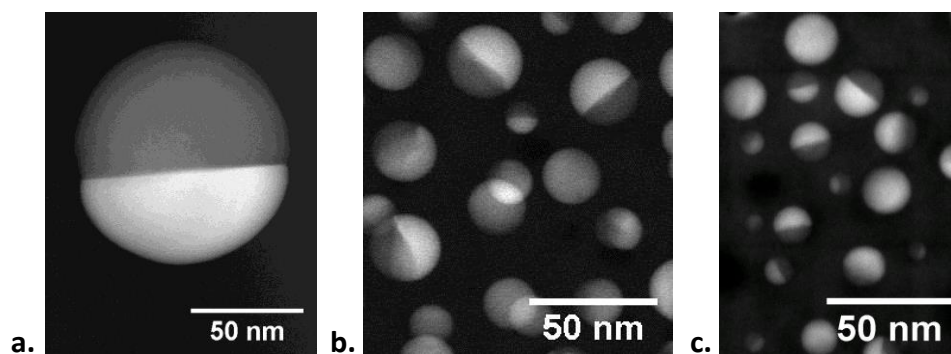
Figure 3-1. HAADF-STEM images of different sizes of Ag-Ge nanoparticles. The images have the same scale. (a) 96 nm diameter particle; (b) distribution centered at 19 nm diameter; (c) distribution centered at 14 nm diameter with smallest particle of 5 nm diameter.

Most of the transmission electron microscopy images referred to in this chapter will be high-angle annular dark-field (HAADF) scanning transmission electron microscope (STEM) images. These types of images are also called "Z-contrast" images because the contrast is derived largely from differences in Z, the atomic number, among different atoms present. For a given thickness, the darkest contrast is from regions of average low Z, and the brightest contrast is from regions of average high Z. In fact, the pixel intensity scales as approximately Z^2.[88] The contrast is also a function of the sample thickness; the scattering increases as the sample thickness increases. As explained in Chapter 4 in more detail, it is clear that for the Ag-Ge bi-

lobed particles, with Z_{Ag}=47 and Z_{Ge}=32, HAADF-STEM is an effective technique to image the two volume fractions of the particle.

This chapter contains a description of the deposition and thermal annealing used to fabricate embedded nanoparticles, and a justification for the choice of the model system, Ag-Ge. In addition, the chapter contains a review of the materials science relevant to particle formation including: 1. State function and relevant variables; 2. Theory of nucleation, growth and coarsening; 3. Solubility; 4. Heats of formation; 5. Segregation and the bulk phase diagram; 6. Model of bi-lobed particle formation; 7. Interface energies; and finally, 8. Diffusion of constituents. In the fourth section the research findings will be combined to describe the history of an Ag-Ge particle. The final section contains a presentation of synthesis pathways for additional embedded particle configurations such as layered structures, large Ge nanoparticles, large Ag nanoparticles, large Ge nanoparticles with Ag surface structures, and Au-Ge nanoparticles.

3.2 Overview of fabrication

3.2.1 Ion implantation of embedded nanoparticles

Formation of bi-lobed binary alloy particles was first introduced in 2010 in the work by Shin with Ge-Sn nanoparticles formed in a silicon dioxide matrix by ion implantation.[27] Subsequently, Ge-Au nanoparticles were formed by depositing thin films of SiO_2 + Au followed by ion implantation with germanium.[28] Both binary systems were investigated for their use as materials that undergo a phase transformation after pulsed laser melting (PLM). Before PLM, the metal and semiconductor are separated in the particle as two distinct volume fractions. After PLM, the particle is an amorphous mixture of Ge and Sn or Ge and Au. This amorphous mixture is a non-equilibrium phase caused by the rapid cooling of the particle after the melting laser pulse. Re-segregation was found to occur after low-temperature rapid thermal annealing. This phase transition was cycled multiple times in the Ge-Au material[28], and it is expected that similar cycling would be possible in the Ge-Sn material.

One drawback of the ion implantation fabrication process is the limited amount of constituents that can be implanted. Ion implantation is predominantly a surface treatment with exact control of the depth profile of a given species into the substrate. The energy of the implant determines the depth of the profile into the substrate, while the dose determines the concentration at each depth. The dose is controlled by the length of the implant and the beam current. Implant times are reasonably short for shallow junctions in semiconductors with concentrations of 10^{15} to 10^{18} atoms/cm^3. Formation of nanoparticles in a matrix requires concentrations of constituents higher than a percent, and consequently, the implantation times are long or the depths are shallow or both. The practical application of ion implantation limits both the size of the particles and the number of particles generated.

3.2.2 Sputtered thin films

The particles that are the subject of this work were synthesized in thin films using sputter deposition. Such processes are commonly used in industrial applications to deposit large or small amounts of material with few special technological demands, such as the need for ultra-high vacuum. The desired material is removed from a target by an energetic heavy ion, such as a positively charged argon atom that has been generated by a plasma discharge. Sputtering deposits a uniform film on almost any substrate material. The precursors are solid targets that can be made from the desired constituents. It is possible to sputter from several targets at the same time or to sputter in layers to achieve the overall composition. Substrate heating is optional, offering a low-temperature process.

This work uses the term "co-sputtering" to mean that the targets are fabricated from multiple materials. The starting material is a ¼" thick fused silica round mounted on an 8" diameter copper base plate. Such an insulating target is used as the precursor to deposit the pure SiO_2 layers. Ag and Ge are incorporated into the matrix with a second SiO_2 target that has 5 mm x 5 mm pieces of Ag metal and Ge crystal attached to the SiO_2, using a thermally conducting colloidal carbon solution as shown in Figure 3-2(b). Carbon has a low sputtering yield, so carbon contamination is minimized. There are a total of 52 pieces of Ge and 4 pieces of Ag randomly distributed on the target. The efficiency with which a material can be removed from the target, called the sputtering yield, is related to the binding energy of the material. Typical sputtering yields, from Ar ions impinging on the target with 500 eV for the materials of interest, are listed in Table 3-1. The sputtering yield of Ag is much larger than Ge, thus, the 52:4 ratio of pieces produces a film with approximately 5:1 ratio of Ge to Ag. The composition of the films as a function of depth was analyzed by Rutherford backscattering spectrometry (RBS). The film composition, and consequently, the size of the particles, can be modified by changing the size of the target area covered by Ag and Ge.

Table 3-1. Sputtering yield of target atom with incident Ar ions of 500 eV.[89]

Target material	Ge	Ag	SiO2	Au	Si
Sputtering yield at Ar+ energy of 500 eV (atoms/ion)	1.1	3.2	1.3	2.3	0.4

A schematic of the sputtering apparatus used in this work is shown in Figure 3-2(a). It is a general purpose Perkin-Elmer 2400 RF sputtering system operating at 13.6 MHz. Standard operating pressures are 10 to 30 mTorr, and the substrate is not heated. The targets are 8" in diameter, and are mounted in a water cooled holder above the grounded substrate plate. Substrates of silicon wafers, fused silica pieces for visible transmission measurements, and prepared TEM sample membranes are placed on the substrate plate. A plasma of argon gas,

containing neutral argon atoms, electrons, and positively charged argon atoms, is excited by the RF generator using a power of 100 to 200 Watts. Because the target is made predominantly from an insulating material (SiO_2), an alternating bias, in this case at RF frequencies, is applied to the target to prevent the build-up of positive charge from the positively charged argon atoms. A positive bias on the target would repel the sputtering species. With an alternating bias on the target, it first attracts electrons and then positively charged species. Because the electrons are much more mobile, the target becomes negatively biased for most of the RF cycle, thereby increasing the amount of time the positive ions are sputtering the target material. Once sputtered, the neutral target atoms deposit on exposed surfaces. Typical deposition rates, resulting from the values used for pressure and power, are listed in Table 3-2. The negative bias established on the target using this set of parameters is also listed. For this work, films with thicknesses of 40-500 nm are deposited.
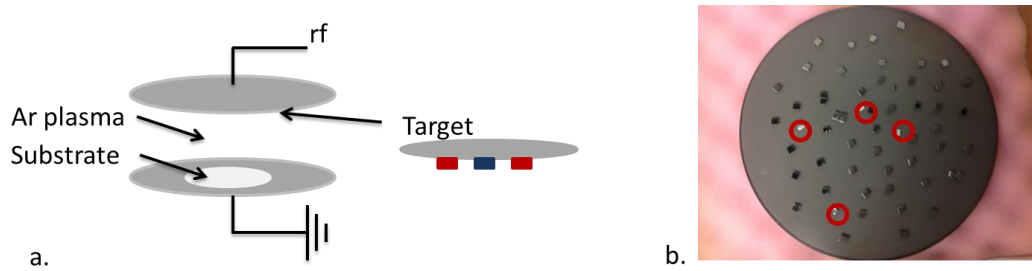
Figure 3-2. Co-sputtering. (a) Schematic of the target and substrate configuration; (b) Photograph of the actual 8" target made from a SiO_2 wafer and Ge and Ag pieces. The ratio of Ag:Ge is 1:13; the Ag pieces are indicated by a red circle.

Table 3-2. Deposition conditions for various targets used in this work.

Target	Target Power	Measured target bias	Chamber Pressure	Deposition Rate
SiO_2	200 Watts	920 V	20 mT	6 nm/min
SiO_2+Ag+Ge	200 Watts	820 V	30 mT	3 nm/min
Ge	100 Watts	825 V	10 mT	10 nm/min
Ag	100 Watts	800 V	10 mT	40 nm/min
Au	100 Watts	800 V	10 mT	30 nm/min

In this sputtering system, the substrate temperature is not controlled. Certainly the surface of the sample experiences an elevated temperature due to bombardment of energetic species. It is estimated that the bulk sample reaches temperatures of 50˚C to 100˚C during

sputter deposition, with the temperature at the surface being potentially higher. The elevated temperature encourages Ag diffusion, and Ag clustering is observed after deposition.

One of the most critical elements of the sputter deposition process is the chamber pressure during deposition. In the Perkin Elmer 2400, the pump efficiency is reduced using a butterfly valve to constrict the pumping throughput. A needle valve adjusts the flow of Ar gas into the chamber to achieve a given chamber pressure monitored by a convectron gauge. The lower the chamber pressure, the larger the mean free path of the target atom in the gas phase, with a corresponding increase in the deposition rate. Shorter mean free paths are indicative of more gas phase collisions that occur when the chamber pressure is increased, and consequently, the deposition rate will decrease. However, more collisions in the gas phase result in better spatial mixing of the constituents. Because the Ag and Ge were spatially defined on the target, without this mixing there would be a preference for line-of-sight deposition, and the composition of the deposited film would reflect the spatial composition of the target. For this reason, an unusually high deposition pressure of 30 mTorr was used to increase gas phase mixing and improve compositional uniformity when sputtering from the SiO_2 target with Ag and Ge pieces attached. Additionally, higher chamber pressure increased re-sputtering from the substrate, which although it reduced the deposition rate, also improved compositional uniformity.

3.2.3 Thermal annealing

The purpose of the subsequent thermal annealing is two-fold. First, time and elevated temperatures are required to facilitate diffusion of Ag and Ge in the SiO_2 matrix. Second, the silicon dioxide becomes malleable near $600^{\circ}C$.[90, 91] Once the matrix is able to conform, the particle can assume its spherical equilibrium shape, minimizing the surface energy contribution to the free energy of the particle.

Previous studies of embedded Ge nanoparticles involved annealing the sample in a low-oxygen environment to prevent oxygen from diffusing into the silicon dioxide and forming GeO_2, which suppresses nanoparticle nucleation.[27, 28, 57] This low-oxygen environment was achieved by placing the sample in a quartz tube and pumping for several hours to pressures of approximately 10^{-7} Torr to remove oxygen. The quartz tube was filled with Ar gas to a pressure of 0.5 atm, ensuring that there was adequate gas inside the tube for heat conduction during annealing in the furnace. The tube was sealed with a hydrogen-oxygen torch creating an ampoule with the sample in an enclosed argon environment. The ampoule can be placed in a furnace without concern for oxygen diffusion at elevated temperatures. This method also avoided undesired contamination from the furnace.

In previous studies of embedded Ge nanoparticles, the ampoule was placed in the furnace once the temperature had stabilized to the highest annealing temperature. At the end of the annealing cycle, the ampoule was removed quickly and cooled rapidly by placing it in cold running water. Although the cooling process occurred in less than a minute, the time was not

short enough to achieve non-equilibrium structures.[27] It is likely that the nanoparticles were in equilibrium even with the quick cooling method. Because this work used thin membranes of SiN and SiO_2 for TEM substrates, there was a concern that the thermal shock during initial heating and rapid cooling might cause the membranes to fracture. Therefore, the annealing procedures used in this work allowed the samples to heat and cool more slowly.

The standard procedure for most of the annealing in this work was to place a sealed ampoule in a Lindbergh/Blue HTF55322A furnace. The sample was placed in the furnace at room temperature and the temperature was increased to 840˚C over a period of 10 minutes. The sample annealed at 840˚C for 1 hour, followed by cooling to 620˚C at a rate of 220˚C/hr, followed by cooling to room temperature at an uncontrolled rate. The complete thermal cycle is shown in Figure 3-3(a).   Initial TEM images indicated that particles achieved more uniform structures after implementing the controlled ramp from 840˚C to 620˚C. This lower rate of cooling, through the Ag-Ge eutectic temperature of 651˚C, may have facilitated more equilibrium conditions.   However, it is now understood that the variability in structures originally observed was due to TEM sample preparation, not due to cooling too rapidly.
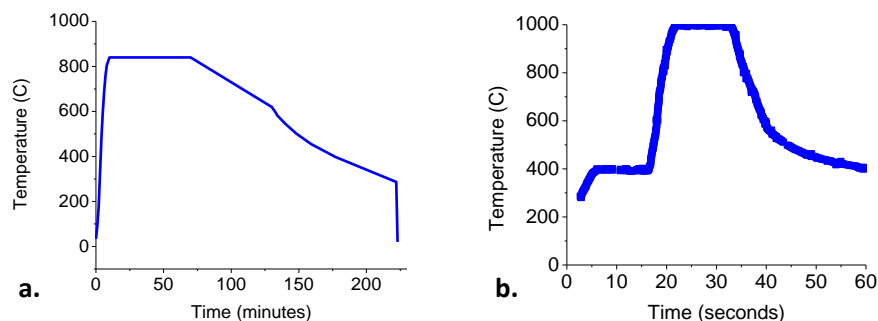
Figure 3-3. Thermal budget for (a) thermal annealing in the furnace at 840˚C for 1 hr followed by a 1 hr ramp to 620˚C; (b) rapid thermal annealing at 1000˚C for 10 s.

A sample was placed in an unsealed tube and then annealed in order to evaluate the necessity of the time-consuming ampoule process. During this test, nitrogen gas was flowing in the furnace to create an oxygen-deficient environment.   This sample formed large Ag nanoparticles; no bi-lobed particles were formed. From EFTEM images, it is apparent that there were clusters of Ge in the matrix. This test confirmed the necessity of using the ampoule process when doing furnace annealing.

It was later discovered that annealing for 30 seconds at 800˚C in a rapid thermal annealing (RTA) system while flowing nitrogen was sufficient to form the bi-lobed particles, provided that a capping layer of SiO_2 is sufficiently thick to prevent the complete out-diffusion of Ge. The system used was an AG Associates Heatpulse 210T-02. RTA heats via tungsten

halogen lamps that produce radiation in the near infra-red to visible wavelength range. The sample is placed on a silicon wafer that efficiently absorbs the radiation by exciting carriers across the silicon bandgap of 1.1 eV. Phonon relaxation heats the crystal. Samples of thin films are deposited on silicon wafers, allowing thermal contact between the oxide and substrate. The SiO_2 does not heat from the lamp radiation because the glass has a bandgap above the energy of the lamp; rather, it heats via radiation and conduction from the silicon substrate. Additionally, the nanoparticles of both germanium and silver absorb in the visible wavelength range. Irradiation excites carriers in the germanium and localized surface plasmons in the silver. Both relax via phonons that cause heating.

One advantage of rapid thermal annealing is increased control over the temperature cycle. In the furnace configuration, a large volume is heated via coils surrounding a quartz tube approximately 2" in diameter and 12" long. A thermocouple is placed in a quartz sheath in the furnace tube, and the signal from the thermocouple is connected to a feedback loop to drive the heating coils. However, due to the large volume, the temperature in the furnace can vary during the thermal cycle, and from run to run. The thermal budget for RTA at 1000˚C for 10 seconds was measured by the manufacturer and is shown in Figure 3-3(b). Although it is not at 800˚C, it demonstrates rapid rise in temperature followed by rapid recovery to room temperature. RTA is a more repeatable process than furnace annealing in these experiments.

This observation, of being able to use RTA to form the bi-lobed nanoparticles, supports other experimental evidence. Rapid thermal annealing for 10 seconds at 800˚C was used to re-segregate the Ge-Sn particles after PLM, even though the melting process resulted in a significant amount of Ge and Sn residing in the matrix.[27] Additionally, experiments in this work using RTA for 10 seconds at 800˚C created large (~5-20nm) Ge nanoparticles indicating that the 10 seconds at 800˚C is sufficient for Ge diffusion to nucleation sites.

3.2.4 Necessity of SiO_2 buffer layer and capping layer

Historically, embedded nanoparticles have been synthesized in this research group using ion implantation of Ge into thermally grown silicon dioxide or Au-doped sputtered silicon dioxide. The depth profile of germanium was tailored by adjusting the energy of the Ge ions such that the maximum concentration achieved a specified depth into the oxide. The standard process consisted of implanting Ge into a 500 nm thick thermal oxide using implant energy of 150 keV with a dose of $4x10^{16}$ atoms/cm^2. Nanoparticles formed in a band centered 50-90 nm from the surface. One advantage of this processing method is that in order for the Ge to diffuse away from the nanoparticle band, it must diffuse a significant distance to either the surface or the oxide/silicon interface, both which serve as sinks for the Ge.[92] A region of SiO_2 absent of Ge has been attributed to chemical formation of GeO_x as oxygen diffused into the near surface region.[92]

It was found that this layered structure was necessary to form the Ag-Ge bi-lobed particles to prevent the out-diffusion of Ge and Ag during furnace annealing. The overall Ge and

Ag concentrations were depleted after annealing, as shown in the RBS depth profiles of Figure 3-4. Ge is presumed to diffuse to the surface and then to leave the sample. Silver is known to be a relatively fast diffuser in SiO_2 at temperatures as low as 200-300˚C; evolution from the surface occurs at temperatures above 400˚C.[93] Consequently, most of the depositions were designed with a minimum 20 nm SiO_2 "buffer" layer between the nanoparticle layer and the substrate, and with a minimum 20 nm SiO_2 "capping" layer between the nanoparticle layer and the surface. This configuration is show in Figure 3-4.
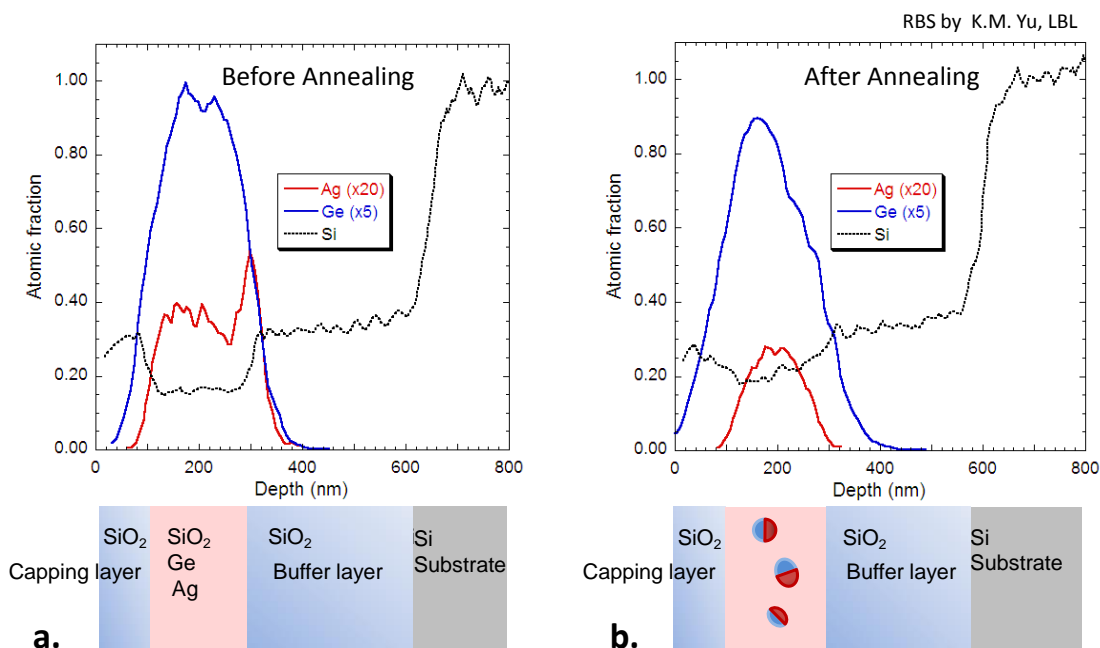
Figure 3-4. Rutherford backscattering spectrometry of layered thin films. (a) After deposition, before annealing, 19% Ge, 2% Ag; (b) After furnace annealing at 840˚C for 1hr with ramp to 620˚C, 16% Ge, 1% Ag. Percentages are atomic percent in the film layer colored pink in the schematic.

3.3 Choice of model system: Ag-Ge in SiO_2

The Ag-Ge system in SiO_2 was chosen as a model system for a number of reasons. Most important, silver was chosen as the metal because it has the strongest plasmonic response in the visible region of the spectrum as described in Chapter 2. In order to create strongly segregating nanostructures, the constituents must be insoluble in one another at room temperature. For a binary system, this requirement is met by systems exhibiting a miscibility gap such as is evident in the eutectic phase diagrams of the Ag-Ge, Au-Ge, Sn-Ge, Ag-Si, and Au-Si systems. All of these binary eutectic systems should form bi-lobed particles in a matrix that has low solubility for the constituents provided that the interface energies relative to one another follow the model of Yuan.[94] Germanium was chosen as the semiconductor because it has a low solubility in SiO_2 and is known to precipitate to form nanoparticles.[57] Silicon dioxide is an ideal supporting matrix

because it has a high melting temperature (>1415˚C), and it is amorphous, so that it will not impose preferences for crystalline orientation of the particle. Additionally, it is transparent in the near-UV to near-IR range, facilitating both the optical spectroscopy and the pulsed laser melting experiments. Both Ag and Ge have a low solid solubility in SiO_2.[95-97] Furthermore, deposited SiO_2 has been fully described in the literature because of its widespread use in the semiconductor industry, and it is a commonly used material. All three of these materials, Ag, Ge, and SiO_2, are non-toxic, naturally abundant, and relatively inexpensive.

3.4 Materials science

3.4.1 State function and relevant variables

In forming the particles, one must consider mass transport, the movement of atoms from one location or phase to another. The Gibbs free energy is used as the state function because the phases are not thermally isolated from one another. The Gibbs free energy has the natural variables: pressure (P), temperature (T), the number of Ag atoms (n_{Ag}), and the number of Ge atoms (n_{Ge}).

$$G(n_{Ag}, n_{Ge}, T, P) = H - TS \qquad 3.1$$

The enthalpy, *H*, which is a measure of the heat of the system, is the sum of the internal energy of the system (*E*) and work done on the system (*PV*).

$$H = E + PV \qquad 3.2$$

For most solids, the change in the PV term is small, so the internal energy and enthalpy are equal.

The partial derivative of G with respect to the addition or removal of a small amount of one constituent is defined as the chemical potential. Two chemical potentials, μ_{Ag} and μ_{Ge} are necessary to understand the movement of the n_{Ag} and n_{Ge} atoms during thermal annealing.

$$\frac{\partial G}{\partial n_{Ag}} = \mu_{Ag}; \frac{\partial G}{\partial n_{Ge}} = \mu_{Ge} \qquad 3.3$$

An example using Ag atoms is given below, although the same formulism applies to the Ge atoms. When the chemical potential at constant temperature and pressure of the Ag atoms in two phases, α and β, are equal, the change in the Gibbs free energy between the two phases is zero and the two phases are in equilibrium.

$$\text{When } \mu_{Ag\alpha}|_{T,P} = \mu_{Ag\beta}|_{T,P} \text{, then } \Delta G_{\alpha \to \beta} = 0 \qquad 3.4$$

When the chemical potentials of the Ag atoms in the two phases are not equal, then there is a gradient in chemical potential that provides the driving force for mass diffusion according to the following expression.[68]

$$J^{Ag} = -D^{Ag} \nabla \mu_{Ag}.$$ 3.5

J_{Ag} is the flux of atoms in atoms/cm^2-s. Mass will flow from regions of high chemical potential to regions of low chemical potential.

D_{Ag} is the mobility of Ag in the solvent and is also called the diffusivity or diffusion coefficient. The solvent could be the SiO$_2$ matrix, Ag-Ge$_{(l)}$, Ag$_{(s)}$, or Ge$_{(s)}$. The mobility will depend on the exact solvent, composition, and temperature. D has units of cm^2/s and it has the form

$$D = D_0 \, e^{-E_A/kT}.$$ 3.6

D_0 is a constant and E_A is the energy barrier the specie must overcome to diffuse. Mass is thus seen to move with a diffusivity D, in response to the force $\nabla \mu$.

Normally the gradient in chemical potential refers to a concentration gradient, but in addition to a concentration gradient, an electric field gradient and a solubility gradient are also relevant. It is easy to understand the application of the concentration gradient in the eutectic system using the example of Ge precipitating out of the Ag-Ge liquid. As solid Ge precipitates out of the Ag-Ge liquid, the concentration of Ge decreases in Ag-Ge liquid near the interface causing diffusion of Ge in the Ag rich liquid. The electric field gradient is relevant because silver diffuses as a charged specie Ag$^+$; however, it is considered a small effect and will be ignored. The gradient in solubility as a function of position will have a large impact on the driving force for diffusion and is described in the next section.

Solubility is the tendency of a solute to dissolve in a solvent, in a homogenous manner. Solubility relates to the chemical potential in the following way. Suppose that $G(\mu_{Ag})|_{T, P})$ describes the free energy of a solid silver particle at constant temperature and pressure. The matrix is amorphous SiO$_2$. The amount of energy required to move an Ag atom from the vacuum to the matrix (Figure 3-5(a)) is different from the energy necessary to move the Ag atom from the vacuum to the particle (Figure 3-5(b)).
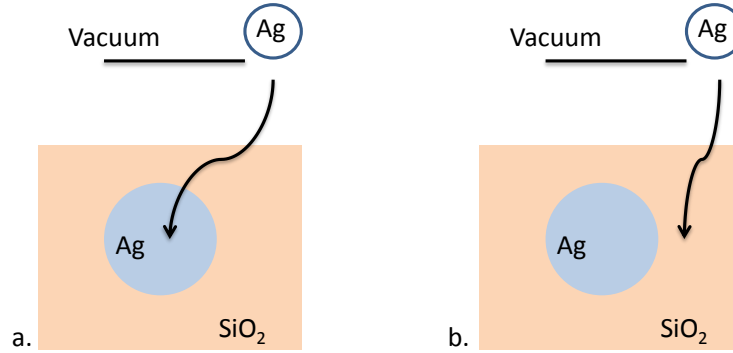
Figure 3-5. Enthalpy for an Ag atom (a) in the SiO$_2$ solid matrix; (b) in the Ag particle. This schematic is not intended to show an energy scale.

Placing the atom in the particle involves the heat of sublimation as shown by Equation 3.7; it is the opposite of the heat of sublimation, which is why there is a negative sign.

$$G_{particle} = -H_{Ag\ sublimation} - T\ S_{Ag\ in\ Ag\ solid} \qquad 3.7$$

Placing the atom in the matrix involves the enthalpy of mixing an interstitial Ag in SiO$_2$. The enthalpy of mixing will be negative for atoms that easily form solid solutions and positive for atoms that segregate at low temperatures.

$$G_{matrix} = H_{Ag\ mixing\ in\ SiO2} - T\ S_{Ag\ in\ SiO2} \qquad 3.8$$

Consequently, the chemical potential in the particle, $\mu_{Ag(particle)}$, is different from the chemical potential in the matrix, $\mu_{Ag(matrix)}$. This difference in chemical potential provides a driving force for diffusion. It is very possible that the mixing enthalpy in the matrix will be so great (low solubility of Ag in SiO$_2$) that the chemical potential for the Ag atom in the Ag particle will be lower than in the matrix. Diffusion will therefore proceed from the SiO$_2$ matrix to the particle, against the concentration gradient of Ag, which does in fact occur when a supersaturation causes precipitation.

The solubility can be affected by three factors: temperature, radius of curvature of the particle, and whether the particle is in a solid or liquid state. In the example above, as the temperature increases, the entropy term becomes more dominant. Solubility increases and the chemical potential decreases.

The solubility of a solute in a solvent is affected by the curvature of a particle because of the Gibbs-Thomson relation. The interface surrounding a particle of Ag, for example, exerts an extra pressure on the atoms in the particle given by

$$\Delta P = \frac{2\,\gamma}{r} \qquad\qquad 3.9$$

where γ is the interface energy between the Ag phase and the matrix, and r is the radius of curvature of the particle. When r is small, for the case of particles 1-100 nm in diameter, ΔP can be significant. The free energy of the particle increases causing a gradient in the chemical potential between an atom in the particle and an atom in the matrix.

$$\Delta G = \Delta P\, Volume_{particle} = \frac{2\gamma\, Volume_{particle}}{r} \qquad\qquad 3.10$$

The effect is to have the solubility increase just outside the particle. This is called the Gibbs-Thomson effect or capillarity effect, and it provides the driving force for particle coarsening, the larger particles growing at the expense of the smaller ones.

Finally, whether the Ag particle is in a liquid state or solid state also affects the solubility and hence the chemical potential. As shown in Equation 3.7, if the particle is in the liquid state, then the enthalpy of vaporization is used instead of the enthalpy of sublimation for a solid particle. This fact will again change the chemical potential. The enthalpy of vaporization is less than the enthalpy of sublimation, so the chemical potential of an atom in the particle will decrease when the particle transforms from a liquid to a solid. The solubility of the solute in the matrix will decrease when the particle changes from a liquid to a solid state.

3.4.2 Nucleation, growth and coarsening

The formation of precipitates, either in the liquid or solid phase, proceeds via stages of nucleation, growth, and coarsening. While the three stages happen sequentially, in a given sample, all three processes can be occurring at the same time; there are no sharp boundaries in time when one process begins or ends.

Nucleation is the first stage when a new phase first nucleates at a defect site, as in heterogeneous nucleation, or spontaneously in the liquid or solid, as in homogeneous nucleation. When the size of the nucleus has reached a critical radius, the particle will continue to grow. Nucleation sites not reaching the critical nucleus size will dissolve back into the matrix. The growth stage is defined as the stage when particles grow in size due to diffusion of the solutes to the nucleation sites, while the number of particles does not change. The coarsening stage is defined as the growth of larger particles at the expense of the smaller particles; during the coarsening stage, the total number of particles decreases.

Once a supersaturation of Ag and/or Ge exists in the silica matrix, there is a driving force for heterogeneous nucleation. The nucleation rate is dependent on the temperature, the concentration of nucleation sites, and most important, on the energy barrier to nucleation, which is a function of the supersaturation.

Although the substrate is not heated during the RF sputtering process, impingement of energetic species adds thermal energy to the substrate. This heating helps to facilitate clustering in the as-deposited films. Clustering is confirmed with the dark-field electron microscope images shown in Figure 3-6. Figure 3-6(a) shows a SiO_2+Ge film prior to annealing with Ge constituents that cluster in a spider web fashion with sizes of 1-3 nm. Figure 3-6(b) shows non-spherical clusters of Ag ranging in size from 2-15 nm; the germanium shown in this film is assumed to be dispersed throughout the matrix as in Figure 3-6(a).
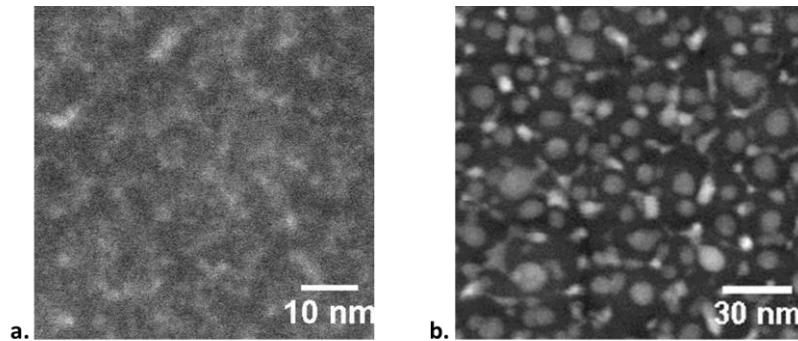
Figure 3-6. As-deposited films with no post-deposition annealing. (a) Ge clusters in SiO_2; (b) Ag islands in SiO_2.

The sample is annealed at temperatures at which the particles are expected to be in a liquid phase. The liquid inclusions nucleate, grow, and coarsen in the same manner as solid inclusions. The difference is that the formation energy, more specifically the enthalpy, will be less for the liquid inclusion than for the solid particle. Consequently the solubility will increase just outside the particle, meaning that the critical radius for continued growth of the particle will be larger for a liquid inclusion than a solid one. A competing effect occurs because of the difference in interface energy between a solid/solid and a liquid/solid structure. Because the liquid/solid interface energy is lower than the solid/solid interface energy, the critical size for a nucleation event to grow is smaller for a liquid particle than for a solid particle.

At the highest temperatures, the importance of entropy becomes even more significant and the liquid inclusions encourage mixing of the Ag and Ge constituents. A one-to-one atomic ratio of Ag and Ge will maximize the entropy which may be important at the highest temperatures. The particle will assume an overall spherical shape to achieve the lowest surface-to-volume ratio. Ultimately, the size of the inclusion will be determined largely by the amount of constituents available, which will be determined primarily by the thickness of the layer containing the Ag and Ge.

51

3.4.3 Solubility in the SiO_2 matrix

Figure 3-7 shows the dependence of the solid solubility on temperature for Ag, Au, and Ge in silicon dioxide. Little data are found in the literature, and values are expected to vary significantly depending on the actual structure and composition of the oxide. Corroboration for the solubility data of Ge in SiO_2 can be found in the reference by von Borany stating that the solubility of Ge in SiO_2 is $< 10^{18}$ cm^{-3}.[92]
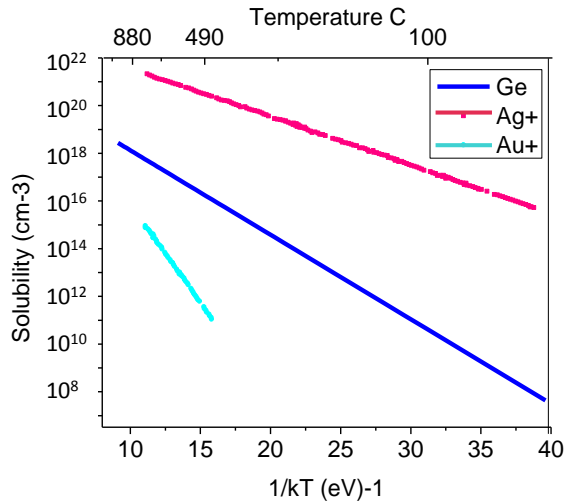
Figure 3-7. Solid solubility in SiO_2. Au$^+$ and Ag$^+$ data is from McBrayer.[95] Ge line is calculated using expression from dissertations of Yuan and Yi.[97, 98]

3.4.4 Formation enthalpy of the oxides

Since Ge will bond to oxygen to form GeO_2, it is necessary to have films that are oxygen deficient in order to prevent GeO_2 formation. The films are deposited after pumping out the chamber for several hours to a base pressure of 1×10^{-6} Torr. Because the chamber is so large (>90 liters) and because it is frequently open to atmosphere, chamber surfaces adsorb water vapor, which provides some oxygen during deposition. However, in general, the deposition is designed to be oxygen deficient, and sputtered oxide films are typically oxygen deficient.[89] It is essential to consider, however, with which atoms the oxygen would most likely bind, if excess oxygen diffuses into the thin film.

The binding energy or bond enthalpy between two atoms is related to the interatomic potential between the two. In general, as the bond energy between the atoms increases, the melting point of the solid increases, and so the melting point can be indicative of the preference for oxygen bonding.[99] Table 3-3 lists the melting points for various oxides. According to the melting points, if extra unbound oxygen is present, it will bind first to Si until all Si bonds are satisfied, then to Ge, and finally to Ag. Although the noble metals are called noble because of their resistance to forming an oxide, Ag_2O will form and is stable up to temperatures of 280°C.[100]

It is worth noting that the tarnishing of utilitarian silver is actually a sulfurization due to sulfur in the atmosphere, not an oxidation. The melting points of Al_2O_3 and SiN are also listed in Table 3-3, as each could be an effective matrix for embedded nanoparticles.

Table 3-3. Melting points of constituents with oxygen. As oxygen becomes available it will preferentially bond with the higher melting point materials. This is an important consideration for choosing the matrix for Ge nanoparticle formation.

Oxide	Melting Point	Crystal structure
SiO_2	1415-1725˚C	Amorphous, tetrahedral short-range order, melting point varies with structure and exact composition
GeO_2	1086˚C	Amorphous, tetrahedral short-range order
Ag_2O	280˚C	
Au_2O_3	160˚C	
Al_2O_3	2045˚C	Trigonal α phase most common
SiN	1900˚C	Trigonal α and β phases most common

The challenge of forming Ag-Si nanoparticles, which would be an interesting complement to this work, is to deposit enough Si in the SiO_2 matrix to precipitate excess silicon as particles. Silicon nanoparticles embedded in SiO_2 have been synthesized using RF sputtering processes.[101] Alternatively, one could deposit Si and either Ag or Au in an Al_2O_3 matrix, which would facilitate Si precipitation. However, the crystalline nature of Al_2O_3 is known to cause faceting in Ge nanoparticles.[102]

3.4.5 Segregation in Ag and Ge – the bulk phase diagram

The bulk phase diagram for the Ag-Ge system is shown in Figure 3-8. The composition of constituents is plotted on the x axis and the temperature is plotted on the y axis. This phase diagram has a classic eutectic shape where the two constituents show a miscibility gap over much of the compositional range. At the lower left-hand corner, one can see that the amount of Ge allowed in Ag at room temperature is roughly 1%, and in the lower right-hand corner, the amount of Ag in Ge at room temperature is significantly less than 1%. Although common eutectic microstructures often involve lamella or other shapes on the micrometer scale, these features will not be present in structures on the nanoscale.
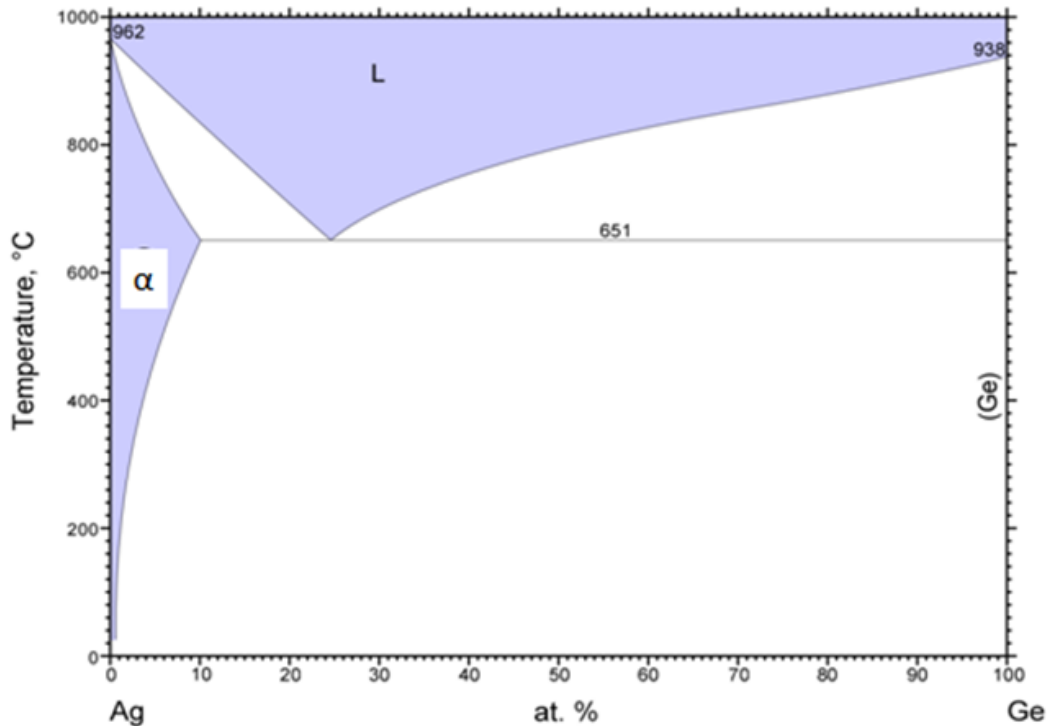
Figure 3-8. Bulk phase diagram of the Ag-Ge eutectic system.[103]

In the Ag-Ge system, the enthalpy of mixing is positive; the atoms segregate from one another forming a miscibility gap. Strongly segregating behavior is predicted for the Ag-Ge system when one considers that silver has twelve nearest neighbors forming metallic bonds and germanium has four nearest neighbors forming covalent bonds. An Ag-Ge bond is not likely. Indeed, the phase diagrams of many of the diamond cubic (dc) semiconductors with face-centered cubic (fcc) metals show a miscibility gap. These binary systems include Au-Ge, Au-Sn, Ag-Si, and Au-Si. In such eutectic phase diagrams, the solidification temperature of the alloy is a function of the composition with a minimum solidification (or melting) temperature being the eutectic temperature. For the Ag-Ge system, this occurs for a composition of roughly 75.5 atomic% Ag and 24.5 atomic% Ge, and at a temperature of 651°C. Because the Ag and Ge atoms in the liquid are not inclined to bond, it makes sense that a liquid state can be sustained for these incompatible atoms at lower temperatures. In fact, the eutectic temperature can be related to the binding energy of the Ag-Ge atoms. A larger incompatibility results in a larger enthalpy of mixing and, consequently, a lower eutectic temperature depression below the melting point of the pure materials.

One must consider whether the bulk phase diagram is representative of particles 10 to 100 nm in diameter. Melting point depression has been observed for Au nanocrystals.[7] Both superheating and supercooling have been observed in Ge nanoparticles averaging 5 nm in diameter embedded in SiO_2.[104] Nanoscale phase diagrams have been calculated recently for the

54

Sn-Ge and Au-Ge binary systems.[90] As distinguished from the situation with the dielectric functions, as reviewed in Chapter 2, where the bulk values appear appropriate for nanoparticles even as small as 5 nm in diameter, it is very likely that the bulk phase diagram is not an accurate phase diagram for these bi-lobed particles. However, it provides a guide to predict the behavior of nanoparticles.

3.4.6 Theory of bi-lobed particle formation

In 2009, Yuan et al. published a model of bi-lobed particle formation for a strongly segregating binary system.[94] This theory established a structure map for bi-lobed particles which has been applied to the Sn-Ge[27] and Au-Ge[28] systems. The model assumes the particles are in equilibrium such that the configuration is determined by the lowest free energy state. It assumes isotropic interface energies and stress-free interfaces. The model predicts that the particle configuration will be determined by the relative values of the interface energies between the metal and glass, semiconductor and glass, and metal and semiconductor, and the volume fraction of either the metal or the semiconductor. For a given volume fraction, for example a 1:1 Ag:Ge, the configuration will be determined by the relative interface energies. The model does not require the metal-semiconductor interface to be flat. In fact, according to the model, for a particle with equal volume fractions of metal and semiconductor, the interface is flat only when the interface energy of the metal-glass is equal to the interface energy of the semiconductor-glass. For most cases, the interface is predicted to have some curvature. Most recently Boswell-Koller elaborated on this model to draw conclusions about the interface energies by measuring a long axis of the particle and an axis perpendicular to the long axis in transmission electron microscope images.[90] The model by Yuan[94] succinctly shows the conditions under which the bi-lobed configuration is energetically more favorable than either core/shell or individual particles.

Chapter 4 includes high-resolution TEM images showing that the interface between the Ag and Ge volume fractions is consistently a plane of the {111} family on the Ag side parallel to a plane of the {111} family on the Ge side. Although silver has a fcc lattice and germanium has a dc lattice, and their lattice constants are very different, matching of the closely packed planes reduces the interface energy compared to interface energies between other planes.[105] This finding is in conflict with one of the assumptions in the Yuan model that the interface energies are isotropic and not a function of the crystallographic plane.

3.4.7 Interface energies

The values of interface energies for most liquids and solids range from 0.2 to 3 J/m^2.[99] The highest values are for the transition metals; metals typically have higher coordination numbers and consequently more bonds are broken to create a surface. For organic or aqueous solutions the values can be as low as 0.1 J/m^2.[99]

Two interfaces are defined as coherent with each other if atomic planes are in complete registry across an interface.[99] This occurs most often for materials with the same crystal structure and similar lattice constants. Often, either or both sides of the interface experience strain in order to accommodate a lattice mismatch. If the strain becomes too great, dislocations often form to alleviate the strain but maintain lattice registry. Nanostructures are able to sustain more strain than bulk material because formation of defects is energetically expensive. Semi-coherent interfaces are those in which there is some lattice registry. An incoherent interface is one in which there is no correspondence of atomic planes on either side of the interface. With an incoherent interface there is no local relaxation resulting in dislocation. Instead, the mismatch is experienced uniformly across the interface. The phases retain their bulk structure up to the interface and then end abruptly. With incoherent interfaces, it is common for the close-packed planes of each crystal to face each other.[99] An upper bound to the interface energy can be estimated from the sum of the two surface energies. Typical interface energies for the three categories of interfaces are provided in Table 3-4.

Table 3-4. Typical values for interface energies for different degrees of interface coherency.[99]

Type of interface	Coherent	Semi-coherent	Incoherent
Typical interface energy	0.005 to 0.2 J/m^2	0.2 to 0.8 J/m^2	0.8 to 2.5 J/m^2

For the Ag-Ge nanoparticles embedded in SiO_2, it is expected that the interface energy of the Ag/SiO_2 and Ge/SiO_2 interfaces will be high because there is disorder in the SiO_2 matrix and a large number of broken bonds. It is possible that the Ag/SiO_2 interface energy is higher than that of the Ge/SiO_2 interface because the Ag does not readily bond with oxygen or silicon. It is possible that the Ge atoms will bond with either the silicon or oxygen, although there will still be disorder.

Based on early studies of metal contacts to Ge, it is known that the {111} planes of Ge and Ag preferentially align and it is expected that this interface energy will be significantly lower than the Ge/SiO_2 and Ag/SiO_2.[106, 107] Table 3-5 shows values for the relevant interface energies from the literature. No values were found for the interface energies of Ag/ SiO_2 or Ag/ Ge.

Table 3-5. Interface energies from the literature.

Interface	Interface energy	Reference
Ge(s)/SiO$_2$	0.82 to 0.99 J/m^2	Boswell-Koller[90]
Ge(s or l)/SiO$_2$	0.7 to 0.9 J/m^2	Xu[104]
Ge/SiO$_2$	1.5 J/m^2	Yuan dissertation[96]
Ge(l)/Ge(s)	0.23 J/m^2	Xu[104]
Ge(s)/SiO$_2$	.91 J/m^2	Shin dissertation[108]
Ge(s)/Sn(s)	0.1 J/m^2	Shin dissertation[108]

3.4.8 Diffusion of constituents

3.4.8.1 Introduction

Diffusion of atoms in either a solid or liquid occurs in response to a gradient of the chemical potential. This gradient can be in the form of a concentration gradient, an electric field gradient (for an atom with a charged oxidation state), or a solubility gradient. In each case, there is a force on the atom, $\nabla\mu$, which motivates it to move with a given velocity. The velocity can be specified by its diffusivity, which generally has an exponential dependence on the temperature as shown in Equation 3.6. The activation energy, E_A, can be either the sum of more than one mechanism of diffusion, the sum of a multiple steps, or it can correspond to a particular dominant mechanism.

A characteristic diffusion length can be defined as

$$x_{diff} \approx \sqrt{D\,t}$$
3.11

This characteristic length, x_{diff}, describes the random walk of a solute atom in a matrix. Although both time and temperature can be used to control a diffusion profile, the temperature has a bigger effect because the diffusivity, D, has an exponential dependence on the temperature.

This section first covers the investigation of the diffusion of Ag and Ge in SiO$_2$. Second, diffusion of Ag and Ge in the solid phases of Ag and Ge, both as self-diffusion and as solutes, will be described. Third, diffusion of Ag and Ge in the liquid phases of Ag and Ge will be reviewed. Finally, an approximation for the diffusivity of Ge in SiO$_2$ at 800˚C from this work will be presented.

3.4.8.2 Ag and Ge in SiO_2 (solid)

Sputtered thin films of silicon dioxide exhibit the amorphous structure of a network solid as shown in Figure 3-9. Each silicon atom is bound to four oxygen atoms, and each oxygen atom is bound to two silicon atoms. Although there is short range order determined by the length and the angles of the covalent bond, sputtered SiO_2 is not crystalline. As deposited, it forms a loose framework which becomes increasingly dense after heating. The density and structure is a strong function of the composition; in general, dopants make the network less dense. Between 500-700°C, SiO_2 goes through a transition allowing it to become more malleable.[90, 91]
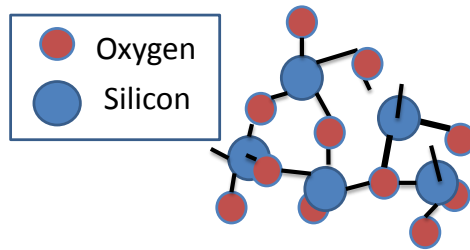
Figure 3-9. Network solid of deposited SiO_2 formed by covalent bonds between silicon and oxygen atoms.

Silver is understood to be ionized in SiO_2 as a singly-charged specie, Ag^+; the free electron from the Ag atom binds to a trap in the glass.[60] Ag^+ is known to be a very fast diffuser in glass; it diffuses as an interstitial, not bonding to either oxygen or silicon.[109] Activation energies for the diffusion have been reported to vary from 1.0 to 2.3 eV, although values on the order of 1 eV are more representative of an interstitial mechanism. Table 3-6 lists data from the literature and the references. Most recently, work has indicated that the activation energy depends on which part of the formation process is occurring – whether the particle is in the growth stage or the coarsening regime.[110]

Table 3-6. Diffusivities of Ag^+ and Ag in SiO_2.

Material	Diffusivity	Reference	Notes
Ag+ in glass	D=2x10^{-13} cm^2/s at 550°C D=4x10^{-14} cm^2/s at 500°C E$_A$ ~ 1 eV	Kreibig[109]	X= 240 nm at 550°C in 1 hr
Ag+ in glass	Frozen at room temperature	Kreibig[109]	
Ag+ in glass	Mobile above 450°C	Kreibig[109]	
Ag+ in thermal SiO_2	D=4.5x10^{-13} at 300°C; E$_A$ = 1.24eV at 275-365°C	McBrayer[95]	
Ag+ in thermal SiO_2	D=1x10^{-15} at 500°C	Nason[111]	
Ag in thermal SiO_2	D$_0$ = 2x10^{-3} at 1100-1350°C E$_A$=1.6eV at 1100-1350°C	Boltaks[112]	For 500°C, D=7.4x10^{-14}; For 840°C D=1.2x10^{-10}; x$_{diff}$ for 1 min = 112 nm at 840°C
Ag in thermal SiO_2	E$_A$=2.3eV 525-590°C	Jimenez[110]	

The diffusion of Ge in SiO_2 is not well understood and systematic studies have not been undertaken, like those for Si diffusion in SiO_2.[113, 114] Ge diffusion in SiO_2 most certainly depends strongly on the structure and composition of the oxide. Values in the literature for the activation energy vary from 0.4 eV to 5.7 eV as shown in Table 3-7. Studies of Si diffusion in SiO_2 have shown that in oxygen-rich SiO_2, diffusion is mediated by Si vacancies, while in silicon-rich SiO_2, diffusion via Si interstitials is favored.[114] Most sputtered SiO_2 films are found to be oxygen deficient.[89] Indeed, this is the condition required for Ge to precipitate out of the matrix; there is no excess oxygen with which to form GeO_2. However, samples of embedded Ag-Ge nanoparticles show Ge remaining in the matrix as small clusters, as shown by the bright contrast from the Ge volume plasmon in Figure 3-10. Even these films, with Ge in the matrix, can still be considered oxygen deficient; it would be unlikely that a large number of Si vacancies exist in these samples. Therefore, it is likely that diffusion of Ge is occurring with an activation energy of 1-3 eV, typical of an interstitial mechanism. A value of E$_A$ ~ 2.5 eV was calculated by Yu, although his calculations were for a substitutional mechanism.[115]

Table 3-7. Diffusivities of Ge in SiO_2.

Material	Diffusivity	Reference	Notes
Ge in glass	$D_0 = 7250$; $E_A = 5.7eV$	Minke[116]	Substitutional diffusion mechanism
Ge in ion-beam damaged thermal SiO_2	$D = 5.5 \times 10^{-5}$ cm^2/s at 800˚C $D_0 = .0042$ cm^2/s; $E_A = 0.4eV$	Sawyer[117]	These values are used in simulations of non-equilibrium processes, largely ion beam processes. The high diffusivity is because the SiO_2 matrix in this work is highly disordered. An interstitial mechanism is assumed for diffusion under these non-equilibrium conditions.
Ge in a-SiO_2	$E_A = 2.5eV$	Yu[115]	Calculated, substitutional diffusion at bond-centered site
Ge in glass fibers	$D_0 = 0.0024$ cm^2/s	Lyytikäinen[118]	Experimental
Ge in glass fibers	$D_0 = 0.0024$ cm^2/s $E_A = 3.2eV$	Yamada[119]	Experimental
Ge in sputtered SiO_2	$D = 3.3 \times 10^{-14}$ cm^2/s at 800˚C	This work	Estimated from experiment described in Section 3.4.8.5. This estimate represents a lower bound.
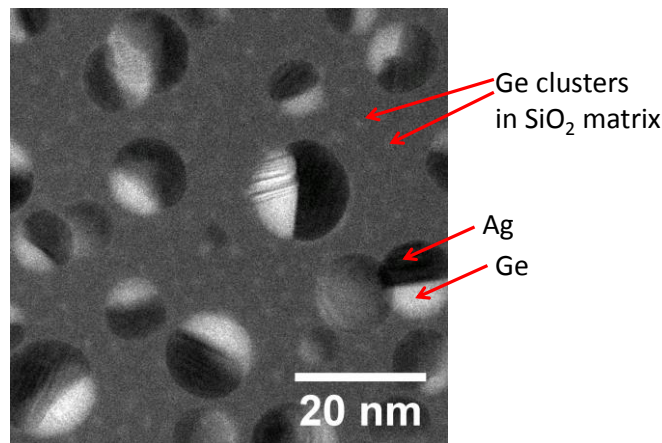
Figure 3-10. Energy-filtered TEM image of Ag-Ge bi-lobed particles. The energy slit width is 1 eV, and is centered at 16 eV, the volume plasmon of Ge. Bright Ge lobes of the particles, as well as small clusters of Ge in the matrix, are evident.

3.4.8.3 Ag and Ge diffusion in Ag and Ge solid

The activation energy for self-diffusion by a vacancy mechanism is the sum of the activation energies for vacancy formation and for vacancy movement. For metals, the activation energy for vacancy formation increases with the melting point of the solid.[120] Because most

metals have diffusivities at their melting points of approximately 1×10^{-8} cm^2/s, the self-diffusion of Ag can be estimated.[120] The activation energy for Ag-self-diffusion is close to 2 eV, as shown in Table 3-8.

Diffusion in Ge, whether self-diffusion or diffusion of dopants, is known to be mediated by vacancies.[121] No evidence for interstitial diffusion in non-irradiated materials has been observed.[121] The vacancies are found to act as acceptors in Ge.[122] In p-type Ge, such as the Ge in this work, the negatively charged vacancies impede the self-diffusion of Ge in Ge.[122] Activation energies for self-diffusion of Ge are close to 3 eV, as shown in Table 3-8.

Table 3-8. Diffusivity for self-diffusion in the solid.

Material	Mechanism	D_0 (cm^2/sec)	E_A	References
Ag in Ag	substitutional	0.40	1.9 eV	Shewmon[120]
Ag in Ag	substitutional	0.724	2.0 eV	Hoffman[123]
Ge in Ge	substitutional	7.8	3.0 eV	Shewmon[120]
Ge in Ge	substitutional	13.6	3.09 eV	Werner[122]
Ge in Ge	substitutional	24.8	3.14 eV	Vogel[124]

As described above for self-diffusion, dopants in Ge diffuse via a substitutional mechanism mediated by vacancies.   The diffusivity of Ag in Ge is calculated by Sharma for the case of substitutional movement as shown in Table 3-9. The diffusion of Ge in solid Ag was measured by Hoffman.[123]

Table 3-9. Diffusivity of Ag in Ge$_{(solid)}$ and Ge in Ag$_{(solid)}$

Material	Mechanism	D_0 (cm^2/sec)	E_A	Reference
Ag in Ge	substitutional	4×10^{-2} at 800-900˚C	2.23 eV	Sharma[125]
Ge in Ag	substitutional	0.084	1.58 eV	Hoffman[123]

3.4.8.4 Ag and Ge in Ag/Ge liquid

A liquid metal is characterized by a decreased number of nearest neighbors as compared with a crystalline solid. For example, in an fcc metal like silver with 12 nearest neighbors, the average number of nearest neighbors decreases to 10-11 near the melting point and decreases further as the temperature is increased above the melting point. There is still some short-range order in a liquid as the atoms have preferences for bonding. It has also been observed that

liquids adjacent to a solid crystalline surface show increased ordering for a few monolayers adjacent to the crystalline template.[99] Generally, diffusion will be faster in the liquid than in the solid because of the liquid's decreased density and increased number of broken bonds.

Table 3-10 lists diffusivities from the literature for Ge in an Au-Ge liquid. Similar data is not available for the Ag-Ge system; however, because Au and Ag share the same crystal structure and a very similar lattice constant (0.409 nm for Ag and 0.408 nm for Au), the behavior is expected to be somewhat similar. Au-Ge has a lower eutectic temperature, indicating that mixing in the liquid has a greater positive enthalpy. It is clear from the high diffusion coefficients, that diffusion in the liquid is very fast; phase transformation in the liquid state is not diffusion-limited during the furnace or rapid thermal annealing.

Table 3-10. Diffusivity of Ge and Ag in metal-semiconductor alloys (liquid).

Material	Temperature	D_0	E_A	Diffusivity	Reference
Ge in Au-Ge liquid	529°C			5.1×10^5 cm^2/s	Wernick[126]
Ge in Au-Ge liquid	563°C			7.8×10^5 cm^2/s	Wernick[126]
Ge in Au-Ge liquid		1.76 cm^2/s	0.72 eV		Chrzan[127]

3.4.8.5 Estimate of Ge diffusivity in sputtered SiO$_2$

Of the different diffusivities described above, it is expected that the diffusion of Ge in SiO$_2$ would be one of the most critical in determining the particle composition. By examining the TEM images of Ge nanoparticles after rapid thermal annealing, an estimate can be made of the diffusivity. A thin film of SiO$_2$ containing 4.5% Ge was co-sputtered with a target containing Ge pieces adhered to a SiO$_2$ target. The layer thickness was approximately 60 nm. Rapid thermal annealing for 10 seconds at 800°C resulted in Ge nanoparticles with well-defined facets as shown in Figure 3-11. The particles are not spherical, most likely, because the temperature did not reach the melting temperature of the Ge. Using ImageJ[128] to measure the average area of the particles, one can calculate an average diameter of 10 nm, assuming a spherical particle. This gross estimate assumes the particles are spheres, which they clearly are not, but it is nonetheless useful as an estimate. The 10 nm particles in the 60 nm thick film will presumably be distributed through the thickness of the film.

The projections of the inter-particle distance can be measured from the TEM image. Many of the distances will actually be longer than those measured because the lines are projections. Lines are drawn between particles as shown in Figure 3-11(b), and the average inter-particle separation is calculated to be 11.5 nm. Again, this distance is a lower bound; the actual distance will be longer when the particles first begin to grow. Dividing 11.5/2 gives an

estimated diffusion length, x_{diff}, of 5.75 nm in 10 seconds at 800˚C. This estimate of a lower bound assumes that the particles are still in the growth stage and have not yet begun to coarsen. Using Equation 3.11, the diffusivity for Ge in SiO_2 at 800˚C is calculated to be $3.3x10^{-14}$ cm^2/s. This is a reasonable value assuming that Ge diffuses via an interstitial mechanism with activation energy of 2-3 eV.
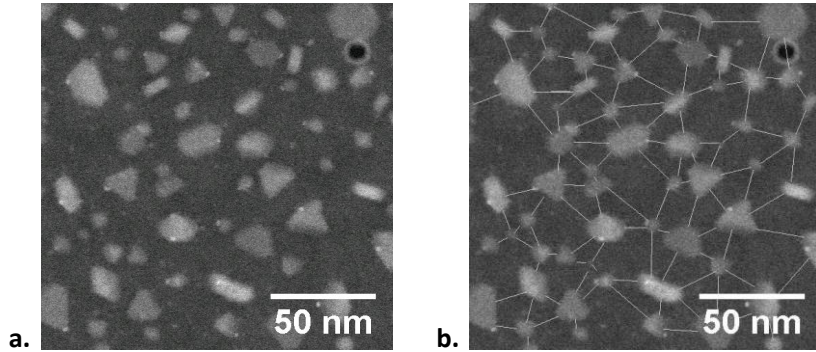
Figure 3-11. HAADF-STEM images of Ge nanoparticles in SiO_2 after rapid thermal annealing for 10s at 800˚C. (a) Particles; (b) Lines drawn as an estimate of the diffusion length of a Ge atom in the SiO_2.

Figure 3-12(a) shows the dependence of diffusivity on activation energy, showing clearly that the value of the activation energy, which is derived from the mechanisms for diffusion, has an exponential effect on diffusion of the atom. In this graph, the value for D_0 was taken to be 1; values for this number typically range from $1x10^3$ to $1x10^{-3}$, and although it is the combination of D_0 and E_A that determine the diffusivity, D_0 affects the diffusivity in only a linear manner. Figure 3-12(b) shows diffusion lengths, x_{diff}, for different diffusivities after annealing at 840˚C for 1hr. In other words, for a particle to travel 20 nm at 840˚C in 1 hr, the diffusivity must be at least $4x10^{-15}$ cm^2/s. If $D_0 \sim 1x10^{-3}$, this could be achieved with $E_A = 4$ eV, but most likely with $E_A < 4$ eV. The pink regions in Figure 3-12 represent reasonable values for the diffusivity.
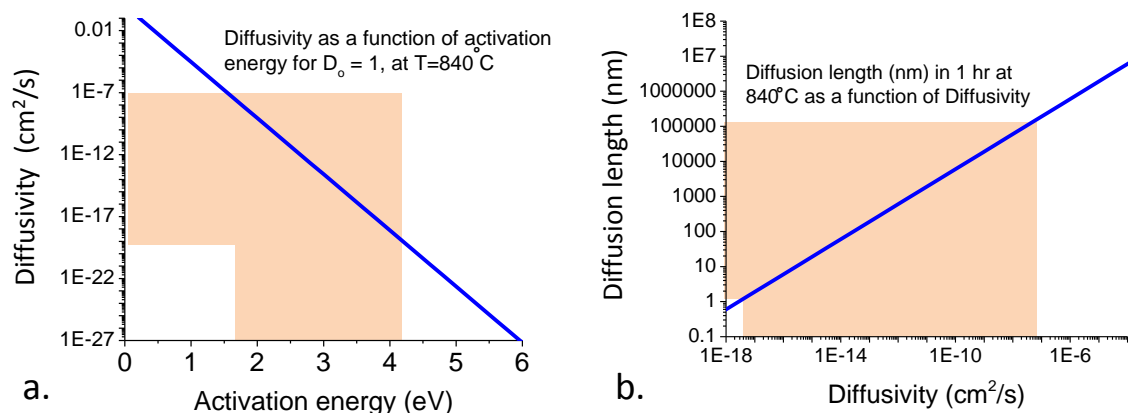
Figure 3-12. Diffusivity and diffusion lengths. (a) Diffusivity as a function of E_A assuming $D_0=1$, at 840˚C; (b) Diffusion lengths as a function of diffusivity at 840˚C after 1hr.

3.5 History of an Ag-Ge particle

This section contains a review of the formation of Ag-Ge bi-lobed nanoparticles during thermal annealing. Figure 3-13 shows the final particle configuration after annealing for three different compositions of particle. The atomic percent of each constituent is read on the bottom x-axis and the volume fraction, observed in the transmission electron microscope images, is read from the top x-axis. The particles in this series of schematics are depicted "edge-on," drawn with a flat interface and with the interface perpendicular to the plane of the paper. This flat interface is apparent in many of the TEM images, but is not assumed a priori, nor is it apparent in all particles. As is evident from microscope images, most of the particles appear to exhibit close to a 50:50 volumetric ratio, and, consequently, the particles described as 25% and 84% volume fraction Ge are at the extremes of the distribution. Each sample with a given overall composition will have a distribution of particles with individual compositions determined by the local environment. In the discussion that follows, percentages are given in atomic percent.

64
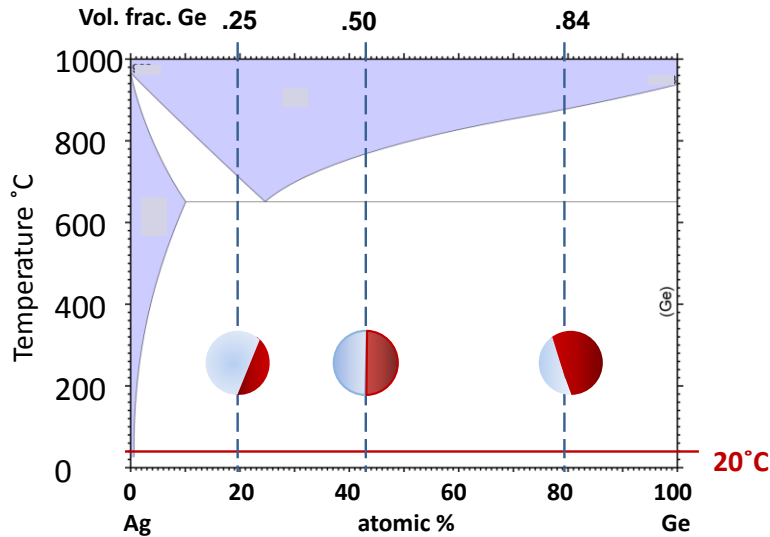
Figure 3-13. Post-annealing bi-lobed particle configurations for three different compositions of particle superimposed on the bulk phase diagram for the Ag-Ge system.

The sample begins as a co-sputtered SiO_2 film with a supersaturation of Ag and Ge. Because of the low solubility in SiO_2, some of the Ag and Ge has clustered in approximately 1 to 10 nm clusters in the as-deposited film. As the temperature is increased, there is random diffusion, and Ag and Ge clusters continue to form. Once the temperature approaches 500-700°C, the silicon dioxide becomes more malleable allowing particles to become spherical.

The sample anneals at 840°C for 1 hr. At this temperature, according to the bulk phase diagram, the Ag and Ge will be liquid for compositions of 10-64% Ge. In fact, based on the likelihood of melting point depression due to nanoscale dimensions, and the fact that spherical particles are observed, it is probable that at 840°C, the inclusions are liquid across all compositions. Because of the increased entropy created in the liquid by mixing, Ag and Ge do not form separate liquid inclusions. In fact, the tendency of entropy to maximize randomization will favor a mixture of 50:50 Ag:Ge atoms, corresponding to a volume fraction of ~42:58. The composition in each inclusion will be different although centered about a mean that is a function of the overall film composition. The composition will also vary, depending on the temperature, as the solubility for Ag and Ge will have different dependence on temperature. It is also probable that the composition will vary as a function of size, if one includes the Gibbs-Thomson effect.

The possibility that at 840°C some of the particle compositions could be below the liquidus line must be examined. For example, the right-hand phase diagram in Figure 3-14 shows a particle with a composition of 80% Ge. The phase diagram indicates that Ge begins to precipitate from the liquid onto the solid wall of the matrix. For this composition, the Ge will

65

precipitate out as pure Ge because of the limited solubility of Ag in solid Ge at the right-hand boundary of the phase diagram. The remaining liquid composition will be given by the intersection of the 840°C line with the liquidus line, shown as ~63%. As the inclusion with this composition cools, more Ge precipitates out and the liquid composition becomes more Ag-rich.

.

Figure 3-14. Bi-lobed particle formation at 840°C for three different particle compositions superimposed on the bulk phase diagram for the Ag-Ge system.

Figure 3-15 shows the configuration of the three inclusions at 675°C, just above the eutectic temperature of 651°C. The inclusion with an overall composition of 80% Ag and 20% Ge has begun to precipitate out Ag. The solid Ag will contain approximately 9% Ge according to the dotted line on the far left, at the intersection of the 675°C temperature line and the solidus line. There will still be liquid remaining that has a composition given by the right-hand dotted line of ~24% Ge.

Figure 3-15. Bi-lobed particle formation at 675°C for three different particle compositions superimposed on the bulk phase diagram for the Ag-Ge system.

Once the temperature reaches the eutectic temperature, the remaining liquid solidifies and the particle exists as a pure Ge fraction and a 91:9 Ag:Ge solid fraction. In many bulk systems, significant undercooling is necessary to solidify the remaining liquid. A decrease in the crystallization temperature below the eutectic temperature has been found when metals are in contact with both silicon and germanium,[129] so it is reasonable to assume that the solidifying

temperature is even lower than 651°C. Figure 3-16 shows the particles after solidification, although the silver fraction contains a significant amount of Ge as solutes in the fcc Ag crystal.

As the particles at all compositions are cooled to room temperature, Ge solutes in the Ag lattice diffuse in the solid to the Ag-Ge interface and find a site on the Ge lattice, growing the Ge crystal further. At room temperature, according to the phase diagram, there could be as much as 1% Ge remaining in the Ag lattice. Actually, that amount could be higher because the decrease in diffusivity as the temperature is lowered would limit the amount of solid state diffusion allowed. However, Ag-Ge interface studies performed to examine the electronic barrier formed when making metal contacts to Ge indicate that, although the interface may have some Ag-Ge intermixing, after about 2-3 monolayers,[130] an almost pure Ag crystal is formed.
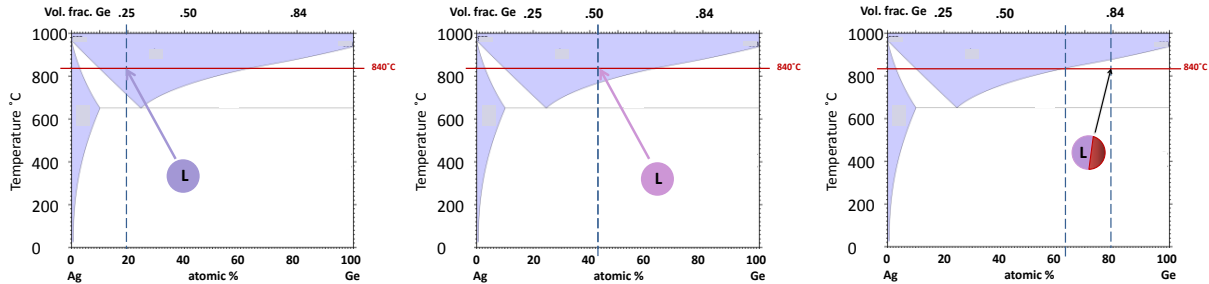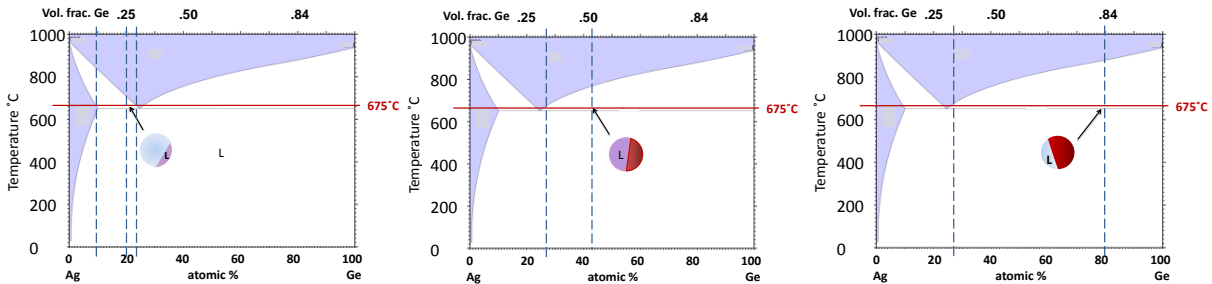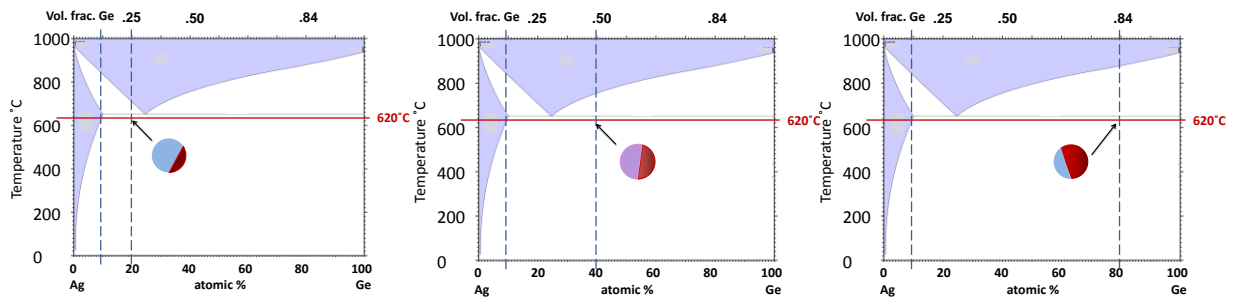

Figure 3-16. Bi-lobed particle formation at 620°C for three different particle compositions superimposed on the bulk phase diagram for the Ag-Ge system.

3.6 Synthesis pathways for alternative particle configurations

3.6.1 Sputtering with layers

Deposition of particles in layers has been demonstrated as shown in in the cross-sectional HAADF-STEM images of Figure 3-17. These samples were prepared, as described in Chapter 4, by mechanical grinding and ion milling so that the deposition layers are visible. One sees three shades of grey defined by the layers. The darkest grey is the hole in the sample. The two SiO_2 layers that contain little or no Ge have an average Z of 10 and consequently have the second darkest grey. These are the two "capping" and "buffer" layers described in Section 3.2.4. The SiO_2 layer that contains the bi-lobed nanoparticles also contains extra Ge atoms that have not precipitated out of the SiO_2 matrix. Consequently the average value of Z is increased, and the dark-field image produces a brighter grey. As an example, the average Z for 7 atomic% Ge remaining in the matrix is 11.2.

The five-layered deposition shown in Figure 3-17(b) consisted of layers of SiO_2 and SiO_2 containing Ag and Ge according to the schematic shown in Figure 3-18. The table in Figure 3-18(b) shows the effect of different layer thicknesses on the particle size; the layer that is 260

nm thick resulted in an average particle diameter of 69 nm, and the layer that is 43 nm thick resulted in an average particle diameter of 16 nm.
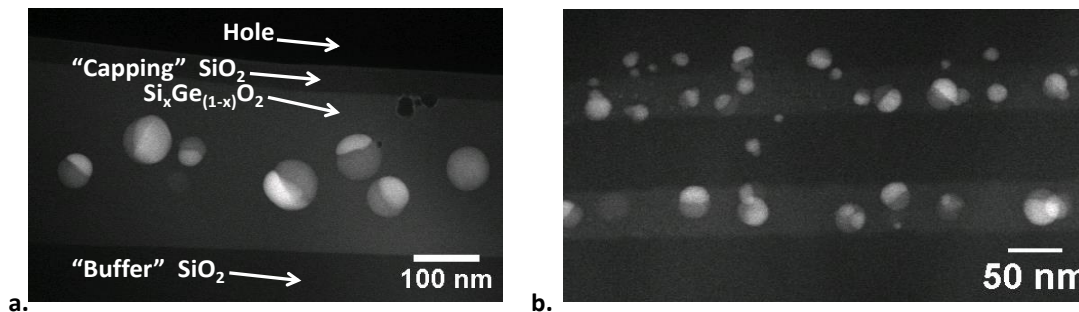
Figure 3-17. Cross-sectional HAADF-STEM images of layers of Ag-Ge nanoparticles. (a) Sample #29, average particle diameter is 69 nm in 260 nm layer; (b) Sample #25, average particle diameter is 16 nm in a 43 nm layer.

TEM Sample	Thickness of particle layer	Average particle diameter
#29 cross-section	260 nm	69 nm
#25 cross-section	43 nm	16 nm
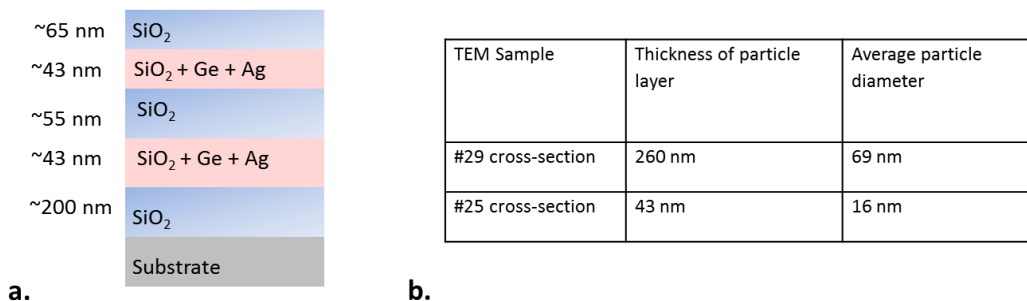
Figure 3-18. Deposition of layers to control particle size. (a) Schematic of 5-layered sample; (b) Particle size as a function of layer thickness.

Similar trends for samples prepared on the nitride membranes are shown in Table 3-11. In this case, the film thickness measured using EELS is the total of all three layers: the buffer layer, the layer with the particles and the capping layer. These samples were annealed using RTA at 800°C for 30 seconds.

Table 3-11. Particle diameter as a function of total layer thickness for RTA treatments.

Sample #	EELS thickness	Average diameter
73	180 nm	26.5 nm
81	66 nm	13.8 nm

3.6.2 Ag nanoparticles in silica

In order to compare the optical properties of the bi-lobed configurations with particles not sharing the Ag-Ge interface, it was necessary to fabricate large particles of both Ag and Ge. Large Ag nanoparticles in SiO_2 were fabricated using the same target used to prepare the Ag-Ge samples. The sample was annealed in an open rather than a sealed ampoule, allowing for oxygen diffusion during the high temperature treatment. In this synthesis method, it is presumed the germanium remains bound to oxygen in the matrix. Ag nanoparticles with an average size of 30 nm in a SiO_2 matrix are shown in Figure 3-19. As detailed in the previous section, nanoparticles of different sizes can be fabricated by adjusting the thickness of the deposited film. Figure 3-19(b) is an energy filtered TEM image using a 1 eV slit centered at 16 eV. The bright contrast comes from the Ge that remains in the matrix.
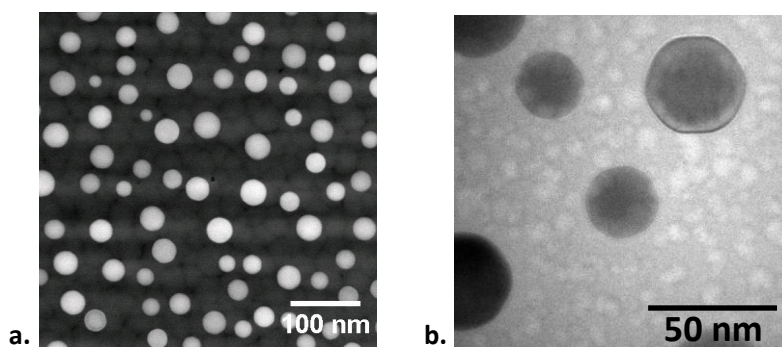
Figure 3-19. Large (average 30 nm in diameter) Ag nanoparticles in $Si_xGe_{(1-x)}O_2$ matrix. (a) HAADF-STEM; (b) EFTEM with 1eV slit at 16 eV, brightest contrast is from Ge clustering in the SiO_2 matrix.

3.6.3 Large Ge nanoparticles in silica

Synthesizing large (>20 nm) Ge particles was not possible using pieces of Ge attached to a SiO_2 target followed by annealing in the furnace. Presumably, the out-diffusion of Ge during the one-hour annealing competed with particle coarsening. Instead, large Ge nanoparticles were synthesized by depositing layers of solid Ge as shown in the schematic of Figure 3-20(a), followed by furnace annealing at 900˚C for 1 hour. The largest nanoparticles in this sample have well-defined facets indicating a preferred growth direction as shown in Figure 3-20(b). An average size was calculated by measuring the area using ImageJ, and then calculating a diameter, assuming a spherical particle. This calculated diameter of 56 nm represents an upper bound on the average particle size. The smaller particles, 20-40 nm in diameter, are more spherical and were used for the single particle optical measurements in Chapter 5.
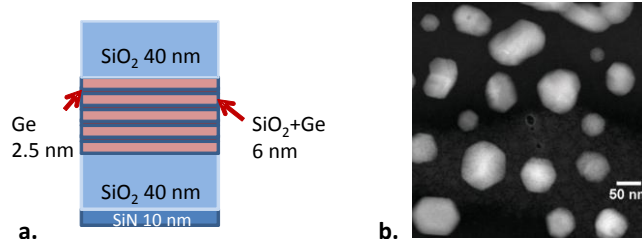
Figure 3-20. Large Ge nanoparticles in SiO_2. (a) Schematic showing deposition of layers; (b) HAADF-STEM image of Ge nanoparticles.

Alternatively, highly faceted Ge nanoparticles were grown in thin SiO_2 layers after rapid thermal annealing at 800˚C for 300 seconds as shown in Figure 3-21(b). The target used has 53 pieces arranged as shown in Figure 3-21(a). The thickness of the layer is ~60 nm.
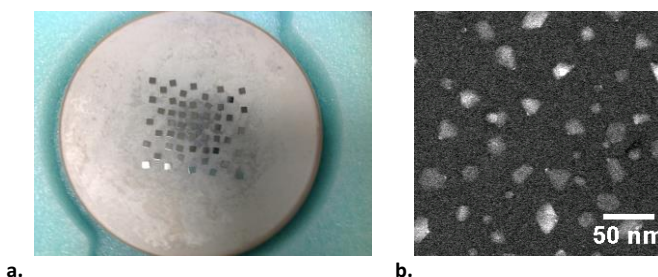
Figure 3-21. Faceted Ge nanoparticles after rapid thermal annealing. (a) SiO_2 sputtering target with Ge pieces used to deposit the sample; (b) HAADF-STEM image of faceted Ge nanoparticles after RTA at 800˚C for 300 s.

3.6.4 Large Ge particles with Ag surface structures

In two instances very large Ge nanoparticles with small Ag structures were grown during furnace annealing. It is possible that the decrease in Ag content or the increase in Ge content facilitated these interesting structures shown in Figure 3-22. They exhibit a strong localized surface plasmon resonance at 1.9 eV, which will be described in Chapter 4.

a.   **b.**
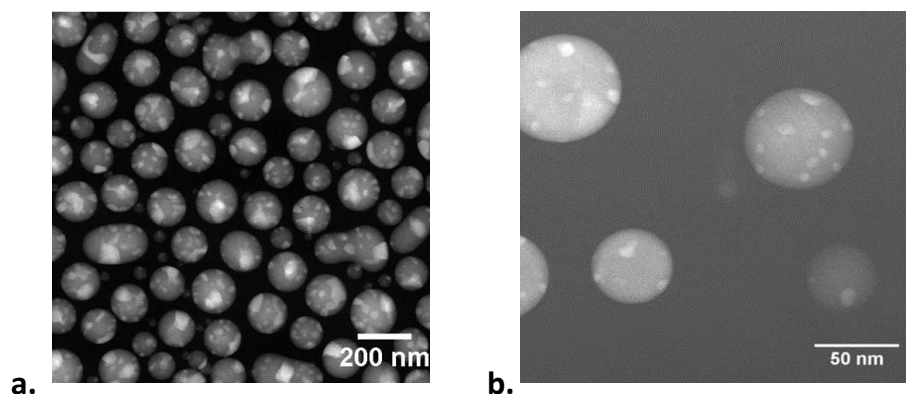
Figure 3-22. HAADF-STEM images of large Ge nanoparticles with surface structures of Ag (a) after annealing at 840˚C for 1hr; (b) after annealing at 900˚C for 1 hr.

3.6.5 Au-Ge nanoparticles in silica

Finally, large Au-Ge bi-lobed nanoparticles were fabricated to measure the localized surface plasmon response of these structures. Guzman successfully fabricated bi-lobed particles averaging 5nm in diameter with a volume fraction ratio of approximately 4:1 Ge:Au.[28] The larger (50nm) particles in this work show a preference for a volumetric ratio closer to 1:1, as shown in Figure 3-23(a). As the particles become larger than 70 nm, surface spots of Au begin to appear Figure 3-23(c). This was also observed by Guzman after the PLM.[28]

The synthesis of large Au-Ge nanoparticles required depositing Au and Ge as pure layers, shown by the deposition parameters and film schematic in Figure 3-24(a) and (b). Island growth of the Ge and Au on the SiO_2 barrier layer, and before any annealing, is shown in Figure 3-24Figure 3-24(c). The nanoparticles shown in Figure 3-23 were formed during furnace annealing for 1 minute at 900˚C in an argon gas environment. The sample was exposed to elevated temperatures during the ramp up to 900˚C and during the cool down to room temperature.

a.   **b.**   **c.**
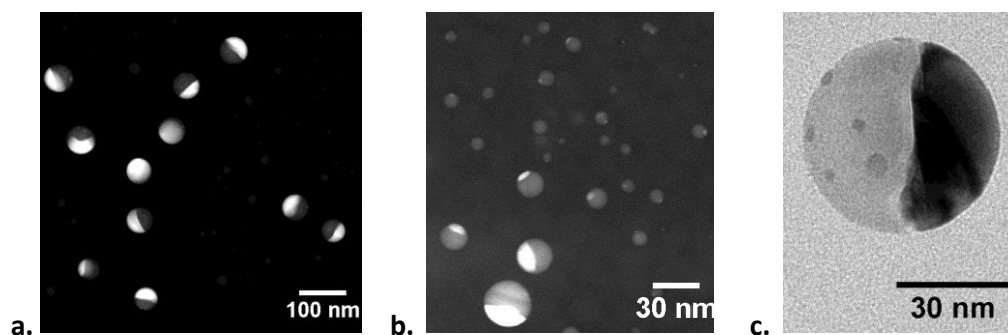
Figure 3-23. Au-Ge bi-lobed nanoparticles embedded in SiO_2: (a) and (b) HAADF-STEM images of Au-Ge nanoparticles; bright region is Au; (c) CTEM dark region is Au.

71

SiO$_2$: 10 min, 20 mT, 200 W
Ge: 25 sec, 10 mT, 100 W
Au: 12 sec, 10 mT, 100 W
SiO$_2$:   7 min, 20 mT, 200 W

24nm SiO$_2$
5nm Au
5nm Ge
34nm SiO$_2$

1000 nm

a.   **b.**   **c.**
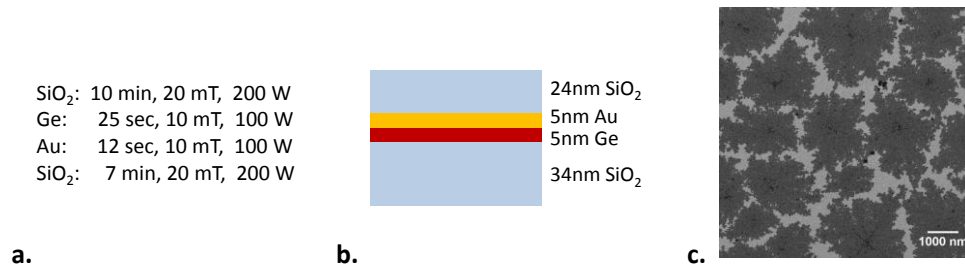
Figure 3-24. Formation of Au-Ge particles. (a) Deposition steps; (b) Layers; (c) HAADF-STEM image showing Ge and Au island growth in SiO$_2$ film.

Chapter 4 Structural and Compositional Characterization

4.1 Introduction

This chapter contains a description of the results of structural and compositional characterization of the Ag-Ge bi-lobed nanoparticles. With the exception of the work described in the last section, all characterization was performed using the transmission electron microscope. All microscopy presented in this dissertation was executed using the FEI Tecnai-20 Ultra-Twin microscope at 200 keV. A schematic of the microscope is shown in Figure 4-1. The Tecnai microscope has a field emission gun as its electron source, resulting in high brightness and small energy spread. The microscope has four different electron detectors: a phosphor screen for viewing during a session, a charge-coupled device (CCD) for capturing digital images and for collecting energy-loss spectra, and two annular detectors for collecting incoherent, elastically-scattered electrons. The phosphor screen must be removed to access the CCD image sensor and annular dark-field detector (ADF). A magnetic prism can be actuated to disperse the electrons exiting from the sample, and the CCD can then either detect an energy-loss spectrum, or a slit can be placed at the entrance to the CCD to form an image from a desired energy band of electrons. An in-line monochromator, with a specified energy resolution of 0.15 eV, can be actuated for spectroscopy requiring high-energy resolution.

FEG

Monochromator

200 keV
electron
beam

Condenser
lenses

Sample between pole
pieces of objective lens

HAADF detector

Phosphor screen

ADF detector

CCD

Magnetic
prism

Slit to select
energy range for
filtered imaging
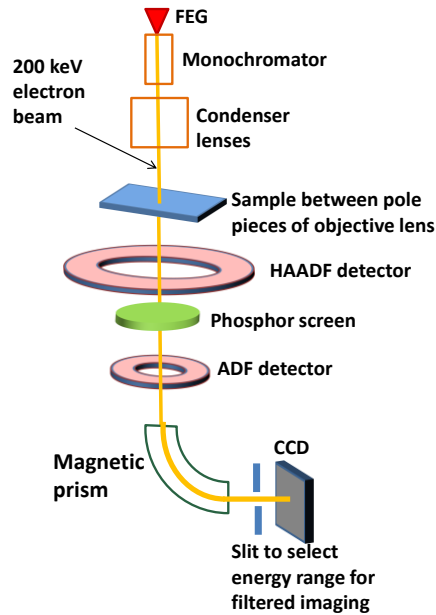
Figure 4-1. Schematic of the FEI Tecnai-20 UT microscope showing the four different detectors: phosphor screen, HAADF, ADF, and CCD. The phosphor screen must be lifted to access the ADF or the CCD.

In this work, the microscope was operated in both conventional TEM mode (CTEM) and scanning transmission mode (STEM). Z-contrast microscopy using HAADF-STEM was used to image dark and light regions of the Ag-Ge bi-lobed nanoparticles. High-resolution phase-contrast microscopy (CTEM) was used to image lattice fringes to evaluate interface orientation and wedge-shaped structures. Nano-diffraction of a single particle was made possible by converging the beam in CTEM mode and capturing the diffraction pattern with the CCD. Core-loss EELS (STEM) was used to confirm the identity of the Ag and Ge components. The characterization results and the respective electron microscopy techniques will be described in this chapter. In Chapter 5, the techniques used to form energy-filtered images and to collect low-loss EELS will be described. Prior to a presentation of the microscopy results, TEM sample preparation and electron beam damage will be discussed. At the end of this chapter, characterization using the atomic force microscope and scanning electron microscope, after particles have been released from the matrix, will be described.

4.2 Sample preparation for transmission electron microscopy

4.2.1 Criteria: thickness, size, robustness, contamination

Integrity of the TEM sample is the most critical factor in obtaining meaningful images and information-rich spectroscopy with the microscope. While valuable information can be collected from a carefully prepared sample in a modest microscope, even the world's best

microscope cannot make sense of a compromised sample. Indeed, the secret to microscopy is to spend the time and effort to prepare a sample carefully, optimized for the material, microscopy technique, and information desired.

A TEM sample must be at least thin enough to be electron transparent. For most techniques, it is desirable that the electrons passing through the sample engage in, at most, one scattering event; in fact, the large majority of electrons are transmitted without interacting at all with the sample. For most electron microscopy techniques, multiple scattering must be avoided.

For incoherent electron waves, when phase information of the scattered waves is lost, the sample thickness should be less than the mean free path of the electron in order to avoid multiple scattering. The electron mean free path is different for different materials. It depends on the energy of the electron and is slightly more for elastic than inelastic collisions. Table 4-1 lists inelastic mean free paths for the materials of interest at 200 keV; in general, the inelastic mean free path is about 100 nm at 200 keV. The mean free path decreases when lowering the energy of the electron beam; for an electron beam of 100 keV, the mean free path is about 1.45 less than at 200 keV.

Table 4-1. Inelastic mean free path of electron at 200 keV. For incoherent detection, TEM samples should be thinner than the mean free path, so that one can assume the electron scatters, at most, one time as it goes through the sample.

Material	Ag	Ge	Si	SiO$_2$	Au
Inelastic mean free path at 200 keV	100 nm	120 nm	145 nm	155 nm	84 nm

For coherent electron waves, those that form phase contrast or diffraction patterns, the "extinction distance" is the distance below which electrons are assumed to scatter only once. The extinction distance is a strong function of the Bragg plane used for scattering, the atomic weight, and the electron beam energy. Table 4-2 lists extinction distances for several Bragg planes, for light, medium, and heavy elements at 100 keV. The extinction distance is directly proportional to the energy of incident electrons; it will increase at higher incident beam energy.

Table 4-2. Extinction distance for 100 keV electrons for light, medium, and heavy elements.[131]

Scattering plane	Light (Aluminum)	Medium (Copper)	Heavy (Gold)
111	57.3 nm	30.2 nm	18.3 nm
200	68.3 nm	33.6 nm	20.1 nm
220	107 nm	45.1 nm	26.5 nm

For HAADF-STEM, the thickness requirement is somewhat more forgiving, and samples approaching 1.5 times the mean free path can yield reasonable contrast, although spatial resolution will be compromised. Thickness of samples prepared for EELS, requiring reasonable spatial resolution, should be 0.4 to 0.6 times the mean free path. For high-resolution phase-contrast images or for atomic-resolution STEM images, thicknesses on the order of 10 to 20 nm are ideal.

The specific characteristics of the TEM holder determine the macroscopic size and shape of the sample. The holder used in this work accepts 3 mm disks with rim thicknesses of 50 to 200 μm. A number of different sample preparation techniques are available for this type of holder. Disks can be cut out of the starting material and subsequently thinned. TEM grids made of C, Mo, Cu, Ta, and W with varying grid sizes can be purchased for drop-casting or atomizing suspensions of solid sample in a liquid. Small wedge-shaped samples can be adhered with epoxy to solid 3 mm TEM grids with an open slot. Finally, thin membranes of SiN, Si, and SiO_2, supported by silicon frames, can serve as substrates for depositing a sample film, or drop-casting or atomizing a sample suspension.

The sample must be robust enough to withstand repeated handling with tweezers, clipping in the sample holder, beam irradiation, and exposure to liquid during sample preparation. While a larger thin area provides a larger region of interest in the microscope, many materials cannot support an extended area only 20 to 100 nm thick. In this work, the most robust samples were fastened to a 50 μm Mo solid grid with an oval slot using M-bond epoxy, G-bond epoxy, or Ag paste. The solid grid provided a less fragile rim for handling the sample.

Contamination during the preparation process is a great concern. Meticulous cleaning of the sample surface with acetone followed by methanol is required at each step. In many cases it is important to clean the sample under the stereomicroscope with a solvent-dampened tissue attached to a toothpick. During the ion milling process, care must be taken to avoid re-deposition of the sample material or grid onto the region of interest. A common contaminant is carbon, which shows up as a bright region during CTEM, the amount growing with time. Carbon can be removed prior to microscopy by cleaning in an oxygen plasma.

4.2.2 Mechanical methods with semiconductors

The approach to preparing an electron transparent sample mechanically is to create a sample gradually thinned until a hole is made. The sample can be configured as a disk or rectangle with a hole in the middle or as a single wedge. The region next to the hole or at the edge of the wedge will be the thinnest and is the region examined in the microscope.

Samples based on silicon substrates are ideally suited for mechanical grinding and polishing. Silicon is soft enough that abrasives such as diamond grit and alumina will abrade the material. It is fairly tough, although it will fracture along crystallographic planes. It becomes transparent to light as the thickness approaches 8 µm, and the changes in color when viewed in the optical microscope can be used to accurately remove the last few microns of material.[132]

It is important to stress that, although not stated explicitly in the methodology below, visually inspecting the sample at each step with both a stereoscope and a high-magnification microscope is essential to repeatable sample preparation. The stereoscope allows one to effectively view scratches and provides a large working distance for cleaning the sample under the microscope. The high-magnification microscope allows one to measure thickness by focusing at different heights. It also allows one to view the sample using bottom illumination and gauge the thickness of the silicon substrate from the color.
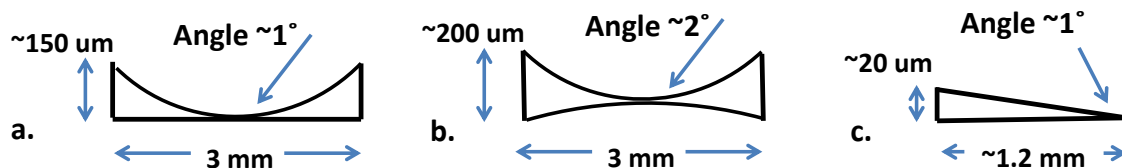
Figure 4-2. Mechanical thinning of the sample requires making a thin wedge either at the edge of a hole as shown in (a) and (b), or as a thin wedge in (c).

4.2.3 Plan-view

A plan-view sample is designed to examine the surface of a substrate. The dimple grinder thins the flat disk in the center by rotating a 15 mm diameter wheel in the center of the disk, forming a dimple. It grinds and polishes the sample on only one side, as shown in Figure 4-2(a) and Figure 4-5(a) and (c). Because there is no specific area of interest, such as an interface, this sample preparation requires less alignment and many fewer steps than a cross-sectional sample. A plan-view design was not used successfully in this work for two reasons. First, because of the capping layer, the particles are covered by a thin film of oxide that adds to diffuse scattering of incident electrons. If the capping layer is only 10-20 nm thick, it does not have a big impact, but if it is more than 50 nm thick, it severely compromises focus and contrast. This problem could be overcome by etching with hydrofluoric acid to remove the capping layer,

either before or after the TEM sample is thinned. Second, when the silicon substrate is removed, leaving a large area that is supported by silicon dioxide only, the silicon dioxide easily fractures or curls at the edges as shown in Figure 4-3(b). This failure mode is seen repeatedly when plan-view samples are made with Al_2O_3.[133] This problem could be solved by making a steeper wedge to allow for more support, although using a steeper wedge reduces the size of the thin region of interest.

a.   **b.**
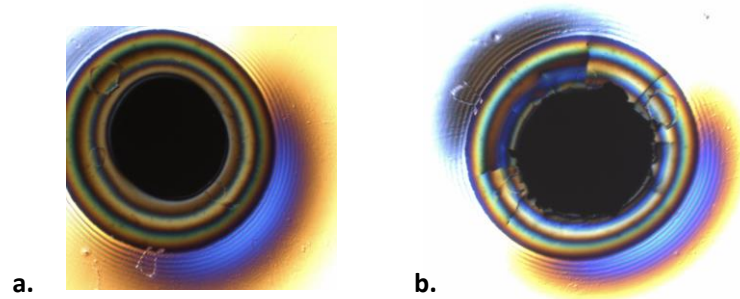
Figure 4-3. Plan-view TEM sample (a) showing interference rings in the SiO_2 near the dark hole; (b) after cracking and curling of the SiO_2 film. The size of the hole is approximately 100 μm in diameter.

4.2.3.1 Cross-sectional stack

The cross-sectional view is ideal for imaging particles aligned in the sputtered layers as shown in Figure 4-4. Once a cross-sectional slab has been fabricated, the sample can be mechanically thinned using a dimpling wheel (Figure 4-2(b)) or a polishing system such as the Allied High Tech MultiPrep system to form a rectangular wedge (Figure 4-2(c)). Many cross-sectional samples were fabricated in this work with good results.
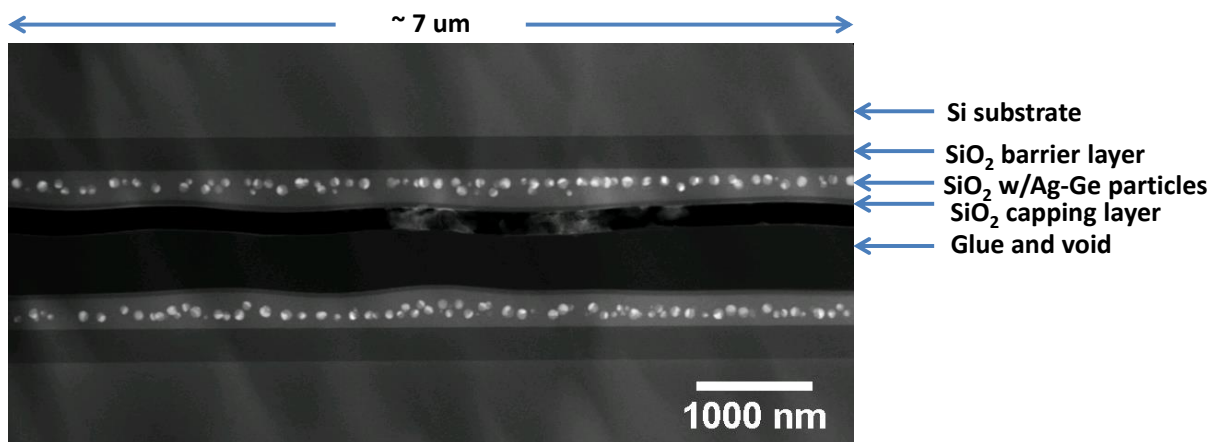
Figure 4-4. Cross-sectional TEM sample showing layers of particles.

The cross-sectional stack is shown in Figure 4-5(b). The stack must be prepared with no particles in the glue line and with a target glue thickness of 1 μm. A 500 μm slab is cut from the center of the stack with a dicing saw as shown in Figure 4-5(b). The length of the slab can be defined by either a disk grinder or the dicing saw, but it must be 3 mm or less (Figure 4-5(d) and (e).
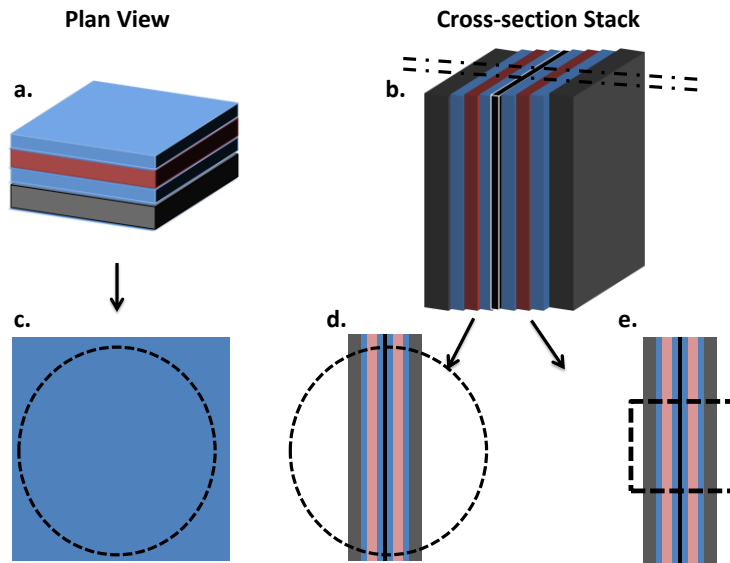
Figure 4-5. Initial preparation of TEM samples. (a) Starting material for a plan view; (b) Cross-sectional stack; (c) Plan view ready to cut out 3 mm disk; (d) Cross-sectional slab ready to cut out 3 mm disk/rectangle; (e) Slab to be cut for a wedge sample.

4.2.3.2 Cross-sectional dimpled disk

The advantage of making a dimpled sample compared with making a wedged sample is that the area of interest can be twice as large because there are interfaces on either side of the hole instead of just one set of interfaces. The first side is thinned with a low curvature using a 3 mm thick wheel, and the second side is thinned with a steeper curvature using a 1 mm thick wheel. It is essential that the interface is centered in the thin region, because the hole will be formed first in the thinnest region, and the hole must extend over the interface. Using the colors of the transmitted light through the silicon, it is possible to reach a thickness of 1-4 μm in the center of the sample. At this point, both surfaces of the dimple should be mirror polished. The dimpled slab or disk is mounted on a 25 or 50 μm Mo grid with a slot, using M-bond epoxy, G-bond epoxy, or Ag paste, depending on the time available and the maximum temperature desired. Ag paste has the advantage that it can be subsequently dissolved if a different TEM holder is desired. Dimpling a cross-sectional sample typically takes 3-6 hours. Once the cross-section is mounted on a grid, it can be milled with an Ar ion source to make a hole in the center of the dimple as shown in Figure 4-6(a).
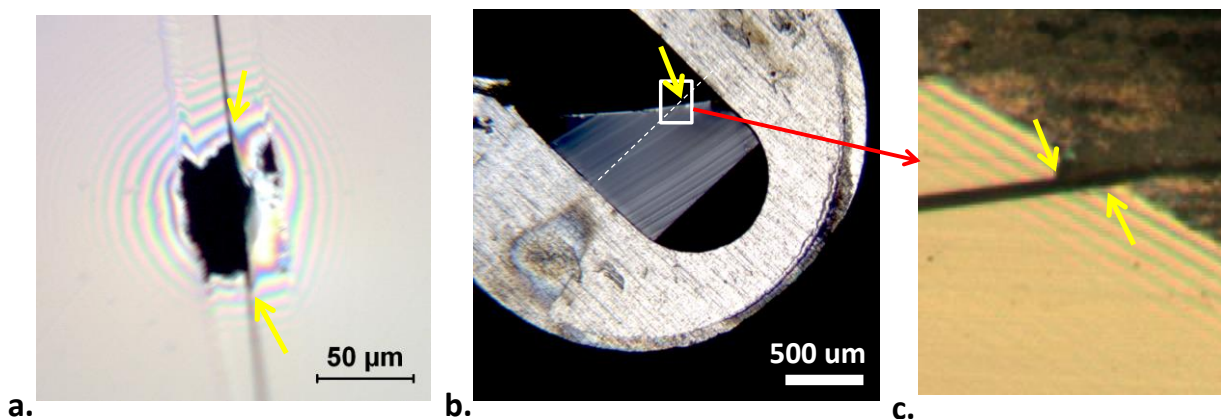
Figure 4-6. Thinned samples at the interface of a cross-section. In all views the yellow arrow points to the thinned interface. (a) Hole in a dimpled disk showing interference fringes and interface; (b) Wedge mounted on a 3 mm Mo solid grid with an oval slot; dotted white line is the interface; (c) High-magnification image of interference fringes at the interface of a cross-sectional wedge.

4.2.3.3 Wedge

Using the MultiPrep system to prepare wedge samples is advantageous because it saves time and requires no careful alignment of the interface. The Multi-prep tool is used to thin the sample by using a slurry of water and successively finer polishing papers. A slab is cut from a cross-sectional stack as in the process for making a cross-sectional dimpled sample. The dicing saw is used to cut a rectangle about 1.2 x 1.2 μm in size, which is secured to the MultiPrep stub. The first-side polishing is performed to a thickness of 200 μm, then the piece is turned over and thinned to 100 μm. At this point an angle of 1.5 to 0.5 degrees is set on the platen, and the entire sample is polished to a wedge as shown in Figure 4-2(c).

Electron transparency, as shown in Figure 4-6(c), is verified by observation of interference fringes in the optical microscope .[132] The small rectangle is mounted onto a solid TEM grid at this point using a permanent epoxy (Figure 4-6(b)). The grid and the sample will be removed together from the stub with acetone. Ion milling at low-energy can then be used to clean the interface or at high-energy to thin the interface. Because the angle of milling is steeper than the wedge angle, it is easy to remove too much material and permanently destroy the sample. The typical time for preparing a wedged sample using the MultiPrep system is 2-3 hours.

4.2.3.4 Ion milling

Ion milling is required to finish mechanically prepared samples. The high-energy argon ions remove contamination from the grinding process and remove the amorphous layer if the crystal was damaged during polishing. If a dimpled sample is being made, the sample is

perforated, creating the hole that abuts the thinnest regions. Figure 4-6(a) shows a hole created by ion milling at the interface of a cross-sectional sample.

Two different ion mills were used in this work: the Fischione Model 1010, a broad-beam system, and the Gatan Precision Ion Polishing System II, a focused-beam system. Both systems have a cold stage that allows for sample cooling to -50°C or lower. Typical recipes for ion milling are shown in Table 4-3. Because the Fischione ion mill has a broader beam, the speed of milling is slower and there is less sample damage than with the Gatan ion mill. The Gatan ion mill, being a newer system, has a microscope attached to a computer screen allowing for easy visualization during ion milling. Both ion mills have top and bottom guns, and the samples can be rotated to specified directions relative to the interface. The Gatan ion mill allows for smaller wedge angles; however, because the Fischione ion mill has a broad beam, it yields a larger thin area more easily. A low-energy beam should always be used as the last step to remove amorphous damage caused by the ion milling process itself. Typical ion milling times are 2 to 10 hours in the Fischione ion mill, and 15 minutes to 2 hours in the Gatan ion mill.

Table 4-3. Recipes for ion milling in the Fischione and Gatan ion mills.

	Gun Current	Gun Voltage	Gun angle	Rotation
Fischione perforate	5 mA	5 kV	8 degrees	+/0 60 degrees
Fischione clean	2 mA	2 kV	8 degrees	+/- 60 degrees
Gatan PIPS 2 perforate	auto	2 kV	3-6 degrees	NA
Gatan PIPS 2 clean	auto	0.5 kV	3-6 degrees	NA

4.2.4 Prepared membranes

Electron transparent membranes supported by silicon micro-machined frames can be purchased from a number of suppliers, at a cost of $15 to $29 each. Figure 4-7(a) shows a schematic cross-section of a membrane window in a silicon frame. The membranes can be made of Si-rich SiN, SiO_2, or Si, and range in thickness from 5 nm to 50 nm. The window sizes vary from 25 μm x 25 μm to 200 μm x 200 μm. Most of the designs have multiple windows in one disk, which is beneficial since routine handling and processing usually break one or more windows. Table 4-4 outlines the membranes tried in this work. In general, the membranes with the smallest windows are the most robust. The material and the thickness are less important in determining the membranes' potential to fail.
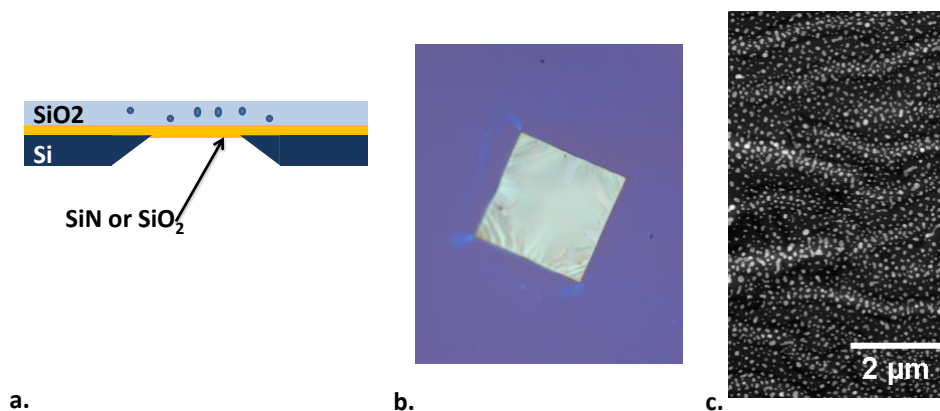
Figure 4-7. Deposition on a purchased membrane. (a) Schematic cross-section of a membrane supported by the silicon frame with a deposited film of SiO_2 containing nanoparticles (blue) on top; (b) Membrane after annealing of the deposited film showing the buckling caused by thermal mismatch between the layers; (c) HAADF-STEM image of the buckling film.

Table 4-4. TEM membranes available for purchase and their specifications.

Vendor	Material	Membrane thickness	Window size	Silicon frame thickness
Norcada	SiN	10 nm	100 µm x100 µm	200 µm
Ted Pella	SiN	50 nm	100 µm x 100 µm	200 µm
Ted Pella	SiN	8 nm	60 µm x 60 µm	200 µm
SimPore	SiN	10 nm	100 µm x 100 µm	100 µm
SimPore	SiN	5 nm	50 µm x 50 µm	100 µm
SimPore	SiO2	40 nm	100 µm x 100 µm	100 µm

The advantages of using membranes as a substrate for the embedded nanoparticles cannot be over-emphasized. Instead of a many-hour process to prepare a sample for the transmission electron microscope, the sample is ready for use after film deposition and annealing. The time savings are enormous, especially considering that more than half of all TEM samples prepared by mechanical grinding are not sufficiently thin for optimal imaging. Using prepared membranes allows quicker feedback for evaluating the deposition process, and permits examination of the deposition at different steps in the process. A sample is prepared by depositing a film containing the Ag and Ge constituents onto the membrane, and then examined in the microscope. It can then be subsequently annealed, and examined again. It can be exposed to pulsed laser melting and examined, and then be thermally annealed and examined. This ability to step through the process with the same TEM sample eliminates the necessity of making four different samples from four pieces of starting material. It also improves the likelihood that

changes viewed in the microscope are caused by the experiment and not by variability in the starting material.

The thin area suitable for microscopy in a membrane sample is much larger, by orders of magnitude, than a mechanically thinned sample. Generally the thin region of a mechanically thinned sample in cross-section can extend for 1-10 μm along the interface as shown in Figure 4-4. If one assumes a 1 degree wedge, with a maximum thickness of 100 nm, the usable area could be, at most, 5 μm. As shown in Figure 4-2(b), if one uses a dimple grinder, there are four thin regions to examine. But, often, only one or two of these regions are satisfactory and their size can be as small as 100-200 nm. In contrast, each membrane has a minimum window area of at least 25 μm x 25 μm. This feels like a vast playground in the microscope as shown in the sequence of images in

Figure 4-8. Individual particles can be probed with the electron beam without concern for permanent damage to a particular particle; with literally millions of particles to choose from, less care is required. Having many particles is also an advantage when wanting to examine a certain orientation of the particle. Instead of trying to rotate a given particle of 10-40 nm in diameter, one can search for a particle that already exists in the desired orientation. Additionally, observing the same particle structure over a large area increases confidence that the images are representative of the actual structure.
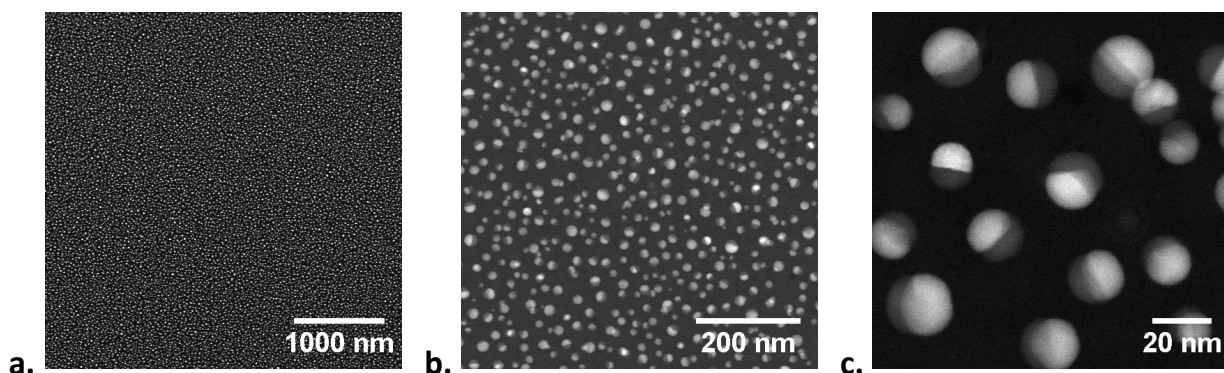
Figure 4-8. Three magnifications of the same membrane showing the vast amount of thin area with the membrane configuration. (a) Particles evident as uniform dots. The area of this image is only 4 x 4 μm; the windows are usually 100 x 100 μm and there are 9 of them per sample; (b) 5 X greater magnification than (a); (c) 10 X greater magnification than (b).

The most important advantage of using purchased membranes, however, is that the sample preparation does not cause damage to the sample itself. It is often unclear whether the mechanically polished sample is manifesting an artifact, damage, or contamination from the dimpling or ion milling. Additionally, a cross-sectional sample is exposed to a minimum temperature of 140°C for several hours during formation of the stack and bonding of the sample

to different platens with melted adhesives. Use of membranes requires no subsequent thermal treatment. They can be cleaned using an oxygen plasma and coated with carbon to reduce charging in the microscope, if necessary. The cost varies from $15-30 per membrane.

The membranes also have some drawbacks. The membrane itself, whether it has a thickness of 5 or 50 nm, adds to the diffuse scattering of the electron beam. This is a minimal effect for membranes of 10 nm or less. In fact the SiN may be substituted as the barrier layer. Because the total thickness should not significantly exceed the mean free path of the electrons, there is a limit to the maximum sample thickness. Good results have been obtained for total film thicknesses approaching 200 nm, but this is not thick enough to form the nanoparticles that average 70 nm in diameter. Targets with additional amounts of Ag and Ge would be needed to increase the constituent concentration to fabricate the 70-100 nm particles. It is possible that the capping layer could be removed by etching with liquid- or vapor-phase hydrofluoric acid after annealing. One final limitation is that in order to see layers of the deposition, and the particle position within a layer, a cross-sectional view is required as shown in Figure 4-4, and this is achievable only by fabricating a cross-sectional sample.

The thin films of silica containing the nanoparticle constituents are sputtered directly on the membranes with no damage to the membrane. The membranes have various degrees of robustness when being subjected to furnace annealing and pulsed laser melting, although no damage occurs during rapid thermal annealing. The damage incurred during the furnace annealing is a result of mechanical shock when the ampoule is opened. The damage during the PLM is assumed to come from the rapid rate of heating or cooling.

The membrane frame is fabricated from 100-200 μm thick silicon disks. As is typical with TEM samples, the disks weigh very little, and are easily lost or moved by a small gust of air or electrostatic charge. They must be secured to something substantial in order to be placed in the sputtering system or the quartz tube for annealing. Under an optical microscope, the 3 mm disks are adhered to a piece of silicon by building a small support around the particle with colloidal carbon. Once the processing is complete, the TEM disk can be lifted out of the support. If necessary, methanol can be used to clean the disk, although the liquid surface tension sometimes fractures the membranes.

The pulsed laser melting experiments described in Chapter 5 demanded the most toughness from the membranes. Figure 4-9 shows the membranes before depositing the film, after annealing, and after rupture due to the PLM. The starting membranes are not stressed as evidenced by the lack of buckling apparent in the membranes. However, after annealing, either in the furnace or in the rapid thermal annealing system, the windows appear buckled, as shown in Figure 4-9(b), indicating stress between the membrane and the deposited film, or stress between the silicon frame and the membrane. Once buckling occurs, the windows are more susceptible to fracture, especially during pulsed laser melting. Presumably, rapid heating and cooling, with a mismatch in thermal expansion between membrane and deposited film, causes membranes to fail

after PLM. SiO_2 membranes were tried, because it was hypothesized that the SiO_2 membrane would share the thermal expansion characteristics of the deposited SiO_2, but there was no reduction in the number of membrane failures. Norcada brand 10 nm thick SiN membranes were the most robust.
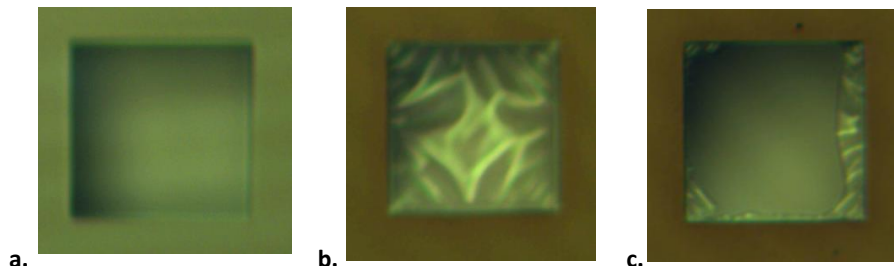
Figure 4-9. Purchased SiN membrane 10 nm thick; window is 100 μm x 100 μm. (a) Before deposition membrane is smooth; (b) After annealing membrane is buckled; (c) After PLM membrane has shattered, but pieces are intact at the edges.

4.3 Beam damage

Electron irradiation of a sample can result in the sample's permanent modification, called beam damage. The two mechanisms of beam damage relevant to the TEM samples in this work are: 1. "Knock-on" or sputtering; 2. Local heating. Beam damage is most common in the STEM configuration when the electron beam is focused to a point and is scanned across the surface. In STEM mode, the dose of electrons per unit of area is higher than in CTEM mode. Figure 4-10(a) shows beam damage of the SiO_2 matrix and of a Ag-Ge nanoparticle; there are holes in the oxide matrix in the upper left corner and debris on the particle, most likely due to "knock-on" damage from the oxygen atoms.

High-energy electrons are able to transfer energy to sample atoms "knocking" them out of lattice positions or sputtering them away from the sample surface. Each atomic bond has a displacement energy, E_d, which is the minimum energy needed to displace an atom from its bonding site; for most atoms this energy is between 10-50 eV, with the average E_d equal to 25 eV.[46] The energy required to sputter an atom from the surface is approximately half the displacement energy. Because the mass of the electron is so small, the amount of momentum transferrable from the electron will be a strong function of the mass of the sample atom, shown in the graph in Figure 4-11. For an electron beam of 200 keV, ~8 eV can be transferred to a Ge atom and ~34 eV can be transferred to an oxygen atom. Eight eV might be enough energy to sputter a Ge atom from the surface, but not enough to displace an atom in the crystal. Thirty-four eV would be enough to displace an oxygen atom from its site in the SiO_2 network. This energetic oxygen could then displace the heavier Ag and Ge elements, which is what is observed in the particle damage of Figure 4-10(a). Energy transferred from the electrons to the oxygen

85

atoms in the matrix creates energetic oxygen atoms that have enough momentum to sputter the heavier elements Ag and Ge.
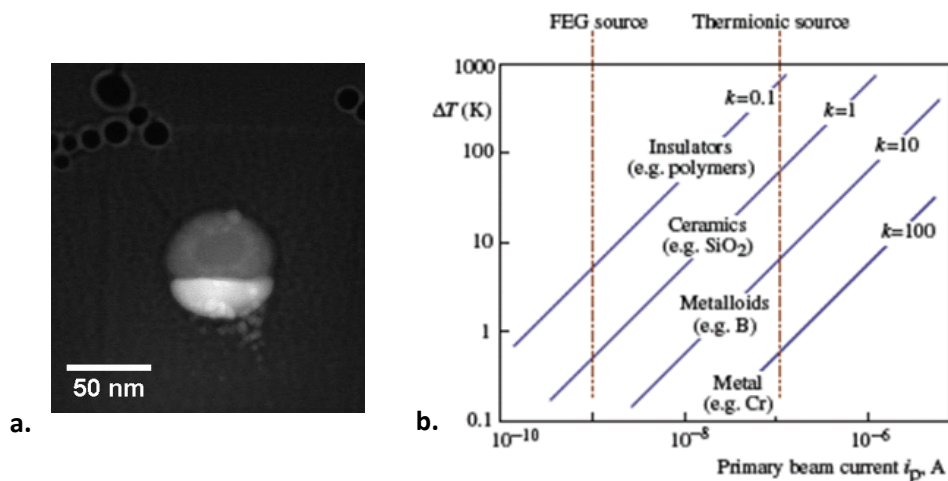
Figure 4-10. (a) Sample damage caused by the electron beam occurs primarily while in STEM mode; (b) Temperature increase due to beam heating for samples with varying thermal conductivities. Figure (b) is from Williams and Carter.[46]

Local heating is most pronounced in samples that have low thermal conductivity like dielectrics. The degree of heating is a function of the thermal conductivity of the material and the beam current, as shown in Figure 4-10(b). The Ag-Ge nanoparticles absorb energy from the electron beam via interband and plasmonic excitations. Because of low thermal conductivity in the matrix, heat dissipated after relaxation may cause the particle temperature to increase. Using data on the graph in Figure 4-10, one would anticipate that the temperature might increase less than 10°K.
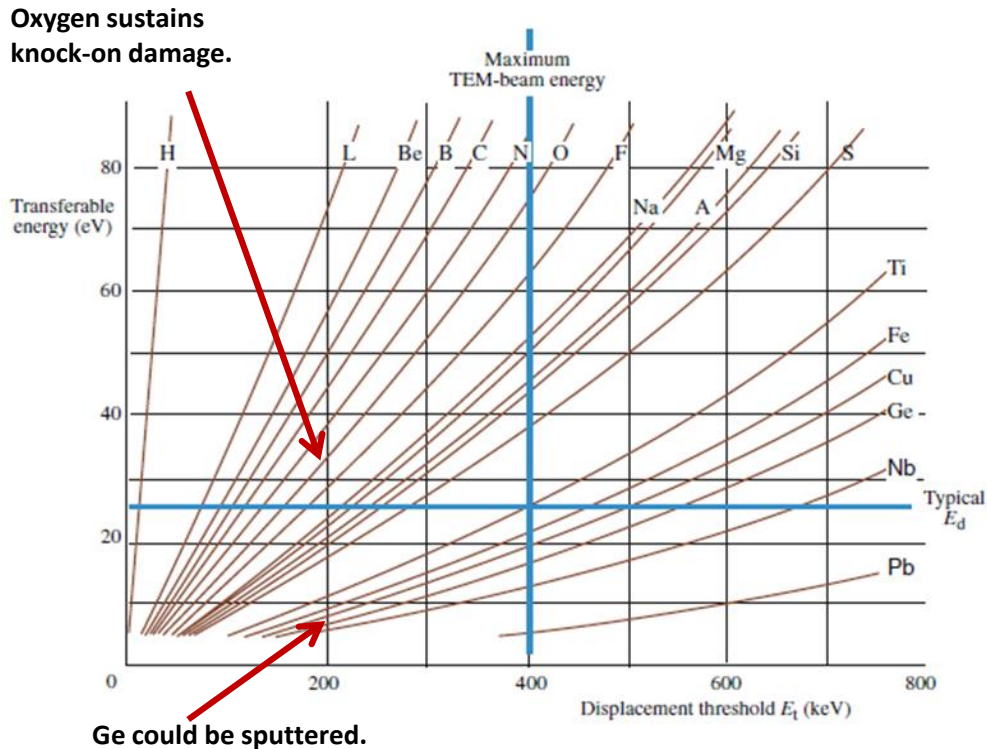
Figure 4-11. Threshold required to incur beam damage by breaking atomic bonds or sputtering. Figure is adapted from Williams and Carter.[46]

4.4 Z-contrast imaging and structure

4.4.1 HAADF-STEM

High-angle annular dark-field scanning transmission electron microscopy is ideally suited to image the bi-lobed particles because it clearly distinguishes the Ge fraction from the Ag fraction due to the difference between their respective atomic numbers. In STEM mode, the electron beam is focused to a probe on the order of several angstroms to several nanometers and scanned over the sample surface. In this mode, the illumination is convergent with a half-angle, α, as opposed to parallel as in the CTEM mode as shown in Figure 4-12. The detector (HAADF, ADF or CCD) is synchronized with the scanning coils and assigns a signal intensity to each pixel defined by the scan coils. The HAADF is a donut-shaped detector that collects electrons scattered through large angles (>5 degrees). These high-angle scattering events arise from interactions of the electron with the nucleus with a scattering cross section proportional to a value approaching Z^2. Provided that the angles are large enough to eliminate phase coherency of the scattered electrons, the images will be devoid of diffraction contrast, which can create

ambiguous image interpretation. Table 4-5 compares some of the characteristics of STEM-HAADF and CTEM modes.
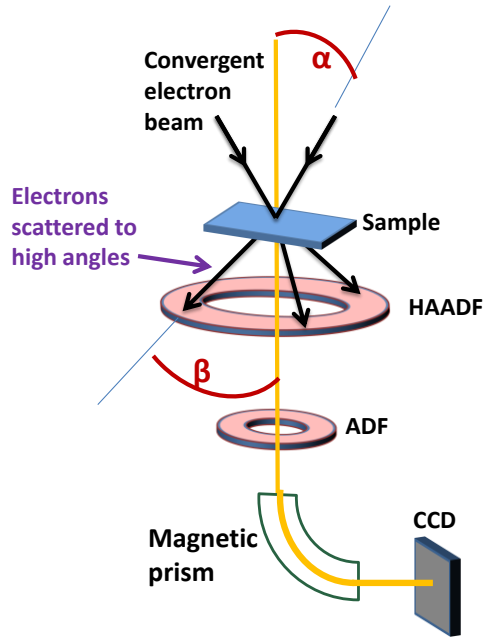
Figure 4-12. Schematic of HAADF-STEM in an electron microscope. The electron beam is converged to a point on the sample at half-angle α. The inner radius of the annular detector defines a collection half-angle β. The gold beam is the transmitted electron beam.

Table 4-5. Comparison of HAADF-STEM and CTEM.

	CTEM	HAADF-STEM
Illumination	Parallel beam	Convergent beam (scanning)
Contrast mechanism	Diffraction contrast	Mass-thickness contrast
Coherency	Coherent Bragg scattering	Incoherent Rutherford scattering
Intensity in image	Ambiguous, pixel intensity is a function of the focus conditions	Pixel intensity proportional to Z^2 and dependent on thickness.
Spatial resolution in Tecnai microscope	1.9 Å at Scherzer focus 1.2 Å information limit	1.4 Å Monochromator off 10 Å Monochromator on

4.4.2 Spatial resolution

There are three major advantages to using STEM mode in the electron microscope: 1. The spatial resolution can be optimized by controlling the spherical aberrations of the lens, 2. The use of high-angle annular detectors removes the contrast ambiguity present in diffraction

contrast images by detecting incoherent electrons, 3. The focused probe enables spectroscopy on a small spot.

In STEM mode, the resolution of the image is determined by the gun brightness, spherical aberration, C_s, of the objective lens, and the convergent half-angle, α. The gun brightness affects resolution when the beam current limits the degree to which one can demagnify the source by strongly exciting the first condenser lens. For the Tecnai-20 UT, the gun brightness is not a factor, so the optimal resolution can be found by balancing the diffraction limit imposed by C_s and the point spread function of the probe determined by α. Using the equations from Browning,[134] with a C_s of 0.5 mm for the Ultra-Twin objective lens as given by FEI, one calculates an optimum convergence semi-angle of 12 mrad.

$$\alpha = \sqrt[4]{\frac{4\lambda}{C_s}} \qquad\qquad 4.1$$

In the Tecnai microscope, a C2 aperture of 100 μm causes a convergence half-angle of 13.5 mrad, while a C2 aperture of 70 mm causes a convergence half-angle of 10.1 mrad. Thus, the ideal C2 aperture value is between the 100 mm and 70 mm. In practice, the best aperture is chosen by fitting the aperture just inside of the rings corresponding to the zeros of the contrast transfer function in the ronchigram.[135] Choosing too small an aperture can result in not enough beam intensity, however. In all of the STEM images in this work, it was found that 100 mm was the best C2 aperture. The STEM spatial resolution is then given by

$$d_{STEM} = 0.43\sqrt[4]{C_s\,\lambda^3} = 0.13\ nm. \qquad\qquad 4.2$$

Although high-resolution electron microscopy has traditionally been an advantage of conventional parallel beam illumination, recent advances in the ability to correct spherical aberrations in electromagnetic lenses to higher orders have made atomic resolution possible using STEM mode.[136] Figure 4-13(a) demonstrates the Tecnai microscope resolution with a STEM-HAADF image of <110> Si lattice in a cross-sectional sample. Figure 4-13(b) shows the simulated <110> lattice with a model showing the separation between resolved planes of ~3 Å.[137] Figure 4-13(c) shows 2 nm Ge amorphous nanoparticles imaged in the silica matrix, demonstrating the contrast achievable with nanometer-sized structures.
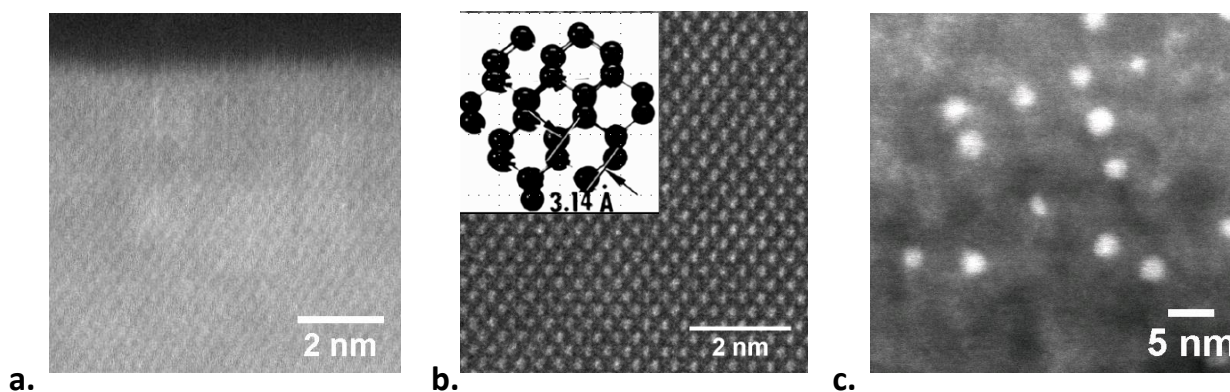
Figure 4-13. Spatial resolution of HAADF-STEM mode on Tecnai microscope. (a) Image of <110> lattice of crystalline silicon from one of the cross-sectional samples showing the lattice planes with 3.14 Å separation being resolved; (b) Simulation of the <110> lattice of Si from the literature with model of Si lattice;[137] (c) Image of amorphous Ge nanoparticles embedded in SiO_2 showing contrast from particles < 2 nm in diameter.

4.4.3 High-angle annular detector

Electrons that are elastically scattered to high angles are detected by one of two annular detectors, as shown in Figure 4-12. The annular detector closest to the entrance aperture of the CCD is called the ADF; the annular detector with the larger inside diameter is called the high-angle annular detector or HAADF. The detectors are made of a single crystal of yttrium aluminum perovskite (YAP) doped with Ce and optically coupled to a photomultiplier tube. The detectors count single electron events over the entire area of the detector during a certain amount of time that is synchronized with the scanning electron beam. The detector assigns an intensity at each pixel in the scan defined by the scan rate and bin size.

The collection half-angle, β, is defined by the inner diameter of the HAADF as shown in Figure 4-12. For the coherently scattered beams to be averaged, the collection half-angle must be >50 mrad (3˚); in general, the collection half-angle should be at least 3 times the convergence half-angle, α.[138] In STEM mode, the collection angle is changed by adjusting the camera length. All the STEM images in this chapter were collected with a camera length of 140 mm or 90 mm corresponding to collection angles of 75 mrad and 110 mrad respectively. A collection half-angle of 75 mrad is more than three times the convergence half-angle of 13.5 mrad, so the signal can clearly be assumed to be incoherent.

4.4.4 Particle orientation

When examining TEM images, it is important to remember that the image is a sum through the thickness of the sample, as if the particles were visually transparent. The Ag-Ge particles are randomly oriented in the sample, and one can estimate the distribution of particle orientations viewed in an image. For this description, it is assumed that the particle is spherical,

has 1:1 Ag:Ge volume fractions, and has a flat interface. The rotations are limited to 90˚ about 4 different axes, as shown in Figure 4-14(a). The particle in the center has an orientation that is "edge-on," meaning that the interface plane is perpendicular to the paper. One can rotate the particle 90˚ in four distinct directions and take snapshots of the orientations. Two more 90˚ rotations will complete the particle orientation possibilities. A total of 13 particle orientations can be divided into three groups of particles, as shown in the table in Figure 4-14(b). In a TEM image, one would expect to see about half of the particles in the edge-on orientation, about 1 in 6 would have a uniform contrast, and 1 in 3 would appear to have 3 regions of contrast. These different particle configurations are pointed out by orange arrows in the HAADF-STEM image of Ag-Ge bi-lobed particles shown in Figure 4-15. Of course, particles exist in gradations of those shown here, but this simplified view helps to confirm that the particles viewed in the TEM images are representative of a random distribution.

Particle orientation			
Frequency	7	4	2
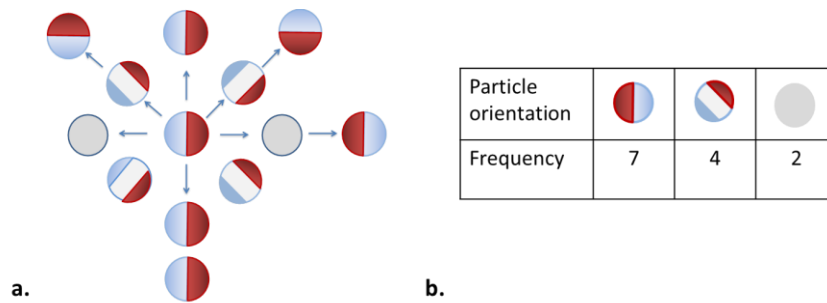
Figure 4-14. (a) Possible orientations of a bi-lobed particle assuming 90 degree rotations about 4 axes; (b) Frequency of the three orientations observed according to (a).
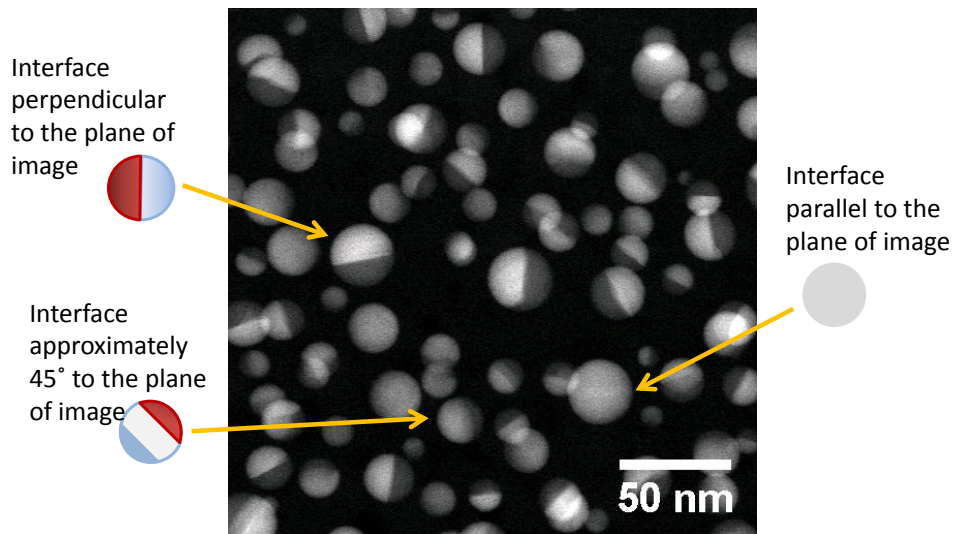
Figure 4-15. Ag-Ge bi-lobed particles embedded in SiO_2. The eye can distinguish at least three different orientations shown by the particle drawings with an arrow pointing to a particle with similar orientation.

4.4.5 Determination of average size and size distribution

The diameters of particles from HAADF-STEM images were measured using ImageJ. Figure 4-16 shows the distribution of particle diameters for a sample that was annealed first at 840°C for 1 hour, and subsequently at 900°C for 1 hour. The average particle diameter was 19.3 nm with a standard deviation of 5.3 nm. Measurements from 111 different particles were included in these statistics. Assuming a normal distribution, for this sample size, there is a 95% confidence that the average particle diameter is 19.3 nm +/- 1 nm.
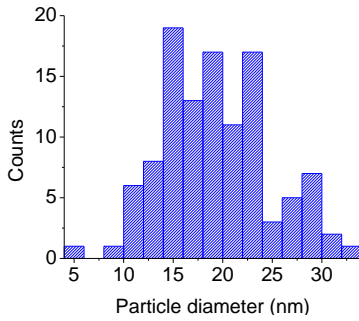
Figure 4-16. Distribution of particle sizes for Ag-Ge bi-lobed particles annealed first at 840°C and subsequently at 900°C. The average particle diameter is 19.3 nm.

It is possible that the distribution of particle sizes will follow predictions for particles in the coarsening regime. Plotting the number of particles as a function of scaled radius gives a FWHM of 0.55, as shown in Figure 4-17. This FWHM is broader than the theoretical particle size distribution from the Lifshitz, Slyozov, and Wagner theory of Ostwald ripening, which approaches 0.40.[139] The LSW theory states that the cube of the average radius increases linearly with time, however, it does not account for finite volume fractions. The model used by our group has a size distribution of approximately 0.52 in the coarsening regime and does account for finite volume fractions.[140]
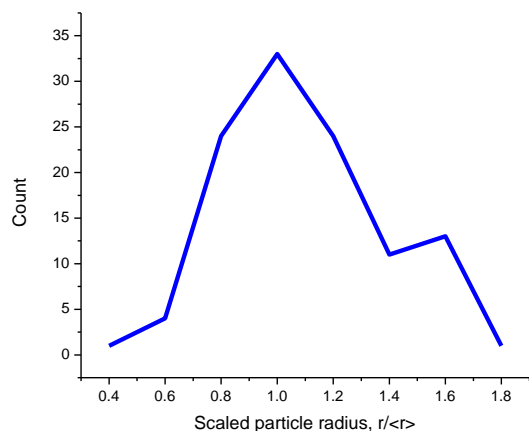
Figure 4-17. Size distribution of Sample 62 from Figure 4-16 plotted as a function of the scaled particle radius.

4.5 High-resolution TEM to elucidate interface orientation and wedge-shaped particles

4.5.1 Phase-contrast microscopy

Phase contrast under parallel illumination arises from the interference in phase of at least two diffracted beams. For the images in this chapter, no objective aperture was used, so the images are constructed from many diffracted waves. Lattice fringes arising from the phase interference can be an indication of crystallographic orientation and can be used to measure lattice spacing.[141] Although it is tempting to believe one is viewing the planes of atoms, it is important to remember that these are interference patterns – a form of contrast. Nevertheless, qualitative assessments can be made about the crystallinity of a material if lattice fringes are observed.[141] The intensity oscillations are normal to the reciprocal lattice vector with a periodicity that depends on excitation errors and thickness.[141] Often computer simulation is performed in conjunction with phase-contrast imaging to confirm atomic positions.

4.5.2 Spatial resolution

The instrumental spatial resolution of the Tecnai microscope in CTEM mode at Scherzer defocus is specified by the manufacturer to be 1.9 Å. At a given defocus amount, called the Scherzer defocus, f_{Sch}, the contrast transfer function is maximized for an objective lens with a given C_s.[46]

$$f_{Sch} = -1.2 \sqrt{C_s \lambda} \qquad\qquad 4.3$$

93

The contrast transfer function is comparatively flat until it crosses the x-axis of length that defines the instrumental resolution limit, as shown in Figure 4-18. For the Tecnai microscope at 200 keV, C_s = 0.5 mm and λ = 2.5 pm, so the defocus amount is ~42 nm. In practice, the minimum contrast can be found by adjusting focus until the rings just vanish while viewing a live FFT of an amorphous area of the sample. Once the minimum contrast is found, one can under-focus by ~42 nm.
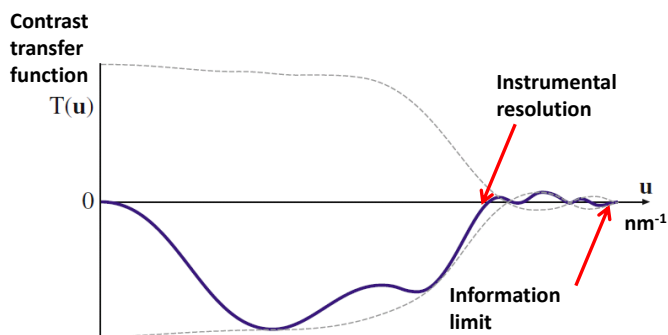
Figure 4-18. Schematic of the contrast transfer function in phase-contrast imaging, showing the instrumental resolution and the information limit. Adapted from Williams and Carter.[46]

The instrumental resolution is then given by the following equation[141] and equal to 1.9 Å in the Tecnai microscope.

$$d_{Sch} \approx 0.66 \sqrt[4]{C_s \lambda^3} \qquad\qquad 4.4$$

The information limit is specified by FEI to be 1.2 Å. The information limit is defined by the envelope of damping functions including chromatic aberrations, angular dispersion of the electron source, specimen drift and vibration, and the instrument function of the detector. Because the information limit defined by this envelope function includes zeros of the contrast transfer function where all information is lost, as well as pass-bands of opposite contrast, the intuitive interpretation of images becomes more complicated. The information limit and pass-bands of opposite contrast are illustrated in Figure 4-18.

In order to evaluate crystalline orientations of Ag and Ge components, distances between lattice planes were calculated using a software package available at the NCEM called MacTempas.[142] The resulting calculations are shown in Table 4-6 for Ag, and Table 4-7 for Ge. Given the resolution limit of 1.9 Å, from the tables of d-spacings, one sees that the phase contrast image can unambiguously resolve the {111} and {002} planes of Ag and the {111} and {022} planes of Ge. It is possible to accurately interpret lattice fringes down to the information limit, provided that the microscope is well-aligned with axial illumination (not tilted) and is focused near the Scherzer defocus condition.[141] In this case, the {022} and {113} planes of Ag and the

94

{113}, {004}, and {133} planes of Ge could also be imaged. Accuracy in measuring the reciprocal lattice vector from the FFT can be better than 1%.[141] At the very least, it is possible to determine whether the interface is coherent or incoherent.[141]

Table 4-6. Ag d-spacings calculated from MacTempas.

Bragg reflection	111	002	022	113	222	004
d-spacing in Angstroms	2.36	2.05	1.45	1.23	1.18	1.02

Table 4-7. Ge d-spacings calculated from MacTempas.

Bragg reflection	111	022	113	004	133	224
d-spacing in Angstroms	3.26	2.00	1.70	1.41	1.30	1.15

4.5.2.1 Cusp at the triple-point

Two striking images of the cusp of a particle approaching 100 nm in diameter are shown in Figure 4-19. A pronounced cusp at the Ag-Ge interface is due to the mechanical force balance as shown schematically in Figure 4-20. The vectors represent interface energies between Ag and SiO_2, Ge and SiO_2, and between Ag and Ge components as fully described in the work by Yuan.[94] Using a clever geometric construction, these vectors have been measured in the Ge-Sn system and the interface energy of Ge-SiO_2 has been deduced.[90] Upon cooling, because the SiO_2 matrix becomes more viscous near 600°C, the cusp is "frozen" in at that point. The Ge-SiO_2 interfacial energy determined is for the temperature of 600°C, when the particle shape was essentially set.[90]
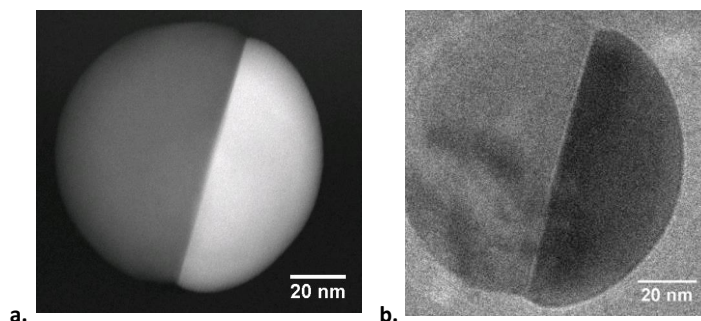
Figure 4-19. Ag-Ge bi-lobed nanoparticle, 96 nm in diameter showing cusp at the triple point of the interfaces. (a) HAADF-STEM; (b) Phase-contrast.

95
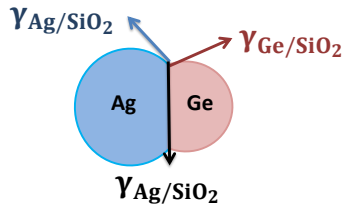
Figure 4-20. Triple point of mechanical equilibrium, showing the necessity of a cusp at the interface of the Ag and Ge volume fractions. The vectors can be modeled as the interfacial energies.

4.5.2.2 HRTEM and FFT

A high-resolution phase-contrast image of an Ag-Ge bi-lobed particle is shown in Figure 4-21. The darker region is the Ag fraction, which diffracts more electrons due to its higher mass as compared with Ge. This Ag-Ge particle is viewed edge-on, although without aligning the particle along a zone axis in diffraction mode, it is not possible to know how close the alignment is to being exactly edge-on. Without a computer controlled stage with little backlash, it is very difficult to rotate a particle on the order of 20 nm and maintain it in the field of view. The Tecnai stage control is not sufficient to orient small particles in a timely manner. Instead, the strategy is to search through the many particles that exist in films deposited on membranes for a particle in the proper orientation. It is very possible that the actual orientation will be off by 1-15 degrees or more, which will add to the experimental error. The faceting on the Ag side is due to preferential growth along these planes.

Imaging the structure of the Ag-Ge interface revealed that the {111} plane of the Ag component is parallel to the {111} plane of the Ge component, as shown by the lattice fringes in the high-resolution phase-contrast image of Figure 4-21. Using Digital Micrograph, a Fourier transformation of a square region inside the particle is performed to obtain the distance between reciprocal lattice spots (Figure 4-22). The reciprocal lattice vectors are perpendicular to the lattice fringes. The spacing between planes in real space is the reciprocal magnitude of the distance between a reciprocal spot and the central spot. The spacing between the Ag planes is found to be 2.37 Å corresponding to a {111} set of planes. The spacing between the Ge planes is found to be 3.29 Å corresponding to a {111} set of planes.
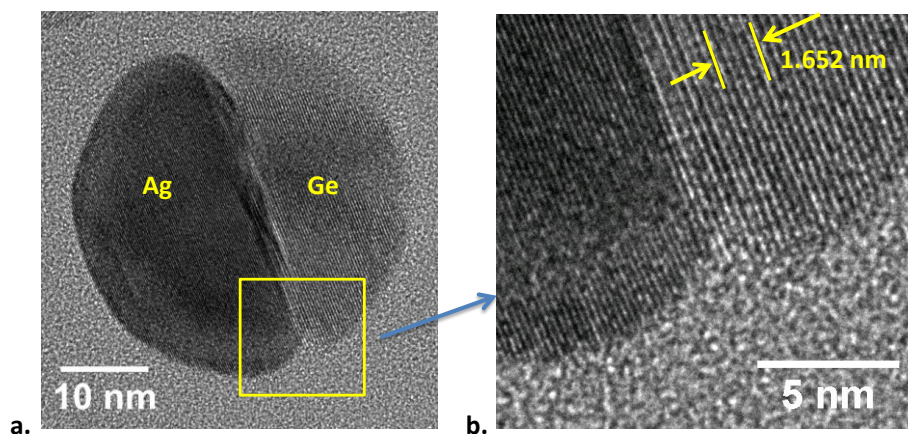
Figure 4-21. HRTEM image of Ag-Ge bi-lobed nanoparticle – Particle 6_1. (a) 37 nm diameter particle shows faceting on the Ag side, a pronounced cusp at the interface, and some diffraction contrast at the interface; (b) Magnified section of particle showing lattice fringe interference arising from {111} planes on both the Ag and Ge sides. The distance measured in ImageJ between 5 planes is 16.52 Å, corresponding to a plane separation distance of 3.3 Å. The calculated spacing between {111} planes in the Ge lattice is 3.26 Å.
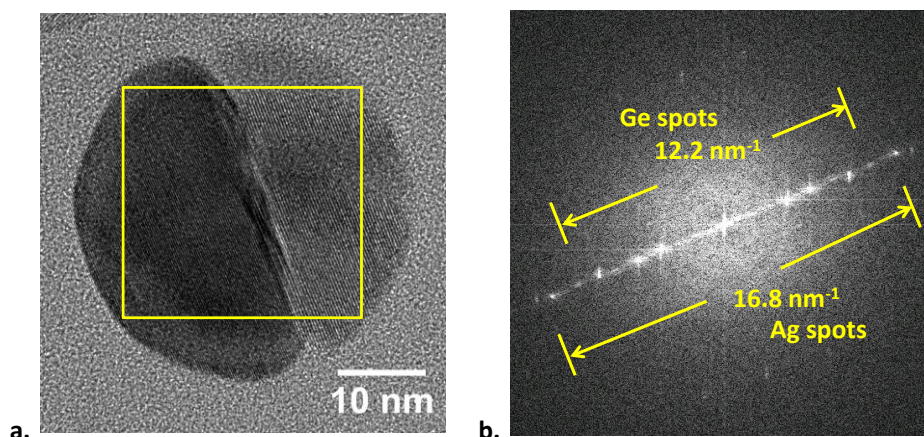
Figure 4-22. Fourier transformation of imaged lattice fringes. (a) Yellow box in particle 6_1 shown in Figure 4-16 defines the area that is Fourier transformed in (b); (b) Distance is measured between four spots for better accuracy. The lattice distances measured from (b) are 3.28 Å for Ge and 2.38 Å for Ag.

Six different particles from three different samples ranging in size from 22 nm to 37 nm were analyzed with respect to the interface. All six particles showed {111} planes of Ag and Ge parallel to each other at the interface as detailed in Table 4-8.

Table 4-8. Results from measuring reciprocal lattice vectors from the FFT of images from six different particles in three different samples.

Particle ID	Particle diameter	Measured d spacing of Ge (Angstroms)	Calculated in MacTempas d{111} of Ge (Angstroms)	Measured d spacing of Ag (Angstroms)	Calculated in MacTempas d{111} of Ag (Angstroms)
1_9	27 nm	3.31	3.26	2.40	2.36
9_5	26 nm	3.35	3.26	2.38	2.36
12_1	25 nm	3.35	3.26	2.38	2.36
1_10	28 nm	3.25	3.26	2.38	2.36
6_1	37 nm	3.29	3.26	2.37	2.36
3_4	22 nm	3.27	3.26	2.37	2.36

Based on the HRTEM analysis above, it is clear that the {111} planes of the Ag and Ge components are parallel to each other. The question arises as to whether the two halves are rotated with respect to one another so that additional registry is found across the interface. Evidence for registry is found in Particle 2_1, as shown in Figure 4-23. In this particle, lattice fringes are clearly seen across the interface. Taking a FFT of this image yields reciprocal lattice points that result from {022} planes of Ag and Ge as shown in Table 4-9. Some lattice planes in the {022} family will be perpendicular to the {111} planes, so this fact substantiates that the {111} planes are parallel and oriented such that {022} planes can align across the interface. Figure 4-24 shows the reciprocal lattice points from the Ag and Ge components separately. All particles were analyzed in this manner.

a.   b.   c.
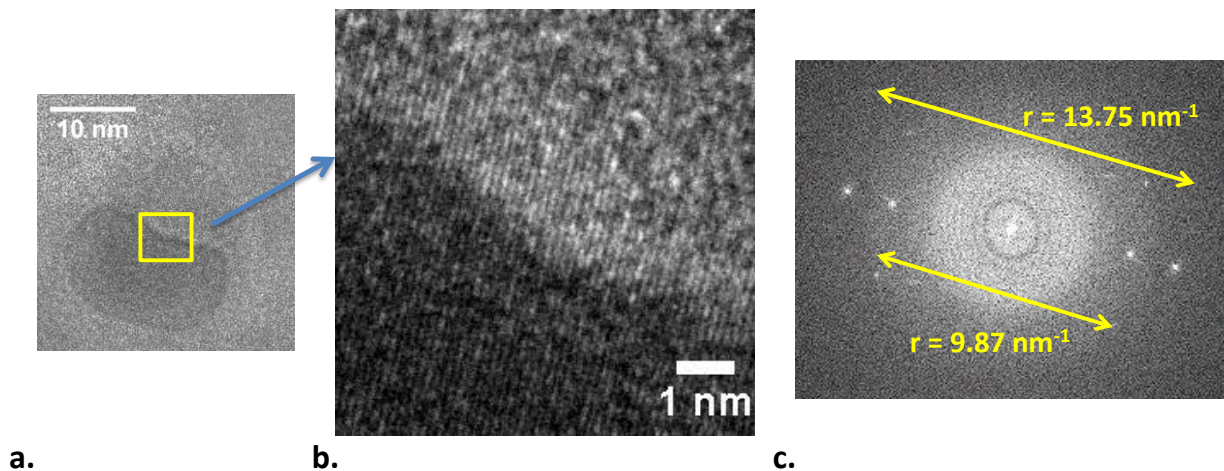
Figure 4-23. HRTEM of Particle 2_1 22 nm in diameter. (a) Yellow box indicates magnified interface in (b); (b) lattice fringes are observed across the interface; (c) FFT of lattice fringes results in d-spacing for {022} planes of Ag = 1.45 Å and d-spacing of {022} planes of Ge = 2.01 Å.
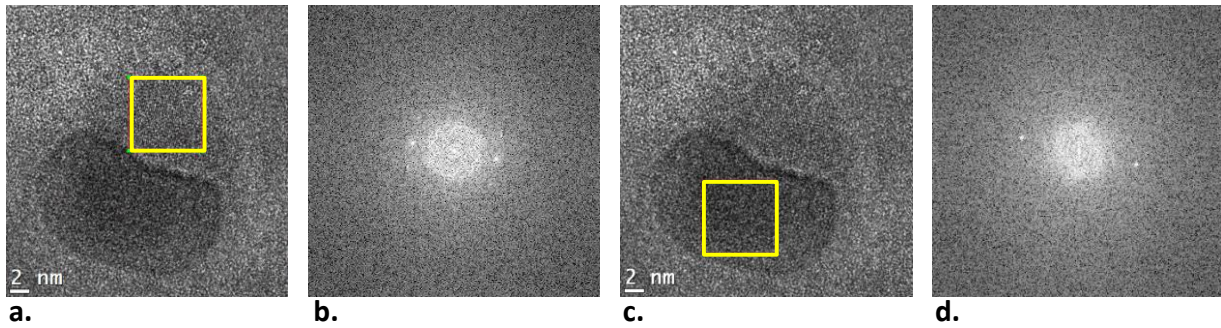
Figure 4-24. HRTEM image of diameter Ag-Ge particle showing the reciprocal lattice spots from the individual components.

Table 4-9. Spacings between {022} planes of Ge and Ag, both measured from the FFT of the TEM and calculated from MacTempas.

	Measured d from FFT	Calculated d from MacTempas
Ge {022}	2.02 Å	2.00 Å
Ag {022}	1.45 Å	1.45 Å

4.5.2.3 Discussion of findings in relation to interface energies, nucleation, and segregation

Based on the HRTEM results described above, it is clear that the film growth at the interface is proceeding in an epitaxial manner. Epitaxial growth is defined as growth of a crystalline film on a preferred orientation of the crystalline lattice of the substrate surface.[141] Based on the bulk phase diagram of Chapter 3, the Ge most likely precipitates as a solid on the SiO_2 surface with its fastest growing {111} surface exposed. The Ag film grows epitaxially on the {111} surface of the Ge precipitate.

The {111} planes of the Ag and Ge components are incoherent. They share no registry of complete planes across the interface, nor do dislocations form to relieve the stress that might be imposed by a semi-coherent interface. However, they do have preferred orientations that allow atomic row matching to occur.[99] It is likely that the Ag-Ge interface energy is "low", as this is the driving force for forming the bi-lobed structure rather than other configurations for this segregating alloy. Figure 4-25, a simulation done by a colleague[140], shows the possible registry of individual atoms in the Ge and Ag crystal, with {111} planes parallel and aligned along a <022> direction. In this drawing, the black dots are the Ag atoms arranged on the fcc lattice with a lattice constant of 4.09 Å. The paper is perpendicular to the <111> direction, so the nearest neighbor atoms are in the <011> directions with bond lengths of 2.87 Å. Four different Ge lattices corresponding to the four different colors in the color key, also from the <111> direction, are superimposed on the black Ag lattice. The nearest neighbor atoms are also in the

99

<011> directions and have bond lengths corresponding to a dc lattice with a lattice constant of 5.6 Å. In agreement with the finding that the {022} planes are parallel across the interface as shown in the HRTEM image of Figure 4-23, three of the four Ge lattices are aligned with the <011> directions parallel. The fourth lattice, yellow-green in the drawing, is rotated by 19.1°.
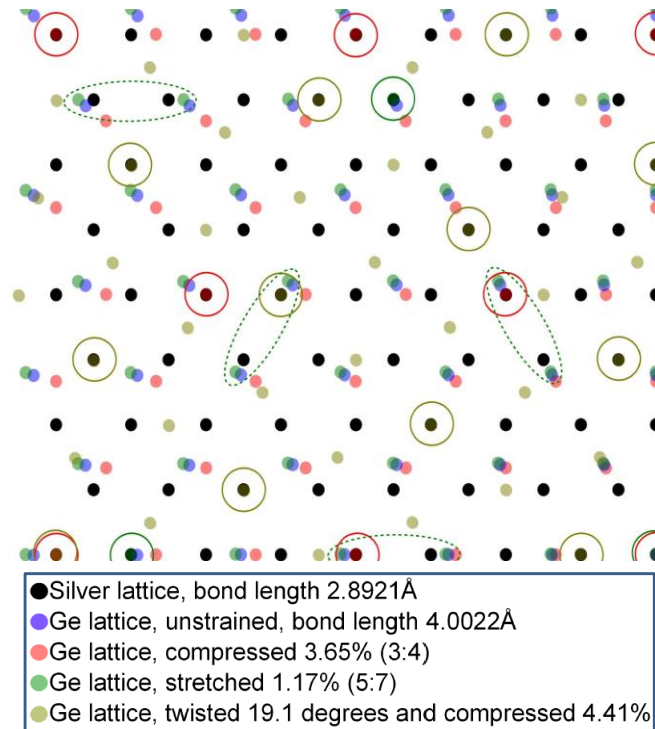
Figure 4-25. Real space drawing of atoms in Ag (black) and Ge (colors) crystals viewing from the <111> axis with the < 011> directions aligned. There are four different Ge lattices represented as indicated by the color key. Registry of individual atoms is indicated by a colored circle representing the lattice that is overlaid. For example, one possibility is a Ge lattice that is in compression by 3.65% as indicated by the red dots. Every eighth atom is exactly overlaid. Figure courtesy of Carolyn Sawyer.

The findings from the drawing in Figure 4-25 are listed in Table 4-10, demonstrating that orientation along an <011> direction may be a low-energy orientation for the {111} planes of Ag and Ge, as determined by the quantity of atoms that would be matched.

Table 4-10. Findings from the drawing above showing atomic matching for the Ge {111} lattice superimposed on the Ag {111} lattice.[140]

Color	Strain on the Ge lattice (no strain on Ag lattice)	Alignment to <011> of Ag lattice	Number of atoms overlaid	% atomic matching
Blue	None	<011>	None	0%
Red	3.65% compression	<011>	1 out of 8	12 %
Blue-green	1.17% tension	<011>	1 out of 24 with several nearly lined up indicated by dotted lines in the drawing	>4%
Yellow-green	4.41% compression	19.1 degree rotation	1 out of 3	33%

To test whether <011> directions are aligned, a nano-diffraction pattern was collected from a Ag-Ge particle with the Ag-Ge interface, and consequently a {111} plane, perpendicular to the beam direction. The schematic of the diffraction pattern along a [Ī11] direction is shown for the case of Ag and Ge lattices aligned in the <022> directions in the left-hand side, and rotated with respect to the <022> direction on the right-hand side.
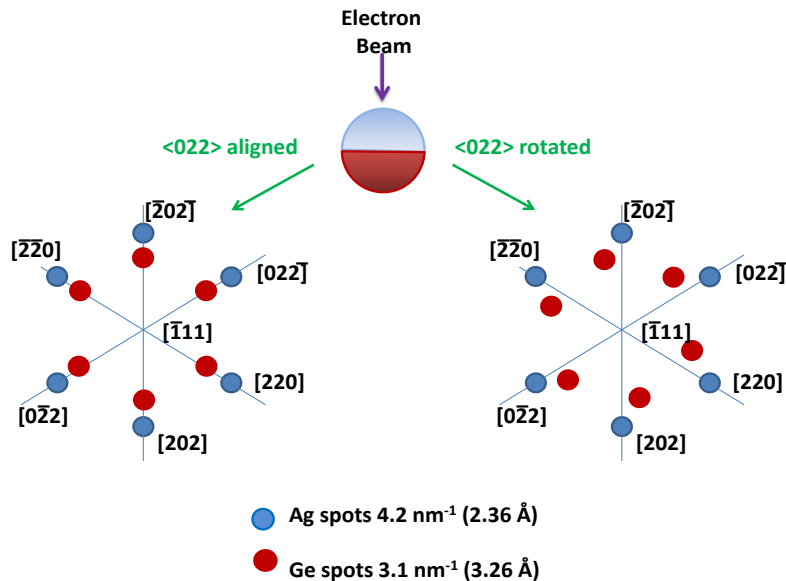
Figure 4-26. Schematic of [Ī11] diffraction pattern for Ag and Ge crystal. The left-hand drawing is with the <022> directions aligned; the right-hand drawing is for the <022> directions twisted with respect to each other.

Nano-diffraction was achieved from a single 20 nm particle in CTEM mode with a convergent beam. The spots in a diffraction pattern from a convergent beam are disks, often overlapping, as opposed to the small spots obtained when using a parallel beam. The first condenser lens was strongly excited to spot size=9, to demagnify the source to a small spot so that it would fit inside a 20 nm particle. Then a small C2 aperture of 50 μm was used to make the beam as parallel as possible. Making the beam more parallel with the C2 aperture decreased the size of the disks in order to resolve the Ag disks from the Ge disks. It was necessary to increase the gun lens excitation to achieve sufficient beam current through the small C2 aperture. The Tecnai microscope is not designed to record an electron diffraction pattern, since the beam block is too far away from the actual back focal plane. A short camera length (52 mm) was used to demagnify the diffraction pattern to fit inside the 5 mm GIF aperture. A time series of 10 exposures at 0.1 seconds per exposure were collected and several of the exposures were added together to increase the signal-to-noise of the diffraction disks. Because the Tecnai stage makes it difficult to rotate a small particle to achieve perfect zone axis alignment, the strategy was to find a large uniform contrast particle in image mode, take an image of it, converge the beam to the center of the particle, and view the diffraction pattern. If the diffraction pattern appeared close to the <111> zone axis, a time series of exposures was collected. This method was successful and the convergent beam electron diffraction pattern from an Ag-Ge particle is shown in Figure 4-27(b), together with the phase-contrast image (Figure 4-27(a)) of the Ag-Ge particle from which the diffraction pattern was collected.
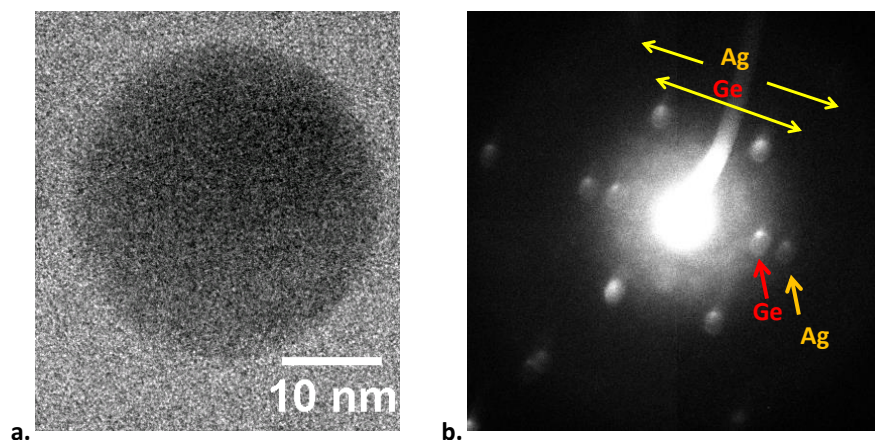
Figure 4-27. Ag-Ge 30 nm diameter nanoparticle. (a) CTEM image with the Ag-Ge interface parallel to the paper; (b) Nano-diffraction from the center of the 30 nm particle showing the <111> diffraction pattern with spots from the what is believed to be the Ge and Ag reflections aligned in the <022> directions.

The diffraction spots along the <022> direction in the <111> diffraction pattern in Figure 4-27 are labeled Ge and Ag. Although the diffraction pattern was not calibrated to a known standard to make an actual measurement of the distance between the reciprocal lattice spots, the ratio of the Ge and Ag labeled spots is equal to the ratio of the Ge and Ag lattice constants. This observation agrees with the observation showing the continuation of the {022} planes across the interface. It is possible that not only are {111} planes of Ag and Ge parallel to each other, but there is orientation preference along the <022> direction.

4.5.3 Wedge-shaped particles

Particles with volume fractions shaped as a wedge are observed in the transmission electron images. Figure 4-28 shows a HAADF-STEM image of a wedge-shaped particle and a collection of different particles. In almost all observed cases, the Ag component is the larger fraction, although at least one particle has been observed where the Ge fraction is the larger component. Particles were divided into categories of clearly bi-lobed, uniform, or graded contrast, and clearly wedge-shaped as shown in Figure 4-28(b). Although the decision whether a particle is wedge-shaped or rotated is somewhat subjective, it was found that the particles that are clearly wedge-shaped represent about 13% of the particles for this sample.
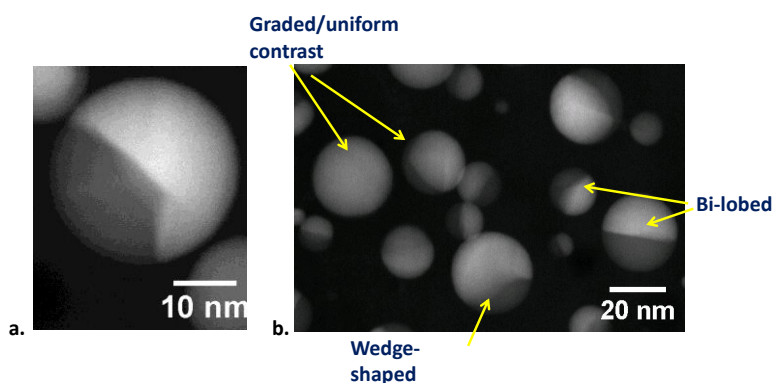
Figure 4-28. HAADF-STEM images. (a) Wedge-shaped particles; (b) Particles identified as bi-lobed, wedge-shaped, or graded/uniform contrast. The wedge-shaped particle represents ~12% of particles.

The question at hand is whether the wedge occurs preferentially on specific planes within the Ag-Ge bi-lobed particle. Figure 4-29 shows conventional TEM images of two wedge-shaped particles; the darker region is silver and the lighter region is germanium. The angle formed by the wedge was measured using ImageJ in five different particles that appeared to be relatively "edge-on." The angles varied from 116° to 132° as listed in Table 4-11. It should be noted that this measurement is subjective and measurements of +/- 3° seem equally reasonable to the eye.
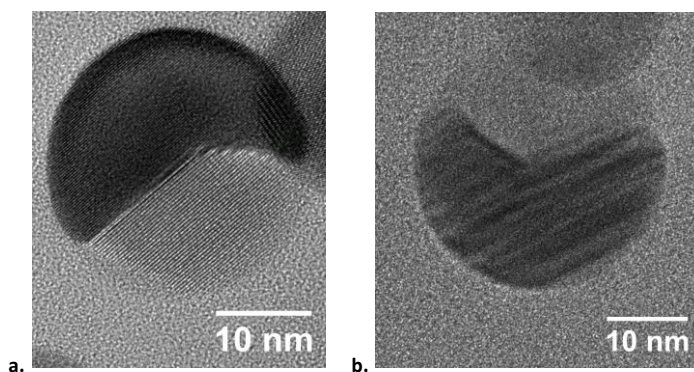
Figure 4-29. CTEM images of two wedge-shaped particles. (a) Particle 1_10, angle measured as 132°; (b) Particle 8, angle measured as 117°.

Table 4-11. Angles of five different wedge-shaped particles.

Particle ID	1_10	8	3_1	7_2-A	7_2-B
Angle measured with ImageJ	132°	117°	126°	116°	121°

Table 4-12 lists the angles that the different planes make with the {111} planes. A plane from the {100} family would result in a wedge of 125°. Another possibility is the family of {113} planes. A {113} plane makes an angle of 121.5° degrees with a {111} plane.

Table 4-12. Angles between the {111} set of planes and other families of planes. A {100} plane could form a wedge with a {111} plane with an angle measuring 125°.

{111}	{110}	{100}	{113}
71° (180° − 71° = 109°)	35° (180° - 35° = 145°) 90°	55° (180° - 55° = 125°)	58.5°(180° − 58.5° = 121.5°) 29.5° (180° - 29.5° = 150.5°) 79° (180° - 79° = 101°)

A colleague[140] created a simulation of a bi-lobed structure rotating about an axis perpendicular to the {111} plane (z-axis) and parallel to the {111} plane (x-axis), as shown in Figure 4-30. One observation that can be made from this drawing is that rotating the wedge-shaped particle results in shapes that are often observed in the TEM images. This leads to the conclusion that the structural uniformity may be better than is apparent by looking at the TEM images. A second observation is that rotating the particle results in measuring a wedge angle that is significantly different from the actual angle. The simulation in Figure 4-30 is for a wedge angle of 125°. One can rotate the particle by 10° about the z-axis and the angle measurements vary from 120° to 131°, even though the particle still appears to be "edge-on." From these observations it is possible to conclude that a wedge-shaped particle with a preference for a wedge on the {100} or {113} planes may be a low-energy configuration and may even be an equilibrium shape.
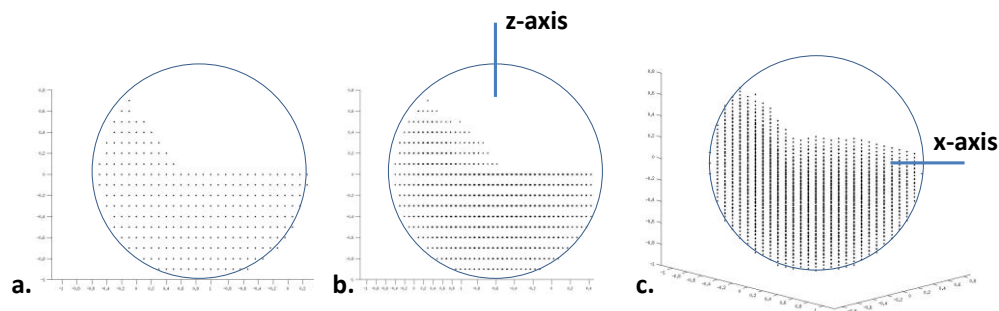
Figure 4-30. Simulated wedge-shaped particles. (a) Edge-on with wedge at 100 plane offset from the center of the particle; (b) Particle in (a), rotated 20 degrees about the z-axis as shown; (c) Particle in (a), rotated 14 degrees about the x-axis as shown. Figure courtesy of Carolyn Sawyer.

4.6 Core-loss energy-loss spectroscopy to verify constituents

Electron energy-loss spectroscopy of core electrons was used to confirm the chemical identity of the two volume fractions of the Ag-Ge particle. Fast electrons can undergo inelastic scattering events in the sample. One of the energy-loss events is excitation of a core electron to a higher state. Because each atom has characteristic energies between different electronic states, the EELS spectrum of a core-loss event is a fingerprint for the atomic specie. The scattering cross section for energy-loss events decreases as the energy-loss increases. Generally, losses less than 2000 eV can produce signal-to-noise levels that make them detectable above the background. For this reason, EELS is more sensitive to the lower-Z elements. The scattering cross sections for each transition are tabulated in a standard EELS table.[74] From this table, the user knows the expected energy-loss and the strength of the scattering event. The microscope user needs only to refer to the EELS chart for the energy range over which to scan. In STEM mode in the Tecnai microscope, one can place the electron beam on a region of the particle and take an energy-loss spectrum that spans the characteristic edges thereby collecting chemical information with high spatial resolution. The monochromator is not excited for the core-loss electron excitations, because the weak core-loss excitations require as much beam current as possible to overcome small scattering cross sections.

Core-loss EELS measurements were collected to identify Ag and Ge fractions. To confirm the light regions as being Ag, the electron probe was placed on the light region of the particle, as shown in Figure 4-31(a), and the energy range centered at the Ag M-5 edge at 367 eV was detected with the CCD. Because it was not quantitative, the signal was collected until an edge was observed, approximately 4 to 16 seconds. Similarly, to confirm the dark regions as being Ge, the electron probe was placed on the dark region of the particle, as shown in Figure 4-31(b), and the energy range centered at the Ge edges, L-2 at 1217 eV, and L-3 at 1248, was detected with the CCD. Again, the acquisition operated in cumulative mode until an edge was observed, approximately 4 to 16 seconds.

Ag side

Ge side

Data from Ge side – no silver edge

Ag M-5 edge at 367 eV

350 400 450 500 550 600 650
Energy Loss (eV)

c.

50 nm

50 nm

a.

b.

Data from Ag side – no germanium edge

Ge L-2, L-3 edge at 1217, 1248eV

1000 1200 1400 1600 1800
Energy Loss (eV)

d.
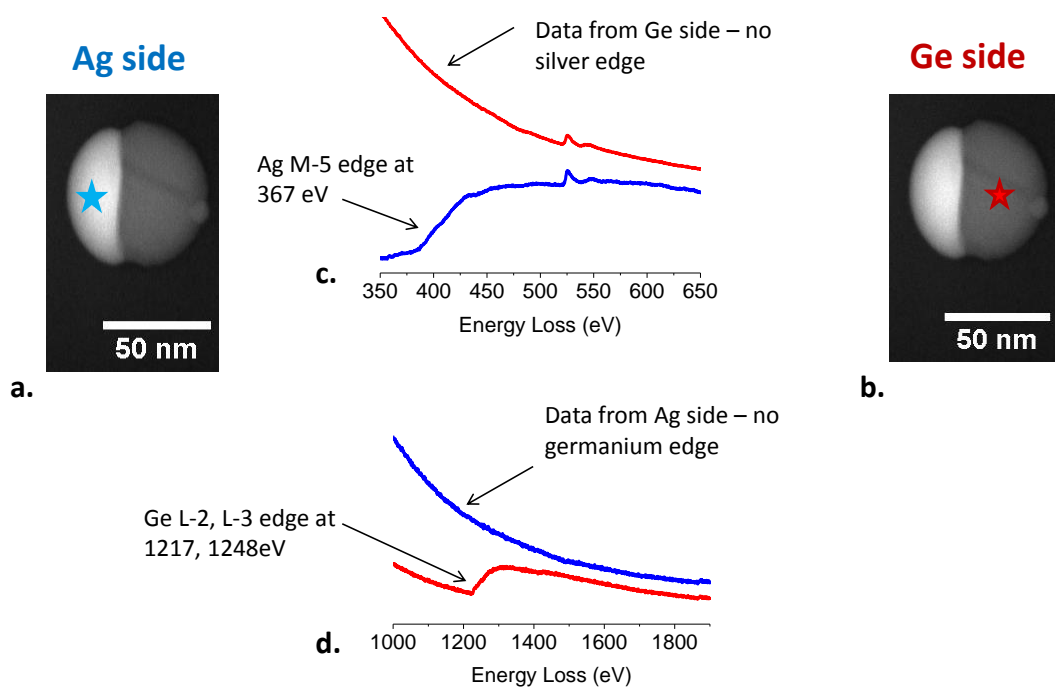
Figure 4-31. Results from core-loss EELS on a Ag-Ge nanoparticle. (a) Location of electron beam while collecting the signal from the Ag component as shown in the blue curves of (c) and (d); (b) Location of electron beam while collecting signal from Ge component as shown in the red curves of (c) and (d); (c) Spectra near the M-5 edge of Ag; (d) Spectra near the L-2 and L-3 edges of Ge.

4.7 X-ray diffraction of nanoparticles

X-ray diffraction of thin films is a common and quick method to evaluate the crystallinity of a film. It can also be used to evaluate the crystallinity of an ensemble of nanoparticles provided that there is enough material to generate a detectable signal. Previous work evaluating the crystallinity of Ge nanoparticles embedded in silica used the easily detectable Raman signal to evaluate crystallinity.[57]   The lineshape for an ensemble of amorphous Ge nanoparticles is easily distinguished from the lineshape for crystalline nanoparticles in the Raman spectrum. Synchrotron X-ray radiation was used to evaluate the crystallinity of bi-lobed Au-Ge nanoparticles.[28]   Electron diffraction of an ensemble of particles in the microscope produces characteristic rings.[104] Phase-contrast imaging of lattice fringes from an individual particle in the electron microscope is also effective at determining the crystallinity of a particle.[102]

With the ability to fabricate larger quantities of embedded nanoparticles using RF sputtering, it was possible that x-ray diffraction from a Cu Kα source would be measureable in a reasonable amount of time. X-ray diffraction data was collected from a Siemens D500 x-ray diffractometer, with Cu-Kα wavelength 0.154 nm in a time of 30 min. The largest Ge nanoparticles embedded in silica produced the x-ray diffraction 2-θ scan shown in Figure 4-32.

This sample was prepared as described in Chapter 3, and a HAADF-STEM image is shown as an inset in Figure 4-32. From a RBS measurement, the amount of Ge in the film is 1.6×10^{17} atoms/cm^2, which corresponds to a ~36 nm layer of solid Ge. Based on the area covered by the nanocrystals from the TEM images, mass conservation confirms that the particles are not thin disks in the 110-140 nm layer film, but rather particles that extend from the nitride membrane to the surface. This is confirmed with the RBS depth profile.
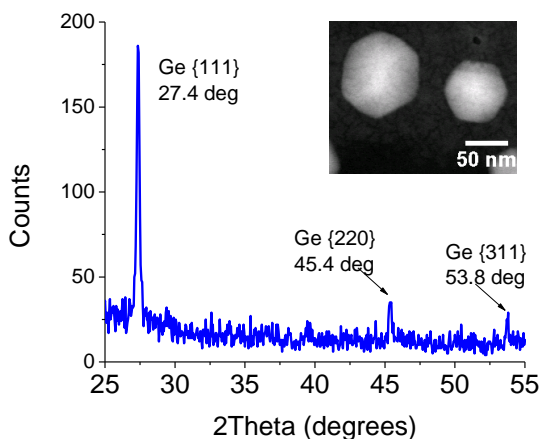
Figure 4-32. X-ray diffraction from large Ge nanocrystals embedded in SiO$_2$. Theta-2-theta scan shows a dominant peak from reflections in the {111} plane indicating preferred growth in this direction. The minimum amount of Ge required to obtain an x-ray diffraction signal using a Cu-K-alpha source was 1.6×10^{17} atoms/cm^2.

The peak height proportions between the {111}, {220}, and {311} peaks are known for an ensemble of randomly oriented crystals to be approximately 2.7:1.8:1.[143] The ratio of peak heights in this sample is approximately 10.3:1.5:1; an almost four-fold increase in the height of the {111} peak is observed. The height of the {111} peak beyond the ratio of a randomly oriented ensemble is an indication that the crystallites have a preferred texture[144] with {111} planes being parallel to the plane of the substrate. This preferred growth orientation is evident in the HAADF-STEM image showing many six-sided shapes indicative of the {111} growth.

4.8 Release and dispersion of particles from matrix

Previous studies of Ge nanoparticles embedded in SiO$_2$ successfully released the Ge nanoparticles from the matrix by etching with either vapor-phase or liquid-phase hydrofluoric acid (HF).[47] The hydrofluoric acid efficiently etches silica and does not etch Ge. The Ge nanoparticles remain stuck to the Si substrate surface via Van der Waals forces. Sonicating the substrate in a methanol bath agitated the aggregated Ge nanoparticles, thereby releasing some of them into the liquid solvent. The remaining Ge nanoparticles were dispersed on the Si substrate,

facilitating analysis with an atomic force microscope (AFM). The AFM is low-resolution in the plane of the substrate because the size of the tip is on the order of 10 nm. However, it has good resolution, +/- 0.5 nm, in the height direction. If one assumes well-dispersed particles, or at least less than a monolayer of coverage, one can use the height as the diameter of the particle. This technique was confirmed with TEM measurements of the particle size, and it was found to be accurate and repeatable.[47]

The motivation for releasing Ag-Ge particles from the matrix is to prepare a sample for single-particle dark-field optical scattering and single-particle cathodoluminescence. Dark-field scattering in an optical microscope is a standard technique for characterizing scattering spectra from individual noble metal nanoparticles.[52, 80, 145] Cathodoluminescence is just beginning to be applied to the study of plasmonic nanostructures,[48] but it is a complementary technique to other optical measurements presented in Chapter 5. Chapter 6 will discuss both dark-field scattering and cathodoluminescence as part of the future work.

In order to evaluate the AFM measurement, a reference sample with 20 nm Au nanoparticles was prepared. A purchased solution of citrate-stabilized Au nanoparticles was dispersed on a cleaned silicon substrate and dried. An AFM image of this sample is shown in Figure 4-33(a), and the distribution of measured heights, labeled as the particle diameters, is shown in Figure 4-33(b). Although the average particle measurement was lower than the specified diameter (14 nm compared to 20 nm), the method was considered reliable. The microscope used is a Digital Instruments Dimension 3100 scanning probe microscope with etched Si probe tips.
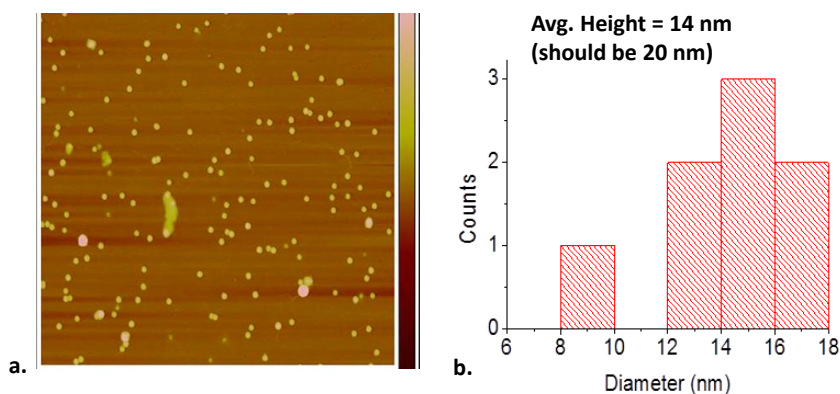
Figure 4-33. AFM results of reference sample: Reference sample: Citrate-stabilized Au nanoparticles, 20 nm in diameter, drop cast on Si substrate. (a) AFM image, 5 μm scan; (b) Size distribution with average diameter = 14 nm.

A sample of Ag-Ge nanoparticles was prepared for AFM. Fortunately, Ag is also resistant to etching by hydrofluoric acid. The complicating aspect of the sample preparation is that Ag nanoparticles are known to aggregate unless they are intentionally separated. Indeed, aggregation has been a challenge for colloidal processing of noble metal nanoparticles; the particles must be synthesized with either attached ligands to physically separate them or with charged surfaces to electrostatically separate them. Once the Ag-Ge nanoparticles were removed from the matrix, a ligand was required to separate them during the time in the liquid solvent. Nitrilotriacetic acid ($C_6H_9NO_6$) easily binds to the surface of the Ag nanoparticle, replacing the bond to the organic solvent. Charge repulsion prevents Ag nanoparticles from aggregating. A solution of 0.04 M $C_6H_9NO_6$ was added to the solvent during sonication to disperse the Ag-Ge nanoparticles on the substrate.

Samples of large embedded nanoparticles (average diameter = 69 nm as determined by TEM) were fabricated on Si substrates. The SiO_2 matrix was etched with a solution of 1:1 HF (49%):H_2O until the surface was visibly clear, approximately 1-3 minutes. The reaction was quenched in methanol and rinsed five times to remove all traces of HF. One part 0.04 M $C_6H_9NO_6$ was added to one part methanol, and the substrate was sonicated in the mixture for five minutes. The sample was then dried with N_2.

An AFM image of this sample is shown in Figure 4-34(a), and the distribution of measured heights, labeled as the particle diameters, is shown in Figure 4-34(b). As with the reference sample, the particle diameters measured with AFM (average = 47 nm) were smaller than measured with TEM (average = 69 nm). However, the dispersion achieved is ideally suited for dark-field scattering and cathodoluminescence experiments.
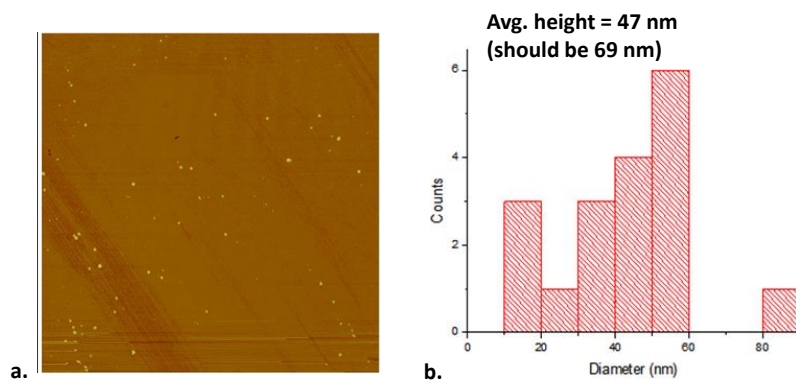
Figure 4-34. Ag-Ge bi-lobed nanoparticles released from the matrix and dispersed on Si substrate. (a) AFM image, 5 μm scan; (b) Size distribution with average diameter = 47 nm.

The same Ag-Ge dispersed sample was examined with scanning electron microscopy (SEM). Figure 4-35(a) and (b) show the Ag-Ge nanoparticles well-dispersed on the Si substrate.
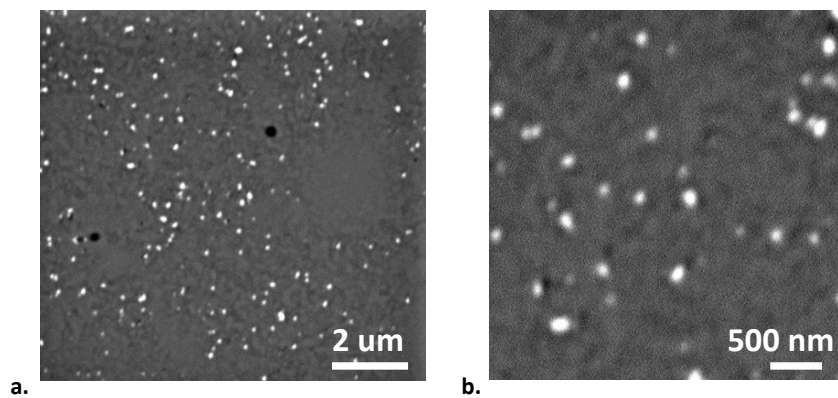
Figure 4-35. SEM images of Ag-Ge bi-lobed nanoparticles released from the matrix and dispersed on Si substrate. (a) Low-magnification; (b) High-magnification.

Chapter 5 Optical Properties

5.1 Ensemble measurements and simulations of the LSPR

5.1.1 Introduction

As described in Chapter 2, spectrophotometry in the UV-Vis-NIR wavelength range is the conventional technique for measuring the peak of the localized surface plasmon resonance (LSPR) of an ensemble of plasmonic nanoparticles.[80] Light is absorbed by the LSPR and then scattered in all directions or dissipated as heat, resulting in a measured extinction of the light transmitted through the sample.

The simulations shown in Chapter 2 demonstrated how the LSPR energy and linewidth depend on nanoparticle size, choice of nanoparticle material, and refractive index of the matrix. The strongest component of the LSPR lineshape from the Ag-Ge nanoparticle is expected to arise from the interface between Ag and SiO_2 in the wavelength range 355 to 420 nm (3.0 to 3.5 eV). A weaker component is expected to originate from Ag at the Ag-Ge interface. Because the Ag-Ge bi-lobed particle has a shared interface, it is expected that the LSPR of the Ag component at that interface will be affected by the refractive index of the Ge. This was modeled in Chapter 2 as a Ag nanoparticle in a Ge matrix, and the corresponding LSPR was simulated and is shown below in Figure 5-1. It was found that the LSPR is expected to red-shift significantly from ~430 nm to 900-1200 nm, depending on the size of the particle, in agreement with the literature.[16, 146] Evidence from both experiments and simulations for this LSPR mode arising from the Ag-Ge interface will be presented in this section.
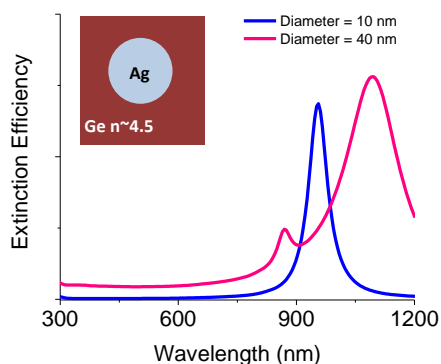
Figure 5-1. Simulated LSPR of Ag nanoparticles (from Chapter 2) showing the effect of a large refractive index on the energy and shape of the surface plasmon resonance.

A number of research groups have investigated the LSPR of a metal nanoparticle in a matrix with a high refractive index. In all cases, the matrix is a semiconductor and all report a red-shift of the LSPR due to the high refractive index of the semiconductor. Mertens et al.[38] measured the broad LSPR of Ag nanoparticles, 5 to 13 nm in diameter, in an amorphous silicon matrix. Because of the high refractive index of a-Si (n~4), the localized surface plasmon resonated between 1.0 eV (1240 nm) and 1.5 eV (827 nm). Similarly, Stenzel et al.[39] measured the LSPR of Ag nanoparticles embedded in a-Si and observed a peak at 1.7 eV (730 nm). Kjeldsen et al.[40] reported a red-shift of the LSPR from Sn nanocrystals from 5.5 eV in a SiO_2 matrix to 2.5 eV in an a-Si matrix. Hanson et al.[147] embedded semimetallic nanoparticles made of Er and a group V element, such as ErAs and ErSb, in thin films of GaAs, $GaAs_{0.5}Sb_{0.5}$, and GaSb. The LSPR peaks were observed in the range from 0.27 eV (4.5 μm) to 1 eV (1.2 μm). Peng et al.[41] deposited Ag hemispheres on Ge nanowires and measured a broad LSPR centered at 480 nm, but extending out to 600 nm. The curved side of the hemisphere was adjacent to an aqueous solution with a corresponding refractive index close to 1.3.

5.1.2 LSPR of Ag-Ge nanoparticles measured with spectrophotometry

Samples of Ag-Ge nanoparticles embedded in SiO_2 were deposited on fused silica substrates. The LSPR extinction was measured in a Perkin Elmer Lambda 950 UV-Vis-NIR spectrophotometer at room temperature from 2600 nm to 200 nm. A tungsten-halogen lamp was the source for the wavelength range from the NIR to 320 nm; a deuterium lamp was the source for the wavelength range from 320 nm to 200 nm. A photomultiplier tube served as the detector for the range from 888 nm to 200 nm, and a Peltier-cooled PbS served as the detector for the NIR range. The spectrophotometer was operated in the difference mode by placing a fused silica substrate in the reference beam and a sample of thin film deposited on a fused silica substrate in the sample beam. In this mode, the instrument function is not included in the data collected. The fused silica substrate does not absorb light in the wavelengths of interest. An aperture 3 mm in diameter was used to define the area of interest. As described in Chapter 2, reflection and transmission were both measured, and the extinction or absorbance, as it is sometimes called, was calculated by taking the logarithm of the incident radiation (taking the reflection into account) divided by the transmitted radiation (Equation 2-17). An extinction of 1.0 is equivalent to 10% transmission. This value will depend strongly on the volume of Ag nanoparticles in the film.

Although the amount of Ag in the films was small, the signal was strong in the extinction spectrum. Rutherford backscattering spectrometry measurements revealed a concentration of Ag per unit area of $1-2 \times 10^{16}$ cm^2, which corresponds to a Ag layer 1.7 to 3.4 nm thick. A strong signal derived from such a thin layer is evidence for the strong extinction cross section described in Chapter 2. From this simple observation, it is easy to understand the allure of using plasmonic particles for the manipulation of light.

Figure 5-2 shows an extinction spectrum from a sample containing nanoparticles with an average diameter of 69 nm. This sample was prepared as described in Chapter 3 with a SiO_2 barrier layer 200 nm thick, a SiO_2 + Ag + Ge layer 200 nm thick, and a SiO_2 capping layer 50 nm thick. The sample was annealed at 840˚C for 1 hr followed by controlled cooling at a rate of 220˚C per hour to 620˚C. The particle diameters were measured with TEM. The red curve is the spectrum collected before annealing the sample; the peak at 2.8 eV is assigned to the LSPR from Ag nanoparticles that have clustered during the film deposition. The peak is slightly red-shifted from that shown in Chapter 2 of Ag nanoparticles in SiO_2 because there was a significant amount of Ge remaining in the matrix, which increased the refractive index from 1.45 toward the value for GeO_2 of 1.6.[148]
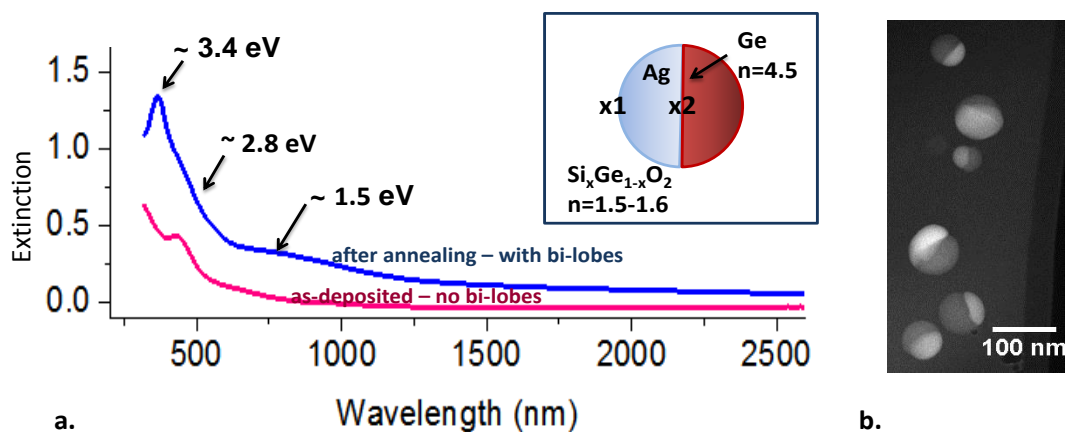
Figure 5-2. Measured extinction of Ag-Ge bi-lobed nanoparticles with an average diameter of 69 nm. (a) The red curve was collected before the sample was annealed, and the blue curve was collected after the sample was annealed. The blue curve shows three distinct components to the lineshape arising from at least three different Mie modes. The inset is a schematic of the Ag-Ge bi-lobed nanoparticle showing location X1 and X2. (b) HAADF-STEM image of Ag-Ge particles from this sample.

After the sample has been annealed, when the bi-lobed particles are formed, the distinctive LSPR from the Ag hemisphere, shown by the blue curve, appears. There are three regions of interest. The shoulder at 440 nm corresponding to the LSPR coming from the Ag and the SiO_2 interface is still present, as shown in position x1 in the figure inset. The strong peak at 365 nm may be a higher-order localized surface plasmon mode, such as a quadrupolar mode, arising because the particle is larger than the mean free path of the electrons and consequently is expressing retardation effects. A shoulder from the higher-order mode appeared in the LSPR simulations referenced in Chapter 2 when the particle reached 20 nm in diameter. The most interesting peak in this spectrum is a shoulder near 800-1000 nm that is attributed to the LSPR of the Ag nanoparticle at the Ge interface, as in position x2, red-shifted because the adjacent Ge has a larger refractive index (n = 4.5 at the 800 nm wavelength) than $Si_xGe_{1-x}O_2$ (n ~ 1.5). It is this mode at the interface that is expected to transduce a response from the Ge semiconductor.

114

5.1.3 Simulation of extinction, absorption and scattering

In 1908, Mie solved Maxwell's equations analytically for the problem of a homogenous sphere in a non-absorbing matrix.[9] Extrapolation to other geometries, such as core/shell structures and bow-ties, has relied on numerical methods to solve for the electromagnetic modes. The Ag-Ge bi-lobed structure, although approximated by a sphere in total surface, is comprised of two different materials with different complex dielectric constants. Numerical simulations of the absorption, scattering, and extinction cross sections, as well as calculations of the electric field intensities were performed by a collaborator[55] and will be presented to add understanding to the measured plasmonic properties.

The absorption, scattering, and extinction cross sections were simulated with the discrete dipole approximation (DDA) using a freeware code called DDSCAT.[149, 150] The DDA approximates the continuum by dividing it into a 3-D grid and assigns a polarizability to each unit volume of the grid. The interaction of light with this array of electric dipoles can then be simulated for a non-standard geometry. The grid used for these calculations was 1 nm^3. The values for the real and imaginary dielectric constants as a function of wavelength were taken from Johnson and Cristy[67] for Ag and from Palik[64] for Ge. The matrix refractive index used was 1.45. The simulations addressed the wavelength range from 300 to 700 nm, so the expected shoulder near 800 nm was not simulated.

The simulations cannot describe exactly the Ag-Ge particle for several reasons: 1) It was assumed that the shape of the particle is a sphere. However, TEM images show a pronounced cusp at the interface instead of a smooth surface. 2) It was assumed that the volume fraction of Ag:Ge was 1:1. Although many of the particles have volume fraction ratios of approximately 1:1, there is a distribution of ratios, as shown in the TEM images. 3) The interface was assumed to be flat, smooth, and abrupt. It is possible that the interface has some step-like curvature that would still preserve the (111) parallel planes that are observed with TEM. Based on interface studies of Ag-Ge thin films, there is most likely one to several monolayers of disorder at the interface.[106, 130] 4) The dielectric constants are assumed to be uniform throughout the volume fraction. As described in Chapter 2, in the Ge crystal near the interface there is most likely charge separation that would lead to different dielectric functions in the near interface region. 5) Finally, Ag and Ge in the bi-lobed particles may be less pure than the material from which the bulk dielectric constants were measured in the references. In particular, according to the bulk phase diagram, it is likely there is a small percentage of Ge in the Ag crystal. Ge atoms would exist as interstitial impurities, increasing scattering of conduction electrons and thereby affecting the dielectric constant.

5.1.4 Comparison of LSPR simulations to LSPR measurements

Figure 5-3 shows the LSPR dependence on nanoparticle diameter, with experimental results shown in (a), and the corresponding simulation shown in (b). As described in Chapter 2,

the extinction increases when the volume of material increases. The simulation demonstrates that as the particle diameter increases, the extinction peak both broadens and red-shifts because of phase-retardation effects.

The y-axis in Figure 5-3(a) is the extinction (log of the ratio of incident to transmitted light), equal to the extinction coefficient, k (units of m^{-1}), times the thickness of the layer. The y-axis in Figure 5-3(b) is the extinction cross section in units of m^2. The extinction = (extinction cross section) x (concentration of Ag atoms) x (thickness of layer). The cross-sectional area of a 100 nm particle is 0.78×10^{-14} m^2; the y-axis values in Figure 5-3(b) for this size particle range from 1.7 to 3.8^{-14} m^2. This simple calculation demonstrates the concept that the "absorption cross section" (or in this case, the extinction cross section) is larger than the physical cross-sectional area of the particle.[60]

Figure 5-3(a) is the experimentally measured LSPR from Ag-Ge bi-lobed nanoparticles from three different samples with average diameters of 69 nm, 26 nm, and 14 nm. The intensity of the extinction increases as the volume of the of the nanoparticles increases. Spectra from the two larger particle sizes have a more pronounced peak near 365 nm, which was assigned to the higher-order mode because retardation effects are less likely in 14 nm particles (although all samples have a distribution of particle sizes).
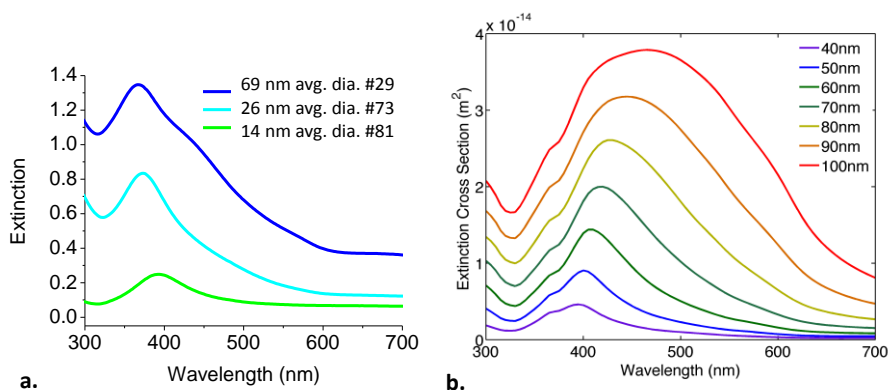
Figure 5-3. LSPR dependence on Ag-Ge bi-lobed nanoparticle diameter. (a) Measured LSPR from three different samples with average diameters of 69 nm, 26 nm and 14 nm. (b) LSPR extinction as a function of Ag-Ge bi-lobed nanoparticle diameter simulated using DDA.

Particle diameters for the sample in Figure 5-2 were measured with ImageJ from the TEM images, and the distribution of particle sizes is shown in Figure 5-4(b). Using this distribution of particle diameters, a weighted extinction spectrum was simulated, shown together with the experimental data from Figure 5-2 in Figure 5-4(a). The blue (measured) and green (simulated) curves have been scaled and offset for clarity. The graph shows similar lineshapes comprised of two components. The lineshape at 365 nm (3.4 eV), assigned to a higher-order

mode, is the dominant measured response, but is revealed as a shoulder in the simulation. The lineshape at 443 nm (2.8 eV), assigned to the dipole mode from the Ag-SiO$_2$ interface, is dominant in the simulation and is revealed as a shoulder in the experiment.
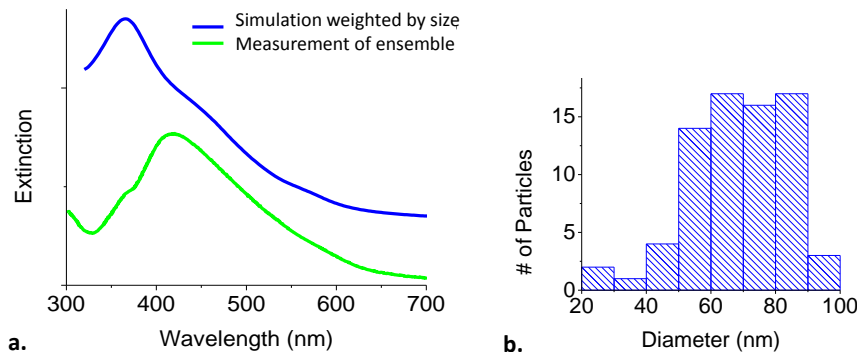
Figure 5-4. (a) Extinction showing LSPR of Ag-Ge nanoparticles. The blue line is from the sample in Figure 5-2 with an expanded x-axis. The green line is a simulation from an ensemble of Ag-Ge nanoparticles with a size distribution as shown in (b); (b) Size distribution of Ag-Ge nanoparticles in Sample #29 as determined by TEM.

The simulations shown in Figure 5-5 elucidate the different contributions from absorption and scattering processes that determine the total extinction. As described in Chapter 2, extinction, or absorbance, is the sum of scattering and dissipative (absorption) processes. The incident light excites a localized surface plasmon mode, and the light is either absorbed, as shown in Figure 5-5(a), or scattered, as shown in Figure 5-5(b). The two simulations show that the absorption cross section dominates for particles with diameters of ~75 nm or less, while the scattering cross section dominates for particles with diameters of ~75 nm or more.

117
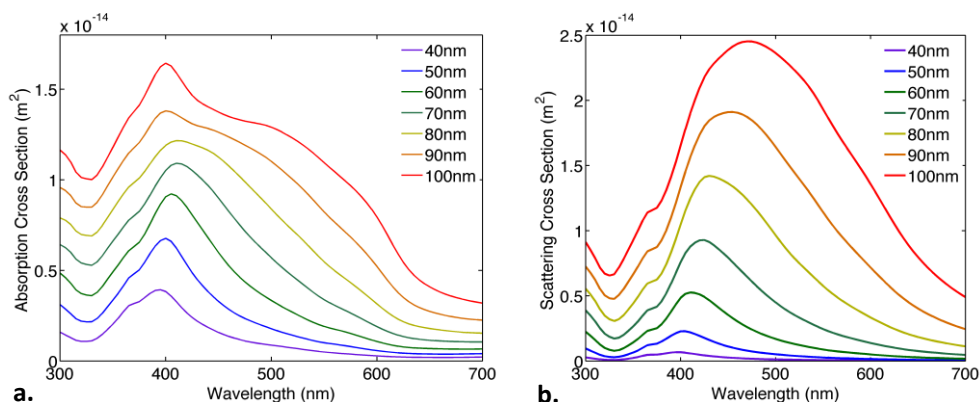
Figure 5-5. DDA simulations of Ag-Ge nanoparticles showing the two parts of extinction: absorption and scattering. Absorption dominates for small particles; scattering dominates for large particles. (a) Absorption cross section as a function of particle diameter; (b) Scattering cross section as a function of particle diameter.

5.1.5 Large Ge nanoparticles with Ag surface structures

Large Ge nanoparticles with Ag surface structures, 10-80 nm in one dimension, produced a strong LSPR in the near-IR region. The peak was measured at 700 nm as shown in Figure 5-6(a). This strong red-shifting of the LSPR from its expected value near 430 nm to 700 nm is further evidence of the effect of the Ge interface on the Ag LSPR. The presence of the LSPR at this wavelength indicates that the mode was not completely damped by the adjacent semiconductor.
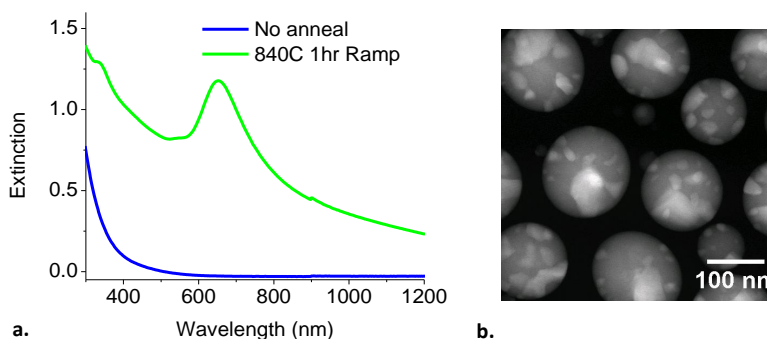
Figure 5-6. (a) Measured LSPR from large Ge nanoparticles with Ag surface spots. The blue line shows sample measurements before the nanoparticles were formed and the green line shows measurements after the bi-lobed nanoparticles were formed; (b) HAADF-STEM image of large Ge nanoparticles with Ag surface spots.

118

5.1.6 Electric field intensity simulations

The electric field intensity inside and outside of the particle was simulated by a collaborator[55] for incident light of three different wavelengths using finite-difference time-domain (FDTD) numerical methods. FDTD finds approximate solutions for Maxwell's system of differential equations by solving finite-difference equations in the time-domain. A commercial-grade simulator based on the finite-difference time-domain method was used to perform the calculations.[151] The dielectric functions used for Ge were from Palik,[64] and the dielectric functions used for Ag were calculated using a Lorentz-Drude fit. Figure 5-7 shows simulations of the electric field intensity for a 100 nm diameter Ag-Ge bi-lobed particle, plotted as the log $|E^2|$. Polarization of the incident light (X and Y) is indicated by the arrows to the left of the simulations.
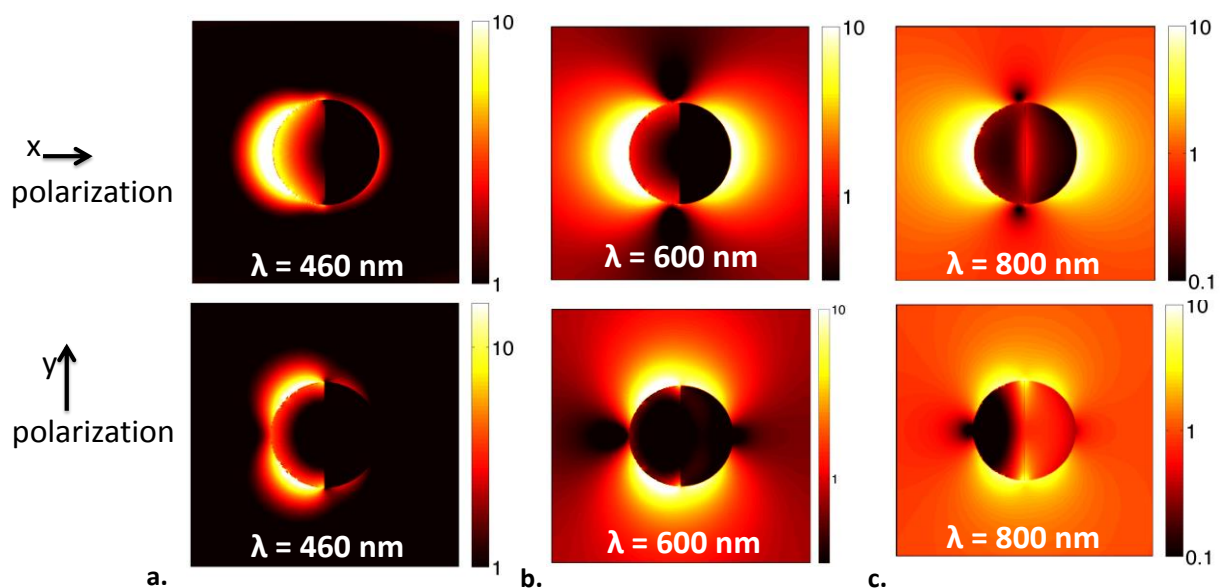
Figure 5-7. Calculated (FDTD) electric field intensity in and around a Ag/Ge nanoparticle of 100 nm diameter for incident light at (a) 460 nm (2.7 eV); (b) 600 nm (2.1 eV); (c) 800 nm (1.6 eV). Polarization of the incident light (X and Y) is indicated by the arrows to the left of the simulations. The color scale is the magnitude of the electric field intensity ($|E|^2$) and is logarithmic.

An examination of the simulated electric field intensity provides insight into the electric field at different locations around the particle. At 460 nm (2.7 eV), near the peak of the expected dipole mode of Ag in SiO_2, the field is at its maximum at the surface of the Ag nanoparticle, but extends some distance into the silica as will be shown later in the EELS results. At 600 nm (2.1 eV), the field is almost as strong on the Ge side of the particle as on the Ag side. It is not clear whether this field is being transduced from the Ag LSPR, or if it arises from an electronic or optical transition in the Ge crystal. It would be interesting to model a 100 nm particle of germanium to see if the field exists without the silver component. At 800 nm there is also

considerable field on the Ge side. There appears to be a field supported at the interface, as observed in the shoulder of the LSPR spectrum (Figure 5-2) in the energy range 800-1000 nm.

5.2 Single particle measurements of the energy loss

5.2.1 Introduction

Fast electrons, like those in a transmission electron microscope, can excite both electronic and optical transitions in materials, thus enabling spatially resolved measurements of the localized surface plasmon resonance. The electric field generated by a moving electron has polarization in both transverse and longitudinal (direction of propagation) directions. Because of the longitudinal polarization, fast electrons are able to excite normally "dark modes" in optical experiments that excite with light possessing only transverse polarizations. For example, bulk plasmons, which are longitudinal waves, cannot couple to the transverse polarization of the E and H fields during optical-only excitation. The electric field of the fast electron contains a large number of frequencies, essentially a broad spectrum excitation.[88, 152] A detailed description of optical excitations accessible in the transmission electron microscope is available in the review article by García de Abajo.[48]

Figure 5-8(a), an EFTEM image, shows the localized surface plasmon on the Ag component of Ag-Ge bi-lobed nanoparticles. The largest two particles are oriented approximately edge-on and the smallest particle is oriented ~ 45˚ to the electron beam. This image was captured by collecting only those electrons that have lost 3-4 eV from the original 200 keV, so the brightest regions are comprised of electrons that have excited transitions in the energy range of 3-4 eV. The optical measurements of an ensemble of these particles, in the previous section, showed the peak of the LSPR to be at 3.4 eV, so this bright feature is assigned to the LSP of Ag. There is also a bright region at the surface of the Ge component, which is assigned to electronic transitions in the Ge. However, it can also arise from the Ag LSP, as a similar region of high electric field intensity was simulated, as shown in Figure 5-7. The zero-loss image of the same three particles, also using a 1 eV energy slit, is comprised of only elastically scattered electrons and more clearly shows the darker Ag regions, which scatter more strongly. Figure 5-8 shows the power of EFTEM to provide insight, with nanometer resolution, into the spatial origin of optical and electronic transitions.
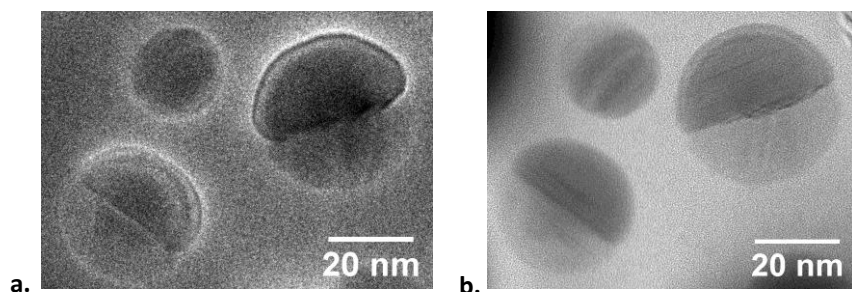
Figure 5-8. Three Ag-Ge bi-lobed nanoparticles; the two largest ones are oriented edge-on and the smallest one is oriented at approximately 45 degrees; (a) Energy-filtered TEM image with 1 eV slit at 3.5 eV energy-loss. The bright region at the surface of the Ag components is the localized surface plasmon; there is some surface contrast on the Ge lobes as well; (b) Energy-filtered TEM image with 1 eV slit at zero loss.

The complementary technique to EFTEM for analyzing the optical properties of nanoparticles is EELS in the low-loss region (<50 eV). In Chapter 4, Ag and Ge components were identified by measuring characteristic excitations of core electrons in the high-loss region of the spectrum: near 370 eV for Ag and 1200 eV for Ge. Figure 5-9 shows an EELS line scan across a 70 nm Ag-Ge bi-lobed nanoparticle in the energy-loss region from 0 to 10 eV. The yellow cross marks the spot on the line-scan, drawn in red, where the energy-loss spectrum was collected. Most notable is the strong peak at 3.4 eV in Figure 5-9(e) from the surface of the Ag component that is assigned to the Ag localized surface plasmon. This LSP decays into the SiO_2 matrix as shown in Figure 5-9(f) and is still measured with the electron beam 10-20 nm from the edge of the Ag particle. The evanescent decay of the LSP was described in Chapter 2 and is seen in the electric field simulation of Figure 5-7. The response is relatively flat over the SiO_2 on the Ge side of the particle, as shown in Figure 5-9(a). Near 3 eV at the surface of the Ge particle, there is a broad peak, which may be arising from electronic transitions in the Ge or arising from an interaction of the LSP of Ag with the surface of the Ge component. The electron beam could be detecting a high electric field at the surface, indicated in the simulations of electric field intensity at 2.7 and 2.1 eV, as shown in Figure 5-7(a) and (b) The spectrum over the Ag-Ge interface is most likely picking up the interband transition of the Ag as well as the LSP of the Ag. When the beam is directly over the Ag component, the peak reaches a maximum at 3.9 eV, the energy of the 4d to 5s interband transition in Ag.
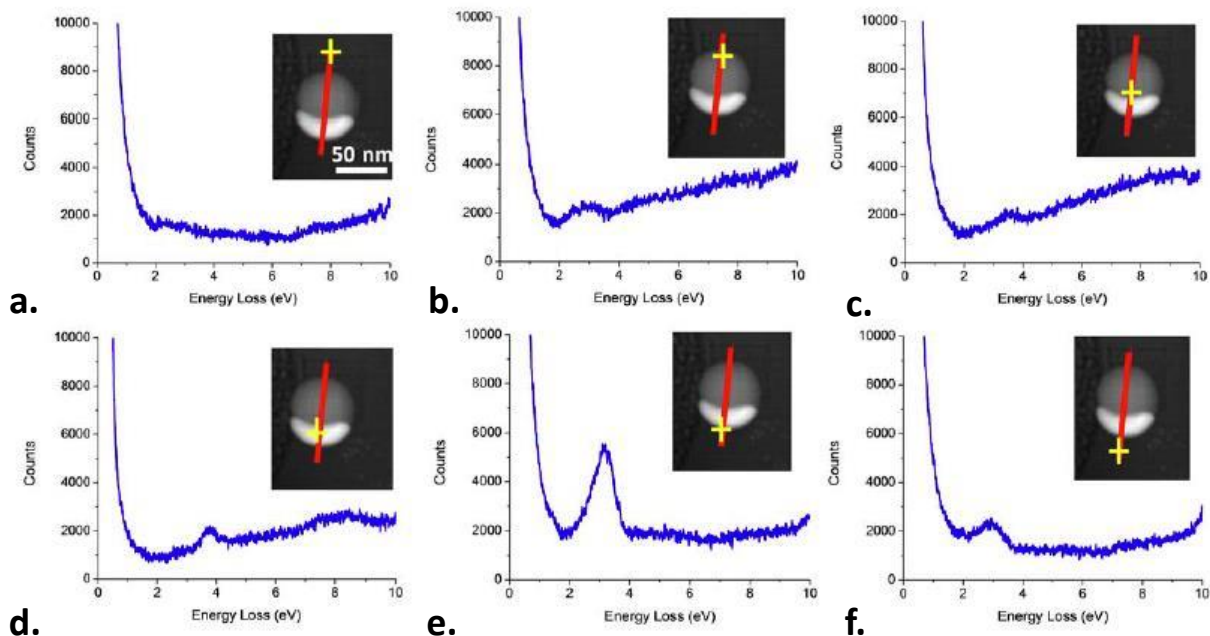
Figure 5-9. EELS line scan across a 70 nm Ag-Ge bi-lobed nanoparticle in the region from 0 to 10 eV energy-loss. The yellow cross marks the spot on the red line-scan where the energy-loss spectrum was collected. (a) Spectrum is over the SiO_2 matrix; (b) Spectrum is at the edge of the Ge component with excitation near 3 eV assigned to an electronic transition of Ge; (c) Spectrum is over the Ag-Ge interface; (d) Spectrum is over the bulk region of the Ag component picking up the bulk interband transition near 3.9 eV; (e) Spectrum is at the surface of the Ag component showing the localized surface plasmon at 3.4 eV; (f) Spectrum is over the SiO_2 matrix, but measuring, at 3.4 eV, the localized surface plasmon electric field that decays exponentially from the surface into the oxide.

5.2.2 Low-loss EELS

The energy-loss spectrum in the low-loss region is comprised of three regions of interest, which are, in order of their strength: zero-loss peak (ZLP), volume plasmons, and surface plasmons or electronic transitions. The ZLP is the dominant signal arising from electrons that have not been scattered and travel through the sample with essentially no energy loss. In samples of Ag-Ge nanoparticles, the intensity of the ZLP is ~80 times the intensity of the next largest peak, the Ge or SiO_2 volume plasmon peak. The ZLP has a FWHM of 0.2 eV, and its tail continues into the low-loss region dominating the signal below 1 eV. The volume plasmons of interest in this work are in the range of 15 to 23 eV. The Ge volume plasmon, in particular, is very strong and makes a definitive fingerprint for the Ge crystal. The region between 1 and 12 eV is the region of electronic transitions and surface plasmon transitions. Because the scattering cross section for energy-loss events decreases as the energy-loss increases, it is the low-loss region that produces the most signal per energy interval and consequently, facilitates both good energy resolution and high-contrast energy-filtered images.

In addition to surface plasmon losses, another surface effect called the "Begrenzungs effect" or "bordering effect" occurs because surface excitations screen the electric field causing a reduced scattering probability of the bulk plasmon.[88] This effect has been analyzed in detail for the geometry of a nanowire.[153] Hanrath et al.,[75] in their experimental study of EELS spectra from Ge nanowires, observed that interband and electronic transitions were more pronounced away from the center of the wire, in agreement with the model of Zabala.[153] Similarly strong interband transitions at the surface were observed in Si nanowires and are predicted for Si nanospheres.[154] The EELS data presented here, as well as the EFTEM images, also show more signal from interband transitions near the surface, and this is attributed to the Begrenzungs effect.

Other excitations, which were not considered in this work, include guided light and whispering gallery modes,[88] and Cerenkov and transition radiation.[152] Cerenkov radiation can be minimized by using thin samples.[88]

The EELS signal from the LSP is proportional to the electric field intensity $|E^2|$ arising from the surface plasmon.[88] The EELS signal measures the electromagnetic density of states or the probability of finding an optical excitation like a plasmon.[88] In practice, the inelastic scattering events are dispersed in energy by the post-sample magnetic prism and then collected by the CCD image sensor. In EFTEM mode, a slit is positioned in front of the entrance aperture to the CCD selects a narrow band of energies that form an image in the x-y plane of the CCD sensor. In EELS mode, the dispersed spectrum is collected as a line across the CCD that is synchronized in time with the scanning electron beam. Because the HAADF detector is located around the solid angle that enters the prism, a HAADF-STEM image can be collected just prior to collecting the EELS spectrum as shown in Figure 5-10. Figure 5-10(b) shows counts on the HAADF detector as a function of position on the line scan. The total number of counts available is 64K, so this image utilized an appropriate portion of the dynamic range.
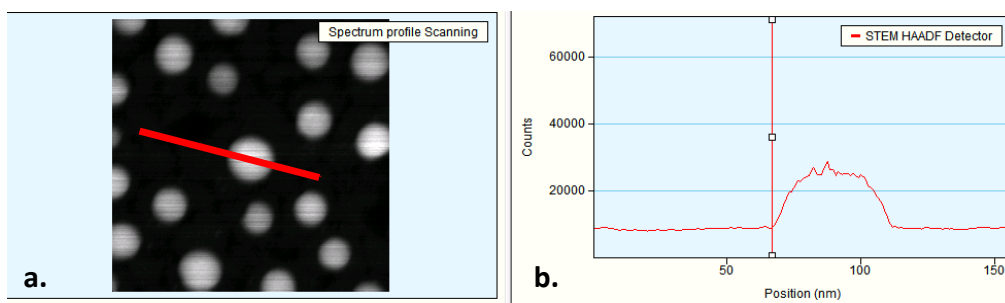
Figure 5-10. Capturing the HAADF-STEM image just prior to collecting the EELS spectrum. (a) HAADF-STEM image of Ag nanoparticles captured just before spectrum collection begins. The red line marks the path of the line scan across the particle; (b) Counts registered by the HAADF detector as a function of position across the line scan in (a).

5.2.3 EELS and EFTEM of plasmonic particles in the literature

A number of studies of EELS measurements of gold and silver nanoparticles have been published,[155, 156] and two chapters in a recent book provide a good review.[88] Both Bosman[157] and Nelayah[158] demonstrated mapping of Ag and Au nanoparticles, respectively. Eccles et al. measured the EELS spectra of Au and Au-Ag alloyed nanoparticles using the Richardsen-Lucy deconvolution routine to extract the 2.4 eV Au peak from the ZLP.[159] Guiton et al. correlated dark-field scattering of single particle Ag nano-rods with single particle EELS mapping.[50] They applied principal component analysis to the EELS data using a software program called Automated eXpert Spectral Image Analysis (AXSIA).[160] Most recently, Scholl et al. were able to measure size-dependent shifts in the LSPR from Ag nanoparticles 2-20 nm in diameter; they attributed these shifts to quantum size-effects.[161] EELS studies of Ge nanowires,[75, 152] and silicon nanocrystals[162] have also been reported. No EELS studies of Ge nanoparticles were found in the literature.

There are a few reports of EFTEM studies of nanostructures exhibiting surface plasmons;[163] the most notable is the 2009 study of gold nanorods, which used a microscope identical to the one used in this work.[164]

5.2.4 EELS and EFTEM data cube

There are two methods to access the energy-loss spectra as a function of position: an EELS spectrum image (SI) or a series of energy-filtered TEM images. These two techniques are complementary and both have been applied to elucidate optical and electronic transitions in the Ag-Ge bi-lobed nanoparticles. EELS SI and EFTEM can best be compared by examining the "data cube"[88] shown in Figure 5-11. An EELS SI collects an energy-loss spectrum for each grid square determined by the step size in the collection grid. A series of EFTEM images is collected by capturing an image from electrons selected by a slit, 0.5 eV to 1.0 eV in this work, for each step in energy. Theoretically, both techniques contain the same data; however, the energy and spatial resolution differ, as well as the potential for sample damage caused by electron dose. One practical concern is whether data analysis software is available to the user.
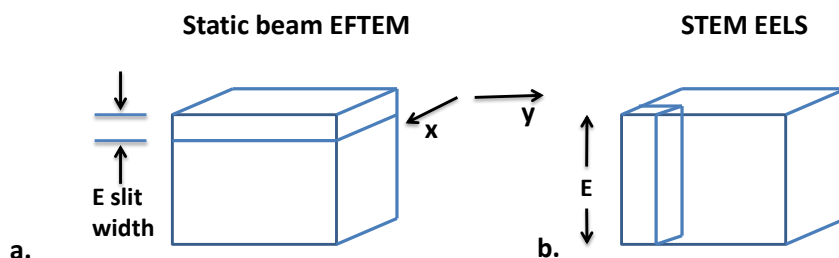
Figure 5-11. EFTEM and EELS data cube showing information as a function of spatial variables x and y, with the variable z representing the energy-loss. (a) EFTEM collects full image slices within a narrow

energy-loss range determined by the slit width; (b) EELS collects an energy-loss spectrum at each point determined by the spectrum image grid size.

5.2.5 Low-loss EELS parameters

In this work, data were accessed with the EELS technique so as to resolve overlapping transitions. The best energy resolution available in the Tecnai microscope is achieved by actuating the monochromator, which is located after the electron source and before the first condenser lens. The monochromator disperses the electrons in a direction perpendicular to the beam; a slit is placed across the line of electrons to select a narrow band of electron energies. The beam has an almost rectangular shape at this point, with its brightness significantly reduced. In STEM mode, the second condenser is not available, so all demagnification of the source to create the small probe must be done by the first condenser lens, C1. The C1 lens is strongly excited to spot size 11, but the spatial resolution has already been compromised, and the probe size will be, at best, 1 nm. A C2 aperture of 150 μm was used, resulting in a convergence half-angle of 12 mrad. Scans of approximately 40 eV in width with a dispersion of 0.02 eV per channel were collected.

It is preferable to collect the EELS scan with the ZLP included in the spectrum in order to adjust each spectrum to the true zero energy-loss. The beam instability has been measured to be +/- 0.05 eV. However, in order to collect a reasonable signal from weak electronic and optical transitions in the region 2 to 8 eV, a long collection time is necessary. The maximum number of counts per pixel allowed on the CCD is 64,000; this defines the dynamic range. If one adjusts the collection time so that the ZLP just reaches this value, the volume plasmon will register 800 counts at best (80 times weaker), and the surface plasmon and electronic transitions will register many fewer than 800 counts. Poisson statistics determines the signal-to-noise ratio, so for a S:N of 33:1, or +/- 3%, 1090 counts are required. For the Ag and Ag-Ge nanoparticle spectra, it was decided to collect the spectrum starting at 1 eV, collect for 3-10 seconds, and not to zero each spectrum collected. The spectra collected for the Au-Ge and Ge nanoparticles included the ZLP. In the future, it is hoped that the ZLP can be characterized well enough that a fit to the shoulder collected at 1 eV will provide a means to zero the spectra. The acquisition software made available by Gatan allows one to set up a line scan and collect the data as a series. Since no software was available for analysis at the National Center for Electron Microscopy (NCEM), the raw data were read into a Mathematica program written by a colleague[165] and plotted.

5.2.6 EFTEM parameters

In this work, EFTEM was used to identify the spatial regions of the nanoparticles giving rise to different energy transitions and also to provide a broader perspective by imaging several particles at one time. In EFTEM mode, the energy resolution is defined by the slit width which has a minimum size of 0.5 eV. There is no advantage to using the monochromator; in fact, its use would serve only to decrease the brightness of the source. Most EFTEM series were

collected with a 0.5 to 1.0 eV slit in 0.5 to 1.0 eV steps. To improve contrast in the images, an objective aperture of 60 μm was used. Watanabe has recently developed SMART EFTEM acquisition software that has three important qualities.[166] First, it collects images starting with the highest energy-loss, and then proceeds to the lower energy-loss images. The lower energy images have a stronger signal and can saturate the detector, producing errors for the next image. Second, the software collects a dark-current image before each image to correct for the thermal noise of the CCD image sensor. Third, it collects an image of the region of interest with zero-loss electrons before each energy-filtered image, and this image can be used to correct for sample drift in the analysis software.

Individual EFTEM images can be selected from the series using Digital Micrograph and ImageJ. Software is available at NCEM to do a principal component analysis (PCA) and/or multivariate statistical analysis (MSA). Using PCA can improve the signal-to-noise ratio in the image. However, the software works only if specimen drift is accurately tracked. Results using PCA for the Au-Ge nanoparticle will be presented in Section 5.3.

The specific considerations of EELS and EFTEM experiments in this work are summarized in Table 5-1.

Table 5-1. Comparison of EELS and EFTEM for experiments in this work.

	EELS	EFTEM
Mode	STEM	CTEM
Monochromator	Yes	No
Company specification ΔE w/monochromator	FWHM ~ 0.2 eV	Slit width ~ 3 eV
Company specification ΔE w/out monochromator	FWHM ~ 0.5 eV	Slit width ~ 0.5 eV
This work Energy resolution	FWHM ZLP is 0.2 eV with monochromator	Slit width is 0.5 to 1.0 eV
Number in series	20 to 200 steps in a line scan	28 to 56
Brightness of FEG	Reduced due to mono	Gun lens at 777
Spatial resolution	Probe size 1 nm with mono	Nanometer range[164]
Typical scan time	1 s	5 s
Scan range	Approximately -10 to 31 eV with dispersion of 0.02 eV per channel, 2048 channels	2 to 30 eV in 0.5 or 1.0 steps
Strength of C1 lens (spot size)	11	3
C2 aperture	150 μm	300 μm
Objective aperture	none	60 μm
Acquisition software	PEELS from Gatan	SMART EFTEM[166]
Analysis software	Tecnai Imaging Analysis (TIA) Automated eXpert Spectral Image Analysis (AXSIA), available for purchase[50]	Digital Micrograph Software available at NCEM for PCA and MSA[167]

5.2.7 Spatial resolution and delocalization

Spatial resolution in the EELS spectrum image or line scan is limited by delocalization effects. Delocalization means that, although the focused electron beam is imaged at a given spot on the nanoparticle, it may actually be probing a distance from that spot.

An instrumental form of delocalization affects the spot size of the electron probe. As described in Chapter 4, in STEM-HAADF mode, the spatial resolution is determined by the probe size; the resulting resolution is a convolution of the object function and the probe intensity profile. The Rutherford scattering cross section, approximately proportional to Z^2, has an object function that is strongly peaked at the atom sites and consequently its width (~0.1 A) does not

limit spatial resolution.[134] Instead, the spatial resolution is limited by the probe intensity profile which can be optimized by balancing the spherical aberration of the objective lens and the convergence half-angle, α. In monochromated STEM, the probe size specification increases from 1.3 A (without monochromator) to 1 nm (with monochromator) as a result of the inability to demagnify the source, as previously explained. The actual probe size depends on the operator's ability to stigmate and focus the monochromated beam, and for this work it may have been closer to several nm.

For inelastic scattering events, the object function can be highly delocalized.[71] This effect is significant in low-loss EELS, since the degree of delocalization increases as the energy loss decreases. Delocalization occurs because the electromagnetic field of the fast electron extends a distance beyond its impact. The distance is a function of the electron speed and the impact parameter, and can be in the nanometer range.[71] This is the "aloof" manner of excitation often referred to in plasmon excitation in low-loss EELS.

Finally, as observed experimentally, the excitations themselves, specifically the LSP excitations, can extend a distance from their origins.

5.2.8 EFTEM of Ag, Ge and Ag-Ge nanoparticles

The characterization of Ag-Ge particles was accomplished by the following process. TEM samples with single element Ag and Ge particles, of similar size and embedded in $Si_xGe_{(1-x)}O_2$, were fabricated and characterized. As described in Chapter 3, all of these samples were deposited as thin films on nitride membranes. Figure 5-12 shows a comparison of the three different samples (Ag, Ge, and Ag-Ge) for three different energy-loss ranges: 2-6 eV from electronic and LSP excitations, 16.0-16.5 eV from the bulk plasmon of Ge, and 22.0-22.5 eV from the bulk plasmon of SiO_2. The top row shows Ag nanoparticles in $Si_xGe_{(1-x)}O_2$. The LSPR at the surface of the particles is shown in the first image, and Ge in the matrix is revealed in the second and third images. The middle row shows large Ge nanoparticles embedded in $Si_xGe_{(1-x)}O_2$. The first image shows signal coming from the surface of the particle. This signal at 2-4 eV is assigned to electronic transitions that are more pronounced on the surface because of the Begrenzungs effect.[75, 154] The signal near 6 eV may be arising from a LSPR on the Ge surface. The second image clearly shows the Ge nanoparticles. The bottom row shows Ag-Ge nanoparticles embedded in $Si_xGe_{(1-x)}O_2$. In the first image, the LSPR of the Ag is clearly visible on the surface of the Ag lobes and there seems to be some brightness at the surface of the Ge lobes as well. The second image shows the bulk plasmon of Ge as a fingerprint for that crystal. The amount of Ge in the matrix appears either less or in smaller clusters in this sample compared with the previous two samples.

EFTEM	Surface plasmons and electronic transitions	Ge bulk plasmon	SiO$_2$ bulk plasmon
	3 to 3.5 eV	16 to 16.5 eV	22 to 22.5 eV
Ag nanoparticles in Si$_x$Ge$_{1-x}$O$_2$			
	2 to 6 eV	16 to 16.5 eV	22 to 22.5 eV
Ge nanoparticles in Si$_x$Ge$_{1-x}$O$_2$			
	3.5 to 4 eV	16 to 16.5 eV	22 to 22.5 eV
Ag-Ge nanoparticles in Si$_x$Ge$_{1-x}$O$_2$			
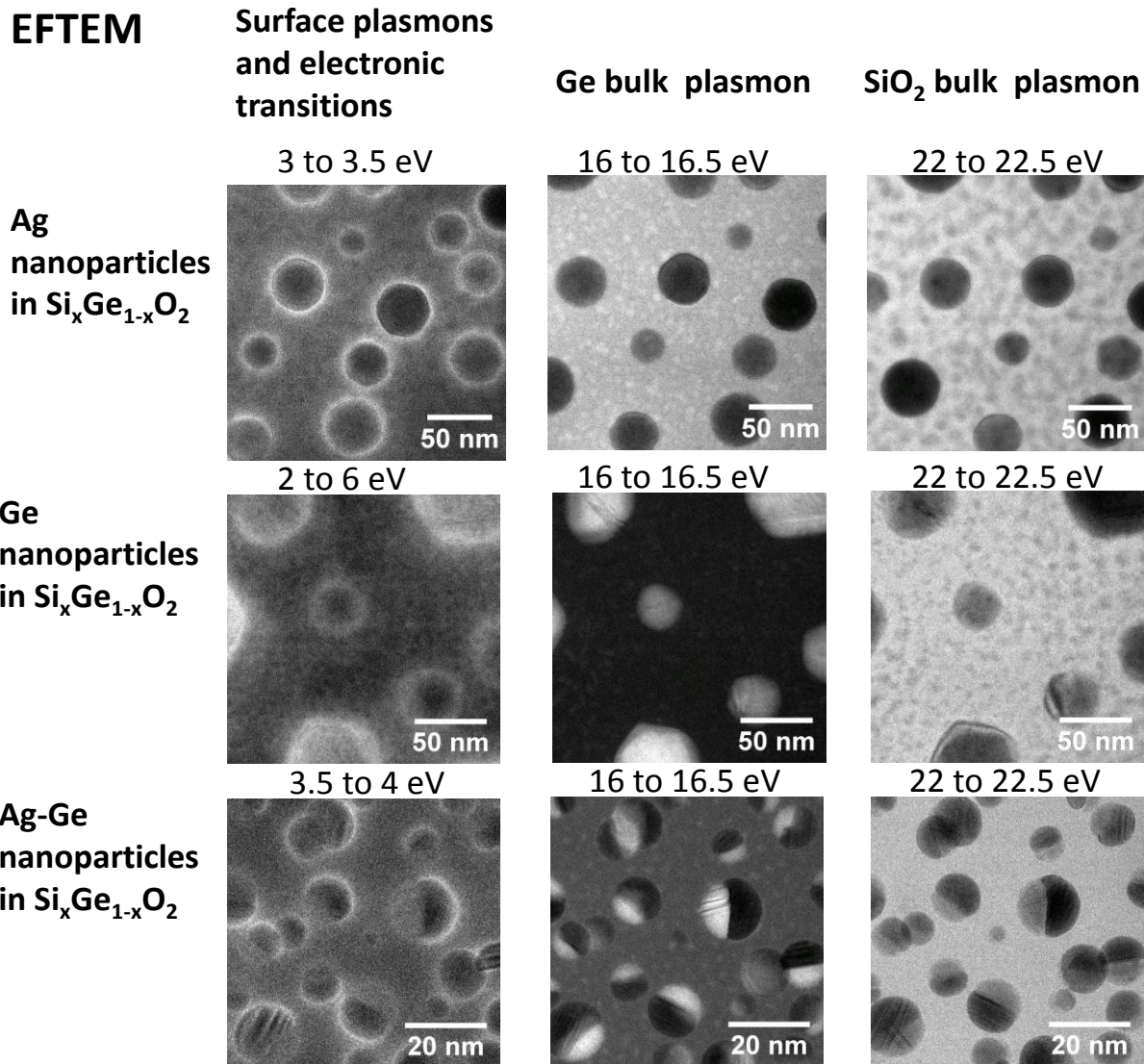
Figure 5-12. EFTEM images of Ag, Ge, and Ag-Ge nanoparticles embedded in Si$_x$Ge$_{1-x}$O$_2$ for three different energy-loss bands: 2-6 eV electronic and optical excitations; 16.0-16.5 eV bulk plasmon of Ge; and 22.0-22.5 eV bulk plasmon of SiO$_2$.

5.2.9 Low-loss EELS results

5.2.9.1 Ag nanoparticles – low-loss EELS results

The EELS spectra from an Ag nanoparticle, 30 nm in diameter, embedded in Si$_x$Ge$_{(1-x)}$O$_2$, are included in Figure 5-13 and Figure 5-14 and the transitions are outlined in Table 5-2. The most notable peak is at 3.4 eV, arising from the LSP at the surface of the Ag nanoparticle and extending exponentially into the silica matrix. The decay of the intensity at 3.4 eV is plotted in Figure 5-14(b) showing a decay length of 10 nm at half intensity. The interband transition of 3.9

eV is resolved in the blue spectrum shown in Figure 5-14 when the beam is directly over the Ag nanoparticle.
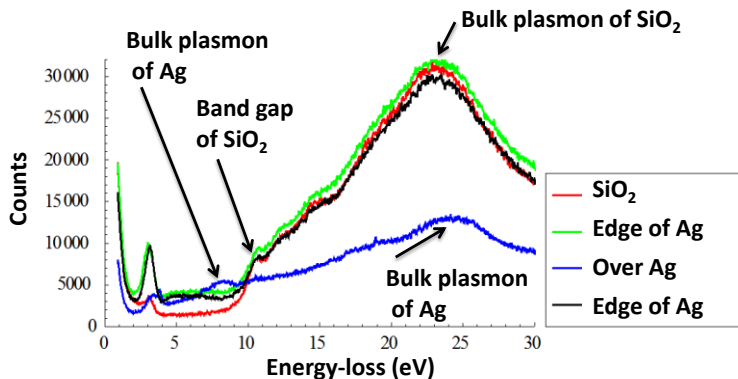
Figure 5-13. EELS spectra from an embedded Ag nanoparticle shown in the top row of Figure 5-12. When the beam is over the SiO_2 or at the edge of the SiO_2, a large signal from the SiO_2 bulk plasmon (~23 eV) and from the SiO_2 band gap (onset ~ 9 eV) is observed. When the beam is in the center of the Ag nanoparticle, the SiO_2 bulk plasmon intensity is reduced, but the bulk plasmon of Ag at ~8 eV is observed.
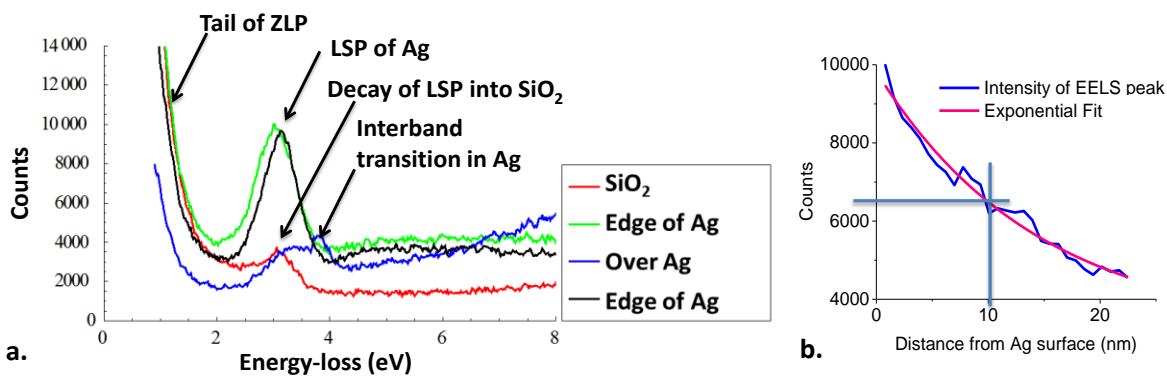
Figure 5-14. (a) Expanded x-axis showing low-loss detail from Figure 5-13. The LSP is observed at the edge of the Ag nanoparticle (green and black) and as it decays in to the oxide (red). When the beam is directly over the center of the Ag particle, the interband transition at 3.9 eV is resolved. (b) Decay of the LSP at 3.4 eV from the surface of the Ag particle into the silica matrix. The y-axis data is the peak maximum near 3.4 eV measured in counts. The decay length at half intensity is ~10 nm.

Table 5-2. Ag only nanoparticle – Electron energy-loss mechanisms measured experimentally in this work from the EELS and EFTEM data.

Label	Description	This work measured Energy-loss (eV)	References
LSP of Ag	At edge of particle and decaying exponentially into SiO_2	3.4 eV	
4d to 5s interband transition	Over center of particle	3.9 eV	3.9[60]
Bulk Plasmon of Ag	Over center of particle	8	7.2[74]
Band to band transition in SiO_2	Edge of particle	10.2	E1 = 8.6 eV; E2 = 9.4 eV[168]
Bulk Plasmon of SiO_2	Over SiO_2 matrix	22.3	22.4[71] , 22.9[168]
Bulk Plasmon of SiN	SiN membrane only	21.2	23.7[71]
Bulk Plasmon of Ag	Over center of particle	25	25[71], 24.7[74]

5.2.9.2 Ge nanoparticles – low-loss EELS results

The EELS spectra from a Ge nanoparticle, 50 nm in diameter, embedded in $Si_xGe_{(1-x)}O_2$, are included in Figure 5-15 and Figure 5-16, and the transitions are outlined in Table 5-3. The most interesting excitations are the sharp transition at 2.1 eV and the broad transitions 6-8 eV, both of which appear to arise from the surface of the Ge nanoparticle. The transition at 2.1 eV is assigned to the E1 direct transition midway between the Γ and L point. It is more pronounced on the surface of the particle because of the Begrenzungs effect as observed in other experiments.[75, 154] The energy-loss at 6-8 eV is assigned to the localized surface plasmon of the Ge nanoparticle as calculated for a Ge nanoparticle embedded in SiO_2. This LSP has been observed with UV absorption as well.[62] As shown in Table 5-3, there are other direct electronic transitions in Ge at 3.2 eV, 4.5 eV, and 5.6 eV.[169]
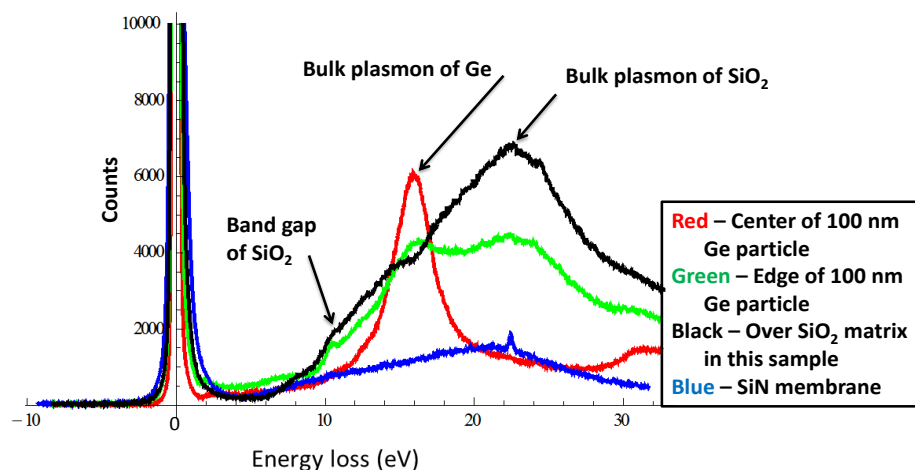
Figure 5-15. EELS spectra of an embedded Ge nanoparticle. When the beam is over the SiO_2 or at the edge of the SiO_2, a large signal from the SiO_2 bulk plasmon (~23 eV) and from the SiO_2 band gap (onset ~ 9 eV) is observed. When the beam is in the center of the Ge nanoparticle, the bulk plasmon of Ge at ~16 eV is observed.

Figure 5-16. (a) Expanded x-axis showing low-loss detail from Figure 5-15 of the 100 nm Ge particle. At the edge of the Ge nanoparticle, a strong surface component at 2.1 eV is observed and is assigned to the E1 electronic transition. There is a lineshape at 6-8 eV that may be evidence for the localized surface plasmon of Ge predicted in Chapter 2 at 6 eV. The peak at 10.5 is from the onset of the silica bandgap at 9 eV. (b) EFTEM image at 6.0-6.5 eV of Ge nanoparticles showing the surface contrast which, may be further evidence for the LSP of Ge predicted at 6 eV.

132

Table 5-3. Ge only nanoparticle - Electron energy-loss mechanisms measured experimentally in this work from the EELS and EFTEM data.

Label	Description	This work measured Energy-loss (eV)	References
Eg	VB max at Γ to CB min at L - Indirect		0.66[76]
E0	Direct at k=0		0.898[76]
E1 electronic transition of Ge	EELS edge of particle	2.1	2.222[76]
E1	Direct midway between Γ and L		2.222[76]
E0'	Direct at k=0		3.206[76]
E2	Direct close to X		4.49[76]
E1'	Direct at L		5.65[76]
Localized surface plasmon resonance of Ge in SiO_2 matrix	EELS edge of particle	6-7	6[62], Measured using UV-Vis Absorption
Localized surface plasmon resonance of Ge in SiO_2 matrix	Dipolar modes at interface of Ge particle ~50nm in diameter and SiO2.		6 eV, KCB: Calculated using bulk dielectric functions of SiO_2 and Ge
Band to band transition in SiO_2	Edge of particle	10.2	E1 = 8.6 eV; E2 = 9.4 eV[168]
Bulk Plasmon of Ge	EELS center of particle	15.92	15.8[71]
Bulk Plasmon of SiO_2	Over SiO_2 matrix	22.3	22.4[71]
Bulk Plasmon of SiN	SiN membrane only	21.2	23.7[71]

5.2.9.3 Ag-Ge nanoparticles – low-loss EELS results

The EELS spectra from a Ag-Ge nanoparticle, 30 nm in diameter, embedded in $Si_xGe_{(1-x)}O_2$ are included in Figure 5-17 and Figure 5-18, and the transitions are outlined in Table 5-2 and Table 5-3. The most interesting feature in these data is the lineshape at 3.4 eV, at the surface of, and directly over, the Ge component. This lineshape is absent in the Ge only nanoparticles and so presumably is not arising from the Ge component. It is, however, predicted in the electric field intensity simulations at 460 nm, where an electric field is shown at the surface of the Ge component. It would be interesting to have simulations at 365 nm (3.4 eV) to see whether the Ge surface electric field is stronger. The electron beam, although over the Ge component is likely exciting the LSP of the Ag in the "aloof" manner; the electric field of the fast electron is able to

extend some distance from the electron and, in this delocalized manner, excite the LSP from the Ag component.
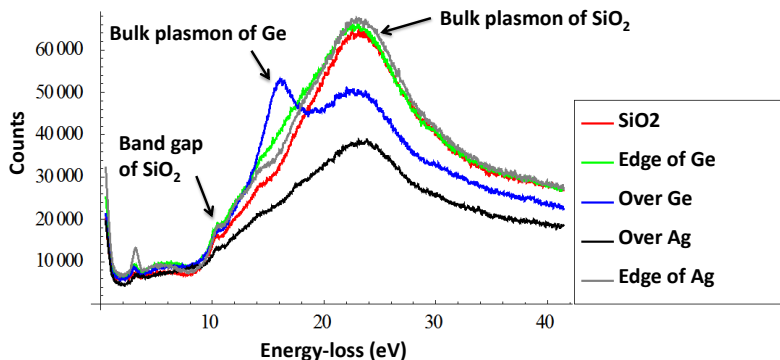
Figure 5-17. EELS spectra of an embedded Ag-Ge nanoparticle. When the beam is over the SiO_2, or at the edge of the SiO_2, a large signal from the SiO_2 bulk plasmon (~23 eV) and from the SiO_2 band gap (onset ~ 9 eV) is observed. When the beam is in the center of the Ge nanoparticle (blue), the bulk plasmon of Ge at ~16 eV is observed.
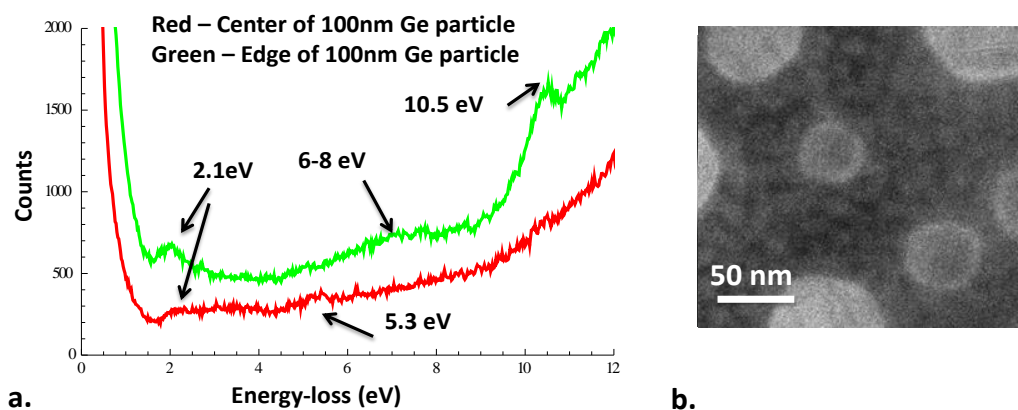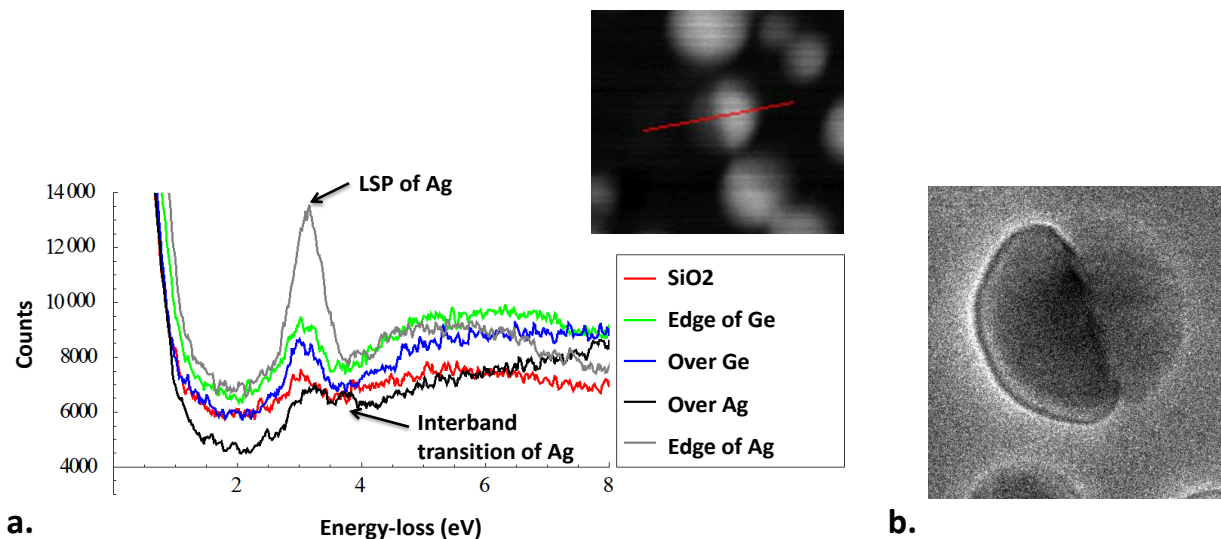

Figure 5-18. (a) Expanded x-axis showing low-loss detail from Figure 5-13. The LSP is observed at the edge of the Ag nanoparticle (grey), and as it decays into the oxide (red). When the beam is directly over the center of the Ag particle (black), the interband transition at 3.9 eV is resolved and the LSP is also observed. When the beam is over the Ge particle (blue), and at the edge of the Ge particle (green), the lineshape near 3.4 eV is observed; this observation has not been explained definitively. (b) EFTEM image with 1 eV slit centered at 3.5 eV shows the surface of the Ge component with a bright region.

5.3 Au-Ge nanoparticles

5.3.1 EFTEM and EELS results

The LSPR for Au nanoparticles embedded in glass is centered near 540 nm (2.3 eV), accounting for the ruby red color in stained glass containing gold nanoparticles. A series of EFTEM images of a Au-Ge nanoparticle, 52 nm in diameter, is shown in Figure 5-19. The darker region is Au and the lighter region is Ge. The bright rim is clearly visible at the surface of the Au component in the image formed from electrons that have undergone transitions of 2.0-2.5 eV. This rim could be either the LSP from the Au or an interband transition in the Au. A bright rim at the edge of the Au component is also visible in the images from 4 to 8.5 eV, although it does not extend as far into the SiO_2 matrix as the image in 2.0-2.5 eV. The bright rim from 4 to 8.5 eV is believed to arise from interband transitions[170, 171] that are more pronounced on the surface because of the Begrenzungs effect.[75, 154]

| 2.0 to 2.5 eV | 4.0 to 4.5 eV | 6.0 to 6.5 eV | 8.0 to 8.5 eV |

| 10.0 to 10.5 eV | 13.0 to 13.5 eV | 16.0 to 16.5 eV | 23.0 to 23.5 eV |
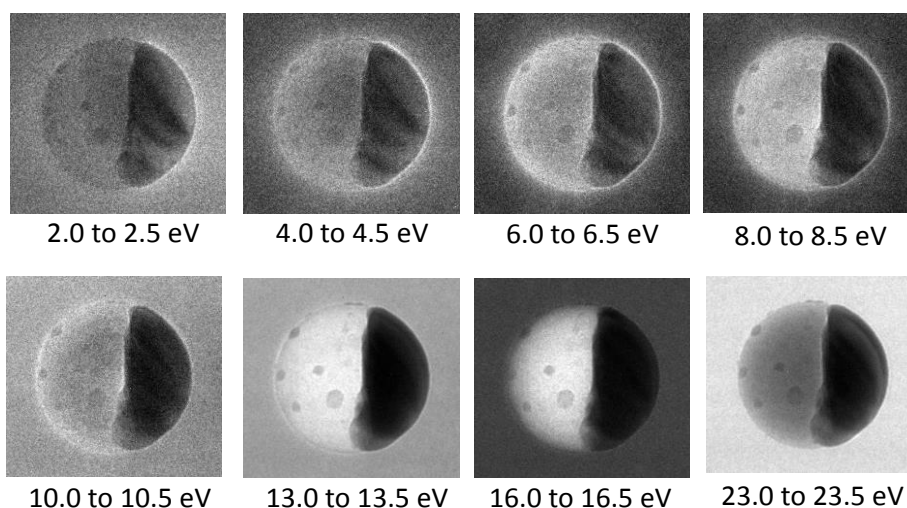
Figure 5-19. EFTEM images of 52 nm Au-Ge particle. Ag component is the darker of the two hemispheres. Either an interband transition or the LSP from the Au can be seen extending into the silica at 2-2.5 eV. There are also bright regions on the surface of the Au component from 4 to 8.5 eV. These images are reconstructed after using PCA to remove components not considered statistically significant.

The EELS spectrum in Figure 5-20 shows relatively flat energy-loss over the region from 2 to 8 eV. The LSP, which should be close to 2.3 eV, is not distinguished from the interband transitions that may be occurring in the region.[170, 171] Table 5-4 outlines the Au transitions; the Ge transitions are outlined in Table 5-3.
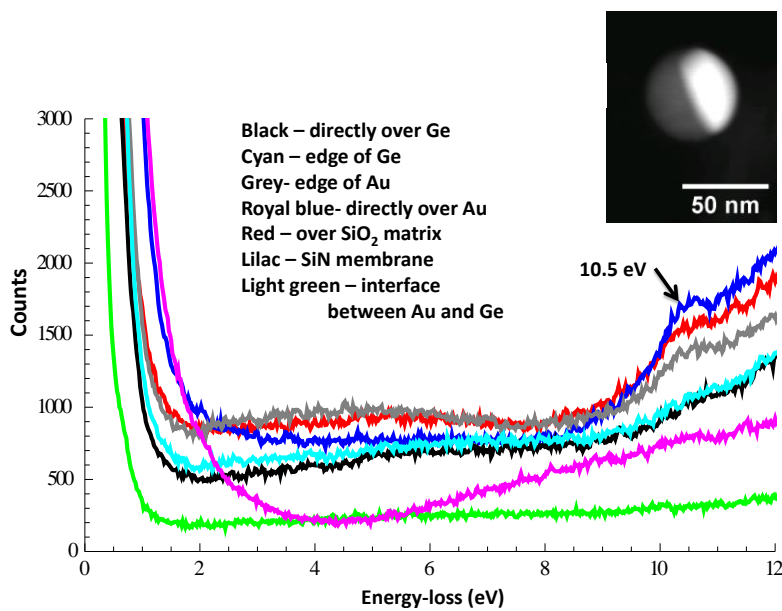
Figure 5-20. EELS spectra of an embedded 52 nm Au-Ge nanoparticle. The lilac to magenta curve is for the SiN membrane alone. There is smooth energy loss in the region 2-8 eV most likely due to interband transitions in Au and Ge. The SiO$_2$ bandgap (onset ~ 9 eV) is observed as a peak at 10.5 eV.

Table 5-4. Au-Ge nanoparticle low-loss excitations.

Label	Description	This work measured Energy-loss (eV)	References
LSP of Au in SiO$_2$	Dipole mode assuming spherical particle	2-2.5 eV	2.3 eV KCB simulated for 20 nm particle using Nanohub
Au interband transitions	Observed as a bright rim on the surface of the Au component in EFTEM images, but not in the EELS spectra	2-8 eV	2-8 eV[171]
Au interband transitions			2.63 eV and 3.76 eV[170]
Bulk plasmon of Au			8.8 eV[170]
Bulk Plasmon of Au			24.8 eV[71]

5.3.2 Principal component analysis

The contrast in the TEM images of Au-Ge nanoparticles at zero-loss was sufficient to allow for drift correction using the analysis software developed by Watanabe.[167] Principal component analysis converts a set of data with correlated factors into a set of components with uncorrelated factors via an orthoganol transformation. It finds the minimum number of

orthoganol components that can describe a data set, thereby reducing the dimensionality of a dataset. Additionally, once the most important factors have been defined, the image can be reconstructed with these factors, thereby eliminating the noise originating from the other components.

A scree plot is a construct used to display results from PCA; the y-axis represents the significance or logarithm of the strength and the x-axis lists the component number in order of significance. Figure 5-21 shows a scree plot from the transformed components. The first five components appear to have more significance than the remainder. The first component corresponds to the average of the data and is shown in a score plot in Figure 5-22(b), showing the SiO_2 bulk plasmon, Ge bulk plasmon, interband transitions, and the tail of the zero-loss peak. The image of the Au-Ge nanoparticle is reconstructed from this component only and is shown in Figure 5-22(a).
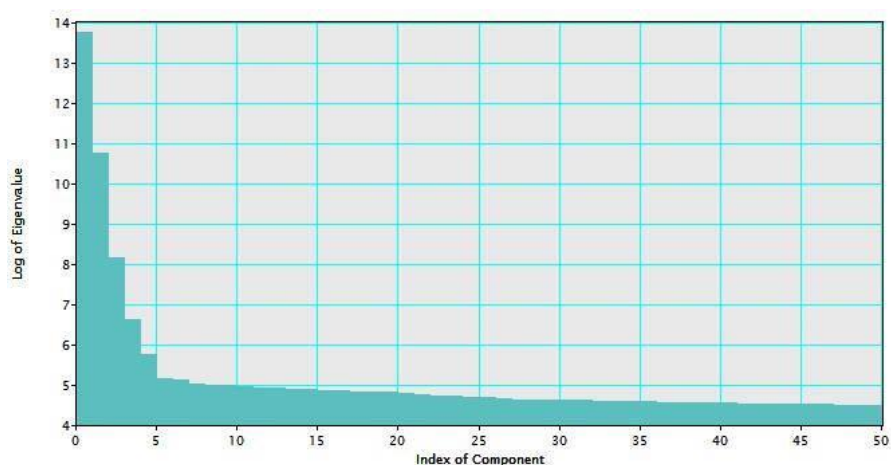
Figure 5-21. Scree plot of orthoganol components from the principal component analysis of a Au-Ge nanoparticle. The first 5 components were considered significant and 6 and 7 were also kept. The components from 8 to 50 are considered noise and were removed from the reconstructed image.

The score plot of the second-most significant component, showing differences from the preceding component, is shown in Figure 5-22(d). Signals that are negative (below the x-axis) are absent in the second component, and those that are positive are increased over the first component. The signal from the second component is clearly arising from the Ge hemisphere as evidenced by the image in Figure 5-22(c) and the bulk plasmon of Ge at 16 eV. A peak centered at 8 eV is assigned to the LSP of Ge in the SiO_2 matrix (slightly higher than the 6 eV calculated LSP for Ge). The images in Figure 5-19 were reconstructed after removing signal from all but the first seven components, thereby improving the signal-to-noise ratio of the images.
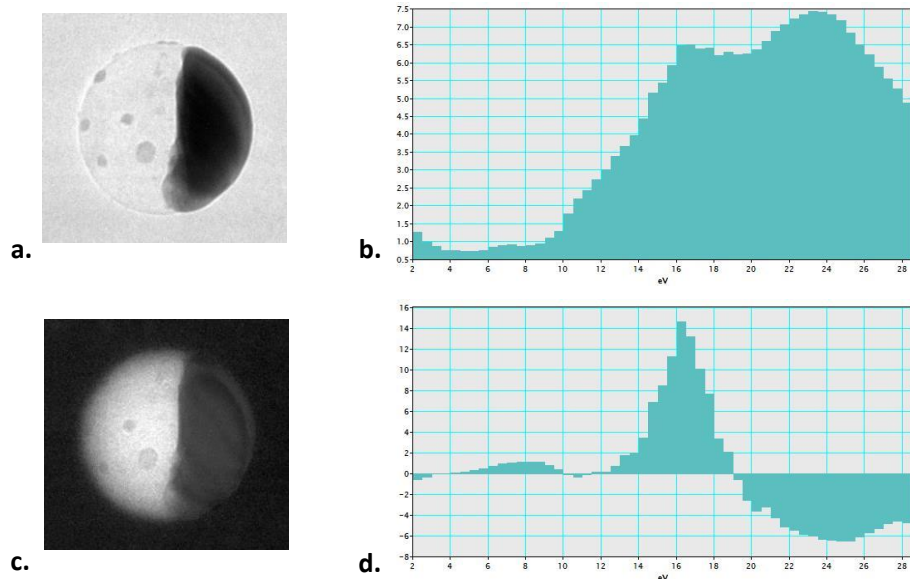
Figure 5-22. The first two principal components and the Au-Ge particle reconstructed from them. a) Loading from data belonging to the first principal component, which is the average; b) Score plot for the first principle component; c) Loading from the second principal component; d) Score plot for the second principal component.

5.4 Plasmonic switch actuated by pulsed laser melting

A plasmonic switch that utilizes the segregating nature of Ag and Ge is presented. The goal is to turn the plasmonic properties of the particles on and off by cycling between a segregated phase and a mixed phase. Such a phase transition has been proposed and successfully cycled[28] for Ge-Au and Ge-Sn bi-lobed nanoparticles.[27, 28] In the case of the Ge-Au and Ge-Sn systems, the application was memory storage. In the case of the Ag-Ge bi-lobed nanoparticle, the objective is to switch the plasmonic properties off with a laser pulse that does not heat the matrix allowing for rapid cooling of the particle into a metastable mixed Ag-Ge phase that is not plasmonic. The plasmonic properties are switched on by recovering the LSPR with RTA to form the segregated Ag-Ge bi-lobed nanoparticle. This process has been successfully demonstrated. This plasmonic switch would also work using nanoparticles from the Au-Ge, Ag-Si and Au-Si systems.

The sample of bi-lobed nanoparticles was deposited in a thin film on both TEM-ready SiN membranes and on transparent fused silica substrates according to the schematic in Figure 5-23(a). The sample was annealed using RTA at 800˚C for 30 s forming the Ag-Ge bi-lobed nanoparticles shown in Figure 5-23(b). The sample was then exposed to a 20-ns pulse from a KrF laser at 248 nm with a fluence of 0.25 J/cm^2. The laser pulse melted the particles and they quickly solidified into a metastable phase that is not segregated, but rather comprised of Ag and Ge atoms that are randomly mixed. Figure 5-23(c) shows a HAADF-STEM image of large (avg.

diameter = 69 nm) Ag-Ge nanoparticles after PLM of slightly higher fluence. Work is in progress to perform PLM on the SiN membrane and retrieve a TEM sample. Rapid thermal annealing at 800˚C for 40 s completed the cycle. This process can be summarized in four steps: 1. Deposit constituents; 2. Form bi-lobed nanoparticle and "turn on" LSPR; 3. PLM to create mixed phase and "turn off" LSPR; 4. RTA to recover bi-lobed nanoparticles and "turn on" LSPR. It is conceivable that RTA could be replaced by a laser pulse with the appropriate fluence.
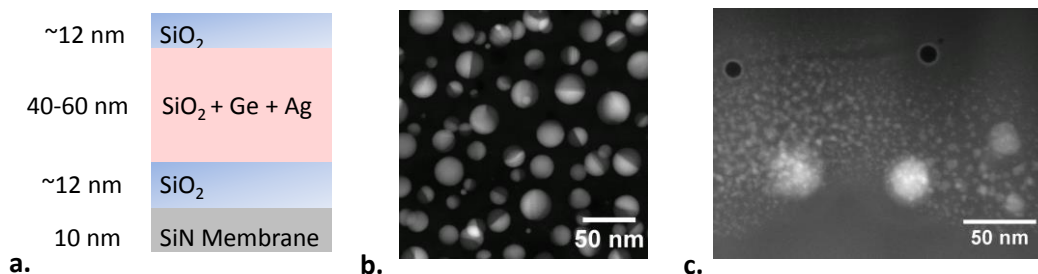
Figure 5-23. (a) Deposition of layers on SiN membrane for plasmonic switch; (b) HAADF-STEM image of Ag-Ge bi-lobed nanoparticles as deposited in a), after 30 s RTA at 800˚C; (c) HAADF-STEM image of large (avg. diameter = 69 nm) Ag-Ge nanoparticles after PLM showing uniform contrast across the particle and debris field.

The results of the four-step process are easily visible with the eye as shown in the optical photos in Figure 5-24. On the left is the triangular piece of fused silica with a golden color caused by the Ag LSPR near 3.4 eV. Blue light is absorbed and yellow light is transmitted. The spot in the center, an ellipse approximately 6 mm x 8 mm, was exposed to the laser pulse and has become more transparent because the Ag-Ge nanoparticles are no longer resonating. The photo on the right shows the sample after RTA for 40s at 800˚C to resegregate the Ag and Ge components. The laser spot has recovered some of its golden color corresponding to the reforming of the Ag-Ge bi-lobed nanoparticles.
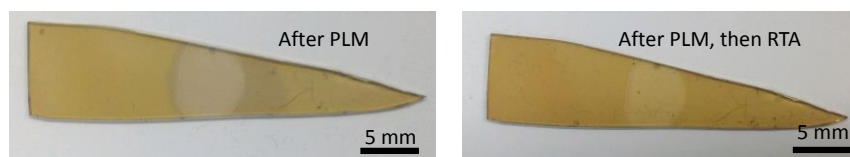
Figure 5-24. Optical photo of deposited SiO$_2$ film containing Ag-Ge bi-lobed particles (shown in Figure 5-23a and b).   a) after PLM in a spot 6 mm in diameter showing the reduced extinction of the light; b) after PLM followed by RTA to recrystallize the bi-lobed structure and recover the extinction. The spot that was exposed to the PLM has recovered some of its golden color.

This series of events can be quantified in the measured LSPR. Figure 5-25 shows the measured extinction from the sample shown in Figure 5-24 and Figure 5-23(a) and (b). Steps 1

through 4 are labeled on the plots. The formation of the LSPR after the first RTA in 2., followed by absence of the LSPR in 3., followed by recovery of the LSPR in 4. The line in green was collected with a different aperture which is the reason it is offset; the important aspect is that there is no surface plasmon resonance evident.
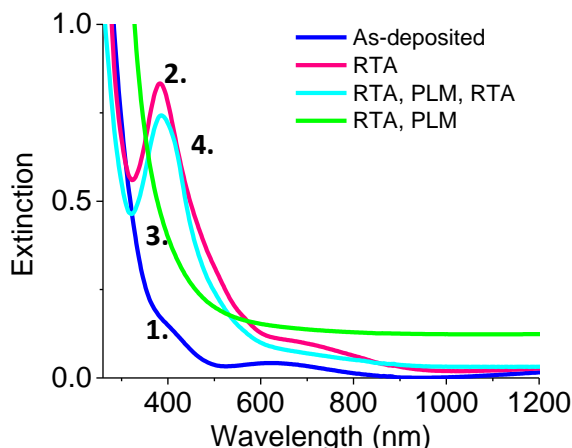
Figure 5-25. Extinction of LSPR from sample shown in Figure 5-23(a) and (b). 1. As deposited with no bi-lobed particles; 2. After RTA for 30 s at 800°C to form bi-lobed Ag-Ge particles and establish LSPR; 3. After PLM at 0.25 J/cm^2, mixed phase does not have a localized surface plasmon resonance; 4. After RTA for 40 s at 800°C to recover the bi-lobed configuration and the plasmonic resonance.

Future experiments are planned to probe the laser fluence process window. The results above are for a laser fluence of 0.25 J/cm^2, although a laser fluence of 0.3 J/cm^2 was also successful. A laser fluence of 0.07 J/cm^2 was insufficient to initiate transparency in the film. Unfortunately, the laser pulse at 0.25 J/cm^2 ruptured the membranes as described in Chapter 4. It is known that the degree of rupturing increases with increased laser fluence. A laser fluence of between 0.07 J/cm^2 and 2.5 J/cm^2 will be tested to find a fluence that will switch the properties while still allowing for a TEM sample that directly confirms the nanostructure of the mixed-phase particle after PLM.

5.5 Raman spectroscopy results

The hypothesis that an electric field can be supported at the Ag-Ge interface can be tested by Raman spectroscopy. An enhanced electric field for radiation 800-1000 nm is predicted by simulation (Figure 5-7c) and observed in extinction measurements of the LSPR (Figure 5-4 and Figure 5-6). Preliminary Raman scattering experiments were performed with a laser at 633 nm and the resulting spectrum is shown in Figure 5-26. This sample has nanoparticles with an average diameter of 69 nm; the LSPR spectrum is shown in Figure 5-4(a) and HAADF-STEM image of the particles is shown in Figure 5-2(b). The peak at 528 cm^{-1} is from the Si substrate

and the peak near 300 cm^{-1} is from the Ge nanoparticles. Although a quantitative analysis is necessary, the strong signal from the Ge as compared with the Si is quite promising. The amount of Ge present in this sample is estimated to be 2.5×10^{17} atoms-cm^{-2} from RBS results. A similar Raman scan of a sample containing 4×10^{16} atoms-cm^{-2} did not show a Ge peak above the second-order Si peak near 300 cm^{-1}. Future experiments are planned with a laser at 785 nm, as described in Chapter 6.
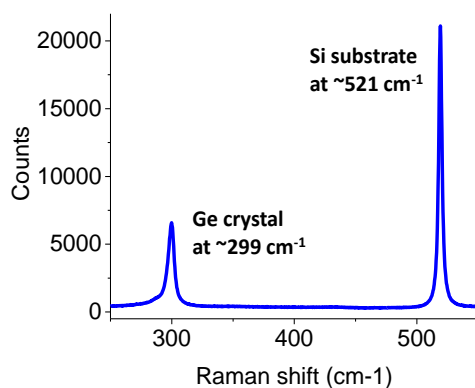
Figure 5-26. Raman scattering from Ag-Ge bi-lobed nanoparticles embedded in $Si_xGe_{(1-x)}O_2$ showing Si substrate peak at 521 ~cm^{-1} and Ge peak at ~299 cm^{-1}. The strength of the Ge as compared with the Si substrate peak indicates that some of the Raman signal from the Ge may be surface-enhanced.

5.6 Summary of optical properties

The optical properties of the Ag-Ge bi-lobed nanoparticles were investigated by making ensemble measurements of the LSPR and single-particle measurements of optical transitions, and comparing these experimental observations to numerical simulations. Remarkable agreement between ensemble and single-particle measurements was found as demonstrated by Figure 5-27, which shows a similar lineshape for the Ag/SiO$_2$ LSPR in ensemble and single-particle measurements.
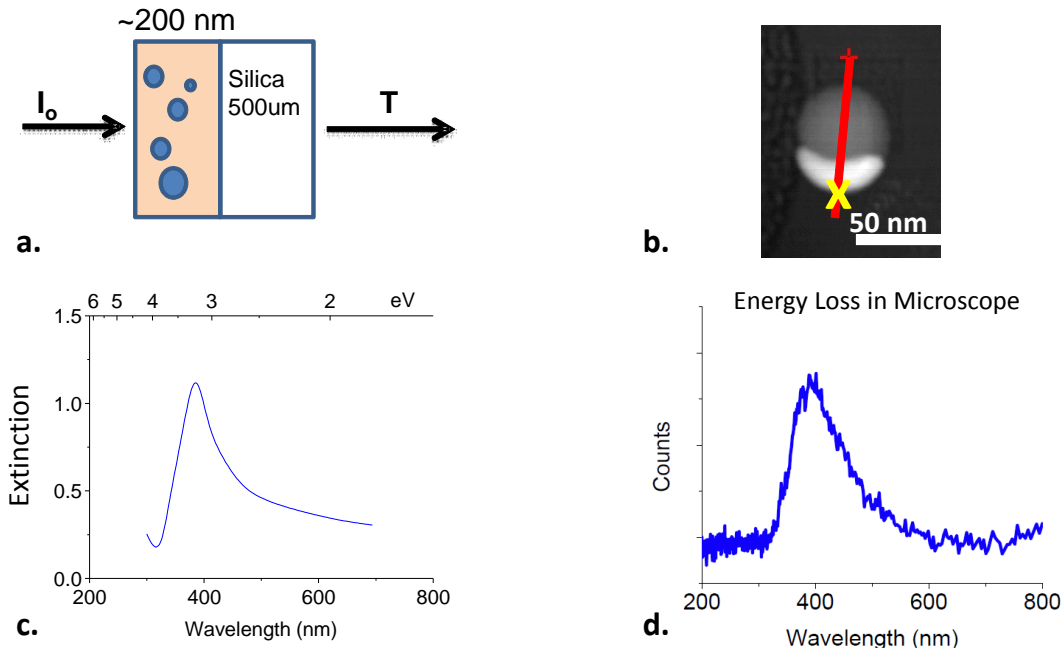
Figure 5-27. (a) Schematic of ensemble measurement of LSPR; (b) EELS line scan across a Ag-Ge bi-lobed nanoparticle, yellow cross at the Ag/SiO$_2$ interface shows location of EELS spectrum in (d); (c) Extinction of LSPR of Ag nanoparticles in SiO$_2$; (d) Low-loss EELS spectrum showing LSPR from Ag/SiO$_2$ interface.

Most interesting findings regarding optical properties:

- LSPR from Ag/SiO$_2$ measured with spectrophotometry and EELS at 3.4 eV.

- LSPR from Ag/Ge measured at 800-1000 nm (1.2 – 1.6 eV) with spectrophotometry and simulated with FDTD.

- E1 interband transition of Ge at 2.1 eV more pronounced excitation near the surface measured with EELS and observed with EFTEM.

- LSPR of Ge/SiO$_2$ at 6 - 8 eV measured with EELS and observed with EFTEM.

- Plasmonic switch demonstrated to "turn on" with RTA at 800˚C for 40 s and "turn off" with PLM of 0.25 J/cm^2 at 248 nm.

- Signal enhancement from LSP at Ag-Ge interface possible in the Ge Raman signal.

Chapter 6 Conclusion and Future Work

6.1 Conclusion

The synthesis and characterization of a metal-semiconductor plasmonic particle has been described in this thesis. Ag-Ge bi-lobed nanoparticles form after annealing from a supersaturation of Ag and Ge in a SiO_2 matrix. The equilibrium bi-lobed structure results from the strongly segregating nature of the Ag-Ge alloy constrained within a matrix with low solid solubility for the constituents. It was found that rapid thermal annealing provided sufficient thermal load to form the particles, and that the particle size could be controlled by the thickness of the layer containing the precursors. Most of the particles formed a structure with {111} planes of Ag and Ge parallel to each other; it is believed that this interface energy is relatively low. It was found that the characteristic localized surface plasmon resonance for the particle is affected by the metal-semiconductor interface. Using electron energy-loss spectroscopy and energy-filtered TEM, Ge interband transitions were observed on the surface of the Ge nanoparticles. Raman experiments to probe the Ge response to the Ag LSPR have been initiated. Most significantly, a plasmonic switch was demonstrated that exhibits an LSPR in the "on" mode (actuated by rapid thermal annealing) and a reduced or absent LSPR in the "off" mode (actuated by pulsed laser melting).

While this dissertation represents completed work, it also poses new questions for future research. In addition to the specific experiments described below, examination of other materials systems would be most interesting. The most interesting alloy would be the Ag-Si system. The Ag component would provide the strong plasmonic response measured in this work, but the Si, with its larger bandgap, would provide less damping of the LSP at the interface. Synthesis of Ag-Si nanoparticles was attempted in this work, but a supersaturation of Si was not achieved and the Si atoms remained bound in the SiO_2 matrix. Some effort will be required to determine the optimum deposition conditions. The interaction of Si with Ag is technologically relevant for photovoltaic applications.

In this work, large (~50 nm in diameter) Au-Ge nanoparticles were fabricated and characterized using low-loss EELS in the electron microscope. Like the Ag-Ge nanoparticles, the Au-Ge nanoparticles are plasmonic with an LSPR predicted near 2.3 eV. The plasmon resonance of a Au component is weaker than that of a Ag component because Au has a larger imaginary part of the dielectric constant at the resonance energy. However, the lineshape of the Au-Ge nanoparticle can still be measured with spectrophotometry and single-particle EELS measurements.

6.2 Raman scattering

Future Raman spectroscopy experiments to probe scattering from Ge components of Ag-Ge bi-lobed particles are outlined. Micro-Raman spectrometers, equipped with excitation lasers at 514 nm, 538 nm, 633 nm, and 785 nm, are available at LBNL facilities. The same samples that were prepared on the TEM windows could be measured with the micro-Raman arrangement by using a microscope to focus the laser to a spot-size small enough to fit in the TEM window. The same films deposited on Si substrates could be used to calibrate the peak intensity to the Si substrate peak. The experiments would measure the strength of the Raman signal near 299 cm^{-1} as a function of excitation wavelength in samples containing bi-lobed nanoparticles and samples containing single component Ge nanoparticles. Raman signal that is enhanced by the Ag LSP would have an intensity profile as a function of excitation wavelength that would track the LSPR spectrum. The energy of the peak might shift if the Ge at the Ag-Ge interface experiences lattice strain.

Three factors not associated with the LSP contribute to the strength of the Raman signal. First, the total number of Ge atoms in a crystalline configuration has a linear dependence on the area under the Raman peak. The amount of Ge can be determined by both RBS and TEM images. Second, the Raman emission intensity depends on the laser frequency to the fourth power. For a given volume of crystalline Ge, the Raman intensity will decrease as the laser wavelength increases. Third, the absorption coefficient of Ge varies significantly in this wavelength range, as described in Chapter 2. For example, at 514 nm the absorption length at half-intensity is ~18 nm. Because both incident and scattered light are absorbed, the penetration depth is half the absorption length. Consequently, at the 514 nm wavelength, as long as the total amount of Ge does not exceed 9 nm, (~4x10^{16} atoms/cm^2), the incident light will penetrate the film thickness and the scattered light will arrive at the detector. When the nanoparticles are deposited on a Si substrate, the substrate peak height can serve as a calibration tool, provided that the absorption of Si at the different excitation wavelengths is accounted for. All of these factors contributing to the Ge peak intensity affect the Raman scattering, whether or not it is enhanced by the local electric field from the LSP.

Enhancement of the Raman signal due to a local electric field caused by plasmonic excitation of the Ag component will result in additional peak intensity. It is anticipated that the Raman signal from Ge at the interface with the Ag will be enhanced with the laser at 785 nm. Since electric field simulations show an enhanced field at the SiO$_2$ surface of the Ge for wavelengths of 600 and 800 nm, it is possible that a Raman signal from the Ge/SiO$_2$ interface will also be enhanced. Initial Raman experiments were described in Chapter 5. Using excitation by a 633 nm laser, the sample with large Ag-Ge nanoparticles showed a strong signal from Ge at ~299 cm^{-1}. Given the many factors involved, a systematic progression through these experiments will be necessary to better understand plasmonic-semiconductor coupling.

6.3 Bandgap measurements of Ge nanoparticles

Germanium nanocrystals embedded in glass have been studied extensively with the hope that if the electrons are confined, the electronic band gap will become direct, facilitating the use of the nanocrystals as light-emitting devices. In addition, the bandgap has been predicted to increase as the particle size decreases.[172] CdSe semiconducting nanoparticles were shown to exhibit size-dependent energy gaps due to quantum confinement.[6] This observation prompted investigation of controlling the luminescent wavelength of semiconducting particles in other materials systems.

Si nanoparticles, with a Bohr radius[173] of 5 nm, have exhibited size-dependent photoluminescence. Ge has a Bohr radius[62] of 17 nm, and, consequently, quantum confinement should be realized with larger nanostructures than is possible with Si. Many studies[57, 174] have observed quantum confinement in the Raman signature of small Ge nanoparticles. Particles with an average radius of 5 nm show an asymmetric lineshape, since the momentum can be less defined as length and energy are confined. The Raman signal is able to sample a larger region of k-space in the phonon modes.

Photoluminescence (PL) and absorption spectroscopy are common methods for measuring the bandgap of semiconductors. Four challenges are inherent in the measurement of Ge PL from embedded Ge nanoparticles: 1) Inefficient emission cross section due to the indirect nature of the lowest energy band; 2) Reduced absorption per Ge atom due to Mie scattering;[62] 3) Competing non-radiative defects, most likely arising from surface states on the particle; 4) A broad PL lineshape due to a distribution of particle sizes. These four issues have prevented the bandgap from being measured directly with photoluminescence. Although size-dependent PL has been measured near 3 eV,[175, 176] it is generally accepted that this PL arises from Ge oxide defects on the surface of the particle.[176] Ge has a large absorption coefficient. However, because of Mie scattering, the absorption per atom in the particles is less than absorption per atom in the bulk crystal.[62] Effects from Mie scattering could be reduced by embedding the nanoparticles in a matrix with a higher refractive index, preferably a refractive index with magnitude similar to the refractive index of Ge.[177] Even with the reduced absorption because of Mie scattering, it is clear that in PL experiments, electron-hole pairs are created. However, recombination of the electron-hole pairs does not occur in quantities large enough to measure. It is now understood that native defects in the Ge crystal, with lifetimes much shorter than the electronic transitions, quench the luminescence.

Kawamura et al. recently reported direct-gap PL from Ge nanowires that had average diameters of 40 nm.[178] Although quantum confinement did not play a role, dominance of the direct transition at 0.8 eV over the indirect transition at 0.66 eV was attributed to the faster recombination rates of the direct transition. The longer indirect transitions were quenched by defect states at the Ge-oxide surface.

Uhrenfeldt et al.[62] recently published an extensive study of absorption from Ge nanoparticles in the energy range 1 to 6 eV. Fabrication of samples containing 2.5 to 13 times the concentration obtained with ion implantation of Ge at 4×10^{16} atoms/cm^2 into SiO_2 was achieved by depositing many SiO_2 layers with Ge nanoparticles 2-6 nm in diameter.[47] Uhrenfeldt et al. concluded that, although electronic transitions were occurring during irradiation, the dominant response was due to Mie scattering caused by the boundary conditions of the surrounding oxide. The study demonstrated a modified absorption spectrum; however, there was no conclusive evidence for quantum confinement.

In an NCEM proposal, I had proposed using low-loss EELS to measure the shift in the indirect bandgap of Ge nanocrystals as a function of nanoparticle size.[179] RF sputtering of embedded nanoparticles on TEM sample membranes results in a distribution of particle sizes to enable these measurements. Theoretical calculations predict that Ge nanoparticles will exhibit indirect bandgaps of 0.7 to 3.0 eV for nanoparticles with 10 to 2 nm diameters.[172]

A sample was prepared and measurements were attempted using the monochromated Tecnai microscope. Unfortunately, the particles incurred too much damage using electrons with an incident energy of 200 keV. It is expected that repeating the experiments at 80 keV, with improved energy resolution from the current 0.2 eV to the manufacturer specified 0.15 eV, will result in measurements of the bandgap as a function of particle size. An additional challenge remains to develop analysis software to remove the tail of the zero-loss peak.

6.4 Er^{3+} photoluminescence and Ag-Ge nanoparticles

Erbium^{3+} is an ideal probe of optical transitions in the Vis-NIR wavelength range, because some its atomic transitions have long lifetimes resulting in sharp photoluminescence lines that can easily be measured at room temperature. The intensity of the Er^{3+} lines can be modulated by changing optical absorption and emission of nearby materials through various energy transfer mechanisms. In particular, energy transfer between isolated erbium atoms and Ge nanoclusters could be facilitated by the overlap of many of the transitions of Er^{3+} with the transitions in Ge crystals.[180]

Erbium is technologically relevant because it is the source of amplification in erbium-doped fiber amplifiers (EDFA) used for infra-red optical communication signals with a wavelength range of 1530-1565 nm in the C-band.[180] The amplification occurs via the intra-4f shell transition of Er^{3+} near 1550 nm. When added to a glass like SiO_2, erbium ionizes to a +3 state and acts like a network modifier.[180] The $^4I_{13/2} \rightarrow {}^4I_{15/2}$ transition is pumped with an external laser, and the incoming optical signal triggers stimulated emission at ~1550 nm. Since the solid solubility of Er in glass limits the Er concentration in the amplifiers, the amplifiers involve great lengths (~ 1 m) of glass fiber. It is well documented that the presence of silicon or germanium nanocrystals increases the magnitude of the Er^{3+} PL.[181] Studies with Si nanoparticles have

suggested that the presence of a gold thin film enhances energy transfer between the nanoparticles and Er^{3+}, and increases the Er^{3+} luminescence.[182] If other materials, such as Ge nanoparticles, were able to absorb the light and then transfer the energy to the Er^{3+} ion, increased amplification would be realized. Similarly, if either the absorption or the emission could be resonantly enhanced with a noble metal, amplification would be more efficient.[183]

Erbium, as well as other lanthanides, is being used in up-conversion schemes for solar energy applications,[184] providing additional motivation for the Er^{3+} PL studies.

A thin film containing Ag-Ge bi-lobed nanoparticles, with Er^{3+} dissolved in the SiO_2 matrix, is easily fabricated by adding pieces of Er metal to the sputtering target. Samples have been fabricated, and preliminary Er^{3+} PL measurements indicate that the signal is sensitive to the amount and configuration of the Ag and Ge constituents. Further investigation of this complicated system would likely require simulations to predict changes in the optical mode densities and lifetimes of the various transitions.[185, 186] It would be beneficial to measure changes in PL intensity as a function of concentration and configuration of nanoparticles. Photoluminescence is not an inherently quantitative technique; a comparison of spectra requires careful calibration with reference samples. However, the potential for successful experimentation is based on the fundamentally strong Er^{3+} PL signal that is sensitive to its local environment.

6.5 TEM tomography to characterize shape of interface –collaboration

Analogous to x-ray tomography, TEM tomography techniques are being applied to nanoparticles to elucidate three-dimensional structures that are not accessible through conventional TEM images. Very thin, ~20 nm samples are prepared, either as "needles," or supported in a slotted TEM grid that allows tilting in the microscope. Images in real space are captured at many tilt angles, and, with the use of computer algorithms, the series of 2-D images is reconstructed into a 3-D object.

The Ag-Ge bi-lobed nanoparticle has been proposed as a model system for proof-of-concept for a new reconstruction algorithm called equally sloped tomography.[187] As opposed to using accumulated images with equal angles, usually 1 or 2 degrees, this algorithm would use accumulated images with equal slopes.[187] The method is iterative between real and reciprocal space, and a reconstruction of the 2-D images is possible without a-priori knowledge of the crystal structure. The accuracy of the algorithm has been demonstrated in work with a 10 nm polycrystalline Au particle.[33] The fact that the Ag-Ge bi-lobed particle is comprised of two elements with differing crystal structures contributes an added complexity to the problem. The TEAM microscope at LBNL has spherical and chromatic aberration correctors that should facilitate atomic differentiation between Ag and Ge atoms in STEM mode.[136] The information gained from these studies will help determine whether the interface between the Ag and Ge (111)

planes is flat or comprised of steps. Additionally, it may be possible to discern the amount of alloying in the interfacial layers and the amount of Ge present in the Ag crystal.

Samples of Ag-Ge bi-lobed particles are being mechanically thinned by the collaborator.[33] The author is developing a process to deposit a thin film containing the nanoparticles on a specially prepared TEM grid that can tilt to high angles. Preliminary results at 80 keV indicate that the particle is robust enough to withstand prolonged exposure to the beam without atomic rearrangement. Sample preparation via deposition on the nitride membrane and supply of starting material are the only contributions the author is making to this project.

6.6 Localized surface plasmon dynamics – collaboration

Since plasmonics is a relatively new field, some fundamental questions are still under investigation, such as the study of plasmon lifetimes and the mechanisms of their decay after excitation in the field of plasmon dynamics. The lifetimes are on the order of femtoseconds, so it is necessary to perform spectroscopy with attosecond pulses. Fortunately attosecond laser pulses (~100 attoseconds) in the extreme UV range (10 to 125 eV) are achievable.[188] A system to generate attosecond laser pulses and probe the plasmon dynamics was designed and constructed by a collaborator.[30] The goal is to pump the LSP of the Ag component of the bi-lobed nanoparticle with either 400 or 800 nm light, and then detect modulation in the Ge absorption spectrum that occurs at 32.4 eV. The excitation at 32.4 eV corresponds to the second-order bulk plasmon of Ge. Figure 6-1(a) shows a schematic of the pump-probe experiment. Figure 6-1(b) shows the transmission of extreme UV radiation for the Ge particle fraction, SiN membrane and SiO_2 matrix of a sample similar to those described in Chapter 5 for the plasmonic switch. The sample has a concentration of 8×10^{16} Ge atoms/cm^2, embedded in 60 nm of SiO_2, and is deposited on a 10 nm thick SiN membrane. Calculations of transmission though the layers (Figure 6-1(b)) indicates that a significant amount of the light at 32 eV will be absorbed by the SiN and SiO_2 layers; the transmission will be reduced to 3.6% of the incident light. Modulation of the Ge absorption in the remaining 3.6% will be measured. Sample preparation is the only contribution the author is making to this project. Samples are being prepared on large TEM windows, 200 μm x 200 μm, to accommodate the laser spot size.
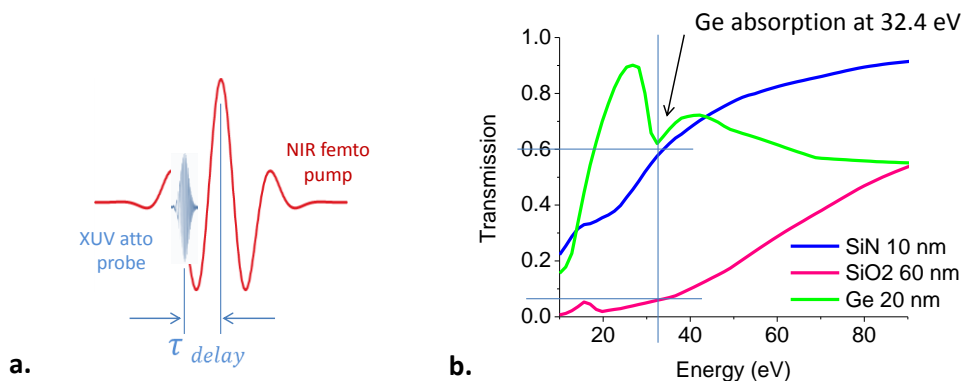
Figure 6-1. Investigation of localized surface plasmon dynamics using Ag-Ge bi-lobed nanoparticles. (a) Schematic of an attosecond pump-probe experiment. Courtesy of Andrey Gandman; (b) Transmission in XUV of the prepared sample including Ag-Ge nanoparticles with Ge concentration of 8×10^{16} atoms/cm^2, 60 nm of SiO$_2$, and 10 nm of SiN.

6.7 Dark-field scattering of single particles

Dark-field scattering (extinction minus absorption) takes advantage of the large angle of scattering to collect a spectrum from a nanoparticle (~100 nm in diameter) in an optical microscope.[145] The particle is first located on a grid using a scanning electron microscope (SEM) and then the grid is used to center the collection optics. The sample preparation to release the Ag-Ge nanoparticles from the matrix and disperse them on a substrate was described in Chapter 4. The author does not have access to a dark-field microscope designed to make these measurements. Like the measurements made in the TEM, they are single-particle measurements. The advantage of this technique is that the energy-loss range below 2 eV, which was not accessible in the TEM, would be accessible in dark-field optical scattering.

6.8 Cathodoluminescence of single particle

Cathodoluminescence (CL), either in an SEM[189] or a TEM,[190] has been used to measure the optical scattering of localized surface plasmon modes in Ag and Au nanoparticles. The information gathered is very similar to EELS in the TEM. The sample preparation is similar to that for dark-field scattering. CL has the advantage of allowing use of thick samples and that it is almost a non-destructive technique. However, because of the ease with which samples are fabricated using the TEM membranes, CL was not pursued in this work.

Bibliography

1. M. Meeker, Venture Capitalist for Kleiner, Perkins, Kaufield and Byers, *Internet Trends*, (2012).

2. G. E. Moore, *Cramming more components onto integrated circuits* Electronics Magazine **38**, 4 (1965).

3. S.-H. Shin, S. Chung, B. Sanii, L. R. Comolli, C. R. Bertozzi and J. J. De Yoreo, *Direct observation of kinetic traps associated with structural transformations leading to multiple pathways of S-layer assembly*, Proceedings of the National Academy of Sciences **109**, 12968-12973 (2012), http://www.pnas.org/content/109/32/12968.abstract.

4. P. W. K. Rothemund, *Folding DNA to create nanoscale shapes and patterns*, Nature **440**, 297-302 (2006), http://dx.doi.org/10.1038/nature04586.

5. E. L. Rosen, R. Buonsanti, A. Llordes, A. M. Sawvel, D. J. Milliron and B. A. Helms, *Exceptionally Mild Reactive Stripping of Native Ligands from Nanocrystal Surfaces by Using Meerwein's Salt*, Angewandte Chemie International Edition **51**, 684-689 (2012), http://dx.doi.org/10.1002/anie.201105996.

6. A. P. Alivisatos, *Semiconductor Clusters, Nanocrystals, and Quantum Dots*, Science **271**, 933-937 (1996), http://www.jstor.org/stable/2889983.

7. P. Buffat and J. P. Borel, *Size effect on the melting temperature of gold particles*, Physical Review A **13**, 2287-2298 (1976), http://link.aps.org/doi/10.1103/PhysRevA.13.2287.

8. S. A. Maier, Plasmonics: Fundamentals and Applications. (Springer Science and Business Media LLC, New York, 2007).

9. G. Mie, *Beiträge zur Optik trüber Medien, speziell kolloidaler Metallösungen*, Annalen der Physik **330**, 377-445 (1908), http://dx.doi.org/10.1002/andp.19083300302.

10. J. Zhao, X. Zhang, C. R. Yonzon, A. J. Haes and R. P. Van Duyne, *Localized surface plasmon resonance biosensors*, Nanomedicine **1**, 219-228 (2006), http://dx.doi.org/10.2217/17435889.1.2.219.

11. M. E. Stewart, C. R. Anderton, L. B. Thompson, J. Maria, S. K. Gray, J. A. Rogers and R. G. Nuzzo, *Nanostructured Plasmonic Sensors*, Chemical Reviews **108**, 494-521 (2008), http://dx.doi.org/10.1021/cr068126n.

12. S. Lal, S. E. Clare and N. J. Halas, *Nanoshell-Enabled Photothermal Cancer Therapy: Impending Clinical Impact*, Accounts of Chemical Research **41**, 1842-1851 (2008), http://dx.doi.org/10.1021/ar800150g.

13. D. P. O'Neal, L. R. Hirsch, N. J. Halas, J. D. Payne and J. L. West, *Photo-thermal tumor ablation in mice using near infrared-absorbing nanoparticles*, Cancer Letters **209**, 171-176 (2004), http://www.sciencedirect.com/science/article/pii/S0304383504001442.

14. N. J. Halas, S. Lal, W.-S. Chang, S. Link and P. Nordlander, *Plasmons in Strongly Coupled Metallic Nanostructures*, Chemical Reviews **111**, 3913-3961 (2011), http://dx.doi.org/10.1021/cr200061k.

15. A. Polman, *Plasmonics Applied*, Science **322**, 868-869 (2008), http://www.sciencemag.org/content/322/5903/868.short.

16. H. A. Atwater and A. Polman, *Plasmonics for improved photovoltaic devices*, Nature Materials **9**, 865-865 (2010), http://dx.doi.org/10.1038/nmat2866.

17. J. A. Schuller, E. S. Barnard, W. Cai, Y. C. Jun, J. S. White and M. L. Brongersma, *Plasmonics for extreme light concentration and manipulation*, Nature Materials **9**, 193-204 (2010), http://dx.doi.org/10.1038/nmat2630.

18. V. E. Ferry, A. Polman and H. A. Atwater, *Modeling Light Trapping in Nanostructured Solar Cells*, ACS Nano **5**, 10055-10064 (2011), http://dx.doi.org/10.1021/nn203906t.

19. Z. Liu, W. Hou, P. Pavaskar, M. Aykol and S. B. Cronin, *Plasmon Resonant Enhancement of Photocatalytic Water Splitting Under Visible Illumination*, Nano Letters **11**, 1111-1116 (2011), http://dx.doi.org/10.1021/nl104005n.

20. S. Linic, P. Christopher and D. B. Ingram, *Plasmonic-metal nanostructures for efficient conversion of solar to chemical energy*, Nature Materials **10**, 911-921 (2011), http://dx.doi.org/10.1038/nmat3151.

21. S. C. Warren, D. A. Walker and B. A. Grzybowski, *Plasmoelectronics: Coupling Plasmonic Excitation with Electron Flow*, Langmuir **28**, 9093-9102 (2012), http://dx.doi.org/10.1021/la300377j.

22. M. B. Cortie and A. M. McDonagh, *Synthesis and Optical Properties of Hybrid and Alloy Plasmonic Nanoparticles*, Chemical Reviews **111**, 3713-3735 (2011), http://dx.doi.org/10.1021/cr1002529.

23. X. Zhao, P. Wang and B. Li, *Surface plasmon enhanced energy transfer in metal-semiconductor hybrid nanostructures*, Nanoscale **3**, 3056-3059 (2011), http://dx.doi.org/10.1039/C1NR10367A.

24. M. Sebastian, *Hybrid nanostructures for efficient light harvesting*, Journal of Physics: Condensed Matter **22**, 193102 (2010), http://stacks.iop.org/0953-8984/22/i=19/a=193102.

25. H.-M. Song, Q. Wei, Q. K. Ong and A. Wei, *Plasmon-Resonant Nanoparticles and Nanostars with Magnetic Cores: Synthesis and Magnetomotive Imaging*, ACS Nano **4**, 5163-5173 (2010), http://dx.doi.org/10.1021/nn101202h.

26. X. Qian, X.-H. Peng, D. O. Ansari, Q. Yin-Goen, G. Z. Chen, D. M. Shin, L. Yang, A. N. Young, M. D. Wang and S. Nie, *In vivo tumor targeting and spectroscopic detection with surface-enhanced Raman nanoparticle tags*, Nature Biotechnology **26**, 83-90 (2008), http://dx.doi.org/10.1038/nbt1377.

27. S. J. Shin, J. Guzman, C. W. Yuan, C. Y. Liao, C. N. Boswell-Koller, P. R. Stone, O. D. Dubon, A. M. Minor, M. Watanabe, J. W. Beeman, K. M. Yu, J. W. Ager, D. C. Chrzan and E. E. Haller, *Embedded Binary Eutectic Alloy Nanostructures: A New Class of Phase Change Materials*, Nano Letters **10**, 2794-2798 (2010), http://dx.doi.org/10.1021/nl100670r.

28. J. Guzman, C. N. Boswell-Koller, J. W. Beeman, K. C. Bustillo, T. Conry, O. D. Dubon, W. L. Hansen, A. X. Levander, C. Y. Liao, R. R. Lieten, C. A. Sawyer, M. P. Sherburne, S. J. Shin, P. R. Stone, M. Watanabe, K. M. Yu, J. W. Ager, III, D. C. Chrzan and E. E. Haller, *Reversible phase changes in Ge--Au nanoparticles*, Applied Physics Letters **98**, 193101 (2011), http://link.aip.org/link/?APL/98/193101/1.

29. C. A. Sawyer, J. Guzman, C. N. Boswell-Koller, M. P. Sherburne, J. P. Mastandrea, K. C. Bustillo, J. W. Ager, Iii, E. E. Haller and D. C. Chrzan, *Modeling pulsed-laser melting of embedded semiconductor nanoparticles*, Journal of Applied Physics **110**, 094307-094310 (2011), http://dx.doi.org/10.1063/1.3658265.

30. A. Gandman, *Department of Chemistry, University of California, Berkeley, CA*, (2012).

31. G. V. Hartland, *Optical Studies of Dynamics in Noble Metal Nanostructures*, Chemical Reviews **111**, 3858-3887 (2011), http://dx.doi.org/10.1021/cr1002547.

32. Y. Lu, G. L. Liu, J. Kim, Y. X. Mejia and L. P. Lee, *Nanophotonic Crescent Moon Structures with Sharp Edge for Ultrasensitive Biomolecular Detection by Local Electromagnetic Field Enhancement Effect*, Nano Letters **5**, 119-124 (2004), http://dx.doi.org/10.1021/nl048232+.

33. M. Scott, *Department of Physics, University of California, Los Angeles, CA*, (2012).

34. J. Miao, *Department of Physics, University of California, Los Angeles, CA*, (2012).

35. A. O. Govorov, G. W. Bryant, W. Zhang, T. Skeini, J. Lee, N. A. Kotov, J. M. Slocik and R. R. Naik, *Exciton−Plasmon Interaction and Hybrid Excitons in Semiconductor−Metal Nanoparticle Assemblies*, Nano Letters **6**, 984-994 (2006), http://dx.doi.org/10.1021/nl0602140.

36. A. O. Govorov, J. Lee and N. A. Kotov, *Theory of plasmon-enhanced Förster energy transfer in optically excited semiconductor and metal nanoparticles*, Physical Review B **76**, 125308 (2007), http://link.aps.org/doi/10.1103/PhysRevB.76.125308.

37. E. Shaviv, O. Schubert, M. Alves-Santos, G. Goldoni, R. Di Felice, F. Vallée, N. Del Fatti, U. Banin and C. Sönnichsen, *Absorption Properties of Metal–Semiconductor Hybrid Nanoparticles*, ACS Nano **5**, 4712-4719 (2011), http://dx.doi.org/10.1021/nn200645h.

38. H. Mertens, J. Verhoeven, A. Polman and F. D. Tichelaar, *Infrared surface plasmons in two-dimensional silver nanoparticle arrays in silicon*, Applied Physics Letters **85**, 1317-1319 (2004), http://dx.doi.org/10.1063/1.1784542.

39. O. Stenzel, A. Stendal, M. Röder and C. v. Borczyskowski, *Tuning of the plasmon absorption frequency of silver and indium nanoclusters via thin amorphous silicon films*, Pure and Applied Optics: Journal of the European Optical Society Part A **6**, 577 (1997), http://stacks.iop.org/0963-9659/6/i=5/a=009.

40. M. M. Kjeldsen, J. L. Hansen, T. G. Pedersen, P. Gaiduk and A. N. Larsen, *Tuning the plasmon resonance of metallic tin nanocrystals in Si-based materials*, Applied Physics A: Materials Science & Processing **100**, 31-37 (2010), http://search.ebscohost.com/login.aspx?direct=true&db=a9h&AN=51624945&site=ehost-live.

41. M. Peng, J. Gao, P. Zhang, Y. Li, X. Sun and S.-T. Lee, *Reductive Self-Assembling of Ag Nanoparticles on Germanium Nanowires and Their Application in Ultrasensitive Surface-Enhanced Raman Spectroscopy*, Chemistry of Materials **23**, 3296-3301 (2011), http://pubs.acs.org/doi/abs/10.1021/cm200186v.

42. J. Lee, A. O. Govorov, J. Dulka and N. A. Kotov, *Bioconjugates of CdTe Nanowires and Au Nanoparticles: Plasmon−Exciton Interactions, Luminescence Enhancement, and Collective Effects*, Nano Letters **4**, 2323-2330 (2004), http://dx.doi.org/10.1021/nl048669h.

43. V. E. Ferry, M. A. Verschuuren, M. C. v. Lare, R. E. I. Schropp, H. A. Atwater and A. Polman, *Optimized Spatial Correlations for Broadband Light Trapping Nanopatterns in High Efficiency Ultrathin Film a-Si:H Solar Cells*, Nano Letters **11**, 4239-4245 (2011), http://dx.doi.org/10.1021/nl202226r.

44. A. I. Carim, J. Gu and S. Maldonado, *Overlayer Surface-Enhanced Raman Spectroscopy for Studying the Electrodeposition and Interfacial Chemistry of Ultrathin Ge on a Nanostructured Support*, ACS Nano **5**, 1818-1830 (2011), http://dx.doi.org/10.1021/nn102555u.

45. N. Hayazawa, M. Motohashi, Y. Saito and S. Kawata, *Highly sensitive strain detection in strained silicon by surface-enhanced Raman spectroscopy*, Applied Physics Letters **86**, 263114-263113 (2005), http://dx.doi.org/10.1063/1.1984105.

46. D. B. Williams and C. B. Carter, Transmission Electron Microscopy: a textbook for materials science. (Springer, London, 2009).

47. I. D. Sharp, Q. Xu, C. Y. Liao, D. O. Yi, J. W. Beeman, Z. Liliental-Weber, K. M. Yu, D. N. Zakharov, J. W. Ager, Iii, D. C. Chrzan and E. E. Haller, *Stable, freestanding Ge nanocrystals*, Journal of Applied Physics **97**, 124316 (2005), http://link.aip.org/link/?JAP/97/124316/1.

48. F. J. García de Abajo, *Optical excitations in electron microscopy*, Reviews of Modern Physics **82**, 209-275 (2010), http://link.aps.org/doi/10.1103/RevModPhys.82.209.

49. M.-W. Chu, V. Myroshnychenko, C. H. Chen, J.-P. Deng, C.-Y. Mou and F. J. García de Abajo, *Probing Bright and Dark Surface-Plasmon Modes in Individual and Coupled Noble Metal Nanoparticles Using an Electron Beam*, Nano Letters **9**, 399-404 (2009), http://dx.doi.org/10.1021/nl803270x.

50. B. S. Guiton, V. Iberi, S. Li, D. N. Leonard, C. M. Parish, P. G. Kotula, M. Varela, G. C. Schatz, S. J. Pennycook and J. P. Camden, *Correlated Optical Measurements and Plasmon Mapping of Silver Nanorods*, Nano Letters **11**, 3482-3488 (2011), http://dx.doi.org/10.1021/nl202027h.

51. A. L. Koh, K. Bao, I. Khan, W. E. Smith, G. Kothleitner, P. Nordlander, S. A. Maier and D. W. McComb, *Electron Energy-Loss Spectroscopy (EELS) of Surface Plasmons in Single Silver Nanoparticles and Dimers: Influence of Beam Damage and Mapping of Dark Modes*, ACS Nano **3**, 3015-3022 (2009), http://dx.doi.org/10.1021/nn900922z.

52. J. Mock, M. Barbic, D. Smith, D. Schultz and S. Schultz, *Shape effects in plasmon resonance of individual colloidal silver nanoparticles*, Journal of Chemical Physics **116**, 6755-6759 (2002), http://dx.doi.org/doi/10.1063/1.1462610.

53. J. Zhao, A. O. Pinchuk, J. M. McMahon, S. Li, L. K. Ausman, A. L. Atkinson and G. C. Schatz, *Methods for Describing the Electromagnetic Properties of Silver and Gold Nanoparticles*, Accounts of Chemical Research **41**, 1710-1720 (2008), http://dx.doi.org/10.1021/ar800028j.

54. S. M. Morton, D. W. Silverstein and L. Jensen, *Theoretical Studies of Plasmonics using Electronic Structure Methods*, Chemical Reviews **111**, 3962-3994 (2011), http://dx.doi.org/10.1021/cr100265f.

55. V. E. Ferry, *Department of Chemistry, University of California, Berkeley, CA.*

56. B. Schaffer, W. Grogger, G. Kothleitner and F. Hofer, *Comparison of EFTEM and STEM EELS plasmon imaging of gold nanoparticles in a monochromated TEM*, Ultramicroscopy **110**, 1087-1093 (2010), http://www.sciencedirect.com/science/article/pii/S0304399109002903.

57. I. D. Sharp, D. O. Yi, Q. Xu, C. Y. Liao, J. W. Beeman, Z. Lilental-Weber, K. M. Yu, D. N. Zakharov, J. W. Ager, Iii, D. C. Chrzan and E. E. Haller, *Mechanism of stress relaxation in Ge nanocrystals embedded in SiO$_2$*, Applied Physics Letters **86**, 063107-063103 (2005), http://link.aip.org/link/?APL/86/063107/1.

58. R. H. Ritchie, *Plasma Losses by Fast Electrons in Thin Films*, Physical Review **106**, 874-881 (1957), http://link.aps.org/doi/10.1103/PhysRev.106.874.

59. J. A. Dionne and H. A. Atwater, *Plasmonics: Metal-worthy methods and materials in nanophotonics*, MRS Bulletin **37**, 717-724 (2012).

60. U. Kreibig and M. Vollmer, <u>Optical Properties of Metal Clusters</u>. (Springer-Verlag, Berlin, Heidelberg, Germany, 1995).

61. A. G. Cullis, L. T. Canham and P. D. J. Calcott, *The structural and luminescence properties of porous silicon*, Journal of Applied Physics **82**, 909-965 (1997), http://dx.doi.org/10.1063/1.366536.

62. C. Uhrenfeldt, J. Chevallier, A. N. Larsen and B. B. Nielsen, *Near-infrared-ultraviolet absorption cross sections for Ge nanocrystals in SiO_2 thin films: Effects of shape and layer structure*, Journal of Applied Physics **109**, 094314 (2011), http://dx.doi.org/10.1063/1.3581015.

63. C. F. Bohren and D. R. Huffman, <u>Absorption and Scattering of Light by Small Particles</u>. (Wiley-VCH, Weinheim, Germany, 2004).

64. E. D. Palik, <u>Handbook of Optical Constants of Solids</u>. (Academic Press, San Diego, 1998).

65. H. Ehrenreich, H. R. Philipp and J. C. Phillips, *Interband Transitions in Groups 4, 3-5, and 2-6 Semiconductors*, Physical Review Letters **8**, 59-61 (1962), http://link.aps.org/doi/10.1103/PhysRevLett.8.59.

66. H. Ehrenreich and H. R. Philipp, *Optical Properties of Ag and Cu*, Physical Review **128**, 1622-1629 (1962), http://link.aps.org/doi/10.1103/PhysRev.128.1622.

67. P. B. Johnson and R. W. Christy, *Optical Constants of the Noble Metals*, Physical Review B **6**, 4370-4379 (1972), http://link.aps.org/doi/10.1103/PhysRevB.6.4370.

68. J. W. Morris, <u>A Survey of Materials Science</u>. (University of California, Berkeley, CA, 2008).

69. P. R. West, S. Ishii, G. V. Naik, N. K. Emani, V. M. Shalaev and A. Boltasseva, *Searching for better plasmonic materials*, Laser & Photonics Reviews **4**, 795-808 (2010), http://dx.doi.org/10.1002/lpor.200900055.

70. J. A. D. Matthew and S. Parker, *Relationships between surface plasmon energy and the surface electronic environment in a range of semiconductors* Surface Review and Letters **03**, 1345-1348 (1996), http://www.worldscientific.com/doi/abs/10.1142/S0218625X96002345.

71. R. F. Egerton, <u>Electron Energy-Loss Spectroscopy in the Electron Microscope</u>, 3rd ed. (Springer Science-Business Media, New York, 2011).

72. H. Raether, <u>Excitation of Plasmons and Interfand Transitions by Electrons</u>. (Springer-Verlag, New York, NY, 1988).

73. K. Sturm, *Electron energy loss in simple metals and semiconductors*, Advances in Physics **31**, 1-64 (1982), http://www.tandfonline.com/doi/abs/10.1080/00018738200101348.

74. C. C. Ahn and O. L. Kirvanek, <u>EELS Atlas</u>. (Gatan Inc., Warrendale, PA, 1983).

75. T. Hanrath and B. A. Korgel, *A Comprehensive Study of Electron Energy Losses in Ge Nanowires*, Nano Letters **4**, 1455-1461 (2004), http://dx.doi.org/10.1021/nl049240t.

76. P. Y. Yu and M. Cardona, Fundamentals of Semiconductors: Physics and Materials Properties. (Springer-Verlag, Berlin Heidelberg, Germany, 1996).

77. B. Tejerina, T. Takeshita, L. Ausman and G. C. Schatz, *Nanosphere Optics Lab Field Simulator*, (2008), http://nanohub.org/resources/3056.

78. V. Siklitsky and A. Tolmatchev, (Ioffe Physico-Technical Institute, 2001).

79. P. L. Stiles, J. A. Dieringer, N. C. Shah and R. P. Van Duyne, *Surface-Enhanced Raman Spectroscopy*, Annual Review of Analytical Chemistry **1**, 601-626 (2008), http://dx.doi.org/10.1146/annurev.anchem.1.031207.112814.

80. M. Rycenga, C. M. Cobley, J. Zeng, W. Li, C. H. Moran, Q. Zhang, D. Qin and Y. Xia, *Controlling the Synthesis and Assembly of Silver Nanostructures for Plasmonic Applications*, Chemical Reviews **111**, 3669-3712 (2011), http://dx.doi.org/10.1021/cr100275d.

81. K. T. Shimizu, W. K. Woo, B. R. Fisher, H. J. Eisler and M. G. Bawendi, *Surface-Enhanced Emission from Single Semiconductor Nanocrystals*, Physical Review Letters **89**, 117401 (2002), http://link.aps.org/doi/10.1103/PhysRevLett.89.117401.

82. A. Pucci, *IR spectroscopy of adsorbates on ultrathin metal films*, physica status solidi (b) **242**, 2704-2713 (2005), http://dx.doi.org/10.1002/pssb.200541131.

83. D. L. Jeanmaire and R. P. Van Duyne, *Surface raman spectroelectrochemistry: Part I. Heterocyclic, aromatic, and aliphatic amines adsorbed on the anodized silver electrode*, Journal of Electroanalytical Chemistry and Interfacial Electrochemistry **84**, 1-20 (1977), http://www.sciencedirect.com/science/article/pii/S0022072877802246.

84. M. G. Albrecht and J. A. Creighton, *Anomalously intense Raman spectra of pyridine at a silver electrode*, Journal of the American Chemical Society **99**, 5215-5217 (1977), http://dx.doi.org/10.1021/ja00457a071.

85. E. C. LeRu and P. G. Etchegoin, Principles of Surface-Enhanced Raman Spectroscopy and related plasmonic effects. (Elsevier, The Netherlands, 2009).

86. W. Hanson, 2012 (personal communication).

87. W. Walukiewicz, *Intrinsic limitations to the doping of wide-gap semiconductors*, Physica B: Condensed Matter **302–303**, 123-134 (2001), http://www.sciencedirect.com/science/article/pii/S0921452601004173.

88. S. J. Pennycook and D. E. Jesson, *High-resolution Z-contrast imaging of crystals*, Ultramicroscopy **37**, 14-38 (1991), http://www.sciencedirect.com/science/article/pii/030439919190004P.

89. B. N. Chapman, Glow Discharge Processes. (John Wiley and Sons, New York, 1980).

90. C. N. Boswell-Koller, *Theoretical Investigation of Binary Eutectic Alloy Nanoscale Phase Diagrams,* Ph.D. Dissertation, Department of Materials Science and Engineering, University of California, Berkeley, 2012 (unpublished).

91. Z. Cao and X. Zhang, *Density change and viscous flow during structural relaxation of plasma-enhanced chemical-vapor-deposited silicon oxide films*, Journal of Applied Physics **96**, 4273-4280 (2004), http://dx.doi.org/10.1063/1.1787910.

92. J. von Borany, R. Grotzschel, K. H. Heinig, A. Markwitz, W. Matz, B. Schmidt and W. Skorupa, *Multimodal impurity redistribution and nanocluster formation in Ge implanted silicon dioxide films*, Applied Physics Letters **71**, 3215-3217 (1997), http://dx.doi.org/10.1063/1.120294.

93. G. W. Arnold and J. A. Borders, *Aggregation and migration of ion-implanted silver in lithia-alumina-silica glass*, Journal of Applied Physics **48**, 1488-1496 (1977), http://dx.doi.org/10.1063/1.323867.

94. C. W. Yuan, S. J. Shin, C. Y. Liao, J. Guzman, P. R. Stone, M. Watanabe, J. W. Ager, E. E. Haller and D. C. Chrzan, *Structure map for embedded binary alloy nanocrystals*, Applied Physics Letters **93**, 193114 (2008), http://dx.doi.org/10.1063/1.3027066.

95. J. D. McBrayer, R. M. Swanson and T. W. Sigmon, *Diffusion of Metals in Silicon Dioxide*, Journal of Electrochemical Society Solid-State Science and Technology **133**, 5 (1986).

96. C. W. Yuan, *Modeling Size Distribution Evolution of Ion-Beam-Synthesized Nanoclusters in Amorphous Silica,* PhD, Department of Materials Science and Engineering, University of California, Berkeley, 2009 (unpublished).

97. D. O. Yi, *Modeling nucleation, growth and stress: Ge ncs embedded in SiO_2,* Ph.D Dissertation, Department of Materials Science and Engineering, University of California, Berkeley, 2005 (unpublished).

98. C. W. Yuan, D. O. Yi, I. D. Sharp, S. J. Shin, C. Y. Liao, J. Guzman, J. W. Ager, III, E. E. Haller and D. C. Chrzan, *Theory of Nanocluster Size Distributions from Ion Beam Synthesis*, Physical Review Letters **102**, 146101 (2009), http://link.aps.org/doi/10.1103/PhysRevLett.102.146101.

99. J. M. Howe, Interfaces in Materials. (John Wiley and Sons, Inc., New York, NY, 1997).

100. M. J. O'Neil, P. E. Heckelman, C. B. Koch and K. J. Roman, The Merck Index: An Encyclopedia of Chemicals, Drugs, and Biologicals, Fourteenth Edition. (Merck & Co., Inc., Whitehouse Station, NJ, USA, 2006).

101. F. Gourbilleau, P. Choppinet, C. Dufour, M. Levalois, R. Madelon, J. Vicens, R. Rizk and M. Prassas, *Emission of Er- and Si-doped silicate glass films obtained by magnetron co-sputtering*, Materials Science and Engineering: B **105**, 44-47 (2003),

http://www.sciencedirect.com/science/article/B6TXF-49W6RPD-1/2/784028545bb1fa4a2907baa6ae2e3d0c.

102.   I. D. Sharp, Q. Xu, D. O. Yi, C. W. Yuan, J. W. Beeman, K. M. Yu, J. W. Ager, D. C. Chrzan and E. E. Haller, *Structural properties of Ge nanocrystals embedded in sapphire*, Journal of Applied Physics **100**, 114317 (2006), http://dx.doi.org/10.1063/1.2398727.

103.   R. W. Olesinski, *Ag-Ge Binary Alloy Phase Diagram*, ASM Alloy Phase Diagrams Center, P. Villars, editor-in-chief; H. Okamoto and K. Cenzual, section editors; (1990), http://www1.asminternational.org/AsmEnterprise/APD.

104.   Q. Xu, I. D. Sharp, C. W. Yuan, D. O. Yi, C. Y. Liao, A. M. Glaeser, A. M. Minor, J. W. Beeman, M. C. Ridgway, P. Kluth, J. W. Ager, D. C. Chrzan and E. E. Haller, *Large Melting-Point Hysteresis of Ge Nanocrystals Embedded in SiO₂*, Physical Review Letters **97**, 155701 (2006), http://link.aps.org/doi/10.1103/PhysRevLett.97.155701.

105.   J. M. Howe, A. M. Mebed, K. Chatterjee, P. Li, M. Murayama and W. C. Johnson, *Effect of phase fraction on the tri-junction in two-phase nanoparticle systems*, Acta Materialia **51**, 1359-1372 (2003), http://www.sciencedirect.com/science/article/pii/S135964540200530X.

106.   M. Padovani, E. Magnano, G. Bertoni, V. Spreafico, L. Gavioli and M. Sancrotti, *Ag island nucleation on Ge(1 1 1)-c(2 × 8)*, Applied Surface Science **212–213**, 213-218 (2003), http://www.sciencedirect.com/science/article/pii/S0169433203000837.

107.   M. Bertucci, G. Le Lay, M. Manneville and R. Kern, *Desorption kinetics of condensed phases two-dimensional phases of silver on Ge(111)*, Surface Science **85**, 471-492 (1979), http://www.sciencedirect.com/science/article/pii/0039602879902668.

108.   S. Shin, *Phase and Shape Evolutions of Ion Beam Synthesized Ge Based Nanostructures,* Ph.D. Dissertation, Department of Materials Science and Engineering, University of California, 2009 (unpublished).

109.   U. Kreibig, *Small silver particles in photosensitive glass: Their nucleation and growth*, Applied Physics A: Materials Science & Processing **10**, 255-264 (1976), http://dx.doi.org/10.1007/BF00897225.

110.   J. A. Jimenez and M. Sendova, *In situ optical microspectroscopy approach for the study of metal transport in dielectrics via temperature- and time-dependent plasmonics: Ag nanoparticles in SiO₂ films*, The Journal of Chemical Physics **134**, 054707-054705 (2011), http://dx.doi.org/10.1063/1.3537736.

111.   T. C. Nason, G. R. Yang, K. H. Park and T. M. Lu, *Study of silver diffusion into Si(111) and SiO₂ at moderate temperatures*, Journal of Applied Physics **70**, 1392-1396 (1991), http://dx.doi.org/10.1063/1.349547.

112.   B. I. Boltaks and H. Shih-yin, Soviet Physics Solid State **2** (1961).

113. G. Roma and Y. Limoge, *Density functional theory investigation of native defects in SiO₂: Self-doping and contribution to ionic conductivity*, Physical Review B **70**, 174101 (2004), http://link.aps.org/doi/10.1103/PhysRevB.70.174101.

114. K. Sunder, M. Grofmeier, R. Staskunaite and H. Bracht, *Dynamics of Network Formers and Modifiers in Mixed Cation Silicate Glasses*, Zeitschrift für Physikalische Chemie **224**, 1677-1705 (2010), http://dx.doi.org/10.1524/zpch.2010.0023.

115. D. Yu and G. S. Hwang, *Structure and Dynamics of Ge in the Si – SiO₂ System: Implications for Oxide-Embedded Ge Nanoparticle Formation*, Electrochemical and Solid-State Letters **11**, P17-P19 (2008), http://esl.ecsdl.org/content/11/12/P17.abstract.

116. M. V. Minke and K. A. Jackson, *Diffusion of germanium in silica glass*, Journal of Non-Crystalline Solids **351**, 2310-2316 (2005), http://www.sciencedirect.com/science/article/pii/S002230930500298X.

117. C. A. Sawyer, 2012 (personal communication).

118. K. Lyytikäinen, S. T. Huntington, A. L. G. Carter, P. McNamara, S. S. Fleming, J. Abramczyk, I. Kaplin and G. Schötz, *Dopant diffusion during optical fibre drawing*, OPTICS EXPRESS **12**, 6 (2004).

119. H. Yamada and H. Hanafusa, *Mode shape convertor produced by the thermal diffusion of different dopants*, Photonics Technology Letters, IEEE **6**, 531-533 (1994).

120. P. G. Shewmon, <u>Transfomations in Metals</u>. (J. Williams Book Company, Jenks, OK, 1983).

121. H. Bracht, S. Schneider and R. Kube, *Diffusion and doping issues in germanium*, Microelectronic Engineering **88**, 452-457 (2011), http://www.sciencedirect.com/science/article/pii/S0167931710003734.

122. M. Werner, H. Mehrer and H. D. Hochheimer, *Effect of hydrostatic pressure, temperature, and doping on self-diffusion in germanium*, Physical Review B **32**, 3930-3937 (1985), http://link.aps.org/doi/10.1103/PhysRevB.32.3930.

123. R. E. Hoffman, *Self-diffusion in dilute binary solid solutions—III: Diffusion in silver germanium and silver thallium solutions*, Acta Metallurgica **6**, 95-97 (1958), http://www.sciencedirect.com/science/article/pii/0001616058901184.

124. G. Vogel, G. Hettich and H. Mehrer, *Self-diffusion in intrinsic germanium and effects of doping on self-diffusion in germanium*, Journal of Physics C: Solid State Physics **16**, 6197 (1983), http://stacks.iop.org/0022-3719/16/i=32/a=012.

125. B. L. Sharma, <u>Diffusion in Semiconductors</u>. (Trans Tech Publications, Clausthal-Zellerfeld, Germany, 1970).

126.   J. H. Wernick, *Determination of Diffusivities in Liquid Metals by Means of Temperature-Gradient Zone Melting*, The Journal of Chemical Physics **25**, 47-49 (1956), http://dx.doi.org/10.1063/1.1742846.

127.   D. C. Chrzan, S. Shin, J. Guzman, C.-W. Yuan, C. Y. Liao, P. R. Stone, C. N. Boswell-Koller, K. C. Bustillo, M. P. Sherburne, T. Conry, R. R. Lieten, O. D. Dubon, A. M. Minor, M. Watanabe, J. W. Beeman, K. M. Yu, J. W. Ager III and E. E. Haller, *Embedded Binary Eutectic Alloy Nanostructures*, Journal of Materials **64** (2012).

128.   W. S. Rasband, (U. S. National Institutes of Health, Bethesda, Maryland, USA, 1997-2012).

129.   S. R. Herd, P. Chaudhari and M. H. Brodsky, *Metal contact induced crystallization in films of amorphous silicon and germanium*, Journal of Non-Crystalline Solids **7**, 309-327 (1972), http://www.sciencedirect.com/science/article/pii/0022309372902670.

130.   G. Rossi, I. Abbati, L. Braicovich, I. Lindau and W. E. Spicer, *Ge-Ag interface at room temperature: An energy-dependent photoemission study*, Physical Review B **25**, 3619-3626 (1982), http://link.aps.org/doi/10.1103/PhysRevB.25.3619.

131.   G. Thomas and M. J. Goringe, Transmission Electron Microscopy of Materials. (John Wiley and Sons, New York, 1979).

132.   J. P. McCaffrey and J. Hulse, *Transmitted color and interference fringes for TEM sample preparation of silicon*, Micron **29**, 139-144 (1998), http://www.sciencedirect.com/science/article/pii/S0968432897000747.

133.   M. Santala, 2012 (personal communication).

134.   N. D. Browning, R. Erni, S. Lopatin, A. Ziegler, J. C. Idrobo, C. Kisielowski, M. K. Clnbulk and R. O. Ritchie, *Scanning transmission electron microscopy in the FEI monochromated Tecnai F20 UT*, FEI Nanoscale Nanosolutions, 12-23 (2006).

135.   Weyland and D. A. Muller, *Tuning the convergence angle for optimum STEM performance*, FEI Nanoscale Nanosolutions **1**, 24-35 (2005).

136.   P. Ercius, M. Boese, T. Duden and U. Dahmen, *Operation of TEAM I in a User Environment at NCEM*, Microscopy and Microanalysis **18**, 676-683 (2012), http://dx.doi.org/10.1017/S1431927612001225.

137.   F. A. Ponce, *High resolution electron microscopy*, Power point presentation at the Pan American Advanced Studies Institute, July 9-22, 2006, Santiago, Chile.

138.   E. M. James and N. D. Browning, *Practical aspects of atomic resolution imaging and analysis in STEM*, Ultramicroscopy **78**, 125-139 (1999), http://www.sciencedirect.com/science/article/pii/S0304399199000182.

139.   A. J. Ardell and V. Ozolins, *Trans-interface diffusion-controlled coarsening*, Nat Mater **4**, 309-316 (2005), http://dx.doi.org/10.1038/nmat1340.

140.   C. A. Sawyer, Department of Materials Science and Engineering, University of California, Berkeley, CA (2013).

141.   J. M. Gibson, *High resolution electron microscopy of interfaces between epitaxial thin films and semiconductors*, Ultramicroscopy **14**, 1-10 (1984), http://www.sciencedirect.com/science/article/pii/0304399184901013.

142.   R. Kilaas, (Total Resolution, Berkeley, CA, 1988).

143.   G. Fei, A. G. Martin, C. Gavin, C. Eun-Chel, H. Yidan, P.-W. Ivan and F. Chris, *Fabrication of multilayered Ge nanocrystals by magnetron sputtering and annealing*, Nanotechnology **19**, 455611 (2008), http://stacks.iop.org/0957-4484/19/i=45/a=455611.

144.   C. Barrett and T. B. Massalski, Structure of Metals. (Pergamon, Oxford, 1980).

145.   L. J. Sherry, S.-H. Chang, G. C. Schatz, R. P. Van Duyne, B. J. Wiley and Y. Xia, *Localized Surface Plasmon Resonance Spectroscopy of Single Silver Nanocubes*, Nano Letters **5**, 2034-2038 (2005), http://dx.doi.org/10.1021/nl0515753.

146.   J. J. Mock, D. R. Smith and S. Schultz, *Local Refractive Index Dependence of Plasmon Resonance Spectra from Individual Nanoparticles*, Nano Letters **3**, 485-491 (2003), http://dx.doi.org/10.1021/nl0340475.

147.   M. P. Hanson, A. C. Gossard and E. R. Brown, *Infrared surface plasmon resonances due to Er-V semimetallic nanoparticles in III-V semiconductor matrices*, Journal of Applied Physics **102**, 043112-043118 (2007), http://dx.doi.org/10.1063/1.2761846.

148.   A. S. Huang, Y. Arie, C. C. Neil and J. M. Hammer, *Study of refractive index of GeO2:SiO2 mixtures using deposited-thin-film optical waveguides*, Appl. Opt. **24**, 4404-4407 (1985), http://ao.osa.org/abstract.cfm?URI=ao-24-24-4404.

149.   B. T. Draine and P. J. Flatau, *Discrete dipole approximation for scattering calculations*, J. Opt. Soc. Am. A **11**, 1491-1499 (1994).

150.   B. T. Draine and P. J. Flatau, *User Guide to the Discrete Dipole Approximation Code DDSCAT 7.2*, arXiv (2012), http://arXiv.org/abs/1202.3424.

151.   *Lumerical Solutions, Inc.*, http://www.lumerical.com/tcad-products/fdtd/.

152.   J. K. Hyun, M. P. Levendorf, M. Blood-Forsythe, J. Park and D. A. Muller, *Relativistic electron energy loss spectroscopy of solid and core-shell nanowires*, Physical Review B **81**, 165403 (2010), http://link.aps.org/doi/10.1103/PhysRevB.81.165403.

153.   N. Zabala, E. Ogando, A. Rivacoba and F. J. García de Abajo, *Inelastic scattering of fast electrons in nanowires: A dielectric formalism approach*, Physical Review B **64**, 205410 (2001), http://link.aps.org/doi/10.1103/PhysRevB.64.205410.

154.   J. Kikkawa, S. Takeda, Y. Sato and M. Terauchi, *Enhanced direct interband transitions in silicon nanowires studied by electron energy-loss spectroscopy*, Physical Review B **75**, 245317 (2007), http://link.aps.org/doi/10.1103/PhysRevB.75.245317.

155.   F. Ouyang, P. E. Batson and M. Isaacson, *Quantum size effects in the surface-plasmon excitation of small metallic particles by electron-energy-loss spectroscopy*, Physical Review B **46**, 15421-15425 (1992), http://link.aps.org/doi/10.1103/PhysRevB.46.15421.

156.   F. Ouyang and M. Isaacson, *Surface plasmon excitation of objects with arbitrary shape and dielectric constant*, Philosophical Magazine Part B **60**, 481-492 (1989), http://www.tandfonline.com/doi/abs/10.1080/13642818908205921.

157.   M. Bosman, M. Watanabe, D. T. L. Alexander and V. J. Keast, *Mapping chemical and bonding information using multivariate analysis of electron energy-loss spectrum images*, Ultramicroscopy **106**, 1024-1032 (2006), http://www.sciencedirect.com/science/article/pii/S0304399106001021.

158.   J. Nelayah, M. Kociak, O. Stephan, F. J. Garcia de Abajo, M. Tence, L. Henrard, D. Taverna, I. Pastoriza-Santos, L. M. Liz-Marzan and C. Colliex, *Mapping surface plasmons on a single metallic nanoparticle*, Nat Phys **3**, 348-353 (2007), http://dx.doi.org/10.1038/nphys575.

159.   J. W. L. Eccles, U. Bangert, M. Bromfield, P. Christian, A. J. Harvey and P. Thomas, *UV-Vis plasmon studies of metal nanoparticles*, Journal of Physics: Conference Series **241**, 012090 (2010), http://stacks.iop.org/1742-6596/241/i=1/a=012090.

160.   M. R. Keenan, *Exploiting spatial-domain simplicity in spectral image analysis*, Surface and Interface Analysis **41**, 79-87 (2009), http://dx.doi.org/10.1002/sia.2949.

161.   J. A. Scholl, A. L. Koh and J. A. Dionne, *Quantum plasmon resonances of individual metallic nanoparticles*, Nature **483**, 421-427 (2012), http://dx.doi.org/10.1038/nature10904.

162.   P. E. Batson and J. R. Heath, *Electron energy loss spectroscopy of single silicon nanocrystals: The conduction band*, Physical Review Letters **71**, 911-914 (1993), http://link.aps.org/doi/10.1103/PhysRevLett.71.911.

163.   P. van Aken, W. Sigle, C. Koch, B. Ögüt, J. Nelayah and L. Gu, *Low-loss EFTEM Imaging of Surface Plasmon Resonances in Ag Nanostructures*, Microscopy and Microanalysis **16**, 1438-1439 (2010), http://dx.doi.org/10.1017/S1431927610056242.

164.   B. Schaffer, U. Hohenester, A. Trügler and F. Hofer, *High-resolution surface plasmon imaging of gold nanoparticles by energy-filtered transmission electron microscopy*, Physical Review B **79**, 041401 (2009), http://link.aps.org/doi/10.1103/PhysRevB.79.041401.

165.   H. Smith, *Department of Materials Science, University of California, Berkeley, CA, 2013*.

166.   M. Watanabe and F. I. Allen, *The SmartEFTEM-SI method: Development of a new spectrum-imaging acquisition scheme for quantitative mapping by energy-filtering transmission electron microscopy*, Ultramicroscopy **113**, 106-119 (2012), http://www.sciencedirect.com/science/article/pii/S0304399111002592.

167.   M. Watanabe, *Analysis of Spectrum-Imaging Datasets in Atomic Resolution Electron Microscopy*, Microscopy and Analysis **23** (2009).

168.   L. A. J. Garvie, P. Rez, J. R. Alvarez and P. R. Buseck, *Interband transitions of crystalline and amorphous SiO2: An electron energy-loss spectroscopy (EELS) study of the low-loss region*, Solid State Communications **106**, 303-307 (1998), http://www.sciencedirect.com/science/article/pii/S0038109898000210.

169.   A. Nazarov, J. M. Sun, W. Skorupa, R. A. Yankov, I. N. Osiyuk, I. P. Tjagulskii, V. S. Lysenko and T. Gebil, *Appl. Phys. Lett*, **86**, 151914 (2005), http://dx.doi.org/10.1063/1.1872208.

170.   P. G. Etchegoin, E. C. Le Ru and M. Meyer, *An analytic model for the optical properties of gold*, The Journal of Chemical Physics **125**, 164705-164703 (2006), http://dx.doi.org/10.1063/1.2360270.

171.   P. Romaniello and P. L. de Boeij, *The role of relativity in the optical response of gold within the time-dependent current-density-functional theory*, The Journal of Chemical Physics **122**, 164303-164306 (2005), http://dx.doi.org/10.1063/1.1884985.

172.   G. Nesher, L. Kronik and J. R. Chelikowsky, *Ab initio absorption spectra of Ge nanocrystals*, Physical Review B **71**, 035344 (2005), http://link.aps.org/doi/10.1103/PhysRevB.71.035344.

173.   D. P. Yu, Z. G. Bai, J. J. Wang, Y. H. Zou, W. Qian, J. S. Fu, H. Z. Zhang, Y. Ding, G. C. Xiong, L. P. You, J. Xu and S. Q. Feng, *Direct evidence of quantum confinement from the size dependence of the photoluminescence of silicon quantum wires*, Physical Review B **59**, R2498 (1999), http://link.aps.org/doi/10.1103/PhysRevB.59.R2498.

174.   A. V. Kolobov, S. Q. Wei, W. S. Yan, H. Oyanagi, Y. Maeda and K. Tanaka, *Formation of Ge nanocrystals embedded in a SiO_{2} matrix: Transmission electron microscopy, x-ray absorption, and optical studies*, Physical Review B **67**, 195314 (2003), http://link.aps.org/doi/10.1103/PhysRevB.67.195314.

175.   I. D. Sharp, *Structural and Optical Characterization of Ion Beam Synthesized Ge Nanocrystals*, Materials Science and Engineering, University of California, Berkeley, 2006 (unpublished).

176.   L. Rebohle, J. von Borany, H. Fröb and W. Skorupa, *Blue photo- and electroluminescence of silicon dioxide layers ion-implanted with group IV elements*, Applied Physics B **71**, 131-151 (2000), http://dx.doi.org/10.1007/PL00006966.

177. S. Parola, E. Quesnel, V. Muffato, J. Bartringer and A. Slaoui, *Influence of the embedding matrix on optical properties of Ge nanocrystals-based nanocomposite*, Journal of Applied Physics **113**, 053512-053518 (2013), http://dx.doi.org/10.1063/1.4789959.

178. Y. Kawamura, K. C. Y. Huang, S. V. Thombare, S. Hu, M. Gunji, T. Ishikawa, M. L. Brongersma, K. M. Itoh and P. C. McIntyre, *Direct-gap photoluminescence from germanium nanowires*, Physical Review B **86**, 035306 (2012), http://link.aps.org/doi/10.1103/PhysRevB.86.035306.

179. K. C. Bustillo, E. E. Haller, D. C. Chrzan, J. W. Ager, K. M. Yu and J. W. Beeman, (Department of Energy, National Center for Electron Microscopy, LBNL, Berkeley, CA, 2011).

180. P. C. Becker, N. A. Olsson and J. R. Simpson, Erbium-Doped Fiber Amplifiers. (Academic Press, San Diego, CA, 1999).

181. J. S. Jensen, T. P. L. Pedersen, J. Chevallier, B. B. Nielsen and A. N. Larsen, *Rare earth ions and Ge nanocrystals in SiO$_2$*, Nanotechnology **17**, 2621-2624 (2006), http://stacks.iop.org/0957-4484/17/i=10/a=029.

182. M. Fujii, T. Nakamura, S. Miura, M. Inui and S. Hayashi, *Energy transfer from Si nanocrystals to Er ions near a metal layer*, physica status solidi (a) **205**, 47-51 (2008), http://dx.doi.org/10.1002/pssa.200776717.

183. H. Mertens and A. Polman, *Plasmon-enhanced erbium luminescence*, Applied Physics Letters **89**, 211107 (2006), http://link.aip.org/link/?APL/89/211107/1.

184. G. Von Plessen, S. Fischer, F. Hallermann, D. Kumar, A. N. Sprafke and J. C. Goldschmidt, 2012 (unpublished).

185. K. J. T. A. de Dood M J A and A. Polman, *Forster transfer and the local density of states in erbium-doped silica*, Phys. Rev. B **71**, 115102 (2005), http://dx.doi.org/10.1103/PhysRevB.71.115102.

186. H. Mertens, A. F. Koenderink and A. Polman, *Plasmon-enhanced luminescence near noble-metal nanospheres: Comparison of exact theory and an improved Gersten and Nitzan model*, Physical Review B **76**, 115123 (2007), http://link.aps.org/doi/10.1103/PhysRevB.76.115123.

187. M. C. Scott, C. C. Chen, M. Mecklenburg, C. Zhu, R. Xu, P. Ercius, U. Dahmen, B. C. Regan and J. W. Miao, *Electron tomography at 2.4-angstrom resolution*, Nature **483**, 444-U491 (2012), <Go to ISI>://WOS:000301771200038.

188. K. Zhao, Q. Zhang, M. Chini, Y. Wu, X. Wang and Z. Chang, *Tailoring a 67 attosecond pulse through advantageous phase-mismatch*, Opt. Lett. **37**, 3891-3893 (2012), http://ol.osa.org/abstract.cfm?URI=ol-37-18-3891.

189.   P. Chaturvedi, K. H. Hsu, A. Kumar, K. H. Fung, J. C. Mabon and N. X. Fang, *Imaging of Plasmonic Modes of Silver Nanoparticles Using High-Resolution Cathodoluminescence Spectroscopy*, ACS Nano **3**, 2965-2974 (2009), http://dx.doi.org/10.1021/nn900571z.

190.   N. Yamamoto, K. Araya and F. J. García de Abajo, *Photon emission from silver particles induced by a high-energy electron beam*, Physical Review B **64**, 205419 (2001), http://link.aps.org/doi/10.1103/PhysRevB.64.205419.